

CORROSION OF STRUCTURAL MATERIALS IN LIQUID METALS USED AS FAST REACTOR COOLANTS

F. Balbaud-Célérier^a, J. L. Courouau^b, L. Martinelli^b

^aCEA, DEN, DADN, F-91191 Gif-sur-Yvette, France.

^bCEA, DEN, DPC, SCCME, Laboratoire d'Etude de la Corrosion Non Aqueuse, F-91191 Gif-sur-Yvette, France.

Abstract. Due to their satisfying properties of heat transfer such as high thermal conductivity, high heat capacities and low vapour pressures, liquid metals are considered for nuclear systems: Pb, Pb-Bi, Na are considered as coolants of Generation IV fast reactors, and Pb-Li is considered for fusion applications. However, structural materials as well as cladding materials are subject to degradation in these liquid metal environments. Liquid metal corrosion can take various forms: dissolution, formation of intermetallic compounds at the interface, penetration of liquid metal along grain boundaries, etc. The corrosion kinetics depends on experimental factors such as: temperature, thermal gradients, solid and liquid compositions, velocity of the liquid metal, etc. In this paper, corrosion processes in these various environments will be presented. The main parameters affecting corrosion in these environments will be focused on and comparison of the behaviour of structural materials in these various liquid metals will be performed using predictive models.

1. Introduction

Liquid metals are frequently considered for nuclear systems. They are considered as coolants of nuclear reactors (Na, Pb, eutectic Pb-Bi, eutectic Pb-Li, Ga) due to their high thermal conductivities giving them exceptional heat transfer properties. Moreover, depending on the liquid metal or alloy, some properties make them specifically interesting for different applications: sodium is considered as coolant due to its low density, very high thermal conductivity and low melting point, heavy liquid metals are considered as spallation targets of accelerator driven systems due to their high atomic numbers, high neutron yields and low vapour pressures, Pb-Li is considered as cooling and breeding medium in liquid breeder in blanket concepts of future fusion reactors.

However, structural materials which are essentially steels (austenitic and ferritic-martensitic steels) as well as cladding materials can be subject to degradations in these liquid metal environments. Liquid metal corrosion can take various forms: dissolution, oxidation, formation of intermetallic compounds at the interface, etc. The corrosion kinetics depends on experimental factors such as: temperature, thermal gradients, solid and liquid compositions, velocity of the liquid metal, etc. Moreover, in nuclear systems, components are hardly and even not replacable and have thus to work over very long durations under multiple stresses. For example, in Generation IV systems, 60 year lifetime is considered for non replacable components. Thus, this requires, in order to guarantee the integrity of the components during the lifetime of the system and to characterize precisely the changes that the materials are going to encounter, (i) to have a very precise understanding of the corrosion mechanisms and (ii) to model these corrosion processes in order to be able to predict the corrosion rates of the materials considered.

In this paper, we will consider different liquid metal/steels systems focusing on sodium and lead alloys.

2. Corrosion processes in liquid metals used in nuclear systems

As it was said above, corrosion of steels can take various forms in the presence of liquid metals or alloys. In the case of liquid metals used in nuclear systems, three kinds of processes are encountered: dissolution, oxidation, and formation of intermetallic compounds at the interface. The occurrence of

these various processes will depend first on thermodynamic data of the various solid material/liquid metal or alloy system: these data give the equilibrium state of the system and thus the products susceptible to form, and second on the kinetics of the system which will allow to determine if these products predicted by thermodynamics will indeed form and in that case at what rate they are going to form.

In this paper, we won't present any data concerning liquid metal embrittlement which is another type of liquid metal/solid material interaction that can also be encountered in some liquid metals. This type of interaction occurs under the simultaneous or successive action of the environment (liquid metal) and an external constraint. Liquid metal embrittlement can be defined as the partial or total loss of the solid material ductility upon contact with the liquid metal. Liquid metal embrittlement leads to the premature rupture of the material and to a diminution of its ductility [1][2][3][4].

Several cases of liquid metal embrittlement have been observed: cadmium/mercury, aluminium/mercury, aluminium/gallium, etc. Some steels can also present a certain sensitivity to liquid metal embrittlement, this is the case for T91 (Fe-9Cr steel) in the presence of liquid lead and lead-bismuth for which a strong reduction of the steel resistance to low cycle fatigue has been observed [2][3][4].

The three kinds of corrosion processes that can occur are described below:

- Formation of solid intermetallic compounds. This corrosion mode can occur when the solubility of the solid material in the liquid metal or alloy is sufficient so that definite solid compounds exist. This is the case of iron alloys in liquid gallium (Figure 1).

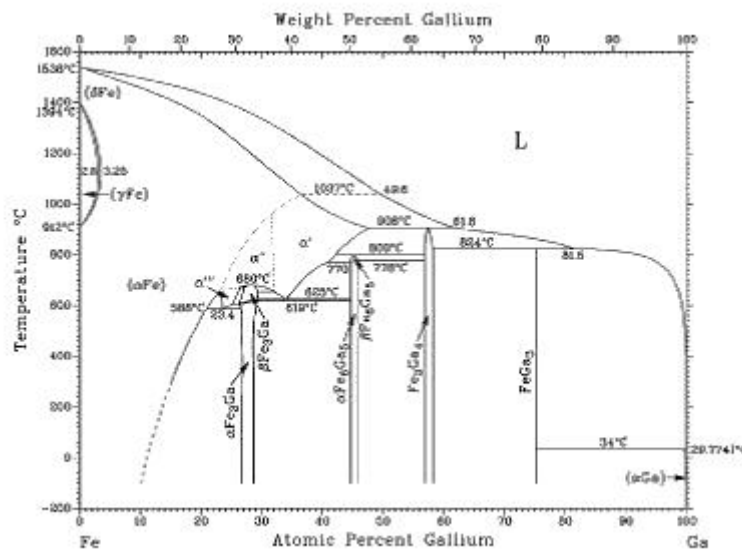


FIG. 1. Fe-Ga phase diagram [5].

- Reaction between elements from the solid material and dissolved species (like oxygen or carbon) in the liquid metal. The reaction product is solid and is a compound constituted of elements coming from the solid material and the dissolved impurity coming from the liquid metal. The existence of such compounds is illustrated in the case of oxygen in an Ellingham diagram (Figure 2 [6]). This diagram represents the equilibrium oxygen partial pressure of pure metal oxidation reactions (or in some cases metallic oxide oxidation reaction). We can see that unlike sodium, lead and bismuth (the BiO/Bi equilibrium is not represented in the figure as it is above PbO/Pb) are oxidized for oxygen partial pressures above the formation of metallic oxides (Fe, Cr and Ni). Therefore, according to thermodynamics, it is possible to form an oxide layer at the surface of a steel in contact with liquid lead and lead-bismuth. In the case of sodium and lithium (or lead-lithium), sodium oxide, Na₂O, and lithium oxide, Li₂O, are more stable than

magnetite, iron-spinel oxide, FeCr_2O_4 , and even Cr_2O_3 (at least for temperatures below approximately 500°C), which shows that none of these oxides will be able to form in liquid sodium or lead-lithium. However, other compounds are susceptible to form in liquid sodium: ternary metallic oxides, like NaCrO_2 , which is more stable than Na_2O as well as chromium oxide, Cr_2O_3 .

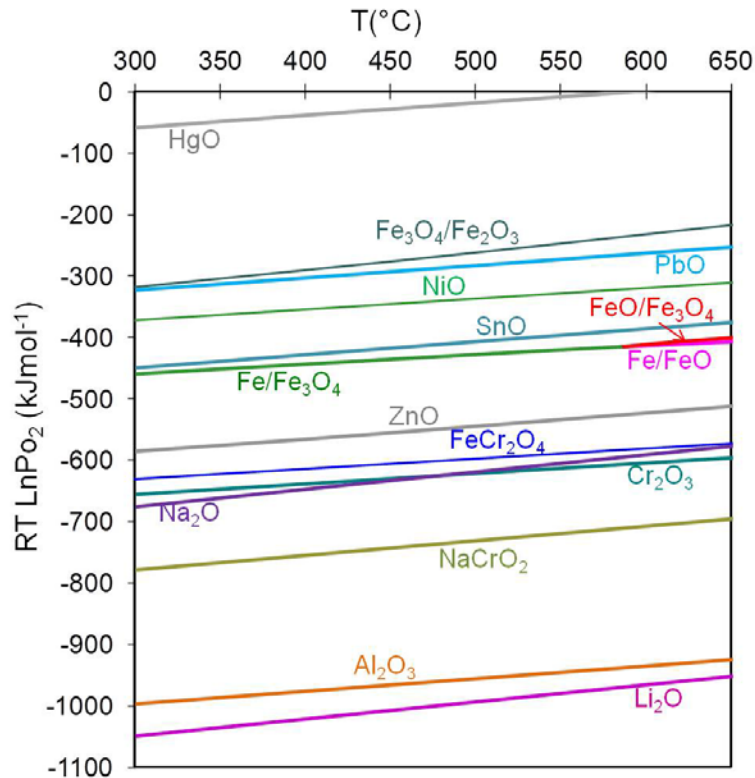


FIG. 2. Ellingham diagram [6].

— Dissolution of the solid material in the liquid metal. The interaction product in that case is liquid under the form of the dissolved species in the liquid metal. This corrosion mode always exists even if the solubilities of the elements from the solid material are extremely low when there is a direct contact between the solid material and the liquid metal which is not prevented by the presence of intermetallic compounds or compounds, like oxides, formed between the dissolved species of the liquid metal and the solid material.

In the case of liquid metals considered for nuclear systems such as : Na, Pb, Pb-Bi eutectic, Pb-Li eutectic and Ga, these three processes are encountered depending on the solid material/liquid metal system considered. In the following, we present the corrosion processes that can occur in these various liquid metals and alloys, the mechanisms, and their kinetics.

2.1. Formation of intermetallic compounds: case of steels in liquid gallium

Two corrosion modes of steels are observed in liquid gallium: dissolution of steels and formation of intermetallic compounds. These two modes occur simultaneously and are difficult to separate. Most of the steels are highly soluble in liquid gallium. Moreover, in most gallium/metals systems, dissolution occurs together with the formation of intermetallics on the solid surface in contact with gallium. Variations of the solubilities of pure metals have been reported in the literature as a function of temperature [7][8][9][10][11][12]. A minimal solubility is observed for refractory metals such as: vanadium, niobium, molybdenum, tantalum, tungsten, etc. The relative solubilities of the metallic elements can be represented as follows:

$\text{W} < \text{Nb} < \text{Mo} < \text{Zr} < \text{V} < \text{Ti} < \text{Cr} < \text{Fe} < \text{Co} < \text{Si} < \text{Y} < \text{Ni} < \text{Mn}$.

The solubilities of metallic elements constituting steels (mainly Fe, Cr and Ni) are extremely high in liquid gallium [12] in [13]. As a comparison, at 400  C, the solubility of iron is 150 wppm in liquid gallium whereas it is 0.3 wppm in liquid Pb-Bi. The iron solubility is thus 500 times higher in liquid Ga than in liquid Pb-Bi, this generally also implies a higher corrosion rate for Fe in Ga.

Corrosion in liquid gallium usually proceeds by dissolution due to the high solubility of metallic species. This leads first to a loss of matter which is followed by the formation of a surface layer leading to a weight gain. For most metals, intermetallic compounds are formed. Figure 3 shows at 400 C, orders of magnitude of corrosion rates depending on the metallic element [12] in [13]. These corrosion rates are consistent with the solubility variations.

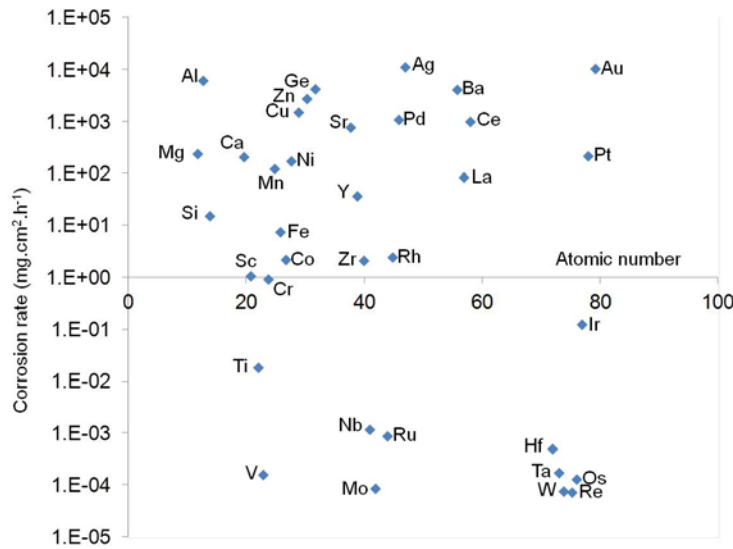


FIG. 3. Corrosion rates of pure metals in liquid gallium at 400  C [12] in [13].

Previous studies have shown that iron, chromium, and nickel have extremely high corrosion rates at 400 C (the rates are a few dozens of mm.yr⁻¹) with the formation of intermetallic compounds which can be adherent (Fe, Ni) or not (Cr) to the metal [13]. The main intermetallic compounds that can form at the contact of a steel are those containing iron: FeGa₃, Fe₃Ga₄, Fe₆Ga₅, Fe₃Ga.

Austenitic steels of the type 316 show a reasonable corrosion at 300 C which becomes significant at 400 C, a thick corrosion layer is observed mainly consisting of iron and gallium. Different corrosion kinetics are observed (first linear and then parabolic for a global duration of 300 hours). This kinetics variation is attributed to an evolution of the corrosion layer morphology. Corrosion rates are around 4 mm.yr⁻¹ [13].

Finally, steels corrode significantly in liquid gallium for temperatures over 300 C. For higher temperatures other materials have to be considered like refractory materials: niobium alloys, vanadium alloys, or molybdenum alloys.

2.2. Interaction between solid materials and impurities dissolved in the liquid metal: case of steels in oxygen containing Pb, Pb-Bi

The Ellingham diagram (Figure 2) shows that the required oxygen concentration for the oxidation of iron can be attained only in the case of lead, lead-bismuth and tin. However, it can also be observed on this diagram that in liquid sodium, a ternary oxide constituted by elements coming from the metal (in that case chromium) and of sodium can be formed. This case will be discussed in chapter 2.3.

In the Handbook on Lead-bismuth Eutectic Alloy and Lead Properties, Materials Compatibility, Thermal-hydraulics and Technologies [14], which compiles the majority of the available data on the corrosion processes in Pb and Pb-Bi, the two corrosion modes predicted by thermodynamics are

indeed observed:

- For oxygen concentrations lower than a concentration close to the one necessary for the magnetite formation (Fe_3O_4), corrosion of steels (Fe-Cr or Fe-Cr-Ni steels) proceeds by dissolution,
- For higher oxygen concentrations, and this up to the PbO saturation concentration, an oxide layer can form at the surface of the steel. The properties of this layer depend on the material tested, the oxygen concentration in the liquid metal, the temperature, etc. In some conditions, this layer can be a protective barrier against dissolution. In that case, corrosion proceeds by oxidation. In some specific conditions (high temperature, intermediate oxygen concentration), both corrosion phenomena can occur (oxidation and dissolution), this is called the mixed mode.

The oxidation of Fe-9Cr steels in Pb-Bi and Pb is characterized by the growth of a duplex Fe-(Cr) spinel oxide scale for the temperature range from 400°C to 620°C in oxygen saturated Pb-Bi.

This duplex scale is constituted of a Fe-Cr spinel layer (stoichiometry $\text{Fe}_{2.3}\text{Cr}_{0.7}\text{O}_4$) in contact with the steel and a magnetite (Fe_3O_4) layer in contact with liquid Pb-Bi. In oxygen saturated conditions, these two scales have approximately the same thickness. In the two layers, lead penetrations are observed on microprobe profiles and SEM observations and confirmed by SIMS analyses.

Few experimental oxidation kinetics have been obtained with sufficient data and for long durations to have a precise characterisation of the oxide layer growth kinetics. However, oxidation kinetics are similar in Pb and Pb-Bi for the same oxygen concentration. Moreover, at 500°C and for durations up to 10,000 hours, the oxidation kinetics obtained shows that the thickness of the oxide layer grows according to a parabolic law:

$$h = \sqrt{k_p t}$$

With t the duration and k_p , the parabolic constant.

Oxidation kinetics obtained for four martensitic steels and two austenitic steels are presented on Figure 4 [15]. This figure shows that the oxidation kinetics obtained are parabolic and that they are higher for martensitic steels than for austenitic steels. Moreover, for martensitic steels, the addition of silicon leads to a decrease of the oxidation kinetics: EP823 compared to T91 and EM10 (the chromium content is also higher).

Table 1 gives the compositions of the steels.

Table 1. Composition of steels (wt %)

Steel	Cr	Ni	Mo	Mn	V	Nb	W	Ti	Si	C
Austenitic 316L	17.0	11.66	2.7	1.53	-	-	-	-	0.42	0.022
Martensitic T91	8.98	0.125	0.962	0.393	0.190	0.075	-	-	0.351	0.086
Martensitic EM10	8.97	0.07	1.06	0.49	0.013	< 0.002	< 0.002	0.01	0.46	0.099
Austenitic EP302	16.0	10.0	-	0.8	-	1.0	-	-	3.0	0.12
Martensitic EP823	12.0	0.8	0.9	0.8	0.4	0.4	0.8	-	1.3	0.18

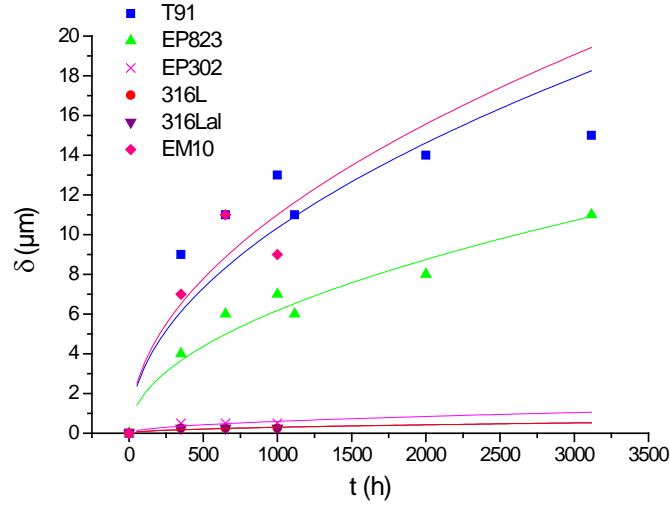


FIG. 4. Evolution of the oxide layer thickness on different steels immersed at 470°C in Pb-Bi containing 10^{-6} wt % dissolved oxygen flowing at 1.9 m.s^{-1} [15].

However, the fitting of this parabolic law only gives a global view of the oxidation kinetics and cannot be used for long term prediction of the materials behaviour. Indeed, this kind of fitting obtained using experimental results for one given material in specific experimental conditions cannot be extrapolated to another material, other experimental conditions and is thus extremely restricted. Moreover, as the physical mechanism of interaction between the solid material and the liquid metal is not known, it is not possible to anticipate an eventual change in the mechanism and then in the kinetics.

Therefore, in order to improve the robustness and the validity on long durations of the choices made for the structural materials it is necessary to understand the mechanisms occurring between the materials considered and the liquid metals or alloys. This requires adequate development of models to allow the prediction of the materials behaviour over the service life..

The oxidation mechanism proposed is the following. The Fe-Cr spinel scale grows at the oxide/steel interface (this was shown by oxidation experiments performed on T91 with ^{18}O tracer in ^{18}O - ^{16}O saturated Pb-Bi at 470 °C [16]) involving the oxygen transport from Pb-Bi to the steel through the oxide scale. The magnetite layer grows at the magnetite/environment interface. The oxygen transport is supposed to be achieved through nanoscale lead penetrations (called nano-channels). However, due to the high oxygen diffusion coefficient in Pb or Pb-Bi, the oxygen transport through the nano-channels cannot be the limiting step of the oxidation process. In fact, the proposed mechanism considers the iron diffusion in the oxide scale as the limiting step. The proposed model is close to the "available space model" [17][18][19][20].

According to the "available space model", the outward iron diffusion (for the magnetite formation) leads to vacancy accumulation in the Fe-Cr steel. These vacancies can segregate at the steel/oxide interface to form nanometric cavities. Oxygen, whose diffusion is fast in the penetrations, can oxidize metallic atoms to form new Fe-Cr spinel oxide filling the nano-cavities. According to this mechanism and to a complex mechanism for oxygen supply [16], the Fe-Cr spinel oxide growth is limited in a fixed volume. In this mechanism, the limiting step is the iron diffusion. The oxidation process is controlled by iron diffusion in both oxide scales. However, the iron flux is just used for the formation of the magnetite layer as the Fe-Cr spinel growth is limited by the fixed available volume. According to these proposals, the Fe-Cr spinel layer thickness depends on the magnetite layer thickness. The Fe-Cr spinel layer thickness is thus calculated as a function of the magnetite layer thickness [16][17][21]:

$$h_{mag}^2 = \left[\frac{Dv}{12} \ln \left(\frac{1 + 2K_v a_{O_2}^{ext/3}}{1 + 2K_v a_{O_2}^{ox/ox^{2/3}}} \right) - \frac{8}{3} D_l K_l \left(a_{O_2}^{ext-2/3} - a_{O_2}^{ox/ox-2/3} \right) \right] t$$

With:

- D_V, D_I , the diffusion coefficients of vacancies and interstitials in the magnetite lattice and in the Fe-Cr spinel lattice,
 - K_V and K_I the thermodynamic constant for formation of vacancies and interstitials in magnetite
 - a_{O_2} : oxygen activities at the two interfaces (ox/ox = spinel/magnetite, ext = magnetite/Pb-Bi).
- Detailed calculations of this equation are presented in [21][22]. Figure 5 shows the results of the simulation compared to experimental results [23].

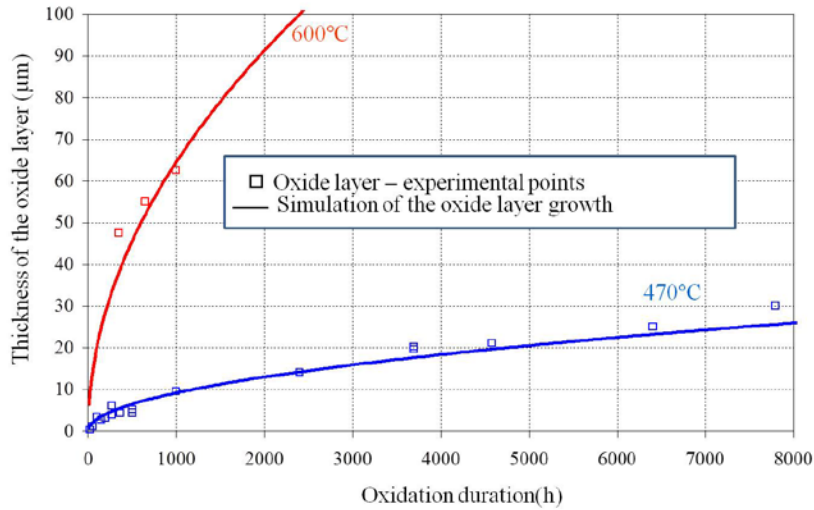


FIG. 5. Simulation of the oxidation kinetics of T91 steel at 470 and 600 °C in oxygen saturated Pb-Bi. Comparison with experimental results [23].

We observe on Figure 5 that we have a very good agreement between the experimental points and the modelling. This result confirms the validation of the oxidation mechanism. What should be noted here is the important oxidation kinetics obtained for T91 even at 470°C. Indeed after 1000 hours of oxidation, the oxide layer is about 10 μm thick which is quite large for this short duration. This thickness can have different impacts on the material: (i) the base material consumption is important leading to a decrease of the thickness of the material, (ii) the oxide layer can be spalled from the material, this spalling releases solid particles in the circuit, and finally the oxide layer has lower heat transfer capacities which may decrease the efficiency of the component if it is a heat exchanging component.

As a conclusion of these results, what can be said is that the maximum temperature of use is around 400-450°C for 316L and 450-500°C for T91. For higher temperatures (500-600°C), other materials are needed. Research is being performed on materials enriched in chromium, silicon, and aluminium (elements which increase the oxidation resistance). However, attention must be paid for core materials due to the irradiation damage. The use of coatings is also investigated: coatings developed by pack cementation or modification of the surface by GESA (or laser) process are studied. For coatings, care must be paid to the mechanical behaviour and resistance of the coating and to the irradiation behaviour as well as to the impact of the coating on heat transfer capability.

2.3. Dissolution of the solid material in the liquid metal: case of steels in Pb-Li and low oxygen containing Pb, Pb-Bi and Na

2.3.1. Dissolution of austenitic steels

Dissolution of austenitic steels (Fe-Cr-Ni) in lead alloys (Pb, Pb-Li and Pb-Bi) and in sodium is heterogeneous: chromium and nickel dissolve preferentially compared to iron. Concerning nickel, this preferential dissolution can be explained by its solubility which is 100 times higher than the solubilities of iron and chromium. The chromium preferential dissolution is still not explained. The corrosion layer, generally, is completely depleted in nickel and strongly depleted in chromium. The

chromium content in the corrosion layer is between 5 and 10 wt% irrespective of the liquid metal or alloy: Pb-Li, Pb, Pb-Bi, Na.

For lead alloys, the dissolution kinetics is linear and the dissolution rate increases with temperature and seems independent of the dissolved oxygen concentration and the liquid metal or alloy velocity for low velocities. An estimation of the dissolution rate of 316L in Pb-Bi and Pb-Li is given [24]:

— For a liquid metal velocity between 0 and 1.3 m.s⁻¹, the corrosion rate can be estimated with:

$$\text{Log}V_{Cor} (\mu\text{m.yr}^{-1}) = 5.3 - \frac{2447}{T(K)}$$

— For a liquid metal velocity higher than 2 m.s⁻¹, the corrosion rate can be estimated with:

$$\text{Log}V_{Cor} (\mu\text{m.yr}^{-1}) = 3.8 - \frac{852}{T(K)}$$

For sodium, the dissolution kinetics is also linear, the dissolution rate increases with temperature, but also with the dissolved oxygen concentration and the fluid velocity in a specific velocity range (Figure 6) [25]. For a fluid velocity higher than 3 m.s⁻¹, the corrosion rate seems to be no longer impacted by the fluid velocity.

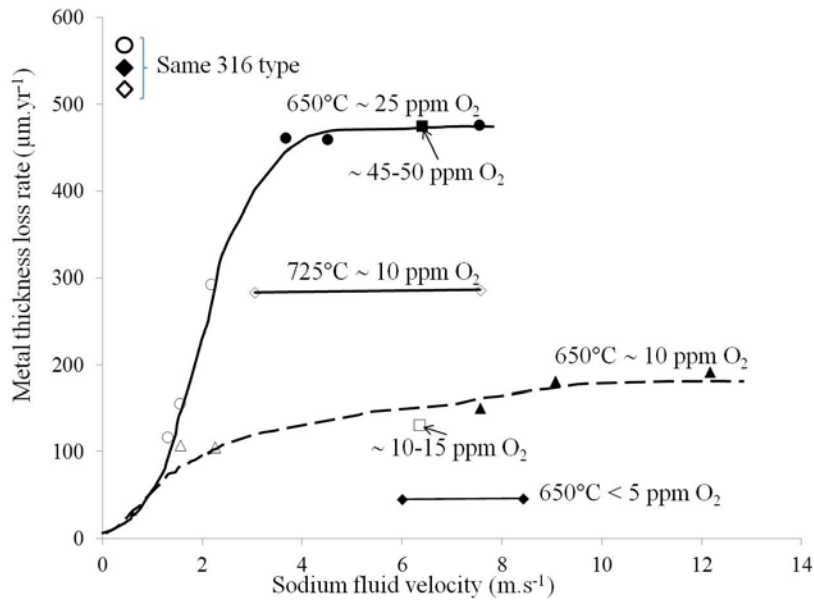


FIG. 6. Influence of the fluid velocity of sodium and of the oxygen concentration on the corrosion rate of different austenitic steels in liquid sodium at 650 and 725°C [25].

In the case of sodium, the specific effect of the dissolved oxygen concentration on the corrosion rate has to be noted. In fact in sodium, when the dissolved oxygen concentration increases, the corrosion rate increases. The mechanism is not clearly understood up to now, however the role of the ternary oxide, NaCrO₂ (Figure 2), which is experimentally observed, is frequently mentioned [25][26][27]. For this reason, the specification on the chemistry of sodium is to have the lowest possible oxygen concentration (<3 wppm) to minimize the corrosion rate.

In liquid sodium, empirical correlations have also been developed based on the proposed mechanisms. For austenitic steels, it is proposed for the high velocity domain (neglecting the downstream coefficient which is attributed to a poisoning of the active sites for iron dissolution) [25]:

$$V_{cor} = \frac{2,01 \cdot 10^{13} T}{x_{Fe}} \left(\frac{O}{O_{sat}} \right)^{2x_{Fe}} e^{-\frac{210254}{RT}}$$

With V_{cor}: corrosion rate (μm.yr⁻¹)

T: temperature (K)

x_{Fe} : iron atom fraction in the steel

O: dissolved oxygen concentration (wppm)

O_{sat} : oxygen solubility (wppm): solubility expression considered: $\log S_O$ (wppm) = $6.46 - 2600/T(K)$

R: Gas constant ($J.K^{-1}.mol^{-1}$)

As an illustration, the corrosion rate of an austenitic steel immersed in liquid sodium at a low oxygen concentration (10 wppm) at 500°C is around $1 \mu m.yr^{-1}$. In lead alloys, for a low fluid velocity, a corrosion rate of $140 \mu m.yr^{-1}$ is obtained and a corrosion rate of $500 \mu m.yr^{-1}$ is calculated for the high velocity domain. However, these corrosion rates are strongly dependent on test realisation conditions. As an example, for 316L in Pb-Bi, at 500°C, a corrosion rate between 70 and $140 \mu m.yr^{-1}$ [28] was measured for a 3000h test whereas, in same conditions, a corrosion rate of $30 \mu m.yr^{-1}$ was also reported for a 6000h test [24].

Consequently, the corrosion correlations must be considered carefully as they give only a macroscopic view of the corrosion rate and of the corrosion process. First, they are restricted to certain types of materials (in this case austenitic steels), secondly they do not take into account all the parameters of influence and they also may not be representative of what occurs on a microscopic scale. Thirdly, these correlations does not allow robust extrapolation of the results. For example, the empirical law for the corrosion rate in liquid sodium considers that if the oxygen concentration is equal to zero, the corrosion rate would be also equal to zero which is clearly not the case. Therefore this relation is only applicable for dissolved oxygen concentrations higher than 3 wppm.

In the case of austenitic steels, this more fundamental approach of the corrosion processes is actually being developed in Pb-Bi and in Na.

2.3.2. Dissolution of ferritic-martensitic steels

Dissolution of ferritic-martensitic steels in lead alloys and in sodium is homogeneous: no preferential dissolution of an element is observed. The dissolution kinetics is also linear.

In liquid Pb-Li, an empirical correlation has been developed allowing the estimation of corrosion rates for ferritic-martensitic steels [29]:

$$V_{Cor} = 8.10^9 e^{-\frac{25690}{1.98T}} v^{0.875} d^{-0.125}$$

with V_{cor} : corrosion rate ($\mu m.yr^{-1}$)

T : temperature (K)

v : Pb-17Li fluid velocity ($m.s^{-1}$)

d : hydraulic diameter (m)

In pure lead and Pb-Bi, no empirical correlation is available. A large variation exists between various experimental results making it difficult to the develop a global empirical correlation. This variation in results can be attributed to the control of the physico-chemistry of the liquid metal or alloy (presence of dissolved oxygen, presence of dissolved metallic impurities). Indeed, these impurities can have an influence on the corrosion rates. The variation in the results can also be linked to the approach used for the measurement of the corrosion rate: the weight loss measurement can be relatively uncertain, the cleaning of the sample must be sufficiently efficient to remove all the remaining liquid metal but without attacking the metal itself. This operation can be relatively complex to perform. The measurement of the residual thickness can also be used but can also be quite uncertain: a very good precision of the measurement has to be guaranteed and the dissolution front has to be homogeneous.

In spite of such uncertainty in the results, an average dissolution rate of $100 \mu m.yr^{-1}$ can be established for ferritic-martensitic steels in liquid Pb and Pb-Bi, for a moderate hydrodynamic regime (fluid velocities lower than $2-3 m.s^{-1}$) and for temperatures up to 400-500°C. For temperatures around

550 C, the dissolution rate is between few hundreds $\mu\text{m.yr}^{-1}$ up to few mm.yr^{-1} , which is extremely high and forbids the use of these materials at these temperatures.

In liquid sodium, another correlation was found which is applicable for both stainless steels and modified Fe-9Cr-1Mo steels. This correlation was established for the evaluation of the corrosion rate of the structural materials specified in the material strength standard for the prototype fast reactor Monju. This equation is applicable for 304SS, 316SS, 321SS, 2.25Cr-1Mo steels and can be conservatively applied to 316FR and modified 9Cr-1Mo steels, for $T = 400\text{-}650$  C and $C_{\text{O}} = 5\text{-}25$ wppm [30].

$$\log V_{\text{Cor}} = 0.85 + 1.5 \log C_{\text{O}} - \frac{3.910^3}{T + 273}$$

With V_{cor} : corrosion rate (mm.yr^{-1}),
 C_{O} : dissolved oxygen concentration (wppm),
 T: temperature ( C).

Literature data give at 500  C, in static liquid sodium containing 10 wppm dissolved oxygen, corrosion rate of Fe-9Cr steels around few microns per year [27]. With the expression above, the calculations leads to a corrosion rate of $2 \mu\text{m.yr}^{-1}$ which is in the same order of magnitude.

As for austenitic steels, the corrosion rate of ferritic-martensitic steels increases with temperature, dissolved oxygen concentration and fluid velocity depending on the hydrodynamic regime.

Concerning the fluid velocity effect, results were obtained in liquid Pb-Bi [31]. Modelling of the dissolution flux was performed assuming that dissolution of T91 steel was equal to iron dissolution (which was confirmed by corrosion tests in the CICLAD device [32]).

The following expression was obtained for the dissolution flux for a mixed control corrosion process that is a process for which neither the diffusion rate in the liquid metal nor the interface reaction rate can be neglected (expressed in $\text{g.m}^{-2}.\text{s}^{-1}$):

$$\frac{1}{S} \frac{\partial m_{\text{Fe}}}{\partial t} = J_{\text{diss}} = \frac{Kk_{\text{pr}}}{K + k_{\text{pr}}} (S_{\text{Fe}} - C_{\text{b}})$$

With m_{Fe} , the weight loss of the steel (g), S the steel/Pb-Bi surface area (m^2), K, the mass transfer coefficient (which is function of the fluid velocity, the hydraulic diameter, the iron diffusion coefficient in Pb-Bi and the Pb-Bi kinematic viscosity) (m.s^{-1}) given for different geometries in [33], k_{pr} the precipitation rate constant (m.s^{-1}) of the iron dissolution reaction, S_{Fe} the iron solubility (g.m^{-3}), and C_{b} the iron bulk concentration (g.m^{-3}) in the liquid alloy.

Finally, if we compare all the dissolution results using the empirical correlations, Figure 7 is obtained. The first comment is that there is an important dispersion in the results obtained with these correlations. Anyway, this figure shows that whatever the temperature, the dissolution rates of the different steels are considerably lower in liquid sodium compared to lead alloys. In lead alloys, even if the dispersion of the different models is quite important, it appears that above 400  C, the dissolution rates of the austenitic steels are lower than the dissolution rates of Fe-9Cr steels. In fact, these empirical correlations give a first overview of the corrosion behaviour of the materials but they cannot be used as robust materials' life predicting tools. This emphasizes the necessity of finely studying and understanding the subjacent corrosion mechanisms in order to develop more robust modelling.

Indeed, the conclusion that can be made is that in the case of lead alloys the choice of materials should be oriented towards materials which will oxidize at very low oxygen concentrations and which will have low oxidation kinetics to avoid the formation of thick oxide layers. Therefore, steels containing Si, Al could be selected and studied for application in these media.

3. Conclusion and perspectives

Even if different liquid metals appear quite different in a first approach, common corrosion features are observed. Essentially, the oxidizing power of the medium will control the corrosion process by generating either dissolution or oxidation phenomena. Even if these phenomena may not encompass necessarily the same mechanisms, similar fundamental approaches for characterizing, understanding and modelling can be used.

What can be said is that generally the corrosion approach is restricted to an empirical approach which only gives a macroscopic view of the corrosion behaviour. However, to guarantee the life duration of structural materials the detailed comprehension of the interaction mechanisms between the solid material and the liquid metals is required as well as the associate modelling. Moreover, this more comprehensive and fundamental approach will also facilitate optimized choices of materials based on their corrosion behaviour.

What has also to be said is that other parameters impact the global corrosion behaviour of a material. One essential parameter which was not discussed in this paper is the influence of the carbon activity which can lead to carburization/decarburization phenomena.

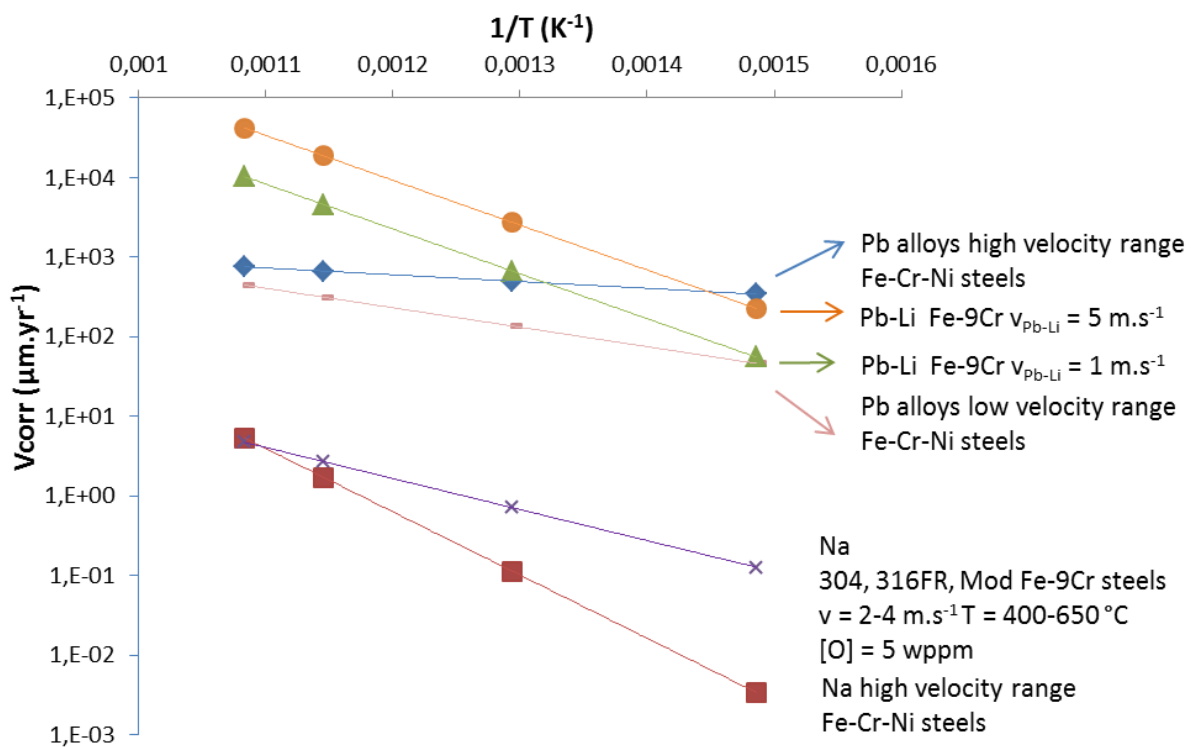


FIG. 7. Comparison of the empirical correlations used for the calculation of the corrosion rates in the different liquid metals or alloys.

REFERENCES

- [1] O. Hamdane, Thèse de doctorat, Etude des mécanismes de plasticité et d'endommagement de l'acier martensitique T91 en présence de sodium liquide, n° 40970, Université de Lille, 2012.
- [2] I. Serre, J.-B. Vogt, Nuclear Engineering and Design 237 (2007) 677.

- [3] A. Verleene, J.-B. Vogt, I. Serre, A. Legris, *International Journal of Fatigue* 28 (2006) 843.
- [4] Z. Hamouche, Thèse de doctorat, Etude de la fragilisation des aciers T91 et 316L par l'eutectique Pb-Bi liquide, Université Paris XI, 2008.
- [5] T. B. Massalski (ed) *Binary phase diagrams*, 2nd edition, ASM international, Materials Park, Ohio (2004).
- [6] S. P. Yatsenko, Yu. A. Anikin, *Sov. Mater.Sci.* 6 (1970) 333.
- [7] S. P. Yatsenko, *Russ. J. Phys. Chem.* 45 (1971) 1095.
- [8] S. P. Yatsenko et al., *Sov. Mater. Sci* 8 (1972) 310.
- [9] S. P. Yatsenko, Yu. A. Anikin, *Russ. J. Phys. Chem.* 45 (1971) 1104.
- [10] S. P. Yatsenko et al., *Russ. Metall.* 3 (1972) 77.
- [11] S. P. Yatsenko, *Gallium. Its interaction with metals*, Nauka, Moscow (1974).
- [12] P. R. Luebbers, W.F. Michaud, O.K. Chopra, Argonne National Laboratory Report, Energy Technology Division, ANL-93/31 (1993).
- [13] *Handbook on Lead-bismuth Eutectic Alloy and Lead Properties, Materials Compatibility, Thermal-hydraulics and Technologies*, OECD 2007, NEA No. 6195, ISBN 978-92-64-99002-9.
- [14] F. Balbaud-Célérier, P. Deloffre, A. Terlain, A. Rusanov, *Journal de Physique IV* 12 (2002) Pr8 177.
- [15] L. Martinelli, F. Balbaud-Célérier, G. Santarini, A. Terlain, S. Delpech, J. Favergeon, G. Moulin, M. Tabarant, G. Picard, *Corrosion Science* 50 (2008) 2523.
- [16] L. Martinelli, F. Balbaud-Célérier, G. Santarini, A. Terlain, S. Bosonnet, G. Picard, *Corrosion Science* 50 (2008) 2537.
- [17] N.J. Cory, T.M. Herrington, *Oxidation of Metals* 29 (1988) 135.
- [18] L. Tomlinson, N. J. Cory, *Corrosion Science* 29 (1989) 939.
- [19] P. Kofstad, *Oxidation of Metals* 24 (1985) 265.
- [20] L. Martinelli, F. Balbaud-Célérier, G. Santarini, G. Picard, *Corrosion Science* 50 (2008) 2549.
- [21] L. Martinelli, F. Balbaud-Célérier, *Materials and Corrosion* 62 (2011) 531.
- [22] L. Martinelli, T. Dufrenoy, K. Jaakou, A. Rusanov, F. Balbaud-Célérier, *Journal of Nuclear Materials* 376 (2008) 282.
- [23] M. Roy, Thèse de doctorat, Mécanisme de corrosion des aciers austénitiques dans l'eutectique Pb-Bi à 500°C, Université Technologique de Compiègne, 2012.
- [24] J. R. Weeks, H. S. Isaacs, *Proceeding of the Chemical aspects of corrosion and mass transfer in liquid sodium*, New York, October 19-20, 1971, Detroit, Michigan, United States

F. Balbaud-Célérier et al.

(1973).

- [25] R. Dillon, "A state of the art review of degradation processes in LMFBR materials", DOE report, Pacific Northwest Laboratories, Richland, Washington, USA (1975).
- [26] J. L. Courouau et al., Proceedings of ICAPP'11, May 2-5, Paper 11152, Nice, France (2011).
- [27] E. Yamaki, K. Ginestar, L. Martinelli, Corrosion Science 53 (2011) 3075.
- [28] T. Flament, P. Tortorelli, V. Coen, H. U. Borgstedt, Journal of Nuclear Materials 191-194 (1992) 132.
- [29] T. Furukawa, S. Kato, E. Yoshida, Journal of Nuclear Materials 392 (2009) 249.
- [30] F. Balbaud-Célérier, L. Martinelli, Journal of Engineering for Gas Turbines and Power 32 (2010) 102912-1.
- [31] F. Balbaud-Célérier, A. Terlain, Journal of Nuclear Materials, 335, 204 (2004).
- [32] F. Balbaud-Célérier, F. Barbier, Journal of Nuclear Materials 289 (2001) 227.

Development of Advanced 9Cr Ferritic-Martensitic Steels and Austenitic Stainless Steels for Sodium-Cooled Fast Reactors ^{*}

T.-L. Sham[†], L. Tan[‡], Y. Yamamoto[§]

Materials Science and Technology Division, Oak Ridge National Laboratory, Oak Ridge, Tennessee

Abstract. Ferritic-martensitic (FM) steel Grade 92, with or without thermomechanical treatment (TMT), and austenitic stainless steels HT-UPS (high-temperature ultrafine precipitate strengthening) and NF709 were selected as potential candidate structural materials in the U.S. Sodium-cooled Fast Reactor (SFR) program. The objective is to develop advanced steels with improved properties as compared with reference materials such as Grade 91 and Type 316H steels that are currently in nuclear design codes. Composition modification and/or processing optimization (e.g., TMT and cold-work) were performed to improve properties such as resistance to thermal aging, creep, creep-fatigue, fracture, and sodium corrosion. Tests to characterize these properties of the subject advanced steels were conducted by the Idaho National Laboratory, the Argonne National Laboratory and the Oak Ridge National Laboratory under the U.S. SFR program. This paper focuses on the resistance to thermal aging and creep of the advanced steels. The advanced steels exhibited up to two orders of magnitude increase in creep life compared to the reference materials. Preliminary results on the weldment performance of the advanced steels are also presented. The superior performance of the advanced steels would improve reactor design flexibility, safety margins and economics.

1. Introduction

The escalating global need for clean energy is driving the rise in operating temperatures of power plants for improved thermal efficiency. This requires the development of advanced materials with superior performance at elevated temperatures. Ferritic-martensitic (FM) steels with 9-12 wt% Cr are candidate materials for many types of reactors, especially for those subjected to greater neutron irradiation displacement damage, such as the Sodium-cooled Fast Reactor (SFR). This is because of the distinct advantages of FM steels compared to austenitic stainless steels in both void swelling resistance and also heat load capability. Among FM steels, 9Cr FM steels are of particular interest because they have smaller radiation-induced ductile-brittle transition temperature (DBTT) shifts as compared with other FM steels, either with higher or lower Cr contents [1]. However, FM steels suffer significant strength degradation at elevated temperatures, i.e., about 650°C and higher. Austenitic stainless steels retain excellent strength at such high temperatures and therefore are prime candidates for high-temperature reactor construction materials.

Creep resistance is one of the essential properties that determine a component's lifetime and design safety margins. It is believed that advanced materials with superior high-temperature performance will greatly improve reactor economics, safety margins and design flexibility. Developed in the 1980s, Grade 92 (Gr92), or NF616, which has a very similar composition, is the latest generation of

^{*} This manuscript has been authored by UT-Battelle, LLC, under Contract No. DE-AC05-00OR22725 with the U.S. Department of Energy. The United States Government retains and the publisher, by accepting the article for publication, acknowledges that the United States Government retains a non-exclusive, paid-up, irrevocable, world-wide license to publish or reproduce the published form of this manuscript, or allow others to do so, for United States Government purposes.

[†] PO Box 2008, MS 6155, Oak Ridge TN 37831-6155

[‡] PO Box 2008, MS 6151, Oak Ridge TN 37831-6151

[§] PO Box 2008, MS 6083, Oak Ridge TN 37831-6083

commercial 9Cr FM steels with higher creep resistance than Grade 91. Despite the recent successful development of high-Co/W alloyed 9Cr FM steels that exhibit significantly enhanced creep resistance compared to Gr92 [2][3], they are not applicable to nuclear applications due to their Co content. As a result, developmental efforts have been focused on advanced nuclear-deployable 9Cr FM steels. The primary approaches have been composition adjustment and processing optimization. Computation thermodynamics using the Calphad approach has guided steel composition adjustment as well as processing temperatures. Use of thermomechanical treatment (TMT), a component of processing optimization, has led to significant properties improvement.

A comprehensive properties assessment of several advanced austenitic stainless steels was conducted, in order to downselect a candidate material for SFR structural applications. Studies were initiated to evaluate the properties of two austenitic stainless steels with different chemical compositions: a) HT-UPS (high-temperature ultrafine precipitate strengthening), developed at the Oak Ridge National Laboratory [4][5], Fe-14Cr-16Ni base; and b) NF709, developed by Nippon Steel, Fe-20Cr-25Ni base. These austenitic stainless steels exhibit excellent creep properties in comparison to similar grades of commercial heat-resistant austenitic stainless steels. The enhanced creep strength is due to the formation of nano-scale MC (M: mainly V, Ti, and Nb) carbides for HT-UPS [4][5], and MX (M: mainly Nb and Ti) carbo-nitrides for NF709 [6][7][8][9] at elevated temperatures. For HT-UPS, it was also reported that prior cold-work (CW) significantly improved the creep-rupture life, since the dislocations introduced by CW act as nucleation sites for the MC carbides, and this allows dense nano-scale MC dispersion in the early stage of the creep deformation [4][5].

HT-UPS has the highest creep resistance, but, unlike NF709, its weldability is very poor. The composition of HT-UPS was modified in an attempt to produce an austenitic stainless steel with balanced properties.

2. Testing

Four types of advanced 9Cr FM steels have been developed. They are optimized-Gr92, Ta-modified, Ti-modified, and V-modified 9Cr FM steels. The compositions were adjusted to favor MX-type precipitates formation and to reduce the amount of Laves phase, $M_{23}C_6$, and Z-phase. A TMT was developed for the optimized-Gr92 and was tested in this work. Aided by computational thermodynamics, the composition of HT-UPS was modified as a part of the project efforts to improve high-temperature strength and weldability. Two additional candidate advanced austenitic stainless steels (Alloys A and B, both Fe-13Cr-16Ni base) were included in the evaluation process.

A variety of property tests including tensile, creep, creep-fatigue, Charpy impact, thermal aging, and sodium compatibility were conducted by the Idaho National Laboratory, the Argonne National Laboratory and the Oak Ridge National Laboratory to evaluate the performance of the advanced steels. In addition, samples of commercial Grade 91 and Type 316H were tested under the same conditions. Microstructural characterization using optical, scanning electron, and transmission electron microscopy were performed to elucidate the microstructure-property relationship of the materials. This paper reports preliminary results on the performance of these steels under thermal aging and creep conditions, as well as on weldability.

Sub-size tensile specimens with a gauge length of 7.62 mm were used for the tensile and creep tests of FM steels. Standard-size creep specimens with a 6.35 mm diameter gauge cross-section were prepared from the austenitic stainless steels. Tensile testing was performed with a strain rate of $3 \times 10^{-4} \text{ s}^{-1}$ at temperatures up to 650°C for FM steels and up to 800°C for austenitic stainless steels. Creep testing was conducted at 600°C with loads of 300 and 260 MPa for FM steels and at 650 and 700°C with the same load of 200 MPa for austenitic stainless steels. Thermal aging was performed on sub-size specimens enclosed in He-filled quartz tubes, at 600°C for 100 and 1,000 h for FM steels, and at 650°C for up to 10,000 h for austenitic stainless steels. Ten-percent (10%) cold-rolling was applied to some of the austenitic stainless steels to examine the effect of CW on mechanical properties.

3. Results and Discussion

3.1. Advanced FM steels

The tensile testing results for the advanced 9Cr FM steels are summarized in Fig. 1, with changes in yield stress ($\Delta\sigma_y = (\sigma - \sigma_{G92})/\sigma_{G92}$) and total elongation ($\Delta\varepsilon_t = (\varepsilon - \varepsilon_{G92})/\varepsilon_{G92}$) relative to Gr92 as a function of testing temperature. The results indicate up to a 60% increase in yield strength and up to a 40% reduction in total elongation for the advanced 9Cr FM steels. The Ti-modified advanced steel exhibited the greatest improvement in yield strength but the largest reduction in total elongation. However, their elongations are still greater than the minimum requirement of Gr92 according to ASTM standard A335/A213. Despite the smallest improvement in yield strength, the more than ~30% increase in yield strength of optimized-Gr92 is an improvement over Gr92.

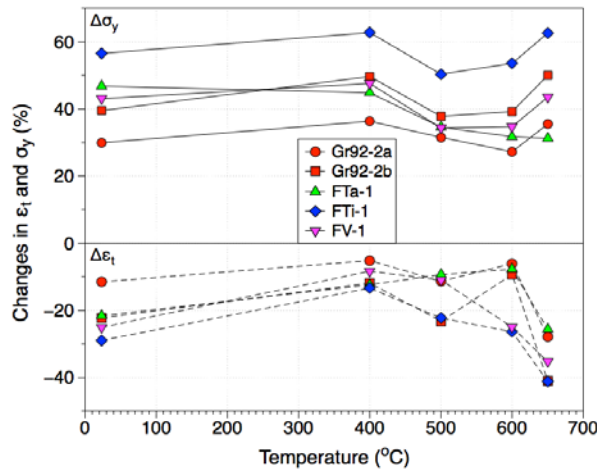


Fig. 1. Relative yield strength and total elongation of the advanced 9Cr FM steels.

Room-temperature tensile tests were performed on the samples thermally aged at 600°C for 100 and 1,000 h. The thermal aging effect on yield strength and total elongation of the advanced 9Cr FM steels is plotted in Fig. 2 with changes in yield strength ($\Delta\sigma_y = (\sigma - \sigma_0)/\sigma_0$) as a function of changes in total elongation ($\Delta\varepsilon_t = (\varepsilon - \varepsilon_0)/\varepsilon_0$), where σ_0 and ε_0 are the values of yield strength and total elongation, respectively, of the steels before thermal aging exposures. The arrows connecting the two data points of each steel denote the changes from the 100 to the 1,000 h thermal aging results. Similar to the general observations in FM steels, the Ta/Ti/V-modified steels showed decreased yield strength but increased total elongation after thermal aging. However, the longer aging (1000 h) recovered the yield strength of the Ti-modified steel to less than 2% reduction from ~5% reduction induced by 100 h, while the longer aging aggravated the yield strength reduction of the Ta-modified steel. In contrast, the optimized-Gr92 with TMT (i.e., Gr92-2b) showed aging-induced hardening with noticeable increases in yield stress and negligible reductions in total elongation. Longer thermal aging time (5,000 h) at the same temperature is in progress for the advanced 9Cr FM steel samples.

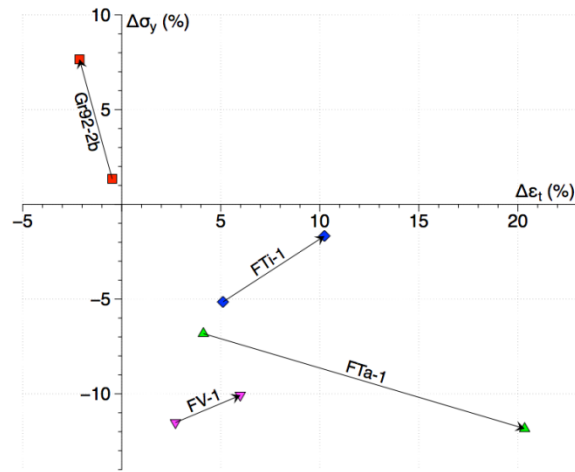


Fig. 2. Effect of thermal aging on yield strength and total elongation.

The aging-induced softening often observed in FM steels is primarily due to dislocation recovery and precipitate coarsening. Figure 3 shows an example of a significant reduction in the number of dislocations in the thermally aged Gr92-2b sample after thermal aging at 600°C for 1,000 h. In contrast to the reduced number of dislocations, the number of ultrafine precipitates was markedly increased after thermal aging, leading to the aging-induced hardening charted in Fig. 2 above.

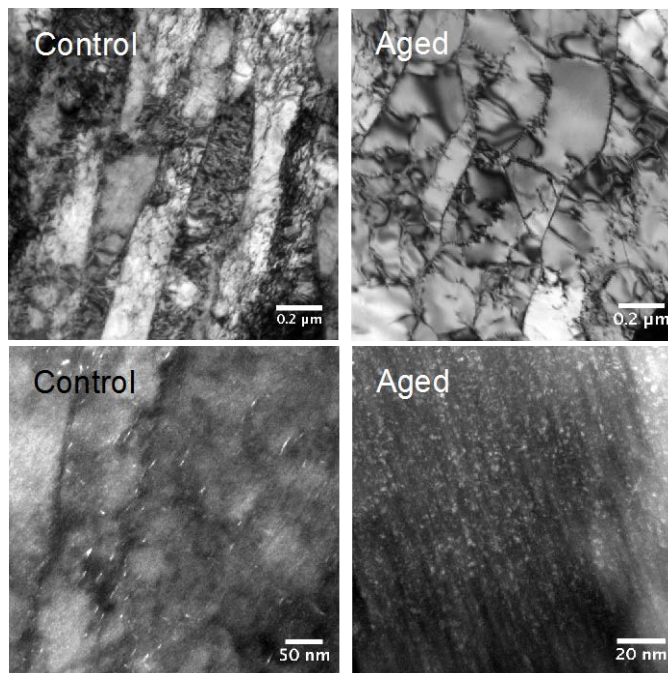


Fig. 3. TEM images of control and aged (600°C for 1000 h) samples of optimized-Gr92 with TMT.

The creep life of the advanced 9Cr FM steels relative to Grade 91 ($X = L/L_{Gr91}$) is presented in Fig. 4. The error bars are from two test specimens per steel. Gr92-2b specimens showed the largest error bar, suggesting that inhomogeneous microstructures may exist in the specimens. It is necessary to develop an optimized TMT for a homogeneous microstructure. All the advanced 9Cr FM steels showed enhanced creep resistance, especially the Gr92-2b and Ti-modified steels, which displayed about 600 to 700 times increase in creep resistance in comparison to Grade 91.

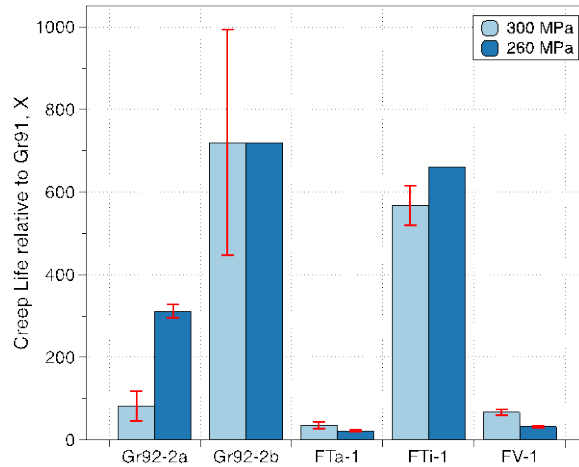


Fig. 4. Creep resistance of advanced 9Cr FM steels.

3.2. Advanced austenitic stainless steels

Improved weldability was successfully demonstrated for two modified HT-UPS steels, designated “Alloy A” and “Alloy B.” Figure 5 shows a comparison of the macro- and microstructure between HT-UPS and Alloy A, after a welding arc with welding parameters similar to a gas tungsten arc weld (GTAW) was laid on the surface of these two steel samples. Both plates received 10% CW prior to laying the welding arc. Cross-sectional microstructure clearly revealed crack formation in the welded material and the adjacent base metal for HT-UPS (Fig. 5a), as expected from the previous report [4]. On the other hand, no evidence of defects could be found in Alloy A (Fig. 5b). Closer inspection of the heat-affected zone indicated no hot-cracking at the fusion boundary in the welded area, although there was a layer consisting of recrystallized grains with no distortion.

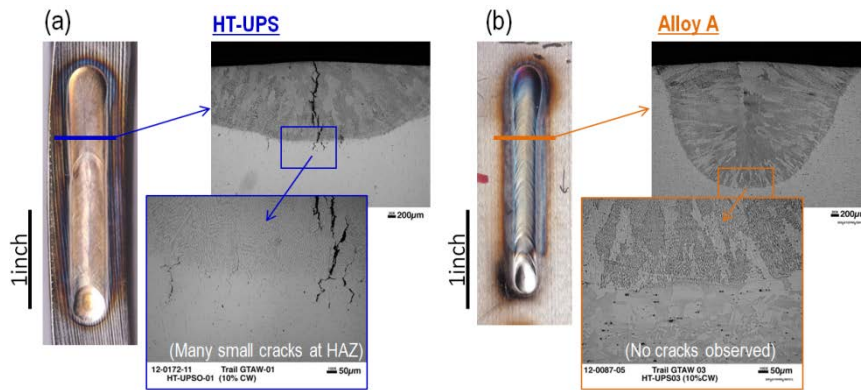


Fig. 5. Comparison of weldability of (a) HT-UPS and (b) Alloy A, by using a gas tungsten arc weld at a condition of 11V, 180A, 8 inch/min, under Ar cover gas, without filler metal. Note that 10% cold rolling was applied to both materials prior to welding.

Subsequently, a GTAW was made by welding two Alloy B plates with 10% CW in a double-V configuration. The GTAW was successfully fabricated, as shown in Fig. 6a. A cross-weld piece with 3/8” thickness was sectioned and subjected to the side-bend test (Fig. 6b). No apparent defect formation was found in the weld, the heat-affected zone or the base metal, indicating excellent ductility.

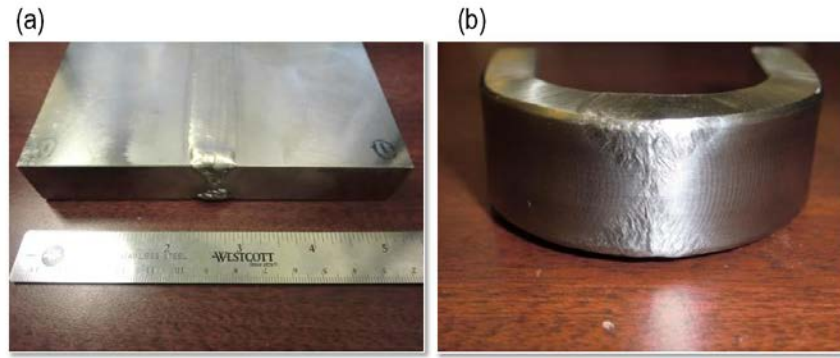


Fig. 6. Double V welded Alloy B with 10% cold work by using gas tungsten arc weld with the same filler material: (a) as-welded plate and (b) a cross-weld specimen after 4T side-bend test.

Figure 7 summarizes the effect of thermal aging at 650°C on the yield stress (YS) of the candidate materials, with and without 10% CW. All tensile tests were conducted at 650°C. All values of YS were plotted relative to those of HT-UPS, with no CW and no thermal aging. In the case of no CW, the changes in YS due to thermal aging were mild, for up to 10,000 h. However, YS of Alloy B and NF709 was relatively higher than HT-UPS in the thermally aged condition. On the other hand, in the condition with 10% CW, NF709 showed the highest YS, followed by Alloy B. There was no significant degradation due to thermal aging for up to 1,000 h. However, after 3,000 h of thermal aging time, HT-UPS and Alloy B showed significant drops in YS, whereas no change was observed for NF709 and Alloy A. Since maintaining tensile properties after thermal aging is indicative of good thermal stability, these results can be used to differentiate the performance of these candidate austenitic stainless steels. Note that the ductility profiles of these stainless steels show adequate elongations with no significant dependence on the thermal aging times in the range of this study.

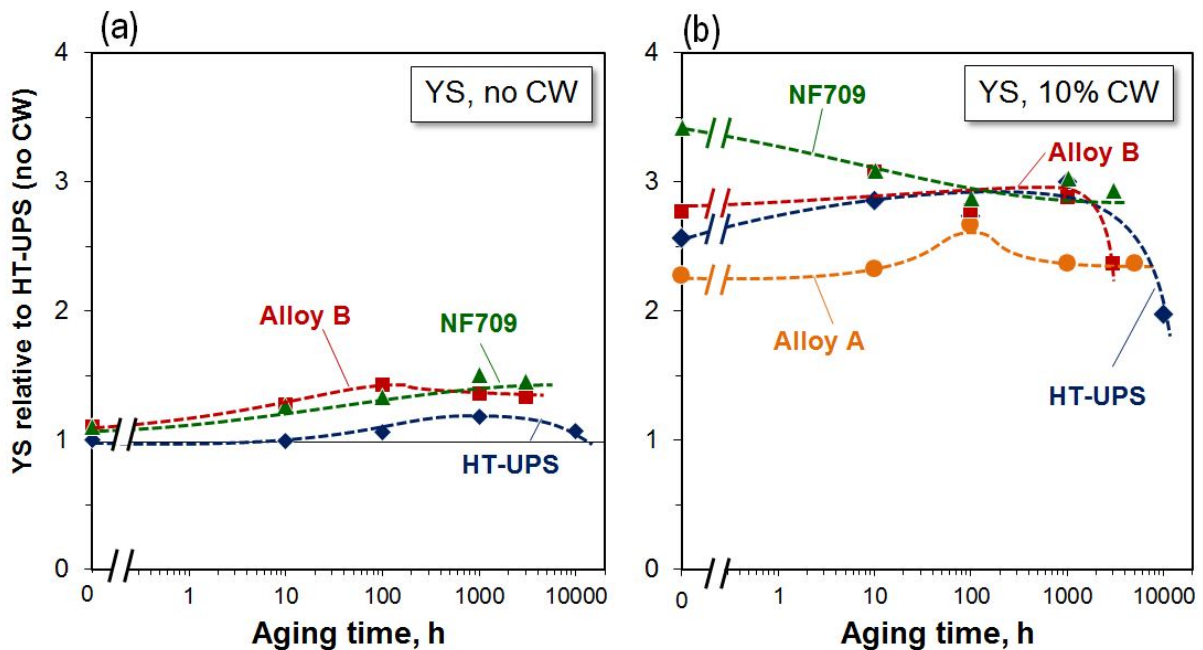


Fig. 7. Effect of aging at 650°C on yield stress of all candidate materials relative to the yield stress of HT-UPS (no cold work) before aging; (a) no cold work, and (b) with 10% cold work.

Comparisons of creep-rupture life for the candidate and reference steels tested at 700°C and 200MPa, and at 650°C and 200MPa, are shown in Fig. 8. All creep-rupture lives were plotted relative to those of 316H with no CW. The results at 700°C clearly demonstrate that 10% CW dramatically improves the creep-life of these steels, extending life approximately 3 to 5 times longer than the steels with no CW.

At any test condition, HT-UPS showed the longest creep life, followed by NF709. Creep life of Alloy B could be comparable to NF709 when 10% CW is applied, although this was not the case with no CW. Alloy A showed the shortest creep life among the candidate austenitic stainless steels, potentially because the alloy composition was slightly different from the optimum condition.

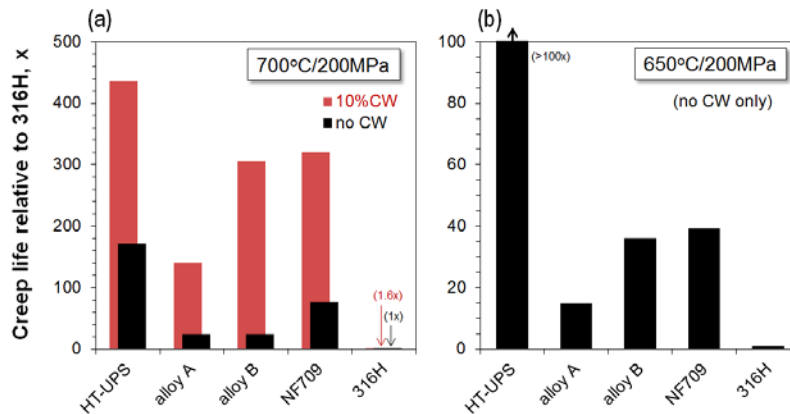


Fig. 8. Summary of creep-rupture life of the candidate materials relative to 316H, with and without 10% cold work, tested at (a) 700°C and 200MPa and (b) 650°C and 200MPa (HT-UPS data from [4]).

The creep-rupture curve of the cross-weld specimen of Alloy B with 10% CW, obtained under the conditions of 700°C and 200MPa, is shown in Fig. 9. The creep curves of the base metal, with and without 10% CW and obtained under the same test conditions, are also included in the figure for comparison. The cross-weld specimen showed a relatively low creep-rate and a comparable creep-rupture life compared to the base metal with 10% CW, indicating that the effect of the weld on the creep properties, such as the microstructural changes at the heat-affected zone shown in Fig. 5 above, was almost negligible. It should be emphasized that NF709 (with no CW) showed less welding effect on creep properties in a wide range of test conditions [10]. Therefore, welding would not be a major factor in degrading the creep properties of Alloy B or NF709.

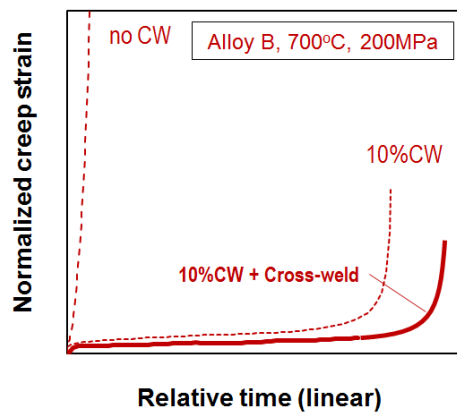


Fig. 9. Cross-weld creep-rupture curves of Alloy B tested at 700°C and 200MPa, compared with the creep-rupture curves of Alloy B, with and without 10% cold work.

4. Conclusion

Further development of 9Cr FM steels and austenitic stainless steels is needed to meet the demanding requirements of advanced sodium-cooled fast reactors. The creep resistance of advanced 9Cr FM steels was greatly enhanced by optimizing their compositions as well as by the use of TMT. The results demonstrate that a creep life enhancement of about 700 times, as compared with Grade 91, can be achieved under the accelerated test conditions employed in this study. The increased density of

ultrafine MX-type precipitates facilitated increased strength and thermal aging stability, leading to improved creep resistance.

Four austenitic stainless steels, HT-UPS, NF709, and two modified HT-UPS (Alloys A and B), were studied and compared to 316H. Alloys A and B exhibited improved weldability compared to HT-UPS. No significant difference was observed in the yield strength of the advanced austenitic stainless steels without CW, when thermally aged and tested at 650°C. However, with 10% CW, HT-UPS and Alloy B showed degradation in yield strength after more than 1,000 h of thermal aging at 650°C. HT-UPS showed the best creep properties among the austenitic stainless steels studied, and NF709 was next. Cross-weld creep-rupture testing of both Alloy B and NF709 revealed no degradation in creep properties due to welding. After evaluating these test results, NF709 is considered the best candidate material because of its relatively well-balanced properties of weldability, thermal stability, and creep resistance.

ACKNOWLEDGEMENTS

This work was supported by the U.S. Department of Energy, Office of Nuclear Energy, Advanced Reactor Concepts (ARC) Program, under contract DE-AC05-00OR22725 with UT-Battelle, LLC. The Shared Research Equipment (ShaRE) User Facility at the Oak Ridge National Laboratory (ORNL) was used to obtain the TEM results. We are grateful to Robert N. Hill of the Argonne National Laboratory and Jeremy T. Busby of ORNL for programmatic guidance.

REFERENCES

- [1] KOHYAMA, A., HISHIMUMA, A., GELLES, D.S., KLUEH, R.L., DIETZ, W., EHRlich, K., Low-activation ferritic and martensitic steels for fusion application, *J Nucl. Mater.* 233-237 (1996) 138-147.
- [2] TANEIKE, M., ABE, F., SAWADA, K., Creep-strengthening of steel at high temperatures using nano-sized carbonitride dispersions, *Nature* 424 (2003) 294-296.
- [3] ABE, F., Analysis of creep rates of tempered martensitic 9%Cr steel based on microstructure evolution, *Mater. Sci. Eng. A* 510-511 (2009) 64-69.
- [4] SWINDEMAN, R.W., *et al.*, Evaluation of Advanced Austenitic Alloys Relative to Alloy Design Criteria for Steam Service: part 1 - Lean Stainless Steels, ORNL-report, ORNL-6299/P1 (1990).
- [5] MAZIASZ, P.J., Developing an austenitic stainless steel for improved performance in advanced fossil power facilities, *J. Metals* 41 (1989) 14-20.
- [6] STAUBLI, M., *et al.*, Materials for Advanced Steam Power Plants: The European COST522 Action, in *Parsons 2003: Engineering Issues in Turbine Machinery, Power Plants and Renewables*, The Institute of Materials, Minerals and Mining, Maney Publishing, London, UK (2003) 305-324.
- [7] KIKUCHI, M., SAKAKIBARA, M., OTOGURO, Y., MIMURA, H., ARAKI, S., FUJITA, T., An Austenitic Heat Resisting Steel Tube Developed For Advanced Fossil-Fired Steam Plants, in *High Temperature Alloys, Their Exploitable Potential*, Elsevier Science Publishing Co., New York, NY (1987) 267-276.
- [8] TAKAHASHI, T., *et al.*, Development of High-Strength 20Cr-25Ni (NF709) Steel for USC Boiler Tubes, *Nippon Steel Technical Report* No. 38, Nippon Steel Corp., Tokyo, Japan, July (1988).
- [9] *Quality and Properties of NF709 Austenitic Stainless Steel for Boiler Tubing Applications*, Nippon Steel Corp., Revision 1.1, Tokyo, Japan (1996).
- [10] Nippon Steel Stainless Steel Seamless Pipes and Tubes, Nippon Steel Corp., Tokyo, Japan, August (2010), website: www.nsc.co.jp/en/product/pipe/pdf/pc318.pdf.

Evolution brought to RCC-MRx Code in relation to ASTRID project

**O. ANCELET^a, M. BLANC^b, O. GELINEAU^c, D. BONNE^c, B. RIOU^c, M. BLAT^d,
J.M. AUGEM^e, C. PETESCH^a, S. DUBIEZ LE GOFF^c**

^aCEA-Saclay, DEN, DM2S, SEMT, LISN, F-91191 Gif-sur-Yvette, France

^bCEA-Cadarache, DER, CPA, Cadarache, France

^cAREVA Lyon, France

^dEDF R&D, Les renardières, France

^eEDF Septen Lyon, France

Abstract. AFCEN (Association Française pour les règles de Conception et de Construction et de Surveillance en exploitation des Matériels des Chaudières Electro-nucléaires) is publishing the fifth edition of the RCC-MR code, named RCC-MRx 2012, the merger of RCC-MX 2008 into RCC-MR 2007.

The main objective of the RCC-MRx is to capitalize the technical feedback of constructions such as SUPERPHENIX, Jules Horowitz Reactor, ITER vacuum vessel, but also to meet the needs of Gen IV projects like the ASTRID project. This paper presents the technical evolutions of the RCC-MRx code which are either already introduced in the 2012 Edition or to be considered for the next addenda : introduction of specific rules for bellows, pumps in sodium, assessment of Modified 9Cr1Mo rules conservatism, consideration of a 60 years life, extension of material database for high temperature, new filler materials...

1. Introduction

Fast Reactors have a unique capability as sustainable energy source in terms of both utilisation of fissile material for energy production and minimisation of the nuclear wastes, due to hard neutron spectrum. As a result of a screening review of candidate technologies and in the frame of the international forum Generation IV, Sodium Fast Reactors (SFRs) are among the selected systems to address the sustainability issues with a coherent set of innovative requirements. Guidelines for the definition of such innovative requirements are the Generation IV goals with significant improvements on economy, safety, environment, waste management and proliferation resistance as promising milestone towards a sustainable nuclear energy.

In terms of safety, improved and robust safety demonstration with regard to former fast reactors is expected: enhanced prevention of whole core melting accidents, exclusion of credible way energetic accident sequences, prevention and mitigation of risks due to sodium chemical reactivity, robustness to external hazards. The level of safety must be at least equivalent to Generation III reactors. Lessons learnt from Fukushima accident will also be taken into account.

A June 2006 French law on sustainable management of radioactive materials and wastes requests that, concerning transmutation of long-lived radioactive elements, studies and investigations shall be conducted, in order to provide by 2012 an assessment of the industrial prospects of those systems. Fast Reactor strategy was confirmed in May 2008 at the Ministry level and in September 2010 an agreement was published between CEA and French Government in order to conduct design studies of ASTRID prototype and associated R&D facilities [1]. ASTRID is a 1500 MWth reactor able to perform experimental irradiation studies. Its Power Conversion Systems (PCS) should deliver 600 MWe [2].

2. Main needs identified for Astrid regarding codification

Regarding codes and material issues, the ASTRID's choices rely heavily on PHENIX, SUPERPHENIX and EFR past experience [4]. A very limited set of well-known candidate materials has been defined, namely 316L austenitic stainless steels with controlled nitrogen for the main vessel and the internals operating at high temperature (550°C), 16MND5 for the forged roof of main vessel, modified 9Cr1Mo ferritic/martensitic steel for SG (Steam Generator), Alloy 800, named "800SPH" (close to grade 1 ASME standard and developed for SUPERPHENIX) for SG helical tubes. The choice of the RCC-MRx code [3] for ASTRID mechanical design is based on the same reasons, as it contains most of the previous RCC-MR code, developed through the past SFR experience.

Despite these very conservative choices, there are many RCC-MRx evolution needs in relation to the ASTRID project.

Firstly, there are many material challenges specific to the ASTRID project.

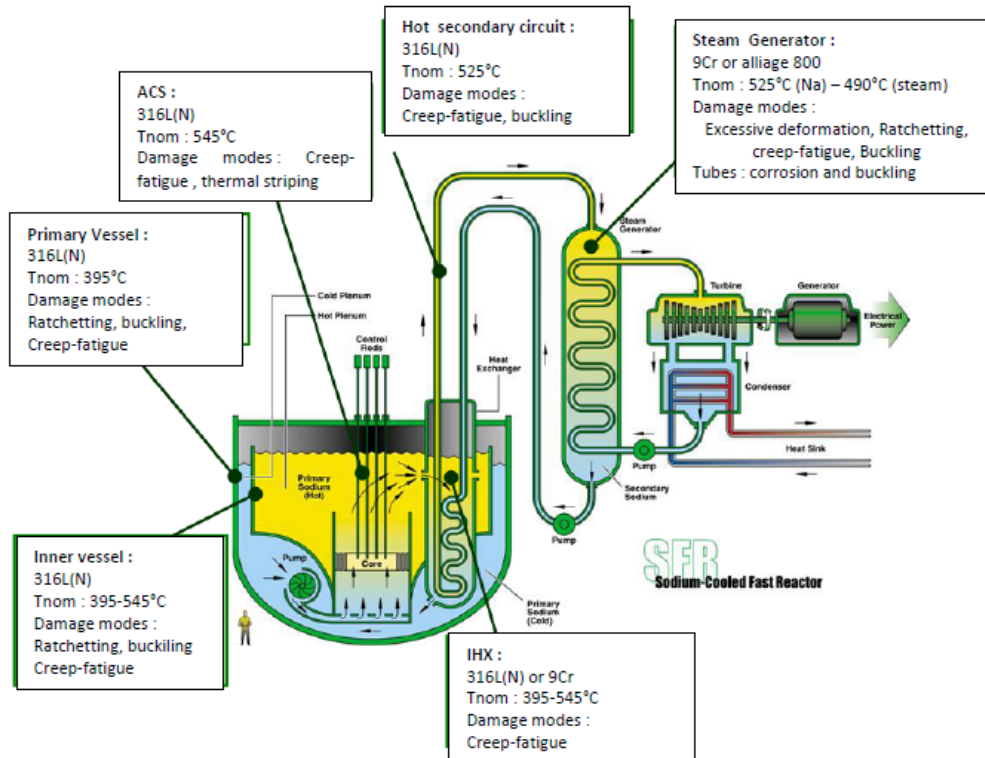
The 60 years targeted lifetime, which is much more than the past projects, demands new experimental data and possibly some mechanical rules update.

Regarding manufacturing, to reduce the number of welds, large forged pieces may be used. In order to increase of the productivity and improve the quality, automatic welding processes are selected, though the SMAW (Shielded Metal Arc Welding) manual process remains necessary, at least for defaults repair. This implies significant filler material research and a lot of testing for all the candidate materials and welds, in the proper reactor conditions.

The Cobalt based stellite hard facing material, largely used in the past, activates too heavily and must be replaced, at least for significant irradiation locations. This objective will be achieved through material research and process development and testing.

The enhanced prevention of accidents, especially core melting implies the study of materials behaviour at higher temperatures.

Consequently a large experimental program has to be conducted to fulfil the ASTRID needs. These results will be capitalized in the RCC-MRx code.



Main damage modes encountered in a SFR

Secondly there are some difficulties specific to SFR reactors which really need some improvements. We can mention irradiation issues (criterion of negligible irradiation, effect of irradiation at high temperature), thermal striping issues, cyclic behavior and creep issues. There is already some ongoing ASTRID R&D on some these issues, which may lead to RCC-MRx rules evolution.

Thirdly, the RCC-MRx code must be fitted to the ASTRID project needs. During the early preliminary design phase (from mid 2010 to the end of 2012), the project's assessment of the code showed some weaknesses for the projected use. Some of them are in relation with the recent evolutions of the code (ie merging with the RCC-MX, ITER modifications and use of the European norms) and have already been addressed and corrected in the 2012 first issue of the code. Other already lacked in RCC-MR, like pumps, bellows, valves, which is an incentive for further code improvements in relation with the ASTRID project.

3. Material and technical challenges specific to the ASTRID and SFR project

Considering the previous elements, the subjects identified as needed developments are detailed hereafter:

3.1. Material characteristics at high temperatures [6]

Regarding the 316L(N) which is the main material used for the primary circuit components, the database for 316L(N) is available today up to 700°C. The data base is globally important but the data are scattered at high temperatures and need to be completed. Today it is noted the following properties to be completed: tension strength, (short term) creep rupture strength, creep laws.

One of the best candidates for the roof is the 16MND5 grade. Indeed, the roof is constituted by thick forged plates which have the benefit from the PWRs experience. Such a material has been introduced

in the RCC-MRx 2012 edition: technical specifications for supplying were introduced as well as thermal and mechanical properties.

Nevertheless, the mechanical characteristics are given up to 370°C, whereas a need exists for higher temperatures in order to be able to perform safety analysis in beyond design situations. The mechanical characteristics (mainly, tensile properties and short term creep rupture) are needed up to 500°C.

Due to their good thermal properties, the ferritic/martensitic steels are good candidates for exchangers, particularly the modified 9Cr1Mo (grade 91) which can bring some improvements for Steam Generators (SG): it combines good resistance in creep, satisfactory resistance to corrosion and correct weldability. It allows having a “compact” SG such as the straight tubes concept.

Nevertheless, no past experience exists on the use of a SG made of modified 9Cr1Mo in the nuclear domain. This grade is included in the RCC-MRx code but its properties have to be completed to be fully used for a SFR application.

In the same way, for welding parts, specific filler material reference sheets (for TIG and SMAW for instance) have to be created in the RCC-MRx and dispositions for PWHT to be integrated also. Those specifications shall be used for the realization of the welded joints to be characterized. Weld coefficients regarding fatigue (Jf) that are missing in the RCC-MRx, could be then defined.

Together with this additional data base, it should be added in the code limitations on the use of materials as regards temperatures. Indeed, some materials, when submitted to high temperatures, may be subjected to a change in their microstructure, making possibly unusable the design rules.

3.2. Lifetime and irradiation issues

3.2.1. 60 Years Lifetime

The past projects have qualified the materials for a lifetime of 30 or 40 years. An important issue for the new generation of plants is the demonstration that these materials are still adequate up to 60 years[6]. The stainless steels such as 316L have proved to be quite stable by the existence of a lot of data coming from cycling tests involving long holding creep or relaxation period, nevertheless some additional tests have to be done to confirm this.

3.2.2. Irradiation issues

For the internal structures of the primary circuit such as the Above Core Structure and the diagrid, the irradiation should not be a real issue as the fluence levels are low (less than 2 dpa). This was the case in the past projects, this is the objective of the present projects in spite of the extension of the life duration up to 60 years.

It is a long process and complicated to carry out experimental irradiations provided realistic data reproducing in an accurate manner all the solicitations (i.e. data at the good temperature, under the neutron flux corresponding to the correct application, and with the correct stress).

The limits expressed in RCC-MRx for negligible irradiation criterion are based on experimental data mainly carried out on base metal. Completion of the database used for the construction of this limit would be beneficial and helpful to justify the confirmation of these limits would be beneficial and needs the acquisition of new irradiation data, specifically corresponding to impact testing of welded materials.

Another track of improvement would be to refine the criterion when creep is significant. Today, the creep-fatigue damage ratio required is equal to 0.1 if irradiation is significant, meaning that very little creep is allowed when irradiation is present. Some new data will allow to a better understanding of the phenomena when little creep is present with few irradiation.

3.3. Structural analysis and design issues

3.3.1. Ratchetting rules

RCC-MR and RCC-MRx codes use an alternative rule to the classical rule “3Sm rule”, called “efficiency diagram rule”. This rule has the advantage to take into account the free level problems by considering that a part of the thermal membrane stress is acting as a primary stress. The question arising is the level of conservatism of this rule especially regarding other problems than free level problems and when creep is significant.

Experimental tests would be useful to lead a reduction of conservatism of the ratchetting rule of the code.

3.3.2. Pumps design rules

The RCC-MRx code does not deal with sodium pumps, whereas it exists a paragraph dealing with water pump. Design rules and testing methods existing have to be re-written introducing the specificity of the sodium pumps.

3.4. Joining processes

3.4.1. Welding

The 316L(N) stainless steel has got a large experience since the construction of SPX1. The principal welding process used was the SMAW. Today the needs have changed and the objective is to have more automatic and more efficient welding processes which are recommended particularly for all the shells of the primary circuit.

This necessitates re-qualifying this material associated with its fabrication process. This means also to characterize the weld joint regarding all the properties introduced in the material Appendix of the Code, including the weld coefficients: Jt, Jr, Jf.

3.4.2. Hard rolling

Intermediate Heat eXchangers installed in the primary system are constituted by expending straight tubes bundle in thick tube plates. The qualification process is described in the RCC-MRx for water exchangers. This has to be evaluated for sodium-sodium exchangers, taking into account the operating conditions in significant creep.

3.4.3. Hard facing materials [5]

Hard facings based on Co base alloy, such as stellite, are largely used in plants for small guiding parts. Shroud tubes are coated in front of subassembly spike to allow the subassembly to be removed and inserted without seizure risk. This stellite is source of important irradiation and high level waste production during dismantling.

Replacing the Stellite is a challenging task, but a lot of studies have been performed worldwide, or are in course of study, to find an equivalent material. A complete physico-chemical characterization of the tested materials shall be done to compare in an appropriate way the friction tests.

Then, this “new” elaboration process shall be introduced in the code together with the way to qualify it.

4. Definition and implementation of the actions to be done for code modification

In addition of the previous needs identified for ASTRID and more generally SFR reactors, a complete examine of the code has been performed by Areva to identified the points to modify to fit the code with the project needs but also with regulation, standards, state of the art up to date.

It led to identify at the end of 2010, more than 40 modifications to implement in the code, with a classification depending on the need of the projet and the difficulties to implement.

Table 1. Improvement actions identified to fit the code for SFR needs

RCC-MRx Chapters	Contents	1: short term 2: medium term 3: long term
A14- 2110	specified mechanical loads and restrain displacements resulting stresses to limit	1
A3	To restore the coherence between STR 16MND5 (RM 212-1 and 213-1) and Annexes A3 13AS	1
A3 - 4S	Limit of negligible irradiation to be reviewed	1
A3.GEN, A3.4S	Molded products: to verify and to validate characteristics	1
RB 3000/RB 4400	Improvement on the coherence between RB400 and RB 3000	1
RB 3200	Rules of progressive deformation/ ratcheting :improvement of the equations, kl+b in significant creep, limitation of the diagram of efficiency rule for specific materials	1
RB 3251.11	List of materials not subjected to measuring defect susceptibility rule to be completed.	1
RB 3290	Consideration of the joints coefficients in the case of the inelastic analysis	1
RB 3600	Use of the CMS2 method for type S damages	1
RB 3691&3692 -RB 6000	Rules of design of supports: improvement regarding creep	1
RB 3800	Text to be improved	1
RB 3800	Introduction of welds for candles	1
RB(RC) 3600	Replacement of EN 49 281 by the NF EN10253-2, modifications concerning the buckling prevention, precisions on the curve to used for linear elastic method of beams	1
RB(RC) 3600	Homogenization of the lists of load to be considered	1
RB(RC)/RD 3600	Creation of a chapter dedicated to the spring effect	1
RB/RC 3800	Applicability of the rules limited when considering creep	1
RB/RC 3800	Adjustment of the categories of the welded assemblies for level 1 or 2 boxes.	1
RB/RC 3900	Rule of design of heat exchangers: editorial modifications	1
RB/RC/RD 3290	Proposal of improvement of the parts on joints authorized	1
RB/RC/RD 2000	Text clarification to have only a practice when a standard is used	1
RB/RC/RD 3600	Editorial corrections	1
RB/RC/RD 3700	Review of the chapters on bellows/ improvement on authorized joints	1
RC 3500	Valves sodium and Argon: code to be completed	1
RD 3600	Adjustment of the RD 3623 f coherence with code RCC-M	1
RD 3600	-Modification concerning the prevention of the risk of buckling , interdiction of the possibility of use of joints with asbestoses , improvements concerning the volumetric examination in RD 3634	1
RD 3600	Modification of the definition of the allowable stress Sh in the analysis of the pipings level 3	1
RDG 4000 REC 2200 - 2300	Level 3 equipments: update of NF EN 13445 and 13480: evaluation of the updates of these standards (creep rules for instance)	1
RB/RD 3000-5000/ RB/RC/RD/RL/RK 2200	For the applications in sodium, limitation of the use of several rules (NF standards EN 13445 and NF EN 13480, valves design rules, pumps design rules, aluminum alloys)	1
RS 1000 to 9000	Coherence between RCC-MRx / RCC-M	1
RS 2900	Clarification: Limits in temperature instead of Limits of Significant Creep in MRx.	1
Tables A3 Gen 1g 1h 1i	Applicability of the data of the appendix A3 for the normalized materials referred in A3GEN	1
A3 GEN	Definition of the level 3 allowable stress: coherence with RCC-M and ASME	2
RB/RC/RD 4000	RB, RC, RD 4000: brazed Assemblies - analysis of the text with regard to the Pressure regulation (ESPN)	2
RS 2000 - RM 3000	Use of KU instead of KV	2
RS 3900	Text to be review for the QMOS in the field of the creep.	2
RS 5000	Adjustment of the text for weld in the field of the creep.	2
RS 8000	Limitation of the use of Iron base and nickel base alloys	2
A3	Validation of negligible irradiation curves for stainless steels	3
RB 3200	Rules for ratcheting: evaluation of rule in significant creep and alternative rule to efficiency diagram for materials others than stainless steels	3
RB 3400/RB 5000	Pumps: rules to be integrated in the code	3
RB 3600	Rules of progressive deformation applied to the pipings	3
RB/RC/RD 3500	Valves design rules: to specify the limit of use, to explicit the consideration pressure equipment regulations, to add buckling rule, to complete rules for bolts and welded assemblies	3
RB/RC/RD 3700	Technical instruction of measures relative to bellows	3

Regarding the identified actions, a strong effort has been put by the ASTRID project to improve as soon as possible the code, and to modify all the points not depending of research and development results.

It has ends in the proposition of most of the modifications identify as priority 1 to the RCC-MRx Subcommittee, see table 2.

Table 2. Propositions of code modifications

RCC-MRx Chapters	Contents	Works Schedule
RS 2900	Clarification: Limits in temperature instead of Limits of Significant Creep in MRx.	DMRx 11-122
RB(RC) 3600	-replacement of NF standard A 49 281 by the NF standard EN10253-2, modifications concerning the prevention of the risk of buckling, precisions on the curve to be used for linear elastic method of beams	DMRx 11-126
RB/RC/RD 3600	Editorial corrections	DMRx 11-127
RD 3600	-Modification concerning the prevention of the risk of buckling - precision to be brought on the way to support the small lines - interdiction of the possibility of use of joints with asbestoses - improvements concerning the volumetric examination in RD 3634	DMRx 11-128
RD 3600	Adjustment of the RD 3623 f coherence with code RCC-M	DMRx 11-129
RB(RC) 3600	Homogenization of the lists of load to be considered	DMRx 11-130
A14- 2110	specified mechanical loads and restrain displacements resulting stresses to limit	DMRx 11-131
RB 3691&3692 et RB 6000	Rules of design of supports: limitation of the effect of the creep on supports recommendation as for the use of unilateral supports on pipings sized for the earthquake.	DMRx 11-131
RDG 4000 REC 2200 - 2300	Level 3 equipments: update of NF EN 13445 and 13480: evaluation of the updates of these standards (creep rules for instance)	DMRx 11-132
RD 3600	Modification of the definition of the allowable stress Sh in the analysis of the pipings level 3 (RD 3600)	DMRx 11-150
RB 3600	Use of the CMS2 method for type S damages	DMRx 11-151
RB/RC/RD 3700	Review of the chapters on bellows/ improvement on authorized joints	DMRx 12-102
RB/RC 3900	Rule of design of heat exchangers: editorial modifications	DMRx 12-176
RB(RC)/RD 3600	Creation of a chapter dedicated to the spring effect	DMRx 12-179
RB/RC/RD 2000	Text clarification to have only a practice when a standard is used	DMRx 12-182
RB 3000/RB 4400	Improvement on the coherence between RB400 and RB 3000	DMRx 12-183
RB/RC 3800	Applicability of the rules limited when considering creep	DMRx 12-186
RB/RC 3800	Adjustment of the categories of the welded assemblies for level 1 or 2 boxes.	DMRx 12-187
RB/RC/RD 3290	Proposal of improvement of the parts on joints authorized	DMRx 12-187
A3 - 4S	Limit of negligible irradiation to be reviewed	DMRx 12-188
RB/RD 3000-5000/ RB to RK 2200	For the applications in sodium, limitation of the use of NF standards EN 13445 and NF EN 13480, valves design rules, pumps design rules, aluminum alloys	DMRx 12-190
RS 1000 to 9000	Coherence between RCC-MRx / RCC-M	DMRx 12-195 to 197 DMRx 12-203 to 208
RB 3200	Rules for ratcheting: evaluation of rule in significant creep and alternative rule to efficiency diagram for materials others than stainless steels	DMRx 12-200 DMRx 12-217
RB 3290	Consideration of the joints coefficients in the case of the inelastic analysis	DMRx 12-209
A3.GEN, A3.4S	Molded products: to verify and to validate characteristics	DMRx 12-210
RB 3800	Text to be improved	DMRx 12-214 et 216

These proposals have been instructed and implemented in the 2012 Edition.

For items identified as priorities 2 and 3, technical working groups but also research and development actions have been initiated to ensure a code completion in adequation with the time schedule for the projects needs.

5. Conclusion

Many RCC-MRx evolution needs in relation to the ASTRID project has been identified and actions has been initiated to ensure and to improve the code but also to guarantee an adequacy between the code and the project needs. Some items need longer developpments such as:

- Consideration of 60 years lifetime : thermal ageing , creep/fatigue approach to re-assess, database to extent (base metal but also welds),
- To strengthen knowledge of modified 9Cr1Mo: re-assessment of high temperature cyclic behavior including cyclic softening , negligible creep curve, ageing factors to assess, weld factors to

O. ANCELET et al.

be completed , technical specifications (procurement and filler material) to complete regarding industrial experience and qualification tests,

- Improvements of design rules: high cycle fatigue/thermal stripping, ratcheting rules in significant creep : reduce the conservatism of present rules, assess and define design rules for bellows according to industrial practices, improved design rules for tubesheets (stiffening effects of tubes),
- Integration of new fabrication specifications: improve specification of welding (higher efficiency automatic process of welding) and NDE, introduce requirements for a new coating replacing stellite, introduce new procurement technical specification to take into account new design features (large forged pieces...)

However, their early identification allows to initiate necessary research and development actions, linked to a codification objective.

NOMENCLATURE

ASTRID	Advanced Sodium Technological Reactor for Industrial Demonstration
DMRx	RCC-MRx Modification Request
EFR	European Fast Reactor
IHX	Intermediate Heat eXchanger
NDE	Nondestructive examination
PCS	Power Conversion System
SFR	Sodium-cooled Fast Reactor
SG	Steam Generator
SGU	Steam Generator Unit
SMAW	Shielded Metal Arc Welding

REFERENCES

- [1] F. Gauché; The French Prototype of 4th Generation Reactor: ASTRID; Annual meeting on nuclear technology, Berlin, May 17-18, 2011.
- [2] P. Le Coz *et al.*; Sodium-cooled Fast Reactors: the ASTRID plant project; Proceedings of ICAPP'11, Nice France, May 2-5, 2011; Paper 11249.
- [3] RCC-MRx 2012 Edition - Design and Construction Rules for Mechanical Components of Nuclear Installations", working document to prepare the fifth edition of RCC-MR named RCC-MRx by AFCEN, Association Française pour les Règles de Conception et de Construction des chaudières Electro-Nucléaires. www.afcen.com.
- [4] O. Gelineau, S. Dubiez-Le Goff, F. Dalle, Ph.Dubuisson, M. Blat-Yrieixd, J.M. Augem, 2011, "materials for sodium fast reactors and prospect for RCC-MRx code" SMIRT2011-171, SMIRT 2011, New Delhi.
- [5] T. Marlauda, D. Pierronb, A-F. Bonnota, M. Blance, L. Forestc, M. Blat-Yrieixd, J-P. Mathieud "Development of Welding and Hardfacing Technology: challenges for ASTRID

O. ANCELET et al.

project", IAEA-CN-199/349, FR13, Paris.

- [6] . Dubiez-Le Goffe, F. Dalleb, M. Blat-Yrieixd, J.-M. Augemcl'article "Qualification of the materials of ASTRID for 60 years lifetime"

Corrosion by oxidation and carburization in liquid sodium at 550°C of austenitic steels for sodium fast reactors

J.-L. Courouau^{1*}, V. Lorentz¹, M. Tabarant², S. Bosonnet³, F. Balbaud-Célériér⁴

¹CEA, DEN, DPC, SCCME, Laboratoire d'Etude de la Corrosion Non Aqueuse

²CEA, DEN, DPC, SEARS, Laboratoire Réactivité des Surfaces et des Interfaces

³CEA, DEN, DMN, SRMA, Laboratoire d'Analyse Microstructurale des Matériaux

⁴CEA, DEN, EC, DADN

^{1 2 3 4}CEA Saclay, F-91191 Gif-sur-Yvette, France.

* Corresponding author : Tel: +33169081643, Email: jean-louis.courouau@cea

Presented by **Error! Unknown document property name.**

Abstract. *In this paper, the recent development on the corrosion behaviour of structural material for SFR is presented. Static corrosion tests on 316L(N) and 15-15Ti steels were performed on the CORRONa setup at 550°C in slightly oxidizing and carburizing sodium. The corrosion proceeds by oxidation of the sodium-steel interface with the formation of a sodium chromite layer (NaCrO₂) in association with a chromium depleted steel matrix where sodium penetrated. This latter layer is followed by a hardened carburized layer. Regular extraction of specimen up to a total time of 5000h allowed gaining kinetics of corrosion based on the determination of each corrosion layer thicknesses from GD-OES analyses. This technique gives accurate evolution of mean thicknesses over a few micrometers range, even though interfaces are partly inhomogeneous. The chemical conditions of the liquid sodium during the test is discussed, especially as regards the expected conditions for both transient and normal operating conditions of a SFR, and as regards the original conditions offered with the setup. Data gained allows setting forward some hypotheses for the corrosion mechanisms', which limiting kinetic should control the overall corrosion kinetics. These hypotheses define the path forwards for the next studies in order to progress towards liquid sodium corrosion modelling.*

1. Introduction

The Sodium Fast Reactors (SFR) are being evaluated by CEA as a generation IV system, as they benefit from the largest technological experience and are considered as one of the most promising systems. The roadmap is set in for the design, construction and operation of prototype reactor, called ASTRID, by the years 2020 [1]. Due to the severe in-core conditions (prolonged neutron irradiation, thermal and mechanical solicitations), innovative materials are being developed to extent the service life-time [2, 3, 4], particularly for the fuel cladding, such as ferritic martensitic steels strengthened with nano-dispersion of oxide particles. Other classes of materials are also studied for different components of the reactor, some of them already benefiting from an important technological feedback: 316L(N) as structural material of the primary circuit of the reactor or 15-15Ti steel; which is another austenitic steel, as reference fuel cladding material for the first core. The operating conditions expected during service life time of the core are as follows: temperature ranging from 370°C to 650°C at the hot peak, hydrodynamic expressed in velocity at the cladding interface in the geometry of former cores as 8 to 12 m/s which represent highly turbulent conditions, very low oxygen concentrations in liquid sodium (< 8 wppm using the Thorley relation [5]). The service life time is expected to last at least 4 years for the thin cladding component of about 500 µm in thickness under high neutron irradiation (200 dpa). The off-normal conditions include the temperature transients ranging from minutes to hours at boiling sodium temperature at the most, as well as the chemical transients. These latter's are here proposed to be taken into account, because of the analysis of the various issues raised by the Nuclear Safety Authorities during the service life time of both Phenix and

Superphenix reactors. Indeed, during the 1990 air contamination incident of Superphenix, the chemical transient for which the assessment of the corrosion had been requested was duration of 100 hours at 210°C of saturation in dissolved oxygen (26 wppm). This is viewed as a preceding issue that must be taken into account as a chemical transient for the primary sodium of the next generation SFR. The conditions for the fixed primary structure are less stringent but the service life time required is 60 years. In addition, the component are thick when compared to the fuel claddings: 370-550°C, a velocity of a few m/s, oxygen being less than 8 wppm, low irradiation damage in normal operating conditions. The transients are defined similarly to the core. The normal operating conditions of the steam generators of the secondary sodium circuits are almost the same, except for the temperature range, 300-550°C, and the chemical transient, now defined by the sodium/water reaction to 200 wppm in oxygen during 2000 h according to the preceding issues raised by the Nuclear Safety Authorities after the Phenix occurrences. This thin component of about 1-3 mm in thickness is expected to last more than 10 years and ideally 60 years too. The excellent compatibility of steel with pure liquid sodium must be emphasized, specifically for the austenitic steels used in the reactors built up to today in their given operating conditions. As a matter of fact, the operating rules of the French operated reactors specified a threshold for the oxygen as regards the issue of the contamination by the radio-activated corrosion products (Co-60, Mn-54, mainly). The oxygen is then controlled at a concentration as low as reasonably achievable to minimize the corrosion products release rate. In addition, the operating experience, associated with rather extensive studies on this issue, although dated of about 25 years for most, allows considering that the corrosion in pure liquid sodium should not be a critical parameter for the design and operation of ASTRID or SFR. However, because of new operating conditions and requirements for materials, there is a need to ascertain this affirmation for both designer and Nuclear Safety Authorities by studying corrosion phenomena and their modelling for long term predictions. Static tests were performed on 316L(N) and 15-15Ti at 550°C for 1600h (test 1) and 5000h (test 2) in slightly oxidising and carburizing liquid sodium. The corrosion phenomena as well as the kinetics measured will be presented and discussed. Some of the results presented here were already partially disclosed [6, 7].

2. Experimental materials and techniques

2.1. Materials

The metal samples exposed to sodium were in the form of flat coupons, 20x10x1 mm for test 1 and 30x20x1.5 mm for test 2. Coupons were cut according to the rolling direction by electrical discharge machining (polished state 900). For test 1, only one of the sides was mirror polished. The 316L(N) (EN1.4401) steel composition is reported in Tab. 1. It presents an austenitic crystalline structure, which is a face-centered cubic crystal structure. The last steps of its fabrication process after rolling consists in a heat treatment at 1120°C followed by water quench. It complies with the RCC-MR-RM 3331 grade 2 specifications. The 15-15Ti alloy composition is reported in Tab.1: it corresponds to the AIM1 grade composition, but not to its metallurgical state which is forged instead of 20% cold worked. It presents an austenitic crystalline structure as well.

wgt. %	Fe	C	Cr	Ni	Mo	Mn	Si	Ti	N	others
316L(N)	Bal.	0.026	17.27	12.13	2.54	1.74	0.31	-	0.069	Cu: 0.29 Co: 0.09 B: 0.0004 S:0.001 P:0.025
15-15Ti	Bal.	0.093	15.16	15	1.3	1.59	0.53	0.49	0.0052	V: 0.03 Al: 0.007 Cu: 0.03 Co: 0.02 Zr: 0.012 B: 0.0065 Ca: 0.0005 Ta: 0.003 S:0.002 P:0.0033

TAB. 1. Composition of alloys coupons.

The sodium used in this work was reactor grade sodium supplied by Métaux Spéciaux SA (Extra refined, 99.95% purity). Calcium (<2 ppm), chloride (4 ppm), iron (1 ppm), potassium (4 ppm) were the main impurities. Sodium was renewed for each test to avoid any accumulation of corrosion

products. Regular samples of liquid sodium were done to ensure negligible variation of these latter. The structures are out gassed prior the initial melting of the liquid sodium in order to limit the initial contamination to the minimum. Then, a purification step by sedimentation at low temperature (110°C), slightly above the melting point, was applied for 48 to 60 hours. This was followed by the skimming out of surface oxides, so as to obtain a mirror like free surface. The expected oxygen concentration should then have been in the range of 3 wppm in weight at the start, which is close to the conditions required. Prototypes potentiometric oxygen sensors using extra high purity yttria doped zirconia with an In/In₂O₃ – Mo internal reference system were tested during the lower temperature stops for the measurement of the dissolved oxygen concentration [8, 9, 10]. During the initial heating of test 1, 6.6 wppm was measured, using the Thorley oxygen solubility relation. Then, the ceramic broke down and contaminated the liquid sodium by 1600 ppm of indium and 20 ppm in oxygen, assuming the total dissolution of the indium oxide, which is thermodynamically less stable than the sodium oxide: -440 kJ/mol(O₂) for In₂O₃ against -610 kJ/mol(O₂) for Na₂O at 550°C. 2 others measurements were done during test 1 at 800 hours: 2.5 ppm and at 1200 hours: 6.4 ppm. Either the indium oxide got dissolved and oxygen was consumed by the corrosion reaction during the test, or its dissolution was kinetically limited, and took some time as could be suggested by the measurements. No measurement was successful for test 2 as the service life-time of prototype sensor was lower than the time required for one measurement. However, all procedures and operations were strictly identical for the two tests, so that identical conditions are assumed in a first approximation. In addition, the contamination released by coupons and structures surfaces when in contact with hot sodium is roughly assessed to an additional concentration of 3 ppm for Test 1 and 10 ppm for test 2. This contamination refers to native oxide dissolution and moisture and other gas out gassing in contact with sodium at high temperature. Then, the initial oxygen concentrations are assumed as 26 ppm for test 1 and 33 ppm for test 2, assuming the instantaneous and total release from contamination sources. The mass balance, performed after the tests, in oxygen consumption for the oxide formation figured out equivalent oxygen concentration reductions of 2.4 wppm for test 1 and 26.4 wppm for test 2 (See latter). Then, depending on release and corrosion kinetics, the oxygen ranged in between 4 to 26 wppm for test 1 and 7 to 33 wppm for test 2. The sodium is then considered as slightly oxidizing for the test conditions, as the concentration is slightly higher than the maximum concentration expected in reactor operating conditions: 8 ppm corresponding to 150°C in oxygen saturation. As thoria doped yttria is no longer available for such oxygen sensor application, studies for substitute ceramic that presents a ionic conduction and a sodium compatibility is engaged since a few years [11, 12] to allow for a continuous oxygen monitoring and for confirming the concentrations obtained by operating procedures. The carbon content in the newly supplied sodium is thought to be in excess in the range of 10-30 ppm, which should be carburizing towards the structural steels. Structural materials in contact with the liquid sodium are the crucible in molybdenum (Ø147x166 mm in contact with sodium) and the thermo well made of 316L steel (Ø6.4x166 mm immersed in sodium). The molybdenum is stabilized by lanthanum oxide dispersion at 0.7% in weight. Apart from being inert toward sodium, it presents a re-crystallization temperature above 1400°C, well above the designed temperature of the setup (750°C), which preclude any embrittlement of the crucible with operating time.

2.2. Experimental setup

The general diagram of a CORRONa setup, which was partly presented elsewhere [6], is presented in Fig. 1. The liquid sodium (1) is contained in the molybdenum crucible (2), which is set in the thermal well (3) and is accessible by the purified argon gloves (O₂ < 5 vpm, H₂O < 10 vpm). The well is heated by a high-temperature oven from the outside (6 kw – 850°C) (4). The higher section of the well comprises coolant channels (5) making it possible to maintain the temperature with a value close to the room temperature by circulation of one coolant, a terphenic oil, maintained at a constant temperature of 55°C by a thermo cryostat. The well is fixed on the floor of the gloves box (6) using a fitting flange. Gas inlets and outlets (7, 11) are used for argon sweeping, whose operation is done before test, and for the pressure monitoring when the well is closed tight from the purified argon with a cover (8) during a sodium test: the low volume of argon then trapped in the well balances itself with the liquid sodium when the temperature is increased, whose contamination is negligible, but this reduces any further contamination. This cover is cooled by the same coolant (10). Various tight passages are present to measure the liquid sodium temperature via a type K thermocouple, beforehand calibrated, set in the

thermal well (9). Sodium vapours are condensed and returned liquid to the sodium bulk thanks to the reflux condenser (12) composed of 316L wire mesh and 304L steel. The condenser allows avoiding any accumulation of sodium aerosols in the upper cooled section of the well. The well is made according to a resistant design to avoid any risk of contact of the coolant with the sodium, as well as any risk of rupture that would generate a sodium fire: seamless manufacturing, 8 to 15 mm in thickness, etc. However, in case of such a contact, a fraction of the oil would be vaporized and give rise to a large pressure increase with potential dramatic consequences such as the destruction of the setup. So, two 6 bars bursting disks (14) of 2.54 cm in diameter are implemented in the upper cooled section of the well to obviate any possible overpressure while maintaining the well tight during normal operation. In case of such event, released gases and products pass through a discharge line equipped with aerosols filter (13). The oxygen monitoring is done with a zirconia doped yttria ceramic thimble (15), which is immersed in the liquid sodium the time just required for the measurement, because of limited service life-time. The steels coupons (17) are fastened to the condenser with molybdenum wire (16).

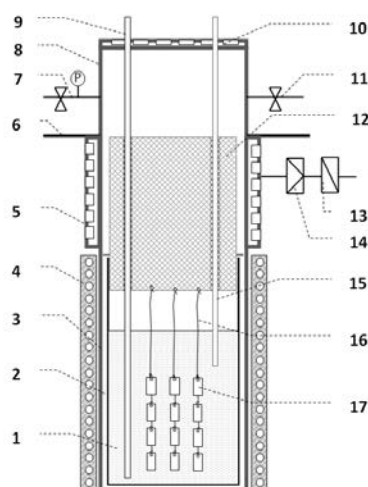


FIG. 1 CORRONa setup in static configuration.

(1- Liquid sodium, 2- Molybdenum crucible, 3- Thermal well, 4- Oven, 5- Cooling channels, 6- Gloves box floor, 7- Gas inlet and pressure monitoring, 8- Well cover, 9- Temperature well, 10- Upper cover cooling section, 11- Gas outlet, 12- Sodium vapour reflux condenser, 13- Aerosols filter, 14- Bursting disks, 15- Oxygen sensor, 16- Molybdenum wires, 17- Corrosion specimen).

This design gives rise to a temperature gradient of 40 to 80 °C in between the well and the crucible because of the isolating argon layer, which explained the over sizing of the oven power to obtain a sodium temperature of at least 650°C. However, because of the very high thermal conductivity of the sodium, the sodium temperature is homogeneous in the crucible excepted near the free level on a very short distance, estimated to roughly 10 mm. This design presents the critical advantages as regards safety to contain the sodium by a second barrier of confinement that can be monitored during operation (well + crucible, cover + gloves box), as well as to facilitate all of the sodium handling operations before and after each corrosion test. The well is made of alloy 625 grade 2 (NiCr22Mo9Nb), which operates up to 950°C in air with insignificant oxidation. As matter of fact, the maximum achievable operating temperature depends on the reflux condenser efficiency, as the cooling of the upper section of the well and cover is not critical. With the various condenser designs tested up to now, a maximum temperature of 660°C was obtained so far. Other functions are under development, such as rotating cylinders to simulate the hydrodynamics directly onto the corrosion coupons and a mini sodium loop implementation within the gloves box to control the liquid sodium chemistry in a way similar to that of reactor circuits [6].

The tests were performed in static conditions at a temperature of 550°C for 1600 hours for test 1 and 5000h for test 2. For test 1, 12 coupons of 3 different steels, 316LN, 15-15Ti and Mod9Cr1Mo, were

immersed and extracted every 400 hours. The ratio of surface over volume was 0.3 dm^{-1} , with 2.8 L of liquid sodium at 550°C and 0.88 dm^2 of steels surfaces in total, including the thermo well and the other coupons. For test 2, 24 coupons of different grade of Mod9Cr1Mo steels as well as 4 coupons of 316LN steel tested so as to provide reference value, were immersed and extracted every 1000h or 2000h. Ratio of surface over volume was 1 dm^{-1} , with 2.82 L of liquid sodium at 550°C and 2.88 dm^2 of steels surfaces in total including thermo well and other coupons.

Coupons were degreased prior to the tests. After the immersion in sodium, they were cleaned of any retained sodium by pure ethanol. Storage is then made under primary vacuum in a desiccator. The examinations consisted in weight variation measurement, X-ray diffraction analysis (XRD), scanning electron microscopy (SEM) and glow discharge- optical emission spectroscopy (GD-OES). Coupons were also cross-sectioned, polished metallographically and examined by SEM and electron probe microanalysis. Some sodium sample and solution of cleaning ethanol were characterised for their impurities content.

Glow Discharge Optical Emission Spectrometry (GD-OES) is an analytical technique used for the determination of depth profiles in a large variety of solids. The instrument used is a GD-Profilier 2 from the company Horiba Jobin Yvon. The glow discharge was powered by a 13.56 MHz radiofrequency generator. A 4 mm diameter copper anode and 99.9999% purity argon gas were used to sputter the sample (800 Pa and 30 W). The emission responses from the excited sputtered elements (O, Fe, Cr, Ni, Mo, Na, C, Si, Mn,...) were detected with a polychromator of focal length of 500 mm. A monochromator was used to determine the concentration of sodium. The calibration curves used to quantify the metal elements were obtained by using bulk reference materials. The resulted depth was measured with a perthometer (PerthoConcept , Mahr Measure) to verify the depth quantification of analysis zone.

3. Results and discussion

All coupons exposed during these 2 tests lost their brightness and became discoloured, progressing from dull grey to near black. All coupons gained mass during the test: from $+ 0.67 \text{ mg/dm}^2/\text{d}$ after 1000 h of exposure to sodium for 316L(N) during test 2, the weight variation decreased gradually to $+ 0.21 \text{ mg/dm}^2/\text{d}$ after 5000 h. Once steady state is achieved, the weight gain (y , mg/dm^2) appeared to follow a parabolic relation with time (t , h), according to $y = 0.4027.\sqrt{t}+15.753$. Weight variations measured for 316L(N) and 15-15Ti of test 1 are similar although not exactly comparable as one of the side was mirror polished. For these latter, the weight variations for 15-15Ti appeared lower by 25% when compared to 316L(N) exposed within the same test and surface conditions.

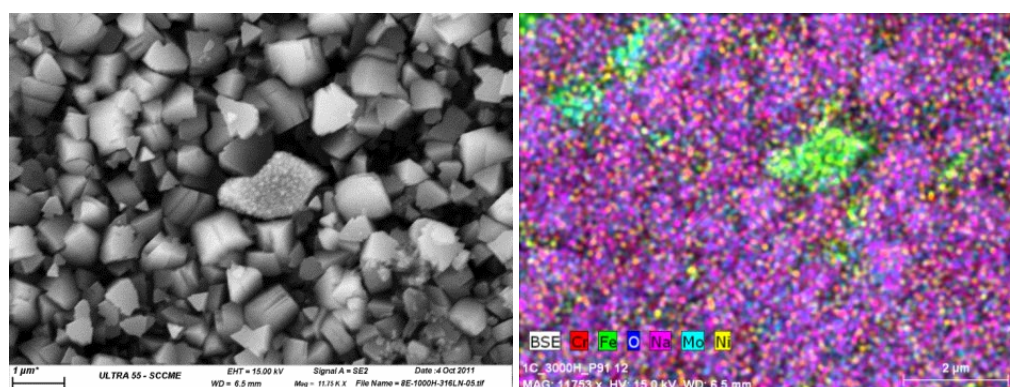


FIG. 2: SEM micrograph of the surface of the 316L(N) exposed at 550°C for 1000 h and associated energy dispersive X-rays cartography (X11750).

The XRD analysis determined with a rather high confidence the presence at the interface of the two followings corrosion products: ferrite phase characterised by a body-centered cubic crystal structure and sodium chromite (NaCrO_2) phase characterised by a rhombohedral crystal structure, with probably a preferential orientation of the plans (006) in parallel to the analysed plan. Indeed, the peak

intensity of this group of plan appeared abnormally high by comparison with the isotropic case. Lastly, all other small peaks were identified as being issued from the sodium degradation products with the atmosphere such as sodium oxide (NaO_2), sodium hydroxide (NaOH) and sodium carbonate (Na_2CO_3). This implies that sodium is present in the layer degraded by the corrosion and is unaffected by the sodium removal step. No carbide (M_{23}C_6), nor molybdenum rich phase (Fe_2Mo), or silicate ($\text{Na}_2\text{O} \cdot (\text{SiO}_2)$) were identified.

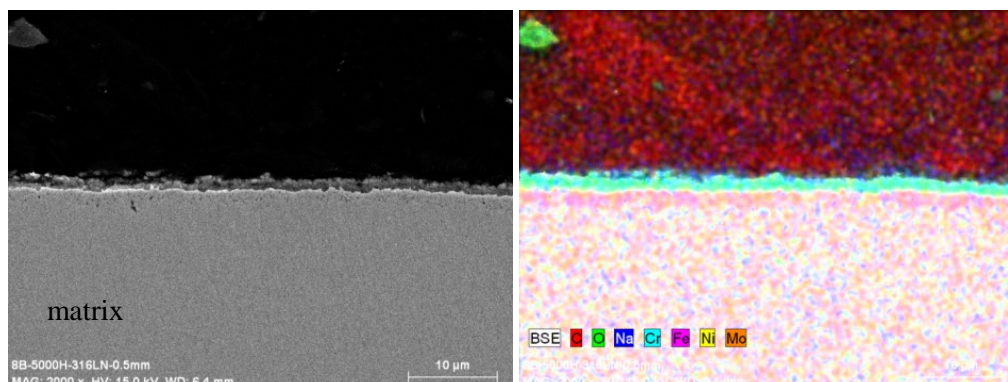


FIG. 3: SEM micrograph of the surface of the 316L(N) exposed at 550°C for 5000 h and associated energy dispersive X-rays cartography (X2000).

The dominant feature observed on the surface of coupons is the presence of sodium chromite crystallites, as well as some steel particles depleted in chromium whose size stays in the range 0.5 to 1 μm (Fig. 2). Sodium chromite shows itself under the shape of small crystals piled some on the others on the surface of the metallic matrix. Sodium chromite crystallites appear equivalent in size for the greater part, of the order of 500 nm, with a possible textured effect that could explain the triangular aspect of most. This layer seems inhomogeneous and very porous. Finally, the last group of particles observed on surface corresponds to the sodium degradation products with air, on the condition of sufficient exposure. For instance, very fine needles of 200 nm to 500 nm of width on 2 to 10 μm of length, rich in carbon and sodium, soluble in pure ethanol, are observed after sufficient exposure to air of the coupon (weeks). They are identified as sodium carbonate, which provide another indirect evidence of sodium insertion into the corrosion layers.

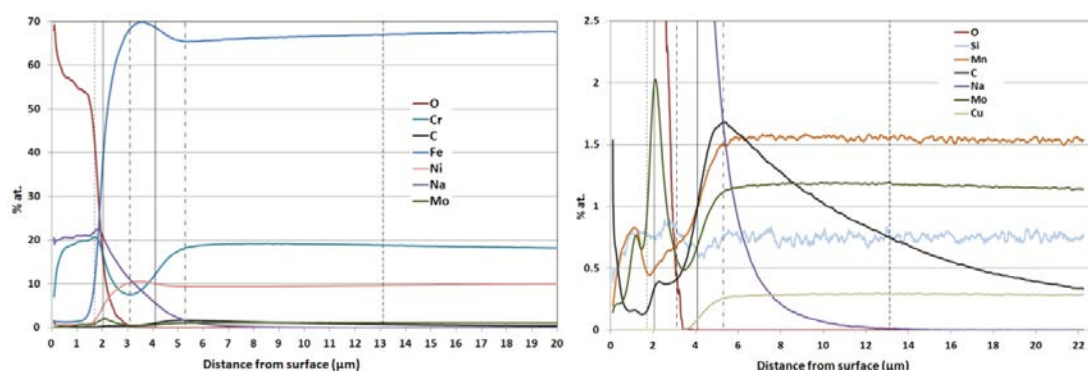


FIG. 4: Quantified GDOES alloying element concentrations of the 316L(N) exposed at 550°C for 5000 h showing position of the corrosion interfaces (left to right : higher to lower concentrations).

The general feature observed on the cross-sectioned coupons for both steels (Fig.3 & fig 5) or based on examination of the GDOES profiles (Fig. 4) showed the formation of a sodium chromite layer on the interface, increasing in thickness and homogeneity with exposure time. For the 316L(N) exposed at 550°C for 5000 h, its thickness reached about 2 μm. The ratio of Na and Cr in this layer is equals to one according to the GDOES profiles, which agrees with the sodium chromite composition. The oxygen is semi-quantified by GDOES, which may explain the higher than expected oxygen level. Below the sodium chromite layer, a chromium depleted layer is found. For the 316L(N) exposed at

550°C for 5000 h, its thickness reached about 2 μm as well. The mean chromium content is 7 at.% for 316L(N) and 4 to at.% for 15-15Ti calculated from the minimum values observed for each GDOES chromium profile. This layer includes a number of fine precipitates or porosities, whose mean size is roughly assessed to 50-100 nm. Their distribution appears as homogeneous within this layer. Precipitates are rich in silicon and oxygen, with a ratio of roughly 2 oxygen for one silicon, as observed on the 15-15Ti with the electron dispersive X-rays spectroscopy (EDS). In addition, although the electron probe microanalysis present an interaction volume of 1 μm in diameter, and although the sodium is an element complex to follow with this technique at such a low concentration, sodium, silicon and oxygen revealed a joint behaviour when the probe passed over one such precipitate. The corrosion feature may then involve internal oxidation of the steel, leading to either SiO_2 or sodium silicate, $\text{Na}_2\text{O}(\text{SiO}_2)$ formation. In addition, the GDOES sodium profile presents a distinct behaviour from oxygen: when oxygen decreased to the null value in the chromium depleted layer (3 μm in Fig 4), sodium decreased at a comparatively lower ratio and disappear only after a depth about 3 times larger (9 μm in Fig. 4). This demonstrates that sodium presents a distinct behaviour in the matrix from the chromite formation mechanism at the matrix interface. It follows that creation of porosities, latter or jointly, filled with sodium is necessary to obtain such profiles. The sodium chromite formation may be preceded or followed by liquid sodium penetrations into the depleted chromium matrix that would explain the presence of sodium in this layer as well as the chromium depletion by selective chromium dissolution toward sodium.

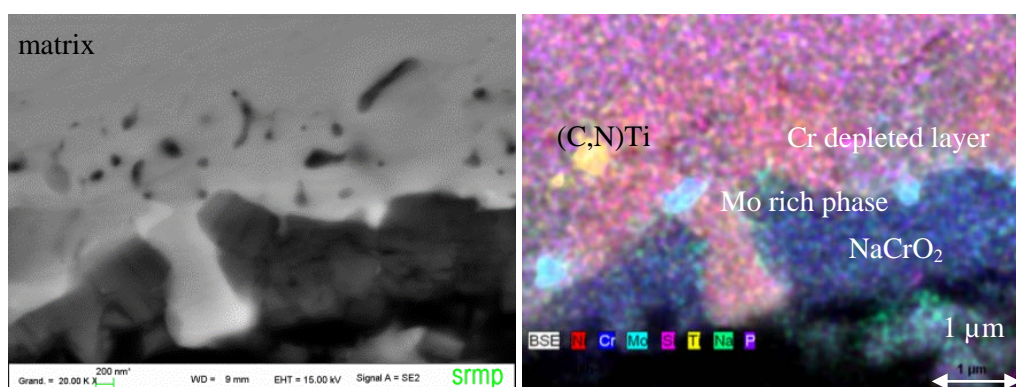


FIG. 5: SEM micrograph of the surface of the 15-15Ti exposed at 550°C for 1600 h and associated energy dispersive X-rays cartography (X20000).

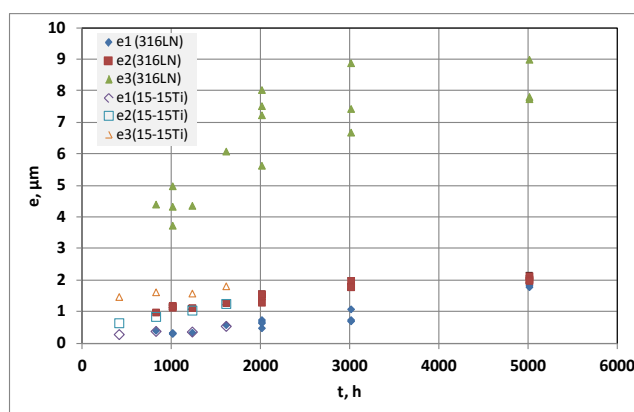


FIG. 6: Evolution of the thicknesses of the corrosion layers of 316L(N) and 15-15Ti exposed at 550°C for 1600 hand 5000h (e1: oxide; e2: Cr depleted; e3:carburized).

Molybdenum presents a peak on the interface in between the oxide and chromium depleted layer, which is explained by the formation of Mo rich crystallites, whose crystal structure could be the Chi phase ($\text{Fe}_{36}\text{Cr}_{12}\text{Mo}_{10}$). The carbon content appeared as unaffected in this layer, whereas the copper disappeared. The iron and nickel increased within the same ratio, which might be due to the chromium

depletion. If Ni and Fe were dissolved, they would do so at the same kinetics, meaning there is no preferential nickel dissolution in these conditions. Finally, one last layer only affected by carbon appeared thanks to the GD-OES profile, with an overall carbon increase by a factor 4. For the 316L(N) exposed at 550°C for 5000 h, its thickness reached about 9 μm assuming that the corrosion interface is set by the chromium inflexion point and the carbon middle height median. The source of carbon is the liquid sodium that presents an excess of carbon in solution when new. Indeed, the mass balance between the carbon lost in the sodium chromite layer, or even in the chromium depleted layer, cannot justify itself the carbon increase of the carburized layer. The position of the carbon maximum on the GD-OES profile coincides with the end of the sodium penetration. This suggests a relation between these two species, which might be the diffusion of dissolved carbon from the sodium bulk through the sodium penetrations, and then, diffusion into the steel. Mean atomic fraction of carbon is assessed to 2% at the maximum on the carbon profile for 316L(N), while for 15-15Ti, it is assessed to a 0.6 to 1.0%. The thickness of the carburized layer is 3 times lower for 15-15Ti too. Measurement of the hardness with a nano-indenter revealed an increase by a factor 2 for the 316L(N) corresponding more or less to the carburized layer.

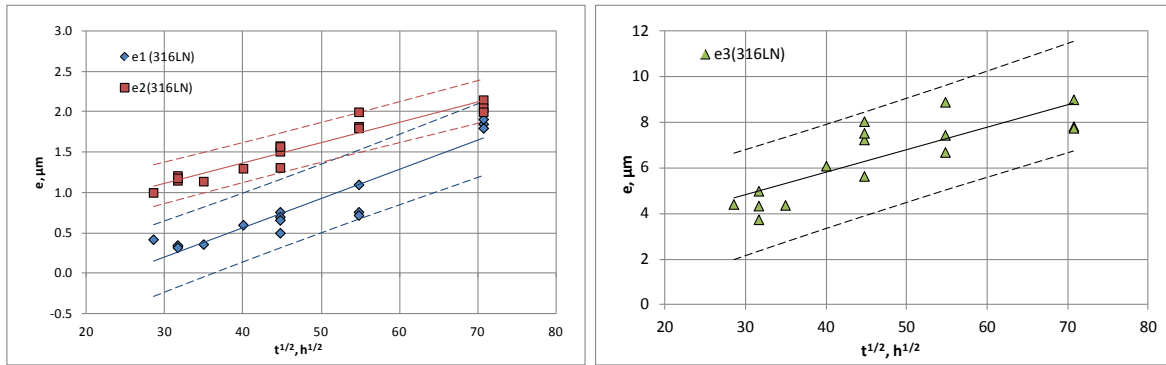


FIG. 7: Parabolic regressions for the oxide and depleted layers (left) and for the carburized layer (right) of 316L(N) at 550°C for 1600h and 5000h plotted with the 95% confidence hyperbolas (e_1 : oxide; e_2 : Cr depleted; e_3 : carburized).

GD-OES analyses the elementary composition of a 4 mm diameter sputtered surface: as interfaces present always a certain roughness, the profile of one element throughout one interface presents a sigmoid evolution whose spreading is proportional to its roughness. The sputtering by the analysis introduces itself a roughness estimated to 200 nm. However, it is possible to assume that the inflexion point represents the mean position of the interface. Then, following the previous observations, the chromium is supposed to be the marker for the sodium chromite layer and the chromium depleted layer, while the carbon profile is supposed to be the marker of the carburized layer. A number of characteristic points are then defined. The initial interface (d_0) is defined as being either the first inflexion point on the chromium profile, if measured, or the middle height median or the origin of the axis in any other case. The oxide-depleted layers interface (d_2) is set as the second Cr inflexion point, which agrees well with those of the nickel, iron, sodium and oxygen. The depleted-carburized layers interface (d_4) is set as the third Cr inflexion point. The last carburized-sound austenite interface (d_6) is defined as being the middle height median of the carbon profile as a first approximation, as the carbon derivative presents no peak in that domain. The minimum or maximum points are quoted as well to compare the mean corrosion layers composition: d_1 and d_3 for the chromium and d_5 for the carbon (Fig. 4). All these characteristic distances are then derived from all GD-OES profiles performed on each coupon. It is then possible to apply simple rules to quantify the thicknesses of the corrosion layers, namely:

- 1-Oxide layer: $e_1 = d_2 - d_0$ or $e_1 = 2 (d_2 - d_1)$
- 2-Depleted layer: $e_2 = d_4 - d_2$
- 3-Carburized layer: $e_3 = d_6 - d_4$

When d_0 is undetermined and if the Cr peak appears as Gaussian, the second relation is then preferred. It supposes a symmetric profile on both sides of the maximum d_1 . All the GD-OES profiles are then handled in an identical way and the results are plotted versus time (Fig. 6). When several measures were made on the same sample, they are handled in the same way to take into account of the scattering induced by the method.

The thicknesses of corrosion increase in time: the oxide and depleted layers evolve in a similar way, whereas the carburized layer evolves in a more different way. On such long duration, it is remarkable that these corrosion thicknesses remain extremely low: of the order of 2 μm for the oxide and depleted layers. The thicknesses obtained for the same grade of steel during the 2 tests present the same evolution, which allows deducting a good reproducibility of the test. Besides, the 15-15Ti and 316L(N) points overlap each other for the oxide and depleted layers, which allow concluding to a similar behaviour towards oxidation for these two steels presenting a relatively close chromium composition: 17 % - 15 %. On the other hand, the behaviour in carburization is very different for the 15-15Ti, as the carburized thickness is lower by a factor 7 compared with that of the 316L(N). Besides, the carburized layer for the 316LN presents a parabolic evolution in spite of a strong scattering that may be due to the hypothesis related to the internal carburized-sound austenite taken into account. Such evolution is generally observed in the case of a carburization (Fig. 7) [13, 14], so that a parabolic fitting curve could reasonably be taken into account for this layer. To the contrary, the oxide and depleted layers evolutions could be fitted either by a linear relation by least mean square regression analysis, or by a parabolic relation. When the former relates to a limiting step corresponding to an interfacial reaction, the latter depicts a limiting step due to a diffusion process. Based from the experiences performed by Cavell and Nicholas [15], the sodium chromite growth assessed by examining the relative intensity of the X-rays diffraction spectral peaks for sodium chromite revealed a parabolic evolution for 316L(N). Then, for comparison, the parabolic evolutions with time of the oxide and Cr depleted layers plotted in Fig.7 are summarized in Tab.2 for 316L(N) and 15-15Ti, although linear regressions would equally fit the points with the same coefficient of regression.

	316L(N)	15-15Ti
Oxide layer	$e_1(t) \pm 0,19 = -0,873 + 3,60.10^{-2} \cdot \sqrt{t}$	$e_1(t) \pm 0,06 = 0,069 + 1,10.10^{-2} \cdot \sqrt{t}$
Depleted layer	$e_2(t) \pm 0,11 = 0,365 + 2,51.10^{-2} \cdot \sqrt{t}$	$e_2(t) \pm 0,04 = 0,033 + 3,01.10^{-2} \cdot \sqrt{t}$
Carburized layer	$e_3(t) \pm 1,01 = 1,88 + 9,82.10^{-2} \cdot \sqrt{t}$	$e_3(t) \pm 0,08 = 1,198 + 1,43.10^{-2} \cdot \sqrt{t}$

TAB. 2. Thicknesses parabolic regressions for 316L(N) and 15-15Ti at 550°C in the conditions of the tests (e_i in μm , t in hours).

The method based on the analysis of GD-OES profiles appears then as quite sensitive for 316L(N) as the standard error is lower than 0.2 μm for the oxide and depleted layer. The carburized layer is a bit less sensitive. The 15-15Ti regressions are based on such a limited number of points that they must be handled with care. Finally, this method of determination of the various corrosion thicknesses proved efficient, even though the various corrosion interfaces present a certain roughness and some heterogeneity. However, the long term tendency of the kinetics in these operating conditions is not yet cleared without any doubt, as several kind of regressions could be used to fit the experimental points, even though converging facts incline to support diffusion limited kinetics. More experimental points at lower as well as at higher exposure times, other kind of tests such as the use radioactive markers (O^{16} – O^{18}), other experimental conditions, characterization of coupons at an even thinner scale or the use of model materials are required to confirm the diffusion controlled process and identify which element is responsible of the diffusion limiting step in the overall corrosion rate in order to progress toward corrosion modeling [16].

In addition, the ferrite phase that was clearly detected on the X-ray diffraction patterns was not observed by the scanning electron microscopy: this issue remains to be solved. All metallic impurities

such as Cr, Ni, Mo, Al, Mn, Cu remains below the detection limit of 0.1 $\mu\text{g/g}$ (ppm) in the liquid sodium sample, except the iron that gradually increased after 2000h to 0.28 ppm, so below its solubility limit at 550°C, assessed to 0.5 ppm [17]. The chemical analyses of the ethanol used to clean each particular coupons indicated an over concentration effect: impurities concentration expressed as function of the remaining sodium on surface of the coupon are higher by one to two order of magnitude when compared to the sodium bulk concentrations : 240 ppm of Fe, 70 ppm of Cr, 60 ppm of Ni, 100 ppm of Mn, 560 ppm of Si 600 ppm of Cu, 1100 ppm of Mo and 8700 ppm of Al and 7200 ppm of In were measured on the ethanol used for the 316L(N) coupon exposed during 3000h at 550°C in test 2. Approximately 50 mg of sodium remained on the surface each coupon. These observations show either that some mass transfer happened during the test as suggested by the indium behaviour, or that the alloying elements dissolution produced these over concentrations. Some elements are more released in proportion, such as Cu, Si, Al, when compared to Fe, Cr, and Ni. Some indium is also measured in the ethanol: a gradual increase to 120 ppm for test 1 and to 10 ppm for test 2. These values are far from the expected 1600 ppm that should have been measured if the liquid sodium was either homogeneous, or the sample representative of the liquid sodium. Know-how about sampling procedure for liquid sodium indicates significant mass transfer during cooling and melting of any sodium sample which implies to analyse the total volume of sample, and especially the outer layers which concentrate most of the impurities. This could explain the discrepancies observed, but requires additional development tools and operating procedures. To date, the assessment of whether the steel dissolution was negligible during the test is still unclear: mechanism of formation of the over concentrations on coupon's surface must be determined. Its formation could be related either to mass transfer within the corrosion coupons immersed at the same time or to reprecipitation of dissolved alloying elements flux from the steel matrix straight on the surface of the coupons. This might explain the origin of iron rich steels crystallites on surface of the coupons and the ferrite detection by XRD. In particular, the exact role played by the oxygen in this dissolution mechanism is an important feature to clarify.

The literature review reported only on some occasion's similar phenomena [15, 18, 19, 20, 21] to the exception of the ferrite detection and Mo rich phase observations at a temperature lower than usually observed, of the sodium penetrations within the chromium depleted layer, and of the carburization after the sodium penetrations. No oxidation kinetics was ever reported to our knowledge in terms of relations that can be related to amount of substances. Several comments could be exposed for discussion. Weight variation measurements to quantify the corrosion phenomena appeared often as a weight loss [17]. Indeed, most of the corrosion tests were achieved in conditions where the sodium chromite formation was not thermodynamically possible, typically above 600°C for oxygen concentration of a few wppm, without speaking of the coupons cleaning methods that could remove or dissolve the sodium chromite. In addition, when the oxygen content was sufficient, the flowing liquid sodium might have spalled off sodium chromite crystallites, whose layer seems sensitive to erosion. Then, the conditions for its reformation in the conditions of the circuit could be lost, as the chromium activity on the steel interface decreased due to the chromium depletion, and as the oxygen content decreased as well after some operating time at normal operating conditions. Sodium chromite observations are often reported as deposits in the colder section of the circuits. In fact, a closed system as represented by a liquid sodium reactor circuit is almost free of any oxygen contamination sources: once the initial contamination (native oxide, adsorbed gas) is released when in temperature which last for a few weeks, the oxygen concentration will be set by the equilibrium value in between the consumption by oxidation and the purification or release due to the purification unit (cold trap). There is a good chance that the oxygen gets buffered by the sodium chromite formation that reduces further oxidation. The oxygen is already reduced to the minimum thanks to the reactors operating procedures that require the oxygen to be low before any increase in temperature, which is the basis for the corrosion protection. This buffer effect might explain the discrepancies in the corrosion value issued from long term corrosion coupon coming from circuits or reactor components [22] from the values calculated with the empirical corrosion relations that underestimate the actual corrosion thickness. These latter relations are based on pure dissolution, which does take into account any transient oxidation. In case of incidental chemical transient such as a pollution event, the diffusion controlled kinetics would limit the corrosion and leave some time for reaction and purification. Even though

these theories require further confirmation, it presents a consistent view of the austenitic steel structure behaviour and liquid sodium chemistry evolution on a reactor circuit.

4. Conclusions

From the static corrosion tests performed with 316L(N) and 15-15Ti steels at 550°C in slightly oxidizing and carburizing sodium, it appeared that the corrosion proceeded by oxidation of the sodium-steel interface with the formation of a sodium chromite layer (NaCrO_2) in association with a chromium depleted steel matrix layer where sodium penetrated. This latter layer is followed by a hardened carburized layer. Regular extraction of specimen up to a total time of 5000h allowed gaining kinetics of corrosion based on the determination of each corrosion layer thicknesses from GD-OES analyses. This technique gives accurate evolution of mean thicknesses over a few micrometers range, even though interfaces are partly inhomogeneous. The chemical conditions of the liquid sodium during the test was discussed, especially as regards the expected conditions for both transient and normal operating conditions of a SFR, and as regards the original conditions offered with the setup. Data gained allows setting hypotheses for the corrosion mechanisms', which limiting kinetic should control the overall corrosion kinetics. These hypotheses define the path forwards for the next studies in order to progress towards liquid sodium corrosion modelling.

ACKNOWLEDGEMENTS

The achievement of the CORRONa tests would not have been possible without people hereafter listed: C. Richet, P. Dubuisson, F. Dalle and others from CEA-Saclay for their various contributions and constant support. P. Bonnaillie and S. Poissonnet from CEA-SRMP in Saclay are thanked for their contribution in the characterisation of the coupons by SEM and microprobe. S. Hemery from CNRS/MSSMAT-ECP is thanked for its nano indentation measurement. The contribution of C. Steil, J. Fouletier from CNRS/LEPMI and V. Ghetta from CNRS/LPSC in the development, supply, understanding and research for ionic ceramic for oxygen sensor is warmly acknowledged as well. Lastly, the authors would like to thank the French CNRS GdR GEDEPEON for the financial support related to the ionic ceramic compatible with liquid sodium for oxygen sensor.

REFERENCES

1. Rouault, J., Serpantié, J.P., and Verwaerde, D. (2009): French R&D programme on the SFR and the ASTRID prototype, Fast Reactors and Related Fuel Cycles: Challenges and Opportunities (FR09), Kyoto, Japan, 7-11 December, IAEA.
2. Balbaud-Célérier, F., Arnoux, P., Cabet, C., Courouau, J.-L., and Martinelli, L. (2009): Corrosion of structural materials for Generation IV systems, International Congress on Advances in Nuclear Power Plants (ICAPP '09), Tokyo, Japan, May 10-14, 2009, ANS.
3. Gelineau, O., Dubiez-Lz Goff, S., Dubuisson, P., Dalle, F., and Blat, M. (2009): Materials challenges supporting new sodium fast reactor designs, International Congress on Advances in Nuclear Power Plants (ICAPP '09), Tokyo, Japan, May 10-14, 2009, ANS.
4. Grabon, V., Marlaud, T., Balbaud-Célérier, F., Courouau, J.L., Martinelli, L., Herms, E., Chêne, J., Blat-Yrieix, M., and Augem, J.-M. (2010): Choix des matériaux pour les futurs réacteurs au sodium d'un point de vue interaction avec l'environnement., Matériaux 2010, Nantes, France, Oct. 18-22, Fédération Française des Matériaux.
5. Thorley, A.W. (1989): Solubility of oxygen in sodium, UKAEA, Northern Research Lab. - NRL-R-1043 (R),
6. Courouau, J.-L., Balbaud-Célérier, F., Lorentz, V., and Dufrenoy, T. (2011): Corrosion by liquid sodium of materials for sodium fast reactors: the CORRONa testing device, International Congress on Advances in Nuclear Power Plants (ICAPP '11), paper 11152, Nice, France, May 2-5, 2011, ANS.
7. Courouau, J.-L., Lorentz, V., Balbaud-Célérier, F., Dufrenoy, T., Tabarant, M., Bonnaillie, P., Poissonnet, S., and Bossonnet, S. (2012): Corrosion des matériaux de structure en sodium: 316LN, 9Cr1Mo, Atelier Gédépeon MATINEX - Les matériaux pour SFR -, Lyon, France, 19-20 Mars, GDR Gédépeon.

8. Courouau, J.L. (2004). "Electrochemical oxygen sensors for on-line monitoring in lead-bismuth alloys: status of development." *Journal of Nuclear Materials*, 335(2), 254-259.
9. Courouau, J.-L. (2007): *Chapter 4: chemistry control and monitoring systems*, in *Handbook on Lead-bismuth Eutectic Alloy and Lead Properties, Materials Compatibility, Thermal-hydraulics and Technologies*, NEA/OECD, n°06195, 129-177.
10. Fouletier, J. and Ghetta, V. (2008): *Potentiometric Sensors for High Temperature Liquids*, in *Materials Issues for Generation IV Systems, NATO Science for Peace and Security Series B: Physics and Biophysics*, 445-459.
11. Courouau, J.-L., Balbaud, F., Lorentz, V., Fouletier, J., Steil, C., and Ghetta, V. (2008): Mise au point de systèmes de mesures électrochimiques des impuretés (oxygène) en milieu sodium liquide pour le contrôle de la corrosion et de la chimie (n°24-2008), Ateliers bilan des actions soutenues GEDEPEON, 10-11 décembre, Paris, France, Gédépeon.
12. Fouletier, J., Steil, C., Courouau, J.-L., and Ghetta, V. (2009): Mise au point de systèmes de mesures électrochimiques des traces d'oxygène en milieu sodium liquide, Ateliers bilan des actions soutenues GEDEPEON, 12-13 Janvier, Paris, France, Gédépeon.
13. Sudha, C., Sivai Bharasi, N., Anand, R., Shaikh, H., Dayal, R.K., and Vijayalakshmi, M. (2010). "Carburization behavior of AISI 316LN austenitic stainless steel - Experimental studies and modeling." *Journal of Nuclear Materials*, 402(2-3), 186.
14. Chopra, O.K., Natesan, K., and Kassner, T.F. (1981). "Carbon and nitrogen transfer in Fe-9 Cr-Mo ferritic steels exposed to a sodium environment." *Journal of Nuclear Materials*, 96(3), 269.
15. Cavell, I.W. and Nicholas, M.G. (1980). "Studies of the formation of sodium chromite on some ferrous alloys and chromium plate exposed to oxygenated sodium." *Journal of Nuclear Materials*, 95(1-2), 145-154.
16. Balbaud-Célérier, F., Courouau, J.-L., and Martinelli, L. (2013): Corrosion of structural materials in liquid metals used as fast reactors coolants, Fast Reactors conference (FR 13), Paris, France, March,
17. Borgstedt, H.U. and Mathews, C.K. (1987). *Applied chemistry of the alkali metals*. New-York, Plenum Press.
18. Cavell, I.W. and Nicholas, M.G. (1980). "Some observations concerned with the formation of sodium chromite on AISI 316 exposed to oxygenated sodium." *Journal of Nuclear Materials*, 95(1-2), 129-144.
19. Thorley, A.W., Blundell, A., and Bardsley, J.A. (1981): Mass transfer of stainless steels in pumped sodium loops and its effect on microstructure, *Material Behaviour and Physical Chemistry in Liquid Metal Systems*, Karlsruhe, Germany, 24-26 March, Plenum press.
20. Crouch, A.G. (1980): The growth and stability of sodium chromite and its influence on corrosion, *Second international conference on liquid metal technology in energy production*, Richland, Washington., April, 20-24, ANS (conf-800401-p2, UC-79A).
21. Nicholas, M.G. and Cavell, I.W. (1980): The formation of sodium chromite on AISI 316 and other sodium containing alloys, *Second international conference on liquid metal technology in energy production*, Richland, Washington., April, 20-24, ANS (conf-800401-p2, UC-79A).
22. Ganesan, V., Ganesan, V., and Borgstedt, H.U. (2003). "Analysis of CREVONA sodium loop material." *Journal of Nuclear Materials*, 312(2-3), 174.

Study on the chemical compatibility of SiC/SiC composites as core materials for Sodium Fast Reactors

J. Braun^a, C. Gueneau^b, C. Sauder^a, F. Balbaud^c, P. Allegri^d, E. Brackx^d

^aCEA/DEN/DANS/DMN/SRMA/LTME_x, Gif-sur-Yvette, France

^bCEA/DEN/DANS/DPC/SCCME/LM2T, Gif-sur-Yvette, France

^cCEA/DEN/EC/DADN, Gif-sur-Yvette, France

^dCEA/DEN/MAR/DTEC/SGCS/LMAC, Bagnols-sur-Cèze, France

Abstract. Silicon carbide (SiC) fibers combined with a SiC matrix constitute an advanced solution for Fast Neutron Reactors (SFR, GFR...) as core materials for their stability at high temperature and their neutron transparency. However, the compatibility with the reactor's fuel and coolant has to be studied within a wide range of temperatures: moderated in normal operation (close-circuit at 550°C) and elevated (open-middle) in accidental conditions. Concerning the compatibility of SiC/SiC with the fuel and, considering in a first step uranium oxide, the stoichiometry of uranium dioxide remains one of the important parameters to be studied. Experimental results on the chemical compatibility between UO_{2.15} and SiC were obtained using high temperature mass spectrometry. The reaction for 6 hours at 1773 K produces the release of mainly CO(g), CO₂(g) and SiO(g) and Si(g) and leads to the formation of uranium silicide compounds. The uranium oxide was fully consumed. Thermodynamic calculations were performed to prepare and interpret the experiments.

1. Introduction

Thanks to its behavior under irradiation and at high temperature, silicon carbide (SiC) is a good candidate as a core material for Fast Neutron Reactors. SiC is not considered as a monolithic material but as a composite with SiC fibers, a pyrocarbon interface and a SiC matrix. It is envisaged as a cladding or a core material respectively in the Gas-Cooled and Sodium Fast Reactors (GFR and SFR). However, the compatibility with the environment (fuel and coolant) has not been extensively studied. The aim of our study is to investigate the chemical interaction between silicon carbide and uranium dioxide at various temperatures ranging from the nominal operating conditions to accidental ones.

At the same time, studies on the interaction between liquid sodium and SiC/SiC composites have been carried out. Samples have been heated in pure sodium containing less than 10 ppm of O₂ for 1000 hours at nominal operating conditions of SFR (550°C, 1bar). Previously, some SiC/SiC samples have been deformed at different levels of damaging. Indeed, over the elastic limit of the composite, cracks appear in the matrix leading to the exposure of the fibers and the pyrocarbon layer to the environment. Then, these composites did undergo cycled traction tests to point out the main characteristics of the material: evolution of the Young Modulus, friction between fibers and matrix and permanent strain. The comparison of the mechanical properties before and after the sodium exposure will be presented in a further publication.

2. Chemical compatibility between oxide fuel and silicon carbide

a. State of the art

Silicon carbide has already been considered as a confinement barrier in TRISO particles in HTGR reactors but its compatibility with the uranium oxide fuel did not constitute a major issue. Indeed, graphite and pyrocarbon layers were included between the UO_2 kernel and SiC.

Crofts' [1] calculations showed that at high temperature (above 1970K), the free energy of the possible reactions between SiC and UO_2 are positive, especially with an hyperstoichiometric uranium dioxide. These reactions lead to the formation of gaseous $SiO_{(g)}$ along with the formation of silica and graphite in the condensed phase. The stoichiometry x of UO_{2+x} constitutes the major parameter to consider because the oxygen potential varies steeply with x [2] and temperature [3]. After heating SiC and UO_2 at 2200K for 10 minutes, Gangler [4] observed the formation of UC and maybe USi_2 . Tulenko [5] did not see any reaction at 1570K but $USi_{1.88}$ was formed at 1920K from a mixture of $UO_{2.10}$ and SiC powders.

Either under vacuum or a rare gas flow, Allen [6] showed that no measurable rate of reaction occurs below 1650K. Above this temperature, carbon and silicon monoxide are detected in the gas as well as $USi_{1.67}$, SiC, $U_3Si_3C_2$ and probably UC in the condensed phase. If the gases are not evacuated, a displacement of the equilibrium is noticed leading to the formation of UC and UC_2 . It also appeared that the reaction is controlled by thermodynamics of the phase equilibria and by the gas diffusion from the reaction sites. Indeed, the reaction rates were found independent on both mole ratios of the reactants (in the range: $1 \leq \frac{n(SiC)}{n(UO_2)} \leq 4$) and size of the SiC particles (between 7 and $53\mu m$).

Depleted UO_2 pellets filled with sintered SiC shells in their center were heated up to temperatures between 1970K and 2270K for few minutes by Lippmann [7]. When gaseous compounds were allowed to escape, the reaction zone was below $5\mu m$ for 10 minutes experiments at temperatures up to 2130K. However, for 15 minutes at 2270K, a thick reaction zone appeared ($80\mu m$). EPMA results showed the presence of USi_x and to a lesser extent, of UC, UO_2 and SiC in this zone. Moreover, a thin layer with increased oxygen content appeared at the interface between UO_2 and SiC, and the reaction zone. Some small isolated SiC precipitates were also found in UO_2 . The thickness of the reaction zone was thicker from top to bottom because gaseous compounds were allowed to escape more easily at the top, causing the displacement of the equilibria. Finally, in the case of a gastight sealed capsule, no reaction was observed at temperatures up to 2070K.

b. Preliminary thermodynamic calculations

In order to have a good understanding of the chemical interaction between SiC and UO_{2+x} and to prepare our experiments, thermodynamic calculations were performed using Thermo-calc[®] software with the FUELBASE thermodynamic database which has been developed for advanced fuel materials (oxides, carbides, nitrides) for next generation reactors [2].

Fig. 1 (a) shows the evolution of the partial pressures of the major species as a function of temperature above a sample constituted of 29.3 mol. % of $UO_{2.15}$ and 70.7 mol. % of SiC. In the Knudsen cell effusion method, to avoid molecule-molecule collisions in the beam produced by the effusion cell, the pressure has to be kept under a relative low level (10 Pa). At thermodynamic equilibrium, the limit in pressure for $CO_{(g)}$ would be attained at 1070K. Nevertheless, in a previous study on UO_2/C interaction by Gossé [10], the measured pressures for $CO_{(g)}$ and $CO_{2(g)}$ with the same method were found to be much lower than the equilibrium pressure data determined by thermodynamic calculations. Thus the limit in pressure shall not be reached in the present experiment.

In our experiments, silicon carbide and uranium oxide powders have been mixed. Above a certain oxygen potential, silicon carbide is oxidized forming SiO_2 and C. Actually, the SiO_2 layer acts as a

passivation barrier that limits the kinetics of oxidation of SiC. According to Honstein's [8] and Gueneau's [2] thermodynamic data respectively on the Si-C-O and on U-O systems, one can determine the composition of the Si-C-O system as a function of the oxygen potential, i.e. the uranium oxide stoichiometry (Fig. 1 (b)). The stability range of SiC and SiO₂ exists for uranium dioxide with a stoichiometry between UO_{2.0042} and UO_{2.016} at 1773K. This can be also observed in Fig. 2 showing the variation of the composition of the system U-Si-C-O as a function of temperature.

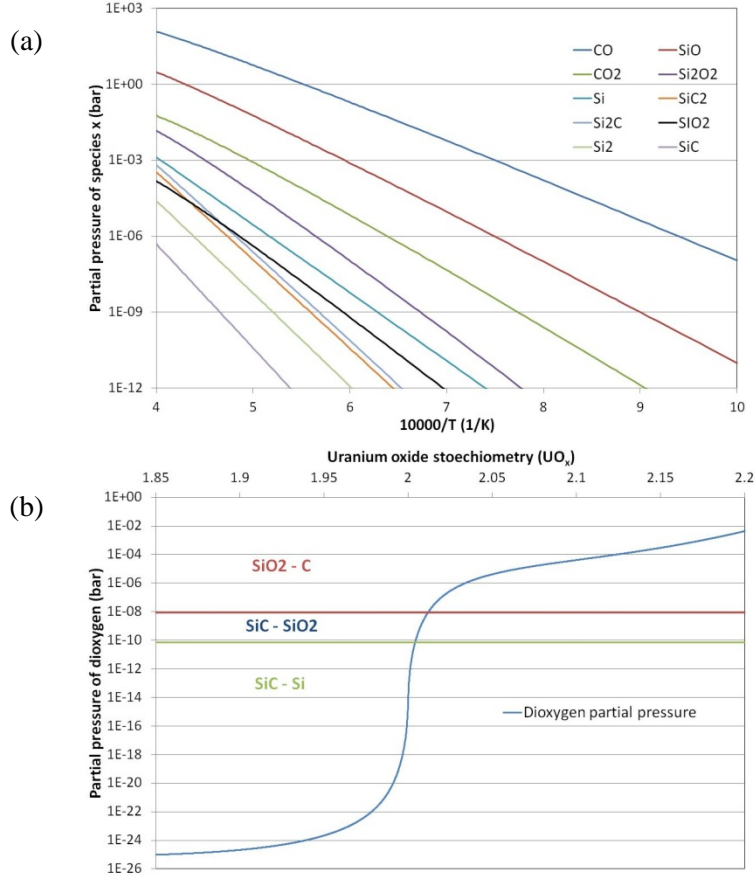


FIG. 1. (a) Calculated partial pressures of the gaseous species above the uranium oxide ($n(\text{UO}_{2.15})=3.72\text{mmol}$) – silicon carbide ($n(\text{SiC})=8.98\text{mmol}$) mixture at the thermodynamic equilibrium ; (b) Phase stability ranges of the Si-C-O system versus uranium oxide stoichiometry at 1773K

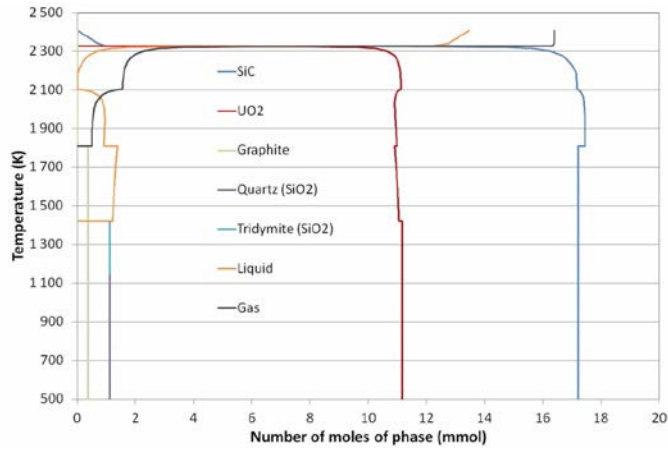


FIG. 2. Calculated number of moles of phases as a function of temperature for a molar ratio of SiC – UO_{2.15} of (2.4 : 1)

Even at low temperature, SiO_2 and $\text{C}_{(\text{gr})}$ are the species stable thermodynamically due to the oxidation by the exceeding oxygen content of the uranium oxide. However, kinetics of oxidation of SiC is limited by the diffusion of oxygen and of gas products (SiO , CO) in the SiO_2 layer [9]. This diagram shows that an ionic liquid phase could form above 1420K, with a composition enriched in SiO_2 and a low content of U (8.33 at % at 1420K). The presence of an eutectic in the UO_2 -Si system was never highlighted. With increasing temperature, the fraction of the UO_2 mixed with SiO_2 to form the ionic phase increases to reach a ratio of 19% before the apparition of the gas phase, which is constituted of carbon and silicon monoxides. Finally, thermodynamic calculations show that SiC and UO_2 are compatible until 2200K.

c. Experimental tests

i. Sample preparation

Silicon carbide powder was provided by Goodfellow. Uranium dioxide powders with various stoichiometries have been prepared by CEA/CAD/DEC/SPUA/LCU: $\text{UO}_{2.02}$, $\text{UO}_{2.10}$ and $\text{UO}_{2.15}$ to study the influence of the oxygen potential of the fuel. After mixing without being pressed, powders were put in graphite crucibles lined with silicon carbide (100 μm) constituting the Knudsen cell. This SiC liner was deposited by chemical vapor infiltration to avoid any contact between the graphite and the sample, that would produce $\text{CO}_{(\text{g})}$. To obtain a molecular flow, the hole in the crucible lid has to be smaller than the mean free path of the gaseous molecule [10]. UO_{2+x} and SiC phases have a molar ratio of (1:2.45). The sample was heated under secondary vacuum ($2 \cdot 10^{-7}$ mbar) for 6 hours at temperatures ranging from 1473K up to 1923K after a heating rate of 30 K/min and a 15 minutes degassing step at 473K. Mass spectrometry was used to detect and measure the released reaction gaseous products (CO , CO_2 , SiO). All the preparations were made under a nitrogen atmosphere. Samples were analyzed afterwards using SEM-EDS, EPMA and XRD at the CEA/MAR/DTEC/LMAC and the mass losses were measured.

ii. High Temperature Mass Spectroscopy

Knudsen cell mass spectrometry is a suitable method to investigate the chemical interaction between uranium compounds and different structural materials at high temperature [10]. The furnace is composed of a tungsten resistor to heat samples at temperatures up to 2300K under secondary vacuum. A multiple Knudsen effusion cell device offers the possibility to analyze in a single experiment up to four different samples. The temperature of the furnace is regulated by a Tungsten-5%Rhenium thermocouple placed in the sample holder. To measure the temperature of the sample, a bichromatic pyrometer is used. This pyrometer has been calibrated using extrapolation at 0 K/min heating rate, melting points of pure elements (Silver, Silicon, Iron and Platinum) [11]. Previous measurements on known eutectics have shown that the measurement error made on the temperature is about 10K.

Measurements are performed using a Nermag R10-10 quadrupolar mass spectrometer. The gaseous species are ionized by an electron beam ($E=15\text{eV}$). The intensities of the ionic species in the molecular beam effusing from the Knudsen cell are measured for a given ratio of atomic mass over electric charge. In this case, partial vapor pressure p_i of the i component is directly linked to the ion current (I_i) measured by the mass spectrometer by the equation:

$$p_i S_i = I_i T \quad (1)$$

where T is the cell temperature and S_i the sensitivity factor which depends on the nature of the species, the cell geometry and the spectrometer parameters [12]. A shutter placed above the effusion cell under investigation ensures the measurement of the background for the different species (closed position) and the molecular flow released above the effusion cell (opened position). The difference between the two measurements leads to the determination of the molecular flow representative of the vapor in equilibrium with the sample.

According to the thermodynamic calculations, the major gaseous products over the system are CO, SiO, CO₂, Si₂O₂ and Si. The main issue is that there is an overlap for those species. CO⁺ and Si⁺ have the same mass over charge ratio at 28 as well as CO₂⁺ and SiO⁺ at 44. The contribution of N₂⁺ is avoided by working at low ionization energy (15eV), which is lower than the ionization energy of nitrogen. Unfortunately, the mass spectrometer resolution does not allow the separation of the molecules. But by considering that CO and CO₂ are non-condensable gases that are only evacuated by primary and turbomolecular pumps and that, on the other hand, SiO and Si can be condensed on the cold spots of the furnace, the analysis of the level of the background was used to determine which species are produced as a function of time and temperature.

iii. Determination of the molecular flows

According to the Hertz-Knudsen relation, the flow of gaseous molecules can be determined by the integration of the half space above the hole of the crucible:

$$\frac{dn_i}{dt} = \frac{p_i s C}{\sqrt{2\pi M_i R T}} \quad (2)$$

where s is the surface of the effusion hole, C is the Clausing factor of the effusion hole, M_i the molecular mass of the species i and R the perfect gas constant.

Combining (1) and (2), the flow is given by relation (3):

$$\frac{dn_i}{dt} = \frac{I_i s C \sqrt{T}}{S_i \sqrt{2\pi M_i R}} = \beta_i \sqrt{T} \quad (3)$$

The weight loss is the sum of the contribution of all the species:

$$\Delta m_{tot} = \Delta m_{CO} + \Delta m_{SiO} + \Delta m_{CO_2} + \Delta m_{Si} \quad (4)$$

$$\Delta m_{tot} = M_{CO} \Delta n_{CO} + M_{SiO} \Delta n_{SiO} + M_{CO_2} \Delta n_{CO_2} + M_{Si} \Delta n_{Si} \quad (5)$$

For general cases, equation (6) can be given:

$$\Delta m_{tot} = \sum_i M_i \beta_i \int_0^{t_f} I_i \sqrt{T} dt \quad (6)$$

where β_i is a parameter specific to the experimental device. It has not been directly determined but the ratio between each β_i can be calculated by the relation (7):

$$\frac{\beta_j}{\beta_i} = \frac{S_i \sqrt{M_i}}{S_j \sqrt{M_j}} \quad (7)$$

The sensitivity factor of the mass spectrometer (S_i) is a function of the intensity of the electron beam I_{e^-} , a geometric factor G , the mass spectrometer transmission η_i , the ionization cross section of the molecule σ_i , the detector yield γ_i and the isotopic abundance ratio f_i . Equation (8) gives the linear relation between those parameters:

$$S_i = I_{e^-} \cdot G \cdot \eta_i \cdot \sigma_i \cdot \gamma_i \cdot f_i \quad (8)$$

Given that the detector yield γ_i is proportional to $1/\sqrt{M_i}$ [13], the detector yield is close for all species and by combining equation (7) and (8), equation (9) can be deduced:

$$\frac{\beta_j}{\beta_i} = \frac{\sigma_i f_i}{\sigma_j f_j} \quad (9)$$

Hence (10) - (11):

$$\beta_i = \frac{\Delta m_{tot} \int_0^{t_f} I_i \sqrt{T} dt}{\sum_j \frac{M_j \sigma_i f_i}{\sigma_j f_j} \int_0^{t_f} I_j \sqrt{T} dt} \quad (10)$$

$$n_i(t) = \beta_i \int_0^t I_i \sqrt{T} dt \quad (11)$$

According to equation (11), the total amount of gases released from the system can be determined at each time. Per subtraction, the composition of the condensed phase can also be determined as a function of time.

iv. Results and interpretation

The results for a sample made of a mixture of SiC and hyperstoichiometric uranium dioxide ($\text{UO}_{2.15}$ – oxygen content measured by TGA) powders with a molar ratio of (2.45 : 1) are presented. The sample has been heated up to 1773K for about 6 hours. Micrographs of the sample after the test are presented on Fig. 3. At first, the persistence of the SiC coating on the crucible is noted although interactions appear on the bottom. No more uranium dioxide was found. The whole mixed powder has reacted to form uranium silicides. SiC aggregates are also observed. The uranium content of the sample is homogenous (74±3 wt. %). At the interface with the SiC coating, areas with high carbon content are found with the presence of a ternary compound $\text{U}_x\text{Si}_y\text{C}_z$. XRD results show the presence of SiC, USi_x and $\text{U}_3\text{Si}_2\text{C}_2$ in the sample. $\text{USi}_{1.67}$ and $\text{USi}_{1.88}$ have close lattice parameters and cannot be distinguished with this technique. EPMA analysis was used to determine the composition of the uranium silicides. Both phases were detected in the sample.

The measured intensities at the ratios mass/charge 28 (CO , Si) and 44 (CO_2 , SiO) using the mass spectrometer are shown in Fig. 4. Si_2O_2 and all the other species mentioned in 2.2 were not detected. At first, the contribution of each species has to be separated. Fig. 5 presents the evolution of the intensity signals measured with either an opened or a closed shutter for the mass/charge 44. During the heating ramp, both signals are very close corresponding to the emission of a non-condensable gas, in this case CO_2 . Above 1500K, a decrease of the signal (opened position) is observed corresponding to the transition between the emission of CO_2 and SiO, which become the predominant species afterwards. Thanks to this approach, the predominant gas can be discriminated versus time for each mass. It can be seen that the signal at 28 (CO^+ and Si^+) is 2 orders of magnitude higher than the signal at 44 (CO_2^+ and SiO^+).

During heating, a strong release for both $\text{CO}_{(g)}$ and $\text{CO}_{2(g)}$ is observed at 750K. Then, at the beginning of the temperature plateau, the intensities remain constant for a short period. This could correspond to the oxidation of SiC by UO_{2+x} into SiO_2 and C combined with the emission of $\text{CO}_{(g)}$ and $\text{CO}_{2(g)}$. This leads to a strong decrease of the oxygen potential with the reduction of UO_{2+x} into UO_{2-x} . When UO_2 is reduced into UO_{2-x} , the formation of USi_x and $\text{U}_3\text{Si}_2\text{C}_2$ may occur as $\text{SiO}_{(g)}$ and mainly $\text{CO}_{(g)}$ are emitted. During the third step of the reaction, once all the UO_2 is fully consumed, the sample may be constituted of SiC and U_xSi_y phases and $\text{Si}_{(g)}$ becomes the only gas species in the vapor. A plateau is observed for the $\text{Si}_{(g)}$ partial pressure. It can be explained by the fact that in a three-phase region of a ternary system, here U-Si-C, the variance of the system is equal to 1. When the temperature is fixed, the activity, chemical potential or partial pressure of the elements is fixed.

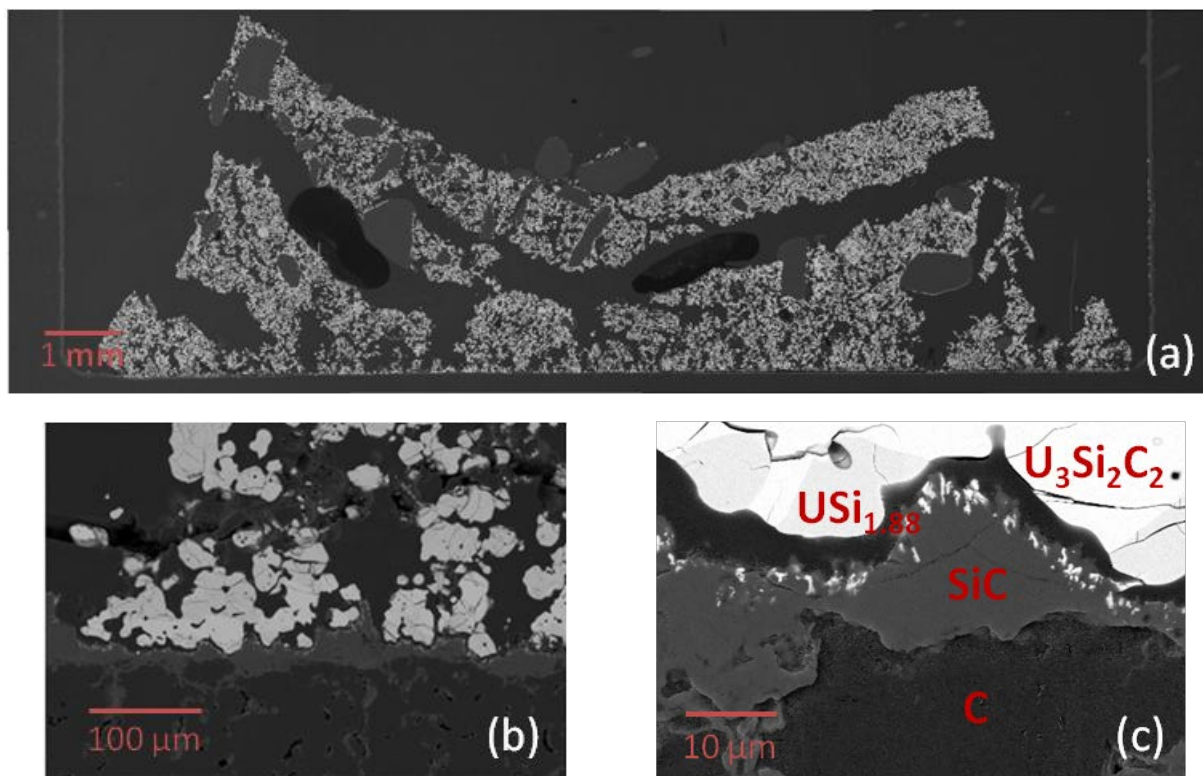


FIG. 3. SEM micrographs of the post-mortem sample $UO_{2.15} - SiC$ (resp. 29.4 – 70.6 at %) at 1770K for 6 hours (a): Whole sample – in grey: SiC aggregates; white: uranium silicides compounds - (b) and (c): Bottom of the sample. Interface between the sample and the SiC liner / C crucible

With the method described in the 2.3.3 chapter, the number of moles of released gaseous species and the composition of each element in the condensed phase can be calculated (resp. Fig. 6 and 7). Uncertainties related to the interaction between the sample and the crucible lined with silicon carbide lead to a small negative calculated value for the final oxygen content in the sample. The different steps previously described are also observable on those figures. Because mainly carbon monoxide is released during the experiment, silicon and uranium are the major elements in the sample.

From the calculated overall composition of the sample, the phase fractions to be formed in the sample can be calculated versus time using Thermocalc software. For that, the thermodynamic equilibrium and the chemical homogeneity of the sample were assumed at each step of the experiment (Fig. 8). The increase of temperature enhanced the kinetics of reduction of SiC in SiO_2 and C. The calculations predict the formation of a liquid phase constituted of SiO_2 and U above 1420K. However, SEM images did not highlight the presence of this liquid. Then, as carbon monoxide constitutes the major gaseous reaction product, uranium silicides are formed along with the decrease of uranium dioxide molar ratio. At the end of the experiment, the calculations lead to a sample constituted of (59 mol. % of USi_2 , 30 mol. % of USi_3 and 11 mol. % of SiC). An overall good agreement between calculated and experimental results on the sample composition at the end is found, except on the formation of USi_3 (instead of $USi_{1.67}$) that was not detected by EPMA analysis.

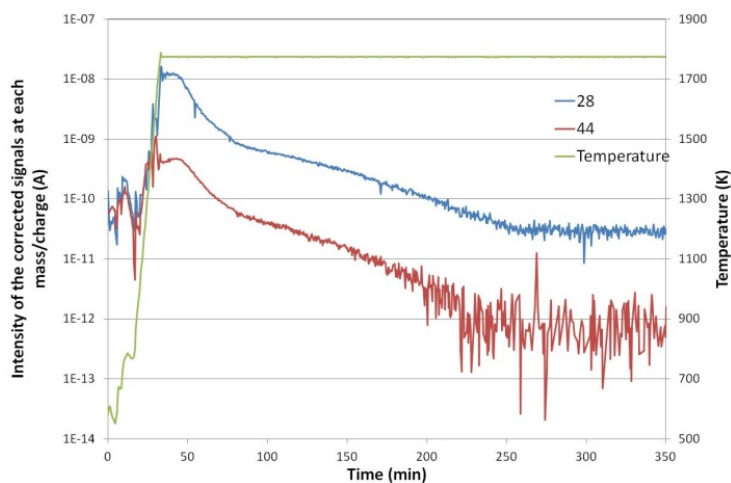


FIG. 4. Intensity signals detected at the mass/charge ratio of 28 (CO, Si – blue), 44 (CO₂, SiO – red) and temperature (green) versus time

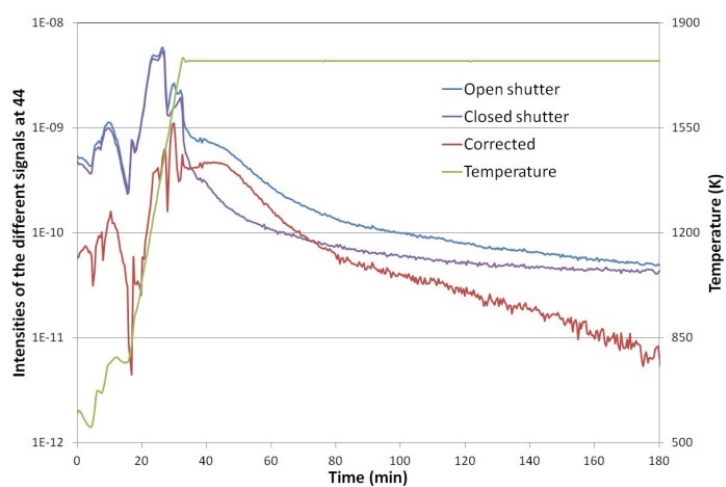


FIG. 5. Opened-shutter (blue); closed-shutter (purple) and corrected intensity signal (red) at the mass/charge ratio 44, temperature (green) versus time

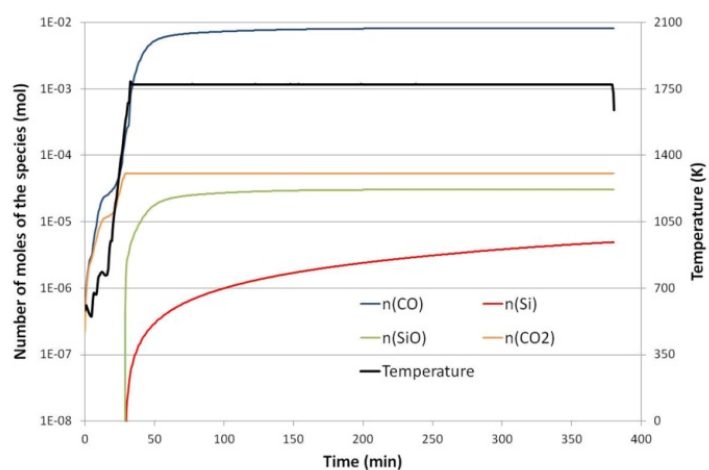


FIG. 6. Number of moles of CO (blue), SiO (green), CO₂ (orange) and Si (red) gaseous species and temperature (black) as a function of time

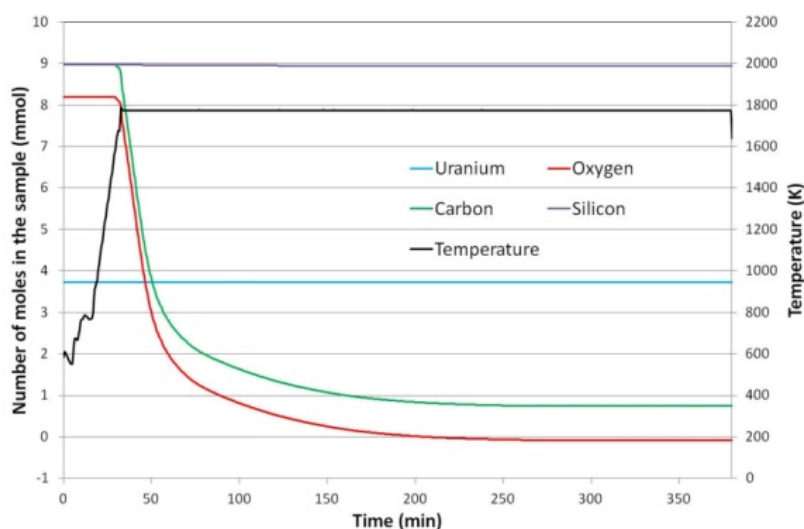


FIG. 7. Evolution of the composition of U (blue), Si (purple), C (green), O (red) in the sample and temperature (black) as a function of time

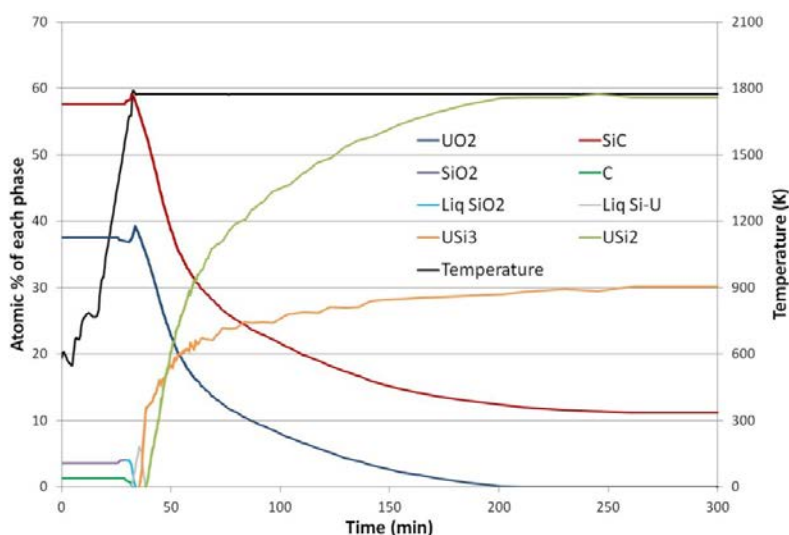


FIG. 8. Calculated mole fractions of the condensed phases in the sample as a function of time

3. Conclusion

Interactions between silicon carbide and hyperstoichiometric uranium dioxide ($\text{UO}_{2.15}$) have been investigated by High Temperature Mass Spectroscopy. The intensities of CO, CO_2 , SiO and Si gaseous species have been monitored leading to the determination of the overall composition of the gaseous phase as a function of temperature and time. The composition of the condensed phase has been determined by difference.

The high oxygen content of the sample combined with the evacuation of gases under vacuum lead to the oxidation of silicon carbide by UO_{2+x} into SiO_2 and C. However, high temperature increases the kinetics of the reaction and leads to the active oxidation of SiC to form $\text{CO}(\text{g})$ and $\text{SiO}(\text{g})$. After few hours (3h) at 1770K, all the oxygen of the sample was consumed leading to the formation of uranium silicides ($\text{USi}_{1.67}$ and $\text{USi}_{1.88}$) and to a lesser extent of $\text{U}_3\text{Si}_2\text{C}_2$ in the sample. Silicon carbide aggregates were also found. An overall good agreement was found between calculated and experimental results concerning the final composition and the nature of the phases at the end of the test. It must be kept in mind that those results were obtained under secondary vacuum inducing the

displacement of the reactions which are enhanced. Further investigations will be carried out with uranium dioxide with a stoichiometry closer to $O/U=2$ ($UO_{2.02}$) at various temperatures ranging from 1470K to 1920K. Investigations will also be carried out to find another crucible material that does not interact with both powders. Moreover, the compatibility in a closed capsule between UO_2 and SiC pellets will also be investigated.

REFERENCES

- [1] J.A. Crofts, 1970, C.E.G.B. Report RD/B/M1589
- [2] C. Guéneau, N. Dupin, B. Sundman, C. Martial, J.-C. Dumas, S. Gossé, S. Chatain, F. De Bruycker, D. Manara, R. J.M. Konings, Thermodynamic modelling of advanced oxide and carbide nuclear fuels : Description of the U-Pu-O-C systems, *Journal of Nuclear Materials*, vol. 419, 2011, p145-167
- [3] A. A. Solomon, Enhanced Thermal Conductivity Oxide Fuels, Final Report Project No. 02-180, 2005
- [4] J. J. Gangler, W. A. Sanders, I. L. Drell, NASA – TND – 262, 1960
- [5] J. S. Tulenko, R. H. Baney, An innovative high thermal conductivity fuel design, PhD Thesis at The University of Florida, 2007
- [6] G. C. Allen, J.A. Crofts, T. Swan, The high temperature reactions between uranium dioxide and silicon carbide, Central Electricity Generating Board, Berkley Nuclear Laboratories, Berkley, Gloucestershire, UK, 1970
- [7] W. Lippmann, J. Knorr, R. Nöring, M. Umbreit, Investigation of the use of ceramic materials in innovative light water reactor – fuel rod concepts, *Nuclear Engineering and Design*, vol. 205, 2001, p13-22
- [8] G. Honstein, C. Chatillon, F. Baillet, Thermodynamic approach to the vaporization and growth phenomena of SiC ceramics. I. SiC and SiC-SiO₂ mixtures under neutral conditions, *Journal of the European Ceramic Society*, vol. 32, 2012, p1117-1135
- [9] G. Honstein, C. Chatillon, F. Baillet, Thermodynamic approach to the vaporization and growth phenomena of SiC ceramics. II. The SiC surface under oxidative conditions, *Journal of the European Ceramic Society*, vol. 32, 2012, p1137-1147
- [10] S. Gossé, C. Guéneau, C. Chatillon, S. Chatain, Critical review of carbon monoxide pressure measurements in the uranium-carbon-oxygen ternary system, *Journal of Nuclear Materials*, vol. 352, 2006, p13-21
- [11] A. Berche, T. Alpettaz, S. Chatain, C. Blanc, S. Gossé, C. Guéneau, Thermodynamic study of the uranium-vanadium system, *Journal of Chemical Thermodynamics*, vol. 43, 2011, p458-466
- [12] P. Gardie, G. Bordier, J.-J. Poupeau, J. Le Ny, Thermodynamic activity measurements of U-Fe and U-Ga alloys by mass spectrometry, *Journal of Nuclear Materials*, vol. 189, 1992, p85-96
- [13] M. G. Inghram, R. J. Hayden, D. C. Hess, Mass spectroscopy in Physics Research, NBS Circular 522, NIST, 1953, p257-264

Mechanical modeling of SiC/SiC composites and design criteria

F. Bernachy-Barbe^a, L. Gélébart^a, J. Crépin^c, M. Bornert^c

^aCEA, DEN, DMN, SRMA, Gif-sur-Yvette, France

^bMines ParisTech, Centre des Matériaux, UMR CNRS 7633, Évry, France

^cLaboratoire Navier, École des Ponts ParisTech, Marne la Vallée, France

Abstract. The design of SiC/SiC composite structures, candidates for the fuel cladding of some 4th generation fast reactors, requires an understanding and a modeling of their mechanical behavior. Therefore, a 3D model using only few scalar damage variables has been developed at CEA and identified with biaxial tension-torsion tests. Based on a few hypotheses on the crack properties (orientation, opening laws and damage kinetics), it gives satisfying results at several tension/torsion ratios for all in-plane components of the strain tensor. Moreover, two damage criteria useful for the design of components are proposed.

1. Introduction

The 4th generation fast reactors have operating and accidental conditions very different from current pressurized water reactors. In particular, the temperatures that structural materials have to withstand are much higher. As an example, accidental temperatures encountered in Gas-cooled Fast Reactors (GFRs) might be up to 1600 °C : there is therefore a need for new core materials, especially concerning fuel cladding. At these temperatures, ceramic materials are considered, and due to the fragile behaviour of their monolithic form, ceramic matrix composites are of a greater interest. . Actually, ceramic matrix composites exhibit a reproducible and non-linear behaviour with a higher strain to rupture, due to the creation of matrix cracks and their deviation along the interphase between matrix and fibers. We therefore consider in this work SiC/SiC composites elaborated with the 3rd generation of fibres (Hi-Nicalon STM), which are also stable under irradiation and neutron transparent. The materials of this study are 2D woven composites, elaborated at CEA, composed SiC fibers (Hi-Nicalon STM) in a matrix of silicon carbide deposited by the Chemical Vapor Infiltration (CVI) process. The fiber-matrix interphase is composed of pyrocarbon, also deposited by CVI. Test samples are tubes of approximately 9.6 mm in diameter and 0.85 mm thick, and are constituted of two woven layers, plus an additional internal filament winding layer. Fibres are at a +/-45° angle with the tube axis. The geometry of these tubes is close to the possible geometry of a GFR fuel cladding tube.

Due to the material's tolerance relatively to the presence of micro-cracks, it would not be relevant to design a component relatively to the initiation of the first micro-crack. However it is also unlikely that a high amount of damage should be tolerated (for operating conditions). In order to design such critical components, a precise knowledge of elastic properties and the definition of damage criteria are therefore needed. In the case of accidental conditions, understanding and modeling of the non-linear and anisotropic behavior of the material are also required as well as a failure criteria. Some work has already been conducted in the study and the modeling of SiC/SiC composites [1], but the improvements in the elaboration process (3rd generation fibers, decrease in porosity, weavings...) and the limited scope of most mechanical tests (tension in the fibre axis, biaxial tests in monodirectional composites...) make necessary a thorough study of the mechanical properties of such materials. In the following work, biaxial tension-torsion tests have been conducted and are used as an experimental

basis for the definition of damage criteria, and the identification of a phenomenological damage model.

2. Tension-torsion tests

2.1. Experimental set-up

In the following, we use the cylindrical coordinate system attached to the tube $(O, \vec{e}_R, \vec{e}_\theta, \vec{e}_Z)$, where \vec{e}_Z is parallel to the tube axis. Tests samples have been subjected to proportional tests (i.e. at a constant biaxiality ratio $\beta = \sigma_{ZZ} / \sigma_{\theta\theta}$) on an hydraulic tension-torsion machine. Measurements are carried out using axial and shear extensometers positionned at the surface of the sample, and images of the sample surface are recorded using a camera equipped with a telecentric lens, for further Digital Image Correlation (DIC) processing. Projected displacement fields at the surface of the tube, calculated using DIC, are then used for the computation of the axial, circumferential, and shear in-plane components of the strain tensor. This calculation of the strain is based on the optimization of a kinematic modeling of the tube strain in order to fit the experimental projected displacement field. The acoustic emission (ultrasonic waves emitted during microscopic changes in the material, such as damage) is also recorded during the test using a piezoelectric sensor. The acquisition system allows for recording several descriptors (amplitude, duration, energy...) of the acoustic events. Some acquisition parameters can be chosen using waveform studies of acoustic emissions in SiC/SiC such as [2].

2.2. Mechanical behavior

At first, it is assumed that the SiC/SiC material (constitutive of the tube) can be replaced by a homogeneous material. Then it must be noticed that even with a homogeneous material, the stress distribution within the thickness of the tube can be heterogeneous (when torsion is applied). As a consequence, to identify the homogeneous behavior of the tube, appropriate stresses and strains must be defined from the experimental measurements.

In the following results, the shear stress is calculated from the torque applied to the sample, assuming a homogeneous shear stress field.. The axial stress is evaluated from the axial force assuming a homogeneous stress field. The axial strain, as well as the circumferential strain is the strain measured at the surface of the sample and the shear strain is evaluated at the average radius proportionnally to the shear strain measured at the outer radius. The following results in FIG. 1 present the stress-strain measurements in the case of $\beta = 0$ (pure torsion test), $\beta = 1.1$ (tension-torsion test) and $\beta = \infty$ (pure tensile test).

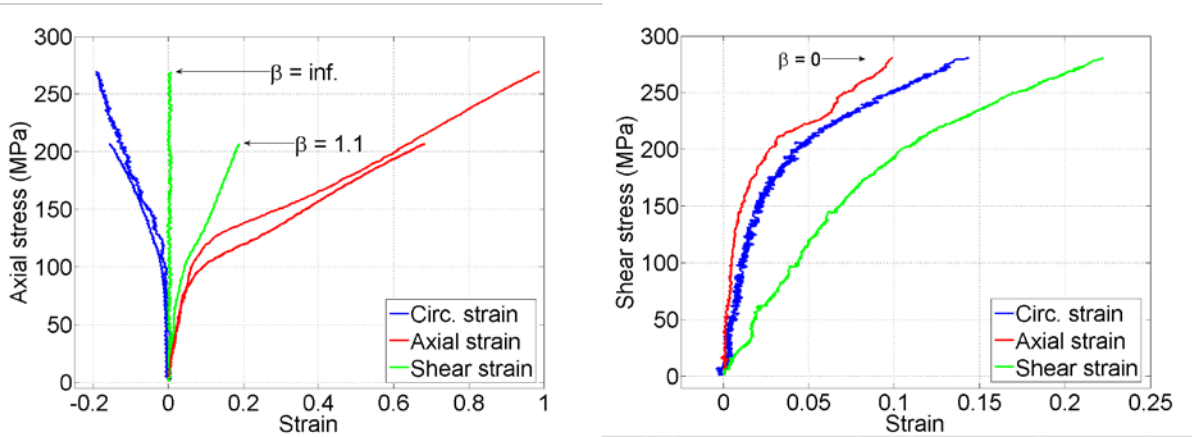


FIG. 1. Stress-strain responses for tension, tension-torsion and torsion monotonous tests.

The equivalent strains reached at failure are higher in the case of tension than it is for the material subjected to pure shear. One can observe non trivial effects of damage on the stress-strain response : the tube subjected to tension has a negative circumferential strain (reduction in diameter). In torsion, we observe a fast loss of orthotropy when the circumferential and axial components of the strain are starting to increase (they are supposed to be zero in an orthotropic material).

3. Damage criteria

3.1. Mechanical definition

As previously mentioned, the definition of damage criteria is extremely important for the design of components in normal operating conditions, in order to define the boundaries of acceptable stresses. Though failure criteria are rather simple to define, using the strain or stress values reached at failure, damage criteria require a measurement of the damage state, preferably using macroscopic data. In the case of SiC/SiC composites, whose damage results in a non-linear stress stress response, one can evaluate a deviation from the initial elastic linear behavior. We propose the use of a criterion such as :

$$\left\| \tilde{\varepsilon} - \tilde{S}_0 : \tilde{\sigma} \right\| = a$$

Where $\tilde{\varepsilon}$ is the strain tensor, $\tilde{\sigma}$ the stress tensor, \tilde{S}_0 the initial compliance tensor and a a constant. $\| \cdot \|$ is a tensor norm. This criteria is therefore only based on the damage effect on the mechanical properties. However, most on the components of these tensors, especially the out-of-plane components cannot be measured using extensometry and acceptable hypotheses on the stress and strain properties. In the following example (FIG. 2.), we use a compliance tensor coming from a mix of components measured experimentally and components calculated using numerical homogenization of the composite microstructure. The out-of-plane components of the stress tensor are assumed to be zero, which is a reasonable assumption. We also do not take into account the out-of-plane damage : these strain components are assumed to remain elastic. The tensor norm is the usual 2-norm.

3.2. Acoustic emission energy definition

Acoustic emission (AE) is a very usual tool when considering composite materials and generally used as a qualitative assessment of damage. The acoustic events recorded during the test are described using a few quantities such as their energy, duration etc.... For our material, no event is detected while we remain below the elastic limit, and past this limit events happen in a complex fashion. However, an interesting quantity to consider is the cumulated energy of all recorded events, which is obviously a monotonous increasing quantity in the history of the material. Due to the lack of reproductibility of this quantity, which depends on sensor position, acquisition parameters, sensor-surface coupling, etc. we use as a criteria the fraction of acoustic energy received relatively to the total acoustic energy received at failure. The criterion is therefore :

$$\frac{E^{EA}}{E_{failure}^{EA}} = b$$

We assume that the energy measured with EA is a relevant parameter to assess the severity of damage in the material, approach suggested for example in [3]. We compare in the example FIG. 2. the two criteria in the axial stress-shear stress plane. The value of constant a is taken as 5.10^{-4} in the mechanical criterion, and taken as 0.1 in the acoustic criterion. For approximately equal values in traction, the AE criterion appears to be more conservative in torsion than the mechanical criterion.

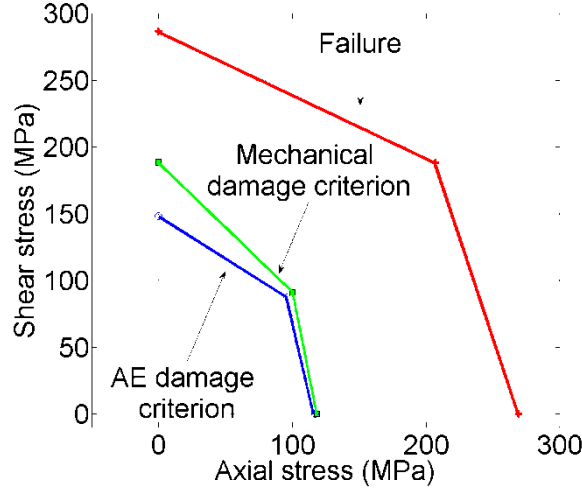


FIG. 2. Plots of the AE damage criterion, mechanical damage criterion and failure surface in the (shear stress – axial stress) plane using $\beta=0$, $\beta=1.1$ and $\beta=\infty$ data.

4. Non linear behaviour

4.1. Damage modeling

Damage in SiC/SiC composites is a complex phenomenon for which properties of cracks are dependent both on microstructural effects and on stress effects. From a modelling point of view, that means that damage in the material should be modelled using scalar damage variables (for the fixed directions of damage associated with the material directions) and tensorial damage variables (for the directions of damage associated with the principal directions of stress, for example). However, we will use a simplified representation of damage, with only four fixed crack orientations, at -45° , 0° , 45° and 90° angles with the tube axis, following work previously carried out at ONERA [4][5][6]. Using simple micromechanical assumptions, we obtain a constitutive law of the form :

$$\tilde{\varepsilon} = \underbrace{\tilde{S}_0 : \tilde{\sigma}}_{\text{Elasticity}} + \underbrace{\sum_{i=1,2,3,4} \eta_i \rho_i \left(\tilde{\delta}_i^S \otimes \tilde{n}_i \right)}_{\text{Damage}} + \tilde{\varepsilon}_S$$

For each crack orientation system i , η_i is a deactivation index, introduced to reproduce the crack closure in compression, ρ_i the crack density, $\tilde{\delta}_i^S$ the crack opening vector, \tilde{n}_i the normal to the crack and $\tilde{\varepsilon}_S$ a stored strain, which solves discontinuity issues met at crack closure [7][8]. These different quantities (density, deactivation, opening vector) are calculated using phenomenological laws functions of the stress tensor. The stored strain is a function of the history of the material.

4.2. Identification of model parameters

The damage model has been identified on the traction-torsion tests performed on the composite, for which, thanks to the symetries of the material, -45° direction is equivalent to the 45° direction, and 0° direction is equivalent to 90° . We therefore have twelve material parameters to identify, i.e. two for the opening vector law, and four for the crack density law, for the two types of crack systems. This identification has been carried out on the tension-torsion experimental curves, by a minimization of the difference between the simulated and the experimental strains. Examples of comparisons between experiment and the identified model can be found in FIG. 3.

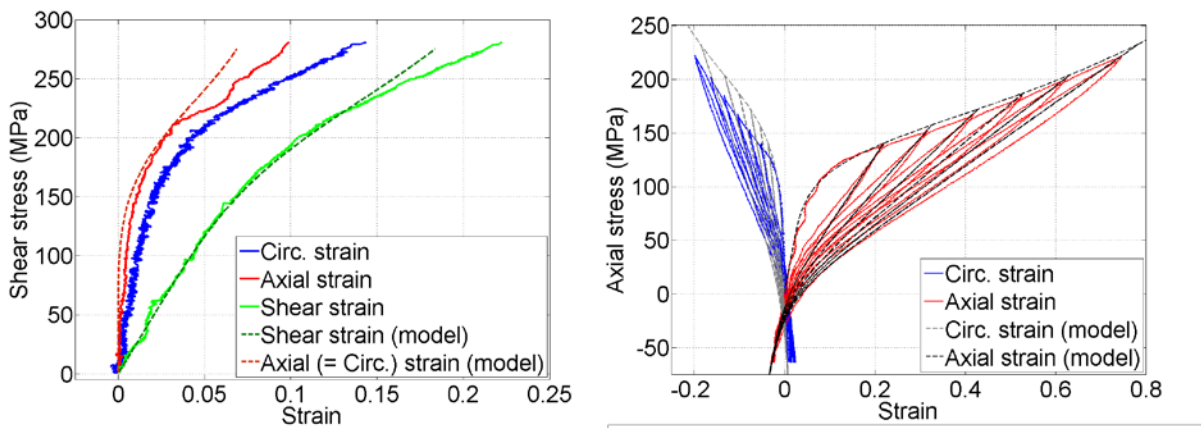


FIG. 3. Examples of simulation results compared to experimental data for torsion and cyclic-tension tests.

Some difference between the measured strains and the strains predicted by the model can be observed in torsion. However, this difference is specific to the very non-linear region close to failure. New damage mechanisms are likely to be active in this high stress area, related to interfaces or fibres, and therefore a more accurate description might require an enrichment of the model. The cyclic behavior is correctly reproduced, except the hysteresis loops (due to friction at interfaces) between unloading and loading which can not be reproduced by the model.

5. Conclusions

A mechanical characterization of a SiC/SiC composite has been conducted on tubes with a microstructure similar to GFR fuel cladding tubes. These different tests allowed to define some damage measurements that could be used for design purposes. The stress-strain responses were used as an identification basis for a damage model which gives satisfying results for monotonic and cyclic proportional tension-torsion tests. Additional tension-torsion tests on this material (as well as on microstructures with different weaving angles) will allow to refine the damage and failure yield surfaces as well as improvements of the model taking into account additional mechanisms. In addition with tension-internal pressure tests, a full in-plane modelling of the material's mechanical behavior should be possible.

REFERENCES

- [1] Maire, J.-F., Pacou, D., Essais de traction-compression-torsion sur tubes composites céramique-céramique, JNC 10, 1996
- [2] Morscher, G. N., Modal acoustic emission of damage accumulation in a woven SiC/SiC composite, Composites Science and Technology, 59, 687-697, 1999
- [3] Morscher, G. N., Modeling the elastic modulus of 2D woven CVI SiC composites, Composites Science and Technology, 66, 2804-2814, 2006
- [4] Carrère, N., Maire, J.-F., Modélisation multiéchelles de composites SiC/SiC, Rapport technique, ONERA, 2005
- [5] Marcin, L., et al., Stratégies de calcul robustes pour l'étude de la tenue de structures CMC, JNC 15, 2007
- [6] Marcin, L., Modélisation du comportement, de l'endommagement et de la rupture de matériaux composites à renforts tissés pour le dimensionnement robuste de structures, PhD thesis, Université Bordeaux I, 2010
- [7] Boursin, A., Chaboche, J.-L., Roudolff, F., Mécanique de l'endommagement avec conditions unilatérales et stockage d'énergie élastique, C. R. Acad. Sci., 1996, 323, 369-376
- [8] Chaboche, J.-L., Maire, J.-F., New progress in micromechanics-based CDM models and their application to CMCs, Composites Science and Technology, 61, 2239-2246, 2001

Fabrication and characterization of aluminum-containing ferritic ODS alloys for improved corrosion resistance

Jan Hoffmann, Michael Rieth, Michael Lorenz, Anton Möslang

Karlsruhe Institute of Technologie, IAM-AWP, Karlsruhe, Germany

Abstract. Future generation nuclear reactors will have demanding requirements on materials. Present materials are unable to cope with the desired operating temperatures and environments. Ferritic ODS alloys are candidate materials which might meet these requirements. Especially, alloys with additional aluminum content have a large potential to withstand the corrosive environments. In the present study, 12-14%Cr ferritic ODS alloys with varying aluminium content produced by mechanical alloying are investigated. After mechanical alloying of a pre-alloyed steel powder with aluminum in an attritor ball mill, the process was investigated by SEM and TEM analysis of the milled powder particles. After compacting by hot isostatic pressing and hot-rolling followed by annealing, the mechanical properties of the materials were assessed by tensile tests and hardness measurements. The results showed that the aluminum content has a big influence on the powder particle size during mechanical alloying. Also a drop in the yield strength could be observed. All further results are analyzed, compared, and discussed in this paper.

1. Introduction

Oxide dispersion strengthened ferritic steels, which have been developed in the recent years have superior properties when compared to conventional high-chromium ferritic steels. These properties qualify them as candidate materials for future generation nuclear power plants. Alloys containing between 12 and 14 % chromium with an addition of 2-4% of aluminium have a large potential to withstand high corrosive environment such as supercritical water reactors and liquid metal cooled conditions.

2. Materials and processes

In this present study, the production of four different ODS alloys was done by mechanical alloying (MA) pre-alloyed powders in an attritor ball mill (ZOZ Simoloyer CM02) for 80 hours at 1200 rpm. The basic alloy powder has a composition of Fe-13Cr-1W-0.3Ti and was produced by argon-gas-atomization by Nanoval, Berlin. 0.3 wt.% Yttrium were added in the form of a powder of an intermetallic phase of Fe₂Y, also produced by Nanoval. The variation of the aluminium content was done by adding different amounts of FeAl₃ powder before mechanical alloying. The dilution of other alloying elements of the pre-alloyed powder by the addition of the iron intermetallic powders was compensated by adding Chromium (Cr) and Titanium-Hydrate (TiH₂) powders to the high-aluminum containing alloys (2,3 and 4% Al).

All processing after MA was done in argon inert gas atmosphere without exposing the powders to air. Following, the material was put into steel cans and HIPped for 2 h at 1150°C with an applied pressure of 100 MPa. After HIPing, the cans were hot-rolled (HR) at 1100°C from a diameter of 40 mm to 6 mm thickness in 5 passes with reheating after each pass at TU Clausthal.

Table 1. Chemical composition of the produced alloys

No.	Cr	W	Ti	Y	Al	Fe
0 (ref.)	13	1	0.3	0.3	-	bal.
2	13	1	0.3	0.3	2	bal.
3	13	1	0.3	0.3	3	bal.
4	13	1	0.3	0.3	4	bal.

Powder particle sized distribution measurements were done on a Horriba LA-950 laser scattering particle analyzer which was operated in flowing iso-proponal condition. All measurements were carried out multiple times at averaged over all results. TEM specimens were produced by thin film cutting with microtomy. The full process was described elsewhere[1].

Miniaturized round specimens with 7.6 mm x 2 mm gauge length were used for the tensile tests, which were performed at temperatures ranging between 23°C and 700°C using a strain rate of $1,6 \cdot 10^{-6} \text{ms}^{-1}$. All specimens were cut by electro-discharge-machining (EDM) and taken out in L-T orientation in the (elongated) rolling-direction. Vickers hardness tests a universal hardness tester with 30 kp loading and averaged over 3 measurements per specimen.

3. Experimental results and discussion

The particle size distribution of the mechanically alloyed powders showed a big variation with increasing aluminium content. A major increase in the particle size can be observed after the addition 3 and 4 wt.% of aluminium. Slight coarsening of the powder particles can be observed with the 2% Al alloy (Figure 5). The increase of the powder particle size and coarsening of the particles with increasing Al-content is caused by the softening of the material due to the Al-content. During the mechanical alloying, softer materials tend to form larger particles after milling. The MA-process is characterized by two dominant mechanisms. Welding of powder particles due to the high milling energies leads to coarser particles at the beginning of the process. When the damage and deformation in the powder reaches a certain level, fracture of particles becomes the dominant mechanism [2]. This was shown in earlier works on ferritic (non-Al) ODS alloys [3]. By looking at the particle size measured after 80 hours milling, it leads to the conclusion that the milling process is still dominated by the cold welding process, especially when compared to the reference (non-Al) alloy.

Table 1 mean particle sizes of different alloys

Alloy	0%-Al	2%-Al	3%-Al	4%-Al
mean particle size (d_{50}) [μm]	40.81	42.52	81.13	109.71

The examinations by transmission electron microscopy were performed in high angle annular dark field mode (HAADF) combined with energy dispersive x-ray spectroscopy (EDS). The obtained images and elemental mappings can be found in Figure 1 and Figure 2. The results of the 2%-Al alloys (Figure 1) show larger areas of chromium enrichments and very small clusters with higher aluminium concentration. This phenomenon increases when looking at the 3%-Al materials (Figure 2). These

enrichments are an effect of the mechanical alloying can be neglected for the properties and structure of the final materials. By looking at the Fe-Al and Fe-Cr phase diagrams, it becomes obvious that both chromium and aluminium will form a solid solution with the iron matrix during compacting and thermo-mechanical treatments due to the high temperatures and slow cooling rates.

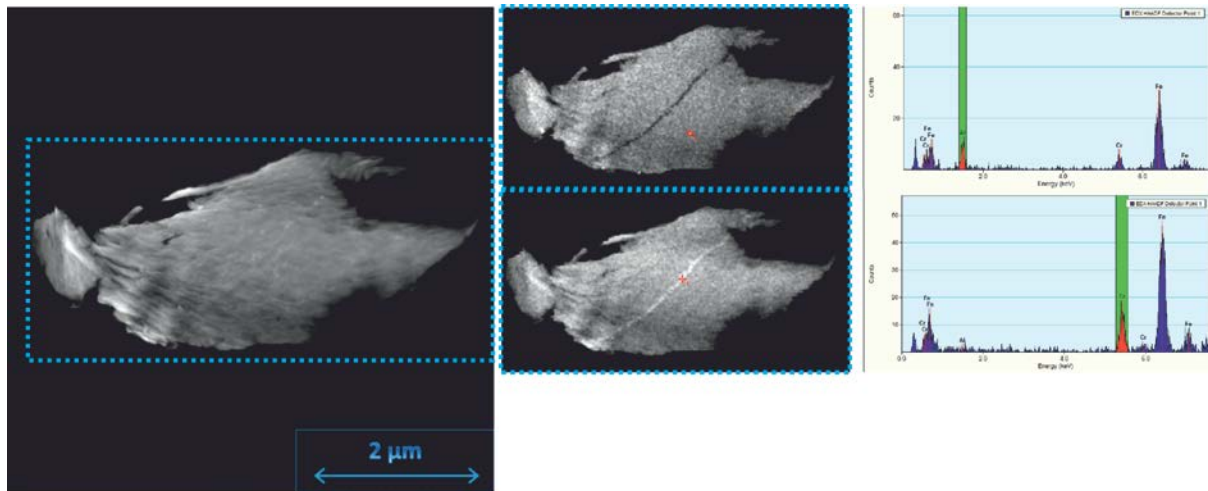


Figure 1 HAADF image and EDS map of 2% Al alloy

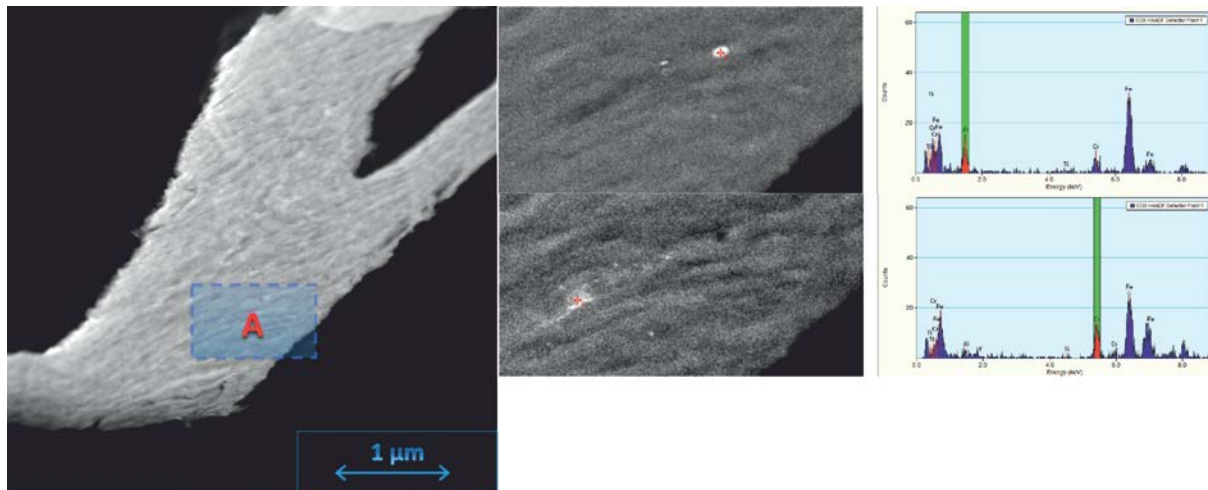


Figure 2 HAADF image and EDS elemental map of 3% Al alloy

The Vickers hardness of the alloys after HIPping and hot rolling shows a significantly lower hardness of the Al-containing materials (Figure 4). In the mechanical properties, a lower strength can also be observed. The addition of aluminium causes the yield strength to drop more than 300 MPa, when compared to the reference alloy (Figure 3). A drop in (yield) strength of the material was expected and has also been seen in works by other groups [4]. A difference in the density and size of nano-oxide clusters inside the microstructure causes the weaker mechanical properties. TEM characterization are planned for the future to reveal this matter. However, it is remarkable that the strength at the desired operating temperatures (550°C+) is independent of the aluminium content.

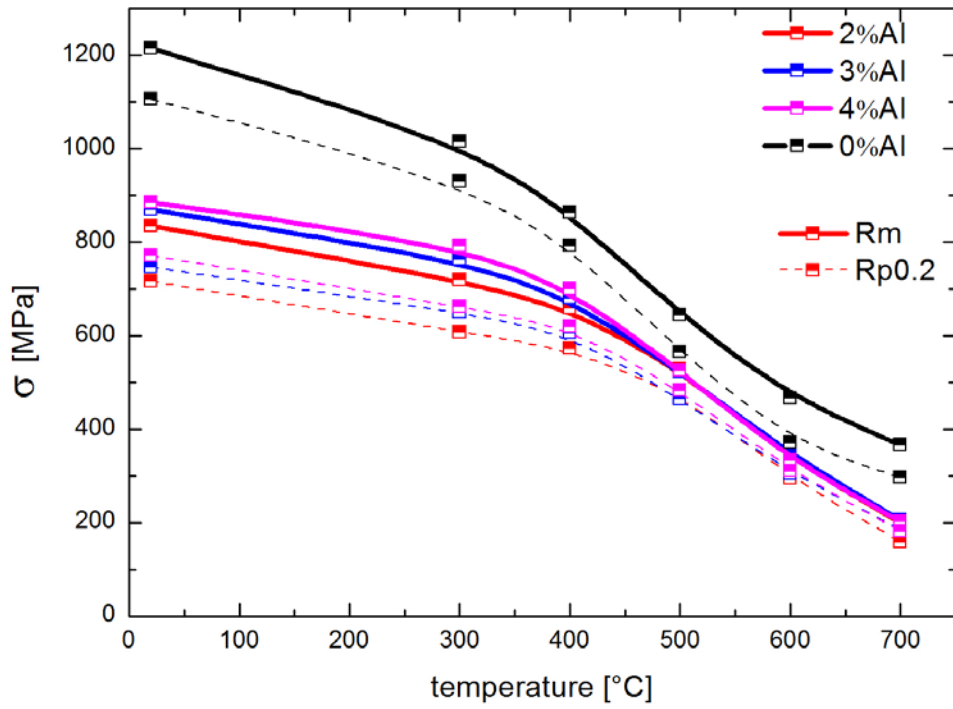


Figure 3 tensile testing of alloys (yield strength and ultimate tensile strength)

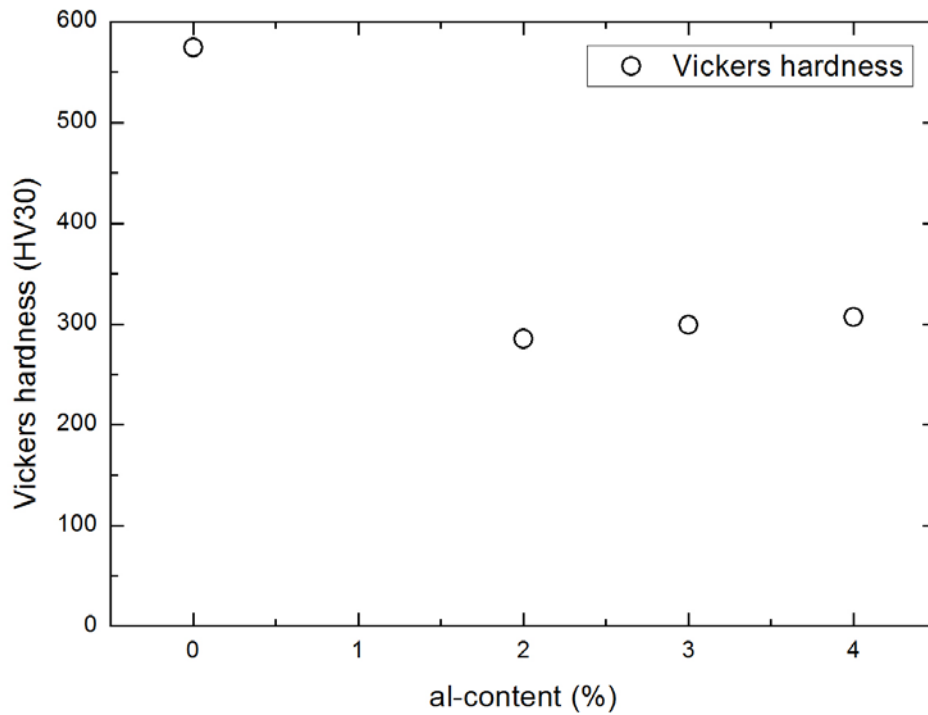


Figure 4 Vickers hardness of alloys

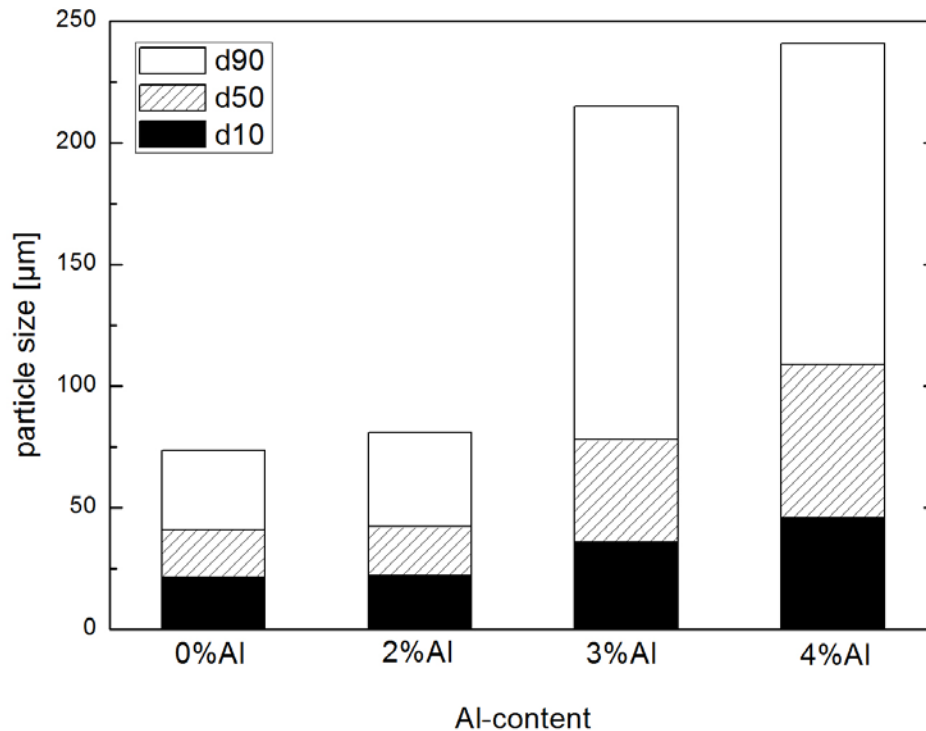


Figure 5 powder particle size distribution

ACKNOWLEDGEMENTS

This project has received funding from the European community's Seventh framework program (FP7/2007-2013) under grant agreement N°269706 - MATTER Project. The Karlsruhe Institute of Technology is acknowledged for the overall use of their facilities. Thanks are also due to Dipl. Ing Marcus Kühn (TU Clausthal) for the assistance in hot rolling of the ODS steels.

REFERENCES

- [1] J. Hoffmann, M. Klimenkov, R. Lindau, M. Rieth, TEM study of mechanically alloyed ODS steel powder, *Journal of Nuclear Materials*, (2011).
- [2] P.S. Gilman, B.J. S., Mechanical alloying, *Annual Review Materials Science*, 13 (1983) 279-300.
- [3] J. Hoffmann, M. Klimenkov, R. Lindau, M. Rieth, Validation of the mechanical alloying process of ODS steel powder, *Proceedings of the Jahrestagung Kerntechnik*, (2011).
- [4] C.H. Zhang, A. Kimura, R. Kasada, J. Jang, H. Kishimoto, Y.T. Yang, Characterization of the oxide particles in Al-added high-Cr ODS ferritic steels, *Journal of Nuclear Materials*, 417 (2011) 221-224.

Thermal stability of moderating material used to enhance the feedback coefficients in SFR cores

Bruno Merk

Department of Reactor Safety at Institute of Resource Ecology
Helmholtz-Zentrum Dresden-Rossendorf

Abstract. The use of fine distributed moderating material to enhance the feedback effects in sodium cooled fast reactors and to reduce the sodium void effect is described. An overview on possible materials is provided and the relationship between hydrogen content and thermal stability is described. A solution for the problem of the limited thermal stability of hydrogen bearing moderating material $ZrH_{1.6}$ is developed by the use of Yttrium-mono-hydride and the similarity to the effects reached by ZrH is demonstrated by comparison calculations. The topic will be closed by an overview on material properties, manufacturing issues, experience in fast reactors and a comparison of raw material costs. The simulation results for the influence of the moderating material on the fuel assembly geometry, the neutron spectrum, the feedback effects, the power distribution, the burnup distribution, and the transmutation performance is given.

1. Introduction

The positive coolant density feedback is inherent to the system in sodium cooled fast reactors (SFRs). This effect is the basis for the sodium void effect, which is the maximal reduction of the sodium density to void state. The reduction of the sodium void effect as well as the enhancement of the feedback effects is an important point in the design of new sodium cooled fast reactors. The feedback effects in fast reactors as well as the sodium void effect itself and the different contributions to the effects are well known since the 1960s. Detailed descriptions have already been given in 'Reactivity Coefficients in Large Fast Power Reactors' in 1970 [1]. Already in the 1970s numerical studies were conducted with the aim to reduce the sodium void effect [2]. These studies were mostly based on full core calculations for the optimization of the core geometry to reduce the sodium void effect by increasing the leakage component. One important outcome of these full core studies is the development of the high leakage cores with their big core diameter (~ 5 meters) combined with a very small core height (≤ 1 meter). Current publications mostly concentrate on the design of sodium cooled fast reactor cores [3] and basic or detailed discussions on the different influencing parameters on the sodium void effect [4], [5] and the limited possibilities for enhancing the feedback effects in traditional designs.

In recent times, a new design proposal for the old idea of introducing moderating material [6, 7] has been given. The positive void effect is here reduced in combination with a significant increase of the absolute value of the fuel temperature effect and a decrease of the positive coolant effect by adding fine distributed moderating material. The study has been focused in the first step on the choice of the ideal moderating material [8], [9] and in a second step on the optimization of the placing of the selected zirconium hydride to obtain the optimal effect without effecting the power distribution and burnup as well as during transients [10], [11]. In the third step the focus has been put on the influence of the moderating material on the transmutation performance of a SFR [12] and on a first glance to solve the problem of thermal stability of the moderating material [12,13].

The calculations for all studies are performed with the lattice transport code HELIOS and based detailed full fuel assembly geometry representation. These possibilities are given due to the rapid development of the spectral codes for LWR analysis which solve the integral transport equation in two

B. Merk

dimensions on unstructured mesh [14], [15]. These codes offer the chance to investigate the feedback effects on fuel assembly level for different designs in full detail including multi-group visualization of integral and spatially resolved neutron flux and cross sections.

In this study a comprehensive investigation for a moderating material with increased thermal stability is performed. First, an overview is given on a number of possible materials and the relationship between hydrogen content and thermal stability is described. Using this information a decision for the most appropriate material is taken. In a next step an overview on material properties, manufacturing issues, experience in fast reactors and a comparison of raw material costs is given. Following this literature study, the material choice is confirmed by calculations for the effect of the new moderating material which will be compared to the results obtained for ZrH material.

2. Possible Moderating Materials

The key requirement for the moderating material is a high slowing down power. An efficient moderation with an acceptably small amount of moderating material can only be achieved using a material with very high slowing down power. The limitation of the amount of moderating material is a requirement, since the geometric arrangement of the fuel assembly should be untouched by the introduction of the moderating material. It has already been demonstrated, that this requirement can only be fulfilled using hydrogen [8], [9]. Theoretically pure hydrogen would be a good solution, but it is impossible to confine this material under operation and especially accidental conditions. The same can be stated for liquid bound hydrogen like in water or organic liquids. These materials cause the same problems of confinement in the operational temperature range. Especially with water, the sodium water reaction would be a possible consequence. Thus the focus will be put to solid hydrogen bearing materials. Hydrogen bound in organic compounds, like polyethylene, is thermally not stable enough, but compounds with metals have the possibility for high thermal stability. A literature survey led to the textbook Metal Hydrides by W.M. Mueller, J. P. Blackledge, and G. G. Libowitz [16].

Mueller, Blackledge, Libowitz suggest the following criterion for the evaluation of the thermal stability of metal hydrides: <<The thermal stability of a reactor component is of utmost importance and in the high-temperature reactors it is the prime criterion for selection of a material. A metal hydride in almost all instances can be expected to dissociate at temperatures well below its melting point or at which its strength is materially reduced. Inasmuch as the degree of dissociation is a function of temperature, the best way to describe the thermal stability is to plot isotherms of hydrogen pressure vs. the composition of the hydride>> [16]. Based on this criterion, a list of possible candidates can be found. Possible materials mentioned for forming stable compounds with hydrogen are: Ce, Zr, Ca, Y, Sc, Ti, Th, V, Nb, Ta. A more detailed look identifies the materials V, Nb, Ta as not efficient enough, thus the possible hydrogen content to be bound is to low. The other materials of the list are possibly interesting candidates. Up to now the reference material has been ZrH_{1.6} and ZrH₂. Based on this reference, Ti can be excluded too, since Ti is only stable until ~600°C and thus dissociates earlier than the Zr based compound. The compounds based on Th, Sc dissociate both about the same temperature range as ZrH but the achievable hydrogen content is lower than for Zr.

Based on this reduced matrix of possible materials (Y, Ce, Ca, and Zr) for forming the hydrogen bearing compound, a detailed comparison is given in [16]. Fig. 1 shows the composition of the hydride represented by the hydrogen number vs. dissociation temperature at a hydrogen pressure at 1 atm. The hydrogen number N_H is defined as the number of hydrogen atoms per cubic centimetre of hydride material $\cdot 10^{22}$

$$N_H = \frac{\rho N_A (H / M)}{\text{mol. wt.}} \cdot 10^{-22}$$

ρ = density of the hydride
NA = Avogadro number

B. Merk

H/M = hydrogen-to-metal atom ration in the hydride
 mol. wt. = molecular weight of the hydrogen

It is obvious, that Zr is the most efficient hydrogen carrier at temperatures below 800°C. The often as moderator suggested ZrH_{1.6} leads to a hydrogen number of

$$N_H(\text{ZrH}_{1.6}) = \frac{5.61 \cdot 6.022 \cdot 10^{23} (1.6/1)}{(91.224 + 1.6 \cdot 1.0079)} \cdot 10^{-22} = 5.82 .$$

This value leads to a temperature of ~800-850 °C where the hydrogen release pressure rises above the 1 atm. The analysis of Fig. 1 shows, that all three other materials have a comparable behaviour. There is an area with a stable NH value for a wide temperature range which is followed by a drop caused by increasing temperature. The major difference is the amount of hydrogen which can be bound in the compound. This amount is comparably low for Ca, slightly higher for Ce and highest for Y. Additionally, the compound based on Y is the thermally most stable one. The information of this figure can be used for the other direction, the choice of the material configuration depending on the required thermal stability, too.

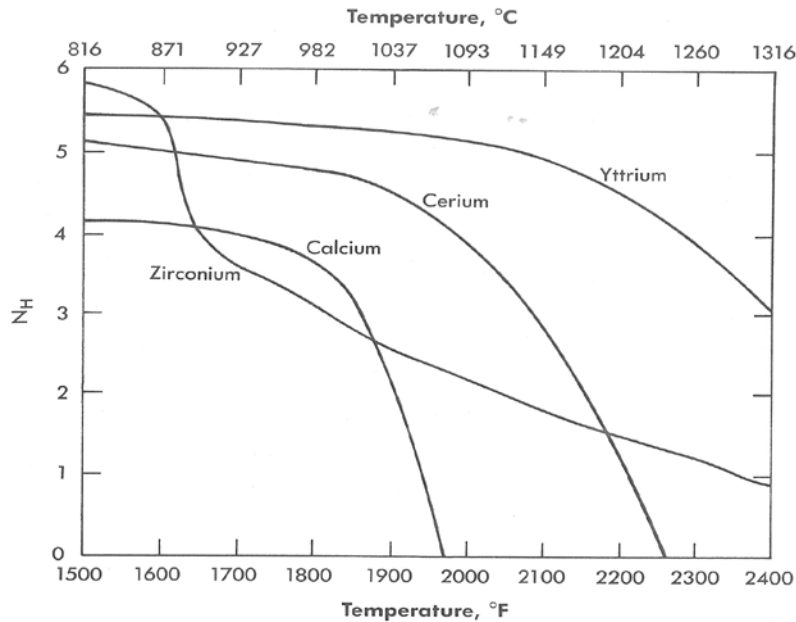


Fig. 1: Hydrogen content in metallic Zr, Ce, Y, and Ca in equilibrium with 1 atm H₂ at various temperatures [17]

When the stability up to 1300 °C is required, Y can carry hydrogen up to a N_H value of 3. Reformulating the equation leads to

$$H = \frac{N_H \cdot 10^{22} \cdot Mm}{\rho N_A - N_H \cdot 10^{22} \cdot Mh}$$

and using N_H = 3 leads to the following acceptable configuration.

$$H(YH_3) = \frac{3 \cdot 10^{22} \cdot 88.906}{4.3 \cdot 6.022 \cdot 10^{23} - 3 \cdot 10^{22} \cdot 1.0079} = 1.04$$

Thus, yttrium-mono-hydride will be stable up to more than 1316°C. A first extrapolation indicates that the halving the hydrogen content from YH to Y₂H could increase the limit temperature by maximal

B. Merk

~100 °C more. Using this data it can be stated, that a stable hydrogen bearing compound can be found for the use in a SFR, since the stability can be assured well above the sodium voiding temperature of ~880 °C.

3. Remarks on Technological Issues and Reactor Experience

After the choice of the ideal metal for forming the hydrogen bearing compound, the attention will be given to some technological issues. It is very often stated, that hydrogen leads to embrittlement of the carrying metal, since hydrogen embrittlement is a well know and dreaded effect. In contrast to this experience, the following statement is given in [16] on the effect of hydrogen on materials: <<It should not be inferred that the presence of hydrogen in metals is always deleterious. When present in amounts less than necessary for embrittlement (this can be as high as 2000 ppm in some zirconium alloys), hydrogen can cause a noticeable increase in strength so long it can be retained in solution. The important point, again, is that hydrogen presents serious problems only when it is not retained in solution or when its concentration exceeds the solubility limits of the alloy so that hydride precipitates or segregation can occur. Otherwise, hydrogen reacts similarly to other alloying elements in most respects.>>

Another important technological aspect is the production strategy for hydrogen bearing materials. A description of the ideal strategy is given in [16], too: <<Although compacted hydrides can be machined, it is more suitable to hydride massive pre-machined sections. These are much easier to handle and have superior mechanical properties. Hydrided alloys provide a range of hydrogen concentrations in combination with considerable variation in nuclear and mechanical properties and good thermal stability. Cladding and canning of the hydrides will prevent severe hydrogen loss at elevated temperatures and maintain structural integrity to some extent.>>

A comment about a possible coating to prevent hydrogen release even more efficiently is given as final technological remark, once more in [16]: <<A number of materials have been investigated as possible barriers to hydrogen migration. Kanigen nickel shows promise as a barrier coating for zirconium hydride of $NH = 4$ on the basis of hydrogen loss for times up to 100 h at 1300 °F in argon, but it is not suitable at $NH = 5$. Oxidation in air and a tendency to crack when the coated hydride was drilled caused Kanigen nickel to be dropped from consideration. ... Preliminary indications where that a modification of an iron – 10% aluminium – 34% manganese alloy would meet all requirements of a good coating for yttrium hydride.>> Thus even on this very special topic, some historic knowledge is available. Nevertheless, when this kind of materials should be inserted into a nuclear reactor, at least some kind of reactor experience has to be available, or a very comprehensive test program would be required.

There is already some limited experience with YH in fast reactors. YH moderators have already been used in the Fast Flux Test Facility (FFTF) for several experimental setups first for tests of the moderating material itself and then for an isotope production experiment. <<The hydrogen-moderated, Multi-Isotope Production Test Assembly contained isotopic samples to reduce uncertainties in key nuclear data associated with isotope production, and was irradiated in May 1989 in the outer reflector region of the Fast Flux Test Facility.>> [18] A more detailed description about this experiment indicates the use of YH moderators. <<Yttrium hydride ($YH_{1.7}$) moderator was used to create neutronic environments with intermediate energy levels between thermal systems and fast systems, Six pins containing $YH_{1.7}$ surrounded the central test pin to provide the required moderated neutron environment. The 12 outer pins contain tungsten up to the elevation of the top of the six central pin test sections, with $YH_{1.7}$ above the tungsten. Three of the six middle $YH_{1.7}$ pins contained dosimetry and actinide samples provided and processed.>> [18] . Before this test some experience has already been available from previous tests. A cobalt test assembly containing YH pins for neutron moderation was irradiated in the FFTF during cycle 9A for 137.7 equivalent full power days at a power level of 291 MW. The assembly contained 19 YH pins and one of the objectives of this test was to provide YH pins for post irradiation examination to determine the stability of YH under prototypic operating conditions [19].

B. Merk

The final view in this chapter is for the prices of different nuclear materials, as given in <https://www.metal-pages.com> (status second half 2011):

- Y metal 170-210\$/kg
- Ce metal 80-170\$/kg
- Gd metal 203-226\$/kg
- Zr metal 50-250 \$/kg (reactor grade at the upper end)

Thus the prices for yttrium metal are in the usual range for special materials used in nuclear reactors.

4. Comparison of Enhanced Feedback Effects

The test calculations are based on the identical EFR configuration like [20 - 23] it has been used for all earlier studies [8 - 13] with 22.4% Pu content in the assembly. The Pu-Vektor is (2.6/54.5/23.7/11.3/6.8) and 1.1% Am-241 in depleted uranium (0.3% U-235 content). The smeared fuel density is 9.26 g/cm³, the average fuel temperature is 900°C. Cladding, wire spacers and can wall are made from stainless steel 304 along the HELIOS 1.9 definition. The moderating material is inserted in the wire wrapper. This solution has been identified as the most promising one [10]. For the comparison all material configurations are kept identical, identical amount of steel, fuel, sodium, and hydrogen to eliminate all influences from the input, only ZrH is replaced by YH.

The applied code HELIOS 1.9 is mostly used for light water reactor calculations. For validation of the very significant results caused by the insertion of moderating material on the feedback coefficients, a cross comparison with MCNP for the initial value of fuel temperature and moderator effect on k_{inf} was performed on a simplified basis at the beginning of the project. Very good agreement has been achieved for both effects [8, 9]. In further comparisons, with the SERPENT and the BGcore Monte-Carlo based codes with burnup capabilities, good agreement was found for the burnup of actinides and minor actinides in fast reactor configurations. The good agreement is given for the use of the 112 and 190 group HELIOS 1.10 libraries and could even be improved using the new 177 group library of HELIOS 2 which was not available at the beginning of the study. This good agreement to continuous energy methods gives confidence in the applicability of the code HELIOS, the methods applied inside the code, and the results for steady state as well as for the burnup calculations. Finally, it has to be kept in mind, that the analysis is based on the changes caused by slight material changes, thus the final absolute amounts are not the major desired information, but the relative differences between the calculated configurations and states.

The basic investigation to check for eventually appearing differences due to the different moderating materials is given for the neutron spectrum, see Fig. 2. The assembly averaged neutron spectrum gives a good overview on the consequences of the insertion of moderating material, even if the very low numbers for neutrons in the thermal energies could have some uncertainties. The 190 group HELIOS 1.9 library is used for these spectral curves to get a sufficiently fine resolution in the thermal groups to be able to visualize the effect of the moderating material. The effect of the insertion of the moderating material can be indicated very clearly. The reference neutron spectrum averaged over the fuel assembly is given in black. The reference spectrum shows only a very small low energy tail with neutrons below 100 eV. This low energy tail is significantly increased as soon as the fine distributed moderating material is inserted. The comparison of the neutron spectrum indicates that the moderation effect is for both materials identical as soon as the identical amounts of hydrogen are inserted into the system.

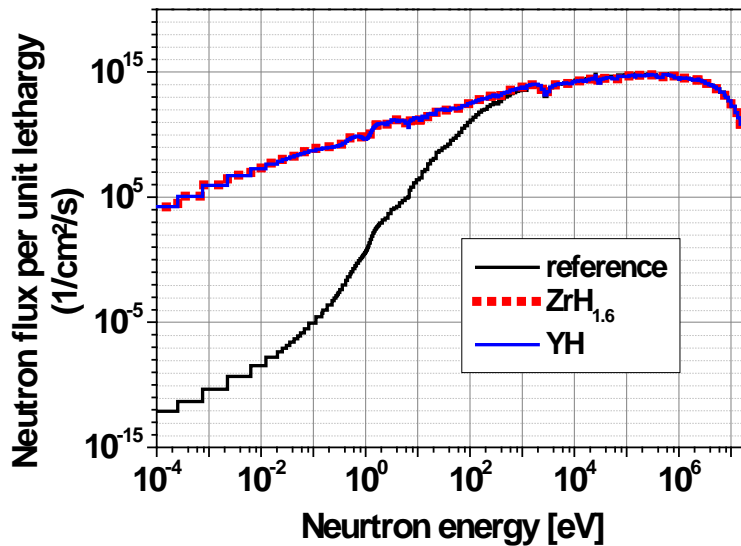


Fig. 2: Neutron spectrum for the reference fuel assembly and for the fuel assembly with moderating material calculated with the 190 group library of HELIOS 1.9

The insertion of the fine distributed moderating material leads to a significant enhancement of the negative feedback effects and to a reduction of the positive feedback effects. The positive sodium void effect is reduced by ~12% due to the insertion of the moderating material, the negative fuel temperature, or Doppler effect is enhanced by ~105%. The positive coolant effect, consisting of the effect caused by the reduced coolant density and the spectral effect due to the coolant temperature change is reduced by ~10%. The comparison of the results for the Zr based and the Y based hydrogen bearing compound, given in Fig. 3, indicates only a minor influence caused by the metallic component of the compound. A detailed comparison of numbers shows, that Zr based material is slightly more efficient, but the difference is very small. It is definitely smaller than the uncertainties in the material data and due to the modelling of the system in the neutron physics code.

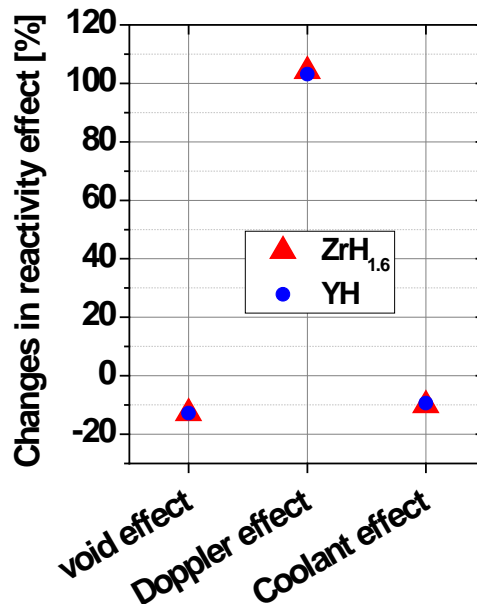


Fig. 3: Comparison of the influence of the hydrogen bearing metal compound on the enhancement of the feedback effects

B. Merk

The assembly burnup distribution after 100 GWd/tHM for the reference case and the cases with the moderator inside the wire wrapper is given in the upper part of Fig. 4. The burnup in the reference case (left) is characterized by a very flat distribution over the fuel assembly as well as over the fuel rod. The reason for this flat burnup distribution can be found in the flat power and neutron flux distribution and in the comparably low total cross sections at the dominating neutron energies. The flat power distribution in the fuel assembly is very favorable, since it disburdens the heat removal. The flat power distribution results in a uniform heat up of the sodium coolant. No hot spots are created and thus all fuel rods can be operated close to the limit power. The burnup distribution for case with distributed moderating material in the wire wrapper (Fig. 4 centre – ZrH and right – YH) is rather uniform, too. A small rim effect appears due to the resonance self shielding in the U-238 and the increased number of neutrons in the resonance region due to the use of the moderating material. A slightly higher burnup occurs at the pins close to the can wall. Nevertheless, the insertion of the moderating material in fine distribution, in the wire wrapper, does not create any severe deterioration in the power and the following burnup distribution. This behavior is in strong contrast to the results for the use of moderating material in pins like it has been discussed in several earlier publications. A locally concentrated introduction of moderating material, like moderator pins would cause a significant power and burnup increase in the pins around the moderator pins and a lower burnup in the pins far from the moderator pins. This uneven burnup distributions causes limitations in the obtainable maximal average burnup of the fuel assembly, since comparably low burnt fuel rods appear in areas far from the moderation pins or from the can wall. Additionally, a very strong power increase and a rim effect with all follow up problems appear at the pins next to the moderating pins [10, 11]. The comparison of the results for the compound based on Zr and on Y show no major difference in the fine distributed case as well as in the pin case.

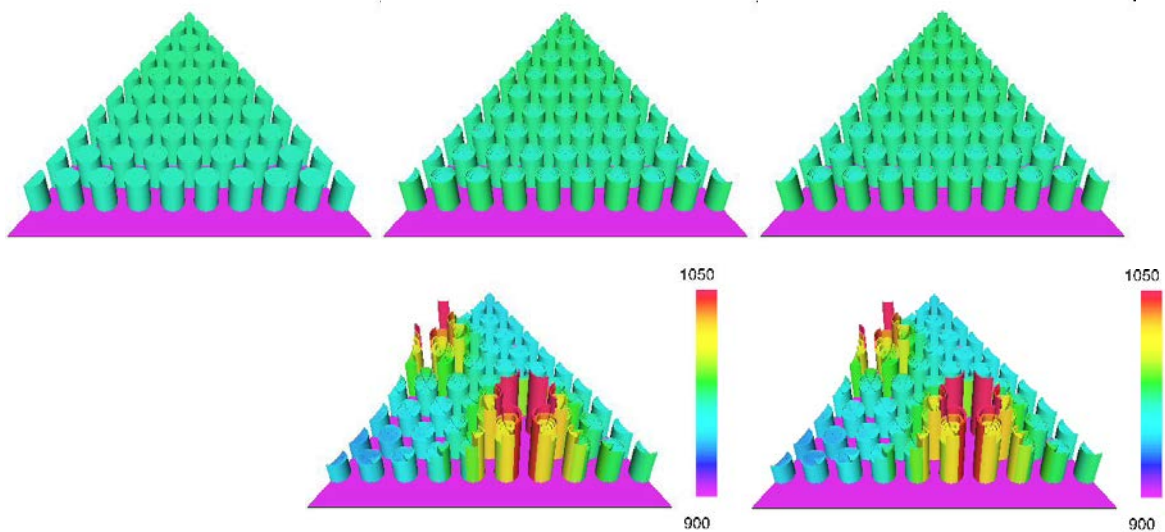


Fig. 4: Burnup distribution at 100 GWd/tHM for the reference case (top left) and the case with the moderating material in the wire wrapper (ZrH centre, YH right) and for moderator in pins (ZrH centre, YH right)

5. Conclusions

The use of fine distributed moderating material offers the possibility to enhance the safety characteristics without changing the major operational and design parameters of a sodium cooled fast

B. Merk

reactor core. Power density and power and burnup distribution, fuel configuration and density, fuel assembly geometry and coolant streaming paths are not changed at all.

The idea offers new degrees of freedom for the optimization of the design of the sodium cooled fast reactor cores, the cycle strategies and the transmutation potential. The fine distributed moderating material increases the inherent system stability significantly and reduces thus the probability of reaching sodium voiding in a transient. The interesting point is the possibility of tailoring the feedback coefficients to an ideal value, which has to be determined from system specific transient and accident analysis, since strong negative feedback is not desired in all accidental scenarios.

Up to now, a major limitation and a point of critics has been the use of ZrH based moderators, since the thermal stability cannot be reliably assured up to the temperature of the onset of sodium voiding. In this publication it has been shown that the replacement of the metallic part of the compound can lead to increased thermal stability. The use of Yttrium is very promising, since with this material a compound can be formed which is stable up to more than 1300°C – yttrium-mono-hydride. The literature review gives the confidence, that this kind of material can be produced, handled, and manufactured. Additionally, there is already some reactor experience from the use in experiments in the Fast Flux Test Facility. The comparison of the effect on the neutron spectrum, the influence on the feedback effects and the burnup distribution demonstrates that there is no major difference between the use of ZrH and YH as long as the hydrogen content is identical. Thus YH is identified as the ideal material for the implementation of the idea of using fine distributed material for the enhancement of negative feedback effects in sodium cooled fast reactors, since the major limitation of the use of ZrH can be eliminated without influencing the desired effects.

REFERENCES

1. H. Hummel and D. Okrent, *Reactivity Coefficients in Large Fast Power Reactors*, ANS (1970).
2. R. N. HILL and H. KHALIL, "Evaluation of LMR Design Options for Reduction of Sodium Void Worth", *Proc. of Int. Conf. on Physics of Reactors*, Vol. 1, p. 11-19, Marseille, France, (1990).
3. G. RIMPAULT et al. , "Towards GEN IV SFR design: Promising ideas for large advanced SFR Core Designs", *International Conference on the Physics of Reactors*, Interlaken, Switzerland (2008).
4. L.BUIRON et al., "Innovative Core Design For Generation IV Sodium-Cooled Fast Reactors", *Proceedings of ICAPP 2007*, Nice, France (2007).
5. K. Sun et al. , "Void Reactivity Decomposition for the Sodium Cooled Fast Reactor in Equilibrium Closed Fuel Cycle", *PHYSOR 2010*, Pittsburgh, USA (2010).
6. R.J.J.C. MacDonald, "The Effect of Enrichment and Moderating Materials in the Sodium Loss and Doppler Coefficients on Fast Reactors", AEEW-M 657 (1966).
7. K. Tsujimoto et al., "Improvement of reactivity coefficients of metallic fuel LMFBR by adding moderating material", *Annals of Nuclear Energy* **28** (2001).
8. B. Merk, E. Fridman, F. P. Weiß, "On the use of zirconium based moderators to enhance the feedback coefficients in a MOX fuelled sodium cooled fast reactor", accepted at *Nuclear Science and Engineering* (2011).
9. B. Merk, F.-P. Weiß, "On the use of a moderation layer to improve the safety behavior in sodium cooled fast reactors", *Annals of Nuclear Energy* **38**, Issue 5, Pages 921-929 (2011)
10. B. Merk, F.-P. Weiß, "Analysis of the influence of different arrangements for ZrH moderator material on the performance of a SFR core", *Annals of Nuclear Energy* **38** 2374–2385 (2011)
11. B. Merk, F. P. Weiß: "On the effect of different placing ZrH moderator material on the performance of a SFR core", submitted to *PHYSOR 2012 – Advances in Reactor Physics – Linking Research, Industry, and Education*, Knoxville, Tennessee, USA (2012)
12. B. Merk, F. P. Weiß: "On the use of moderating material to enhance the feedback coefficients in SFR cores with high Minor Actinide content", ICAPP 2012, Chicago, , USA, June 24-28, 2012, Paper 12428

B. Merk

13. B. Merk: "On the Use of Fine Distributed Moderating Material to Enhance Feedback Coefficients in Fast Reactors", IAEA TM on Innovative Fast Reactor Designs with Enhanced Negative Reactivity Feedback Features, Vienna, 27-29 Feb. 2012
14. E.A. Villarino, R.J.J. Stammler, A.A. Ferri and J.J. Casal, "HELIOS: angularly dependent collision probabilities", *Nucl. Sci. Eng.* **112** (1992).
15. R. Sanchez et al., "APOLLO II: a user-oriented, portable, modular code for multigroup transport assembly calculations", *Nucl. Sci. Eng.* **100** (1988).
16. W.M. Mueller, J. P. Blackledge, G. G. Libowitz, *Metal Hydrides*. Academic Press Inc., New York, USA (1968)
17. Funston, ES: Physical Properties of Yttrium Hydride, in Nuclear Metallurgy, A Symposium on Metallic Moderators and Cladding Materials, Philadelphia, Oct. 19, 1960
18. D. W. Wootan et al. "ISOTOPE PRODUCTION TEST IN THE FAST FLUX TEST FACILITY", in PROCEEDINGS LMR: A DECADE OF LMR PROGRESS AND PROMISE, Washington, D.C. November 11-15, 1990, American Nuclear Society, Inc. La Grange Park, Illinois 60525 USA
19. D. W. Wootan et al.: "Analysis and Results of a Hydrogen-Moderated Isotope Production Assembly in the Fast Flux Test Facility, *Nucl. Sc. and Eng.* 103, 150-156 (1989)
20. IAEA Fast Reactor Database - 2006 Update,
<http://www.iaea.org/inisnkm/nkm/aws/frdb/auxiliary/generalInformation.htm>
21. J. C. Lefèvre, C. H. Mitchell, G. Hubert: "European fast reactor design", *Nuclear Eng. and Design* **162**, 133-143 (1996)
22. A. E. Waltar, A. B. Reynolds, *Fast Breeder Reactors*, Pergamon Press, New York, USA (1981).
23. A. Pay, E. Francillon, B. Steinmetz, D. Barnes, N. Meda, " European Fast Reactor (EFR) Fuel Element Design", http://www.iasmirt.org/iasmirt-3/SMiRT10/DC_250515, *10th International Conference on Structural Mechanics in Reactor Technology*, Anaheim, USA (1989)

Development of vanadium fuel cladding for Sodium Fast Reactors

M. Le Flem^a, J.M. Gentzittel^b, Wident^a, Rouillard^c, Guéneau^c, Sornin^a

^aCEA Saclay, DEN/DANS/DMN, Gif sur Yvette, France

^bCEA Grenoble, DRT/LITEN/DTBH, Saint Martin d'Hères, France

^cCEA Saclay, DEN/DANS/DPC, Gif sur Yvette, France

Abstract. Vanadium alloys are promising material for some core components of the Sodium Fast Reactors, especially for fuel cladding applications. With good mechanical properties up to 800°C at least, good behavior under irradiation above 400°C and limited swelling, they also have the benefit from fusion program. In 2010, CEA launched the manufacturing of a V-4Cr-4Ti alloy, well documented in literature, to validate the uneasy fabrication process linked to interstitial element sensitivity and potential pollution in master alloys. 30kg of CEA-J57 alloy (7 mm-plates) were fabricated for the CEA by GfE Metalle und Materialien GmbH, Nuremberg, Germany. The program includes the investigation of recrystallization, resulting microstructure and DBTT values, high temperature mechanical properties such as tensile strength and creep resistance, chemical compatibility with both the oxide fuel and the coolant and assessment of tube fabrication, actually a triplex tube with inner and outer liners to protect vanadium from oxidation during the hot processing

1. Introduction

Because of the limitation in irradiation dose for the austenitic steels (incubation dose before swelling) and the questionable fabrication and behavior of high chromium ODS, the assessment of non-Fe alloys was suggested. Some vanadium alloys exhibit a good compromise between mechanical strength up to 750°C, neutron compatibility (limited activation) and irradiation resistance (limited embrittlement above 400°C). The V-4Cr-4Ti alloy in particular has been developed in the purpose to have a very low swelling under irradiation and benefits from a large feed back from fusion programs (but vanadium alloys had never been investigated in France). At the moderate operating temperatures of the SFRs, meaning limited strain by thermal creep, the thermomechanical evaluations made at CEA confirmed that V-4Cr-4Ti was promising as the cladding material.

In 2008, the very first studies on vanadium alloys were launched at CEA to assess the feasibility of a SFRs by 2012-2013. This paper summarizes the major results obtained on the CEA-J57 grade in terms of microstructure, mechanical properties at low and high temperature (impact, tensile, creep tests) and the attempts to avoid the issues related to the bad chemical compatibility with the environment.

2. Fabrication of CEA-J57 and resulting microstructure

The fabrication steps of CEA (CEA-J57) were based on the protocols reported in literature for the manufacturing of Japanese, American and Russian V-4Cr-4Ti grades [1-5]. CEA gave specifications to the manufacturer (GfE Metalle und Materialien GmbH, Nuremberg, Germany) who used the following process (detailed elsewhere [6]). First, vanadium was purified by aluminothermic reaction by triple electron beam melting and a 50/50 Cr-Ti master alloy was fabricated by double vacuum arc

remelting. V and Cr-Ti bars were then plasma welded together and double vacuum arc remelted to get the V-4Cr-4Ti ingot. This was forged to billets at 900°C with intermediate annealing at 950°C, processed at low temperature to 9.2 mm-thick sheets with one intermediate annealing at 1050°C and finally mechanically machined to final thickness of 7 mm.

The total content of interstitial impurities O, C, N is 470 ppm, i.e. it lies between the characteristics of the Japanese reference grades (340 ppm [4]) and those of American grades (524 ppm et 600 ppm [7,8]): this evidences a good control of the pollution for this very first attempt of V-4Cr-4Ti fabrication by CEA.

The resulting microstructure consists in grains elongated in the rolling direction, the plates exhibiting a hardness of 218 Hv. Heat treatments were performed between 850°C and 1200°C allowed to determine the recrystallisation temperature, 1000°C. The hardness is decreased down to 143 Hv and the microstructure reveals equiaxial grains with Ti(O,C,N) precipitates oriented in the rolling direction (Figure 1): these precipitates were actually created during the processing at high temperature. Annealing at higher temperature induced an increase in hardness typically due to a partial dissolution of the inclusions and release of O, C and N in the matrix (solid-solution hardening). After 1h at 1100°C, the hardness is 152 Hv.

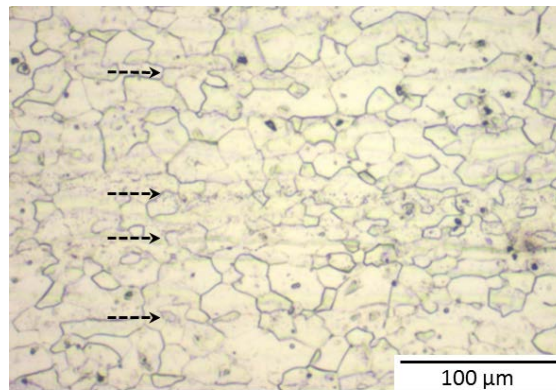


Figure 1: Optical micrograph of V-4Cr-4Ti, CEA-J57, after recrystallization at 1000°C. Ti(O,C,N) precipitates, aligned in the rolling direction, are arrowed.

3. Mechanical properties

3.1. Impact tests

Impact tests were performed between -160°C and 325°C in order to determine the DBTT of plates recrystallised at 1000°C and 1100°C. V-notched beams ($3 \times 4 \times 27 \text{ mm}^3$) were tested to assess the crack propagation in conventional longitudinal and transversal sample orientation [9]. Whereas the as-rolled samples were very anisotropic and brittle, after recrystallisation at 1000°C, the anisotropy of the material disappears and an upper-shelf energy value of about 10 J can be defined from -120 to 25°C, which is quite high according to the small size of the samples. The DBTT is estimated to be just below -160°C. The hardening induced by a recrystallisation annealing at 1100°C is confirmed, the DBTT being shifted to -100°C (same upper-shelf energy).

From these measurements, a recrystallisation treatment at 1000°C was finally chosen for the mechanical characterisation at high temperature.

3.2. Tensile and creep tests

The tensile properties were determined at room temperature and between 600°C and 950°C, both in the longitudinal (LT) and transversal direction (TL) [9]. The change in the yield stress and the ultimate stress are presented in Figure 2.

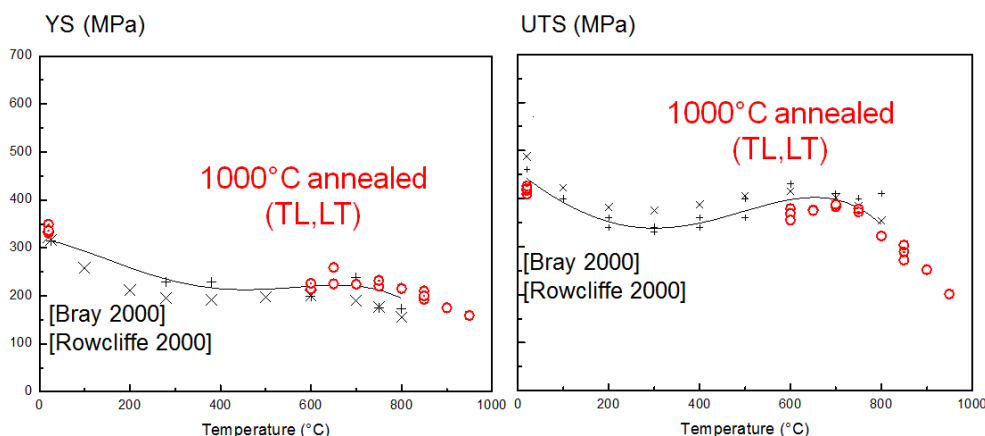


Figure 2: Yield stress and ultimate stress of V-4Cr-4Ti, CEA-J57, recrystallized at 1000°C and compared with literature [10,11].

No anisotropy between the LT and TL directions was detected. The mechanical characteristics of CEA-J57 slightly decrease up to 600°C and then do not significantly change up to 750°C, which is in agreement with previous works [10,11]. Above 800°C, the data are consistent with the expected trends and confirm the decrease in tensile strength. Moreover, the elongations and fracture surfaces confirm the high ductility of V-4Cr-4Ti.

Uniaxial creep tests were performed between 650°C and 850°C (under high vacuum and with sample protections). The creep curves exhibit a very limited primary domain (several hours), a well defined linear secondary domain (the duration depends on the stress and temperature), and finally a wide tertiary domain beginning when the creep strain has reached ~1%. This last step leads to high creep strains until the specimen breaks (ductile behavior). The creep strain rates determined in the secondary creep domain of the CEA-J57 are consistent with literature. The stress exponent n is around 2-3 at 800-850°C (in agreement with results at 800°C by [12,13]) and n reaches 7 at 650-750°C (in agreement with results at 600-700 by [12,13]). The present results confirm the good performance of CEA-J57.

The LMP parameter of CEA-J57 lies in the upper part of the data previously reported by [13], as shown in Figure 3. Additional tests are in progress to build the laws in the conditions targeted by SFRs.

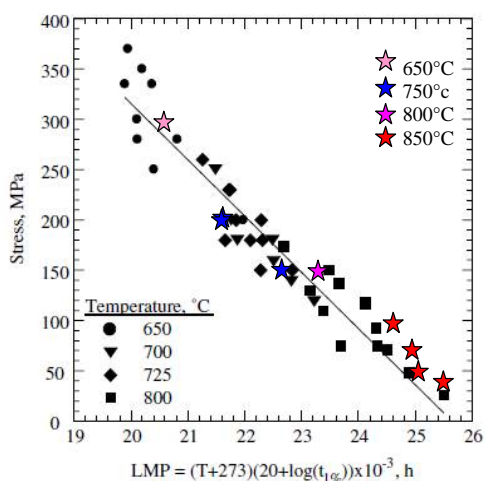


Figure 3: Larson Miller Parameter of V-4Cr-4Ti grades (1% strain): colored plots correspond to CEA-J57 and are compared to the compilation by [13].

4. Compatibility with environment

Vanadium and its alloys are very sensitive to oxidation. Oxygen solubility can reach 22at% and is very detrimental because it induces a dramatic loss of ductility. In addition, depending on the oxygen activity, many oxides of various stoichiometries ranging from VO to V_2O_5 can form. In sodium, neither V nor Cr,Ti get dissolved but, still, V-4Cr-4Ti is sensitive to impurities such as C, O, H et N. The formation of ternary oxides is highlighted (Na-V-O, $NaVO_2$, Na_4VO_4 ...), the accurate description of oxide formation and kinetic being complicated because of the uneasy control of oxygen content in sodium.

A preliminar study of CEA-J57 in helium and sodium is presented in Figure 4: oxygen diffuses deeply in the substrate and induces its hardening. The oxide formed in sodium ($NaCrO_2$ and/or $NaVO_2$) are not adherent. These results suggest that vanadium protections are needed for a use in sodium.

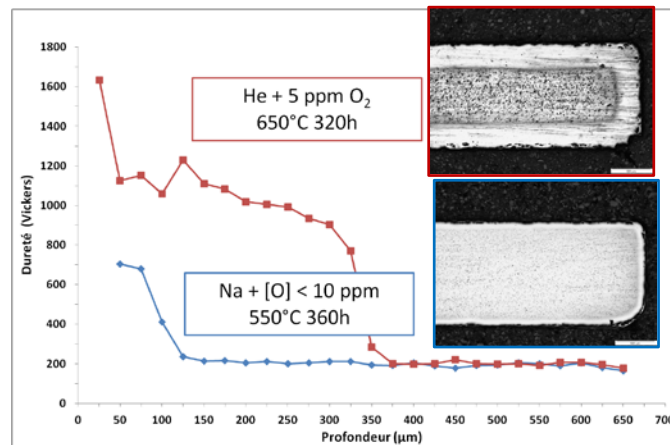


Figure 4: V-4Cr-4Ti, CEA-J57, after exposure to impure He at 650°C and exposure to Na at 550°C – Optical micrographs of the polished cross-sections and corresponding hardness profile.

Also, the compatibility of vanadium alloys with the fuel (UO_2 , MOX) is an issue and strongly depends on the oxide fuel stoichiometry and on the oxygen activity which both evolve with the burn-up. Again, the embrittlement of vanadium by oxygen diffusion is expected and inner protections should be needed. Compatibility experiments between vanadium and various metals, that could act as inner liners, are in progress at CEA.

5. Fabrication of vanadium tubes

To protect vanadium against the oxidation and the resulting embrittlement, a suitable outer coating could be used which would generate stable oxide compounds with slow growing rate. Recently, multi-layered silicide coatings gave very promising result in low pO_2 environment and their assessment is on going [14]. Beside, concerning the interaction with the fuel, appropriate inner liners could be the answer and many candidates are under investigation.

This considerations lead to consider a technological solution consisting in outer and inner liners (~50-100 μm in thickness) made of a well documented material, compatible with both fuel and sodium: a high chromium stainless steel acting as protection only, the mechanical performance being guaranteed by the vanadium alloy.

Hot extrusion was used to fabricate a triplex tube from a triplex rough shape made of a vanadium tube inserted between two stainless steel (SS) cans (Figure 5). After heating at 1100°C, the rough tube was extruded on a needle to get the final tube. In this configuration, the steel acts as a barrier to protect vanadium from the atmosphere and is “joined” to vanadium during the process at high temperature.

This first attempt lead to an heterogeneous chemical interaction between the SS liners and vanadium, mainly due to their differences in terms of flow during the extrusion. The interaction zone mainly consists in interdiffusion of V in SS and Fe in V and results in the occurrence of a 1 μm -zone identified as sigma phase (Fe-V solid solution). Locally, the interaction zone is larger (20 μm) suggested intimate contact and/or hot spots and inducing the formation of vanadium carbides (V_2C). The assessment of the V/SS compatibility was lead through diffusion couples heated at various temperature and times which confirms the V/Fe interdiffusion as low as 600°C and the carbide formation above 1000°C.

To mitigate the formation of these brittle phases at the V/SS interfaces, several parameters can be optimized: increasing the V/SS gap in the rough shape to avoid contacts, promoting a fast pre-heating to avoid long-time diffusion, dans using a low extrusion ratio to decrease the operating temperature.

Besides, other cold-temperature joining process are to be adressed to fabricate the triplex rod.



Figure 5: SS/V/SS billet before extrusion (left) and piece of the "triplex" rod after extrusion (right).

6. Conclusions and prospects

The very first studies on vanadium at CEA were launched in 2008 for applications as cladding especially in SFRs. The fabrication of a V-4Cr-4Ti alloy (CEA-J57 grade) was successful in terms of control of the chemical composition (impurities), microstructure, and mechanical behavior at low and high temperature. Additionnal mechanical tests are in progress to have an accurate description of the beavior at high temperature, particularly at the end of the secondary creep domain.

The obvious bad compatibility with the environment, both the fuel and the coolant, lead to consider a triplex clad made of a vanadium core, and outer/inner stainless steel liners (coatings solutions are also investigated). A very first manufacturing was attempted which highlighted some interactions at the interfaces resulting in formation of brittle phase, a priori detrimental to the mechanical performance. Other attempts are in progress to assess the feasibility of such a concept by the end of 2013.

Finally, the CEA-J57 grade is being tested under neutron irradiation in the reactor BOR60 (TIRAMISU experiment) which will allow assess its stability up to 80 dpa

REFERENCES

- [1] "Vanadium alloys – overview and recent results". Muroga, T., Nagasaka, T., Abe, T.K., Chernov, V.M., Matsui, H., Smith, D.L., Xu, Z.Y., Zinkle, S.J., Journal of Nuclear Materials, Volume 307-311, pp. 547-554. 2002
- [2] "Recrystallisation and precipitation behavior of low-activation V-Cr-Ti alloys after cold rolling". Heo, N.J., Nagasaka, T., Muroga, T., Journal of Nuclear Materials, Volume 325, pp. 53-60. 2004

- [3] “Development of vanadium alloys for fusion applications”. Chung, H.M., Loomis, B.A., Smith, D.L., *Journal of Nuclear Materials*, Volume 239, pp. 139-156. 1996
- [4] “NIFS Program for Large Ingot Production of a V-Cr-Ti Alloy”, Muroga, T., Nagasaka, T., Iiyoshi, A., Kawabata, A., Sakurai, S., and Sakata, M., *Journal of Nuclear Materials*, Volume 283-287, pp. 711-715. 2000
- [5] “Manufacture of semifinished items of alloys V-4Ti-4Cr and V- 10Ti-5Cr for use as a structural material in fusion applications”. Potapenko, M.M., Drobishev, V.A., Filkin, V.Y., Gubkin, I.N., Myasnikov, V.V., Nikulin, A.D., Shingarev, E.N., Vedernikov, G.P., Votinov, S.N., Zurabov, V.S., and Zolotarev, A.B., *Journal of Nuclear Materials*, Volume 233-237, pp. 438-441. 1996
- [6] “French investigation of a new V-4Cr-4Ti grade: CEA-J57 - Fabrication and Microstructure”. Duquesnes, V., Guilbert, T., Le Flem, M., *Journal of Nuclear Materials*, Volume 426, pp. 96-101. 2012
- [7] “Fabrication of a 1200 kg ingot of V-4Cr-4Ti alloy for the DIII-D radiative divertor program”. Johnson, W.R., Smith, J.P. , *Journal of Nuclear Materials*, Volume 258-263, pp. 1425-1430. 1998
- [8] “Analysis of V-Cr-Ti alloys in terms of activation of impurities”. Grossbeck, M.L., Klueh, R.L., Cheng, E.T., Peterson, J.R., Woolery, M.R., Bloom, E.E., *Journal of Nuclear Materials*, Volume 258-263, pp. 1778-1783. 1998
- [9] “Assessment of a European V-4Cr-4Ti alloy - CEA-J57”. Le Flem, M., Gentzbittel, J.M., Wident. P., *Proceedings of ICFRM-15*, Charleston, USA. 2011
- [10] “Tensile and impact properties of V-4Cr-4Ti alloy heats 832665 and 832864”. Bray, T. S., Tsai, H., Nowicki, L.J., Billone, M.C., Smith, D. L., Johnson, W.R., and Trester, P.W., *Journal of Nuclear Materials*, Volume 283-287, pp. 633-636. 2000
- [11] “Vanadium-base alloys for fusion first wall/blanket applications”. Smith, D.L., Billone, M.C., Natesan, K., *International Journal of Refractory Metals & Hard Materials*, Volume 18, pp. 213-224. 2000
- [12] “Uniaxial creep behavior of V-4Cr-4Ti alloy”. Natesan, K., Soppet, W. K., Purohit, A., *Journal of Nuclear Materials*, Volume 307-311, pp. 585-590. 2002
- [13] Kurtz, R.J., Abe, K., Chernov, V.M., Hoelzer, D.T., Matsui, H., Muroga, T., Odette, G.R., *Journal of Nuclear Materials*, Volume 329-333. pp. 47-55. 2004
- [14] “Multi-layered silicides coating for vanadium alloys for generation IV reactors”. Mathieu, S., Chaia, N., Le Flem, M., Vilasi, M., *Surface and Coatings Technology*, Volume 206, pp. 4594-4600. 2012

Interaction Energy Calculations of Edge Dislocation with Point Defects in FCC Cu

Zhongwen Chang^a, Pär Olsson^a, Nils Sandberg^a, Dmitry Terentyev^b

^aReactor Physics, KTH, Sweden

^bSCK-CEN Belgium

Abstract. Swelling has always been a limitation for long term operating reactors. The simple Bias model has done a good job in describing swelling in electron irradiation. In order to apply it to neutron irradiation, there's the key parameter named Bias Factor (Bd), which plays an important role in the model, has to be figured out. However, the Bds fitted from experiments are not consistent with those derived from elasticity theory. The major problem lies on the fact that analytical interactions based on elasticity theory are not valid around the dislocation core region. Hence a careful work about the interaction energy map is required in order to have numerical solution of Bd. In the present work, we apply large scale of atomistic calculations with EAM potential to get the interaction energy map between Point Defects (Vacancy and dumbbell SIAs along $\langle 100 \rangle$ directions) and dislocation in FCC Cu, as a demonstration of general FCC based material. General properties are checked in atomistic calculation results; Comparison has been made between the elasticity results and the atomistic results. The atomistic calculation of interaction maps show reasonable profiles. And they give better description around the dislocation core region.

Introduction

Swelling is dimensional change in materials. It is problematic especially for structure materials in power plants due to long-term irradiation. In the scope of GEN IV, this problem is more serious. Because the fast neutron spectrum give more challenge on materials. Researches on radiation damage have been ongoing both experimentally and theoretically for dozens years. Micro-structure change under irradiation is regarded as the basic reason for damage. The injected high energy particles collide with atoms sitting in lattice positions, which initiate collision chains. Energy dispersed in material results in formation of different point defects and clusters. Those point defects and defect clusters go through rearrangement of structures, exhibit macroscopically as radiation damage, such as swelling, creep, brittleness and so on. In Dislocation Bias model, swelling is regarded as the absorption bias of dislocation on SIAs than vacancies in the revolution process. This is also a traditional approach to investigate swelling. It has been successfully applied to explain swelling under electron irradiation, which include only Frenkel pairs. A parameter in this model, which is called Bias factor, is of importance. It quantitatively describe the "preference", that is, the excess flux of Point Defects (PDs) to the dislocation core. The interactions originate from the strain field around dislocation core and PDs, which are different in vacancies and SIAs because of their different dilatation volumes. However, this parameter is either experimentally fitted to use in the model or analytically overestimated. In order to get more physics insight about swelling, we need more understanding and easy approach about this parameter Bias factor.

In this work, large scale of atomistic calculations have been applied to calculate the interaction energy between Edge Dislocation (ED) and PDs in FCC material. The interaction energy landscape is the most important step heading for correct Bias factor.

Theory

The interaction between the ED and a PD could be described by elasticity theory if we assume an infinite, straight edge dislocation. The interaction originates from the overlap of stress-fields of two defects. In the simplest case, the crystal is treated as isotropic elastic medium, and PDs are considered as spherical elastic inclusions. Considering only the first-order size interaction, which arises essentially from the interaction between the long-range stress field of the dislocation and the stress field induced by atomic displacements around the PD, the analytical expression for the interaction energy was written by Bullough et. al as¹:

Equation 1

$$E = -A \frac{\sin \theta}{r}$$

$$A = \frac{\mu b}{3\pi} \frac{1+\nu}{1-\nu} v$$

in polar coordinates (r, θ). μ is the shear modulus, ν is the Poison's ratio, b is the Burgers vector, and, v is the dilatation volume of the PD. The only difference for vacancies and SIAs in this approach is the dilatation volume. SIAs have larger dilatation volume than vacancies, which leads to biased interactions measured by Bias factor.

With this analytical interaction, Ham² was able to solve the steady-state diffusion equation for a straight non-split edge dislocation. He gave the analytical expression of sink strength. Wolfer³ later applied perturbation method to improve Ham's solution by taking consideration of size interaction, the inhomogeneity interaction and the effects of externally applied loads. However, both of their approaches are still not sufficient applicable due to the fact that no split core is used in their model; And the assumptions they made are not suitable in the region near the core, where the interaction energy gradient is high. Wolter⁴⁵ carried out a series experiments on Austenitic steel. With the swelling data from those experiments, he fitted it back to the model, hence got some "experimental value" of Bias factor. Indeed, the values fitted from experiments are order of magnitude lower than analytical results.

Setting up and Computational methods

The details of how to set up an ED is described in⁶ ref[dis-set]. It's a positive dislocation in our case. The Burgers vector is chosen along [110], which we refer as x-direction in the following parts; dislocation line is along [-11-2], which we refer as y-direction in the following; and gliding plane in [-111], which we refer as z-direction. With periodic boundary condition in x- and y- direction, and fixed boundary condition in z-direction, we have a dislocation density of $2.61 \times 10^{15} \text{ m}^{-2}$. Considering both the boundary effects and the cost of computational resource, we set up a system with $70.039 a_0$ $7.327 a_0$ and $41.2805 a_0$ in x, y and z direction respectively. Full relaxing has been applied in ideal dislocation structure.

Both type of PDs are introduced in the fully relaxed dislocation system. For vacancy we investigate with example of single vacancy; For SIA, we calculate three different orientations: [100], [010] and [001]. They are all dumbbell type, which is $0.2 a_0$ from original lattice site.

Classical molecular static calculation implemented in DYMOKA code⁷ with empirical interatomic potentials⁸ are used in our calculations.

Results

The potential we applied to relax the dislocation has a Stacking Fault Energy (SFE) of about 40 mN/m [cite{mishin2001structural}], which leads to a dislocation-core-splitting distance of $10 a_0$. The partial core centres are detected by the maximum total energy in each atomic position.

The interaction energies on gliding plane of four different PDs (vacancy, SIA [010], SIA [100] and SIA [001]) with dislocation obtained from atomistic calculation have been shown in Fig.1. The location of attraction energy field of vacancy is opposite to that of SIAs. That's because the compressive field attracts vacancy while tensile field attracts SIAs. As the dislocation line is along [111] direction, [100] and [010] are actually equivalent. Hence, the energy profiles are more similar compared with the one of [001].

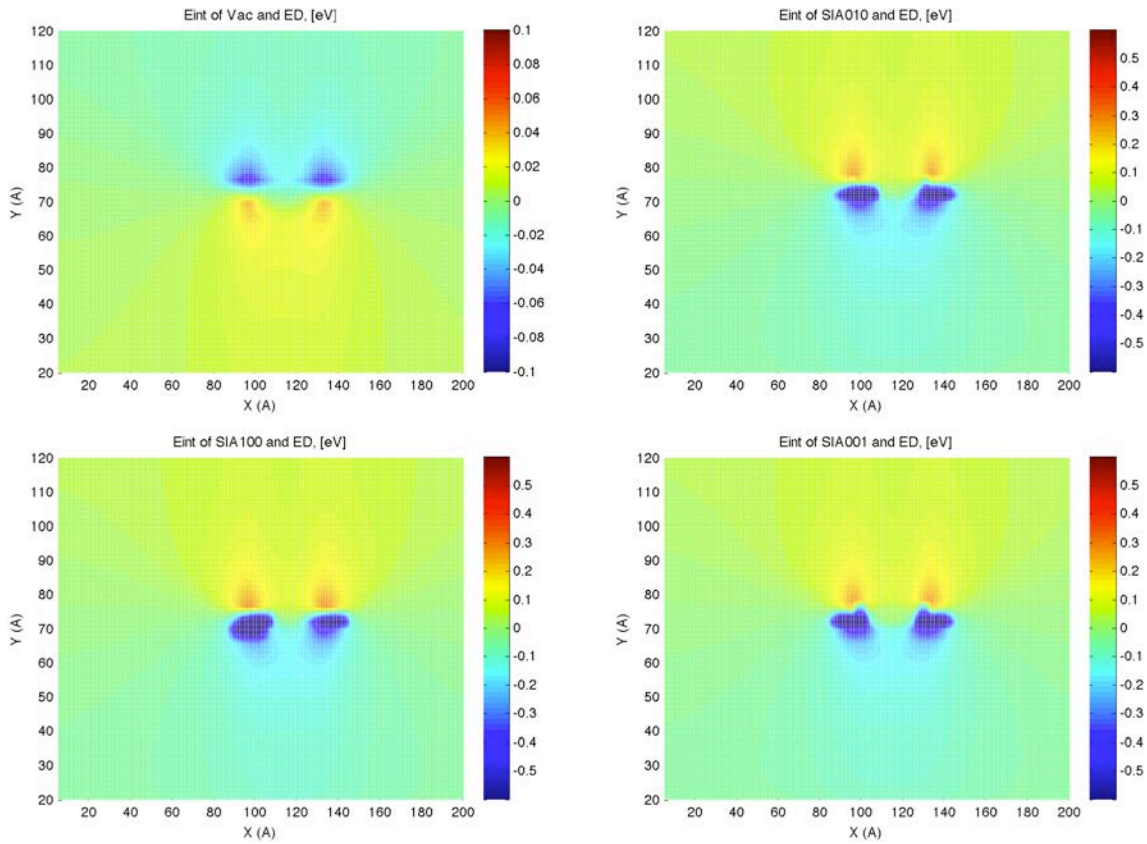


Figure 1 Atomistic results of interaction energy profile for Vacancy and SIAs with edge dislocation

Table 1 Strongest interaction energy of dislocation with PDs

	Vac	SIA		
		[010]	[100]	[001]
Maximum Eint (eV)	0.04	0.28	0.3	0.27
Minimum Eint (eV)	-0.07	-1.04	-0.87	-0.9

Fig.1 it could easily be seen that the strongest interaction appears in partial dislocation core center. The strongest attractions and repulsion are listed on Table. It's obvious that the strongest attractive energy in SIAs are of one order of magnitude larger than in vacancy in the near core region, which is consistent with the fact that dislocation has stronger interaction with SIAs than vacancies.

A location far enough from the dislocation cores is chosen to look into detail how the interaction gives impacts on atomistic arrangement. We select the first nearest neighbours of SIA [010] and relax the whole system. The snapshots of perfect SIA [010] is shown in Fig.2. It gives the atomic arrangement before interacting with ED. While the snapshots after SIA [010] interacting with dislocation is shown in Fig.3. We see that the dilatation volume for SIA is enlarged. The first nearest neighbours rearrange themselves from square shape to circular shape, trying to occupy more space for SIAs. While in vacancy case, the first nearest neighbours keep their shape and even shrink towards the vacancy, as shown in Fig.4 and Fig.5. This is consistent with the analytical explanation about preferential absorption.

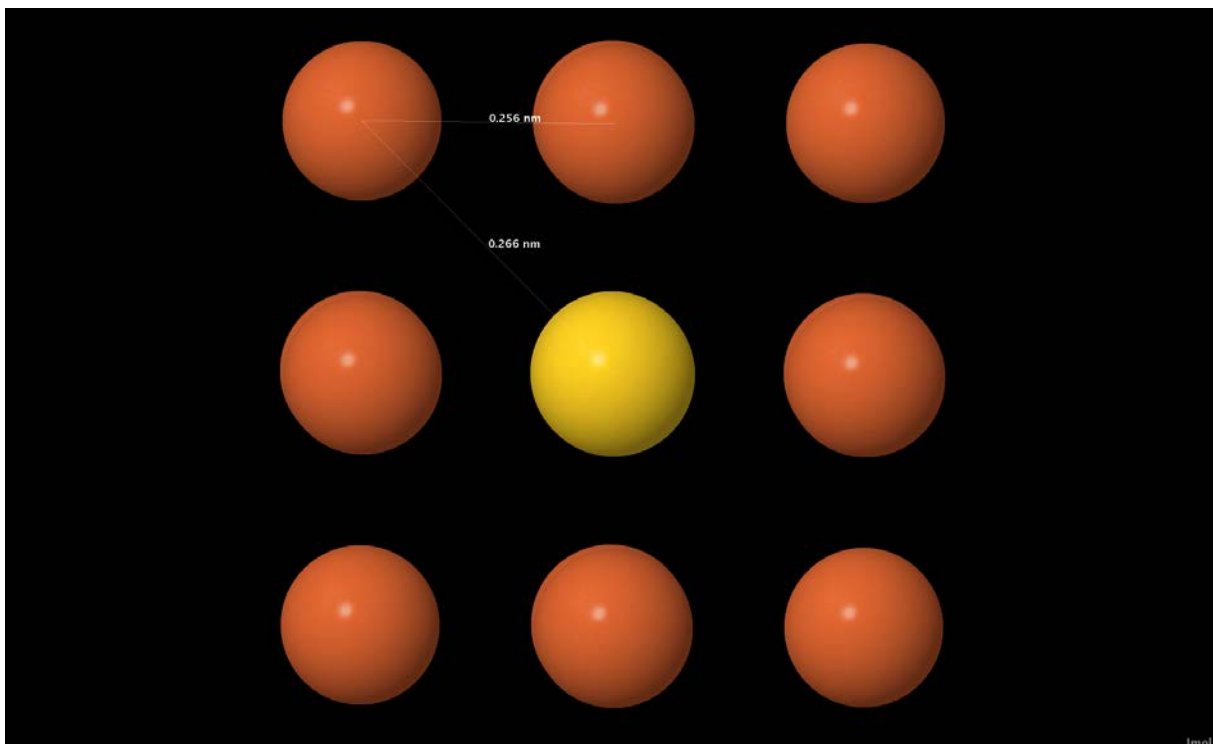


Figure 2 Before SIA [100] interaction with ED in FCC Cu

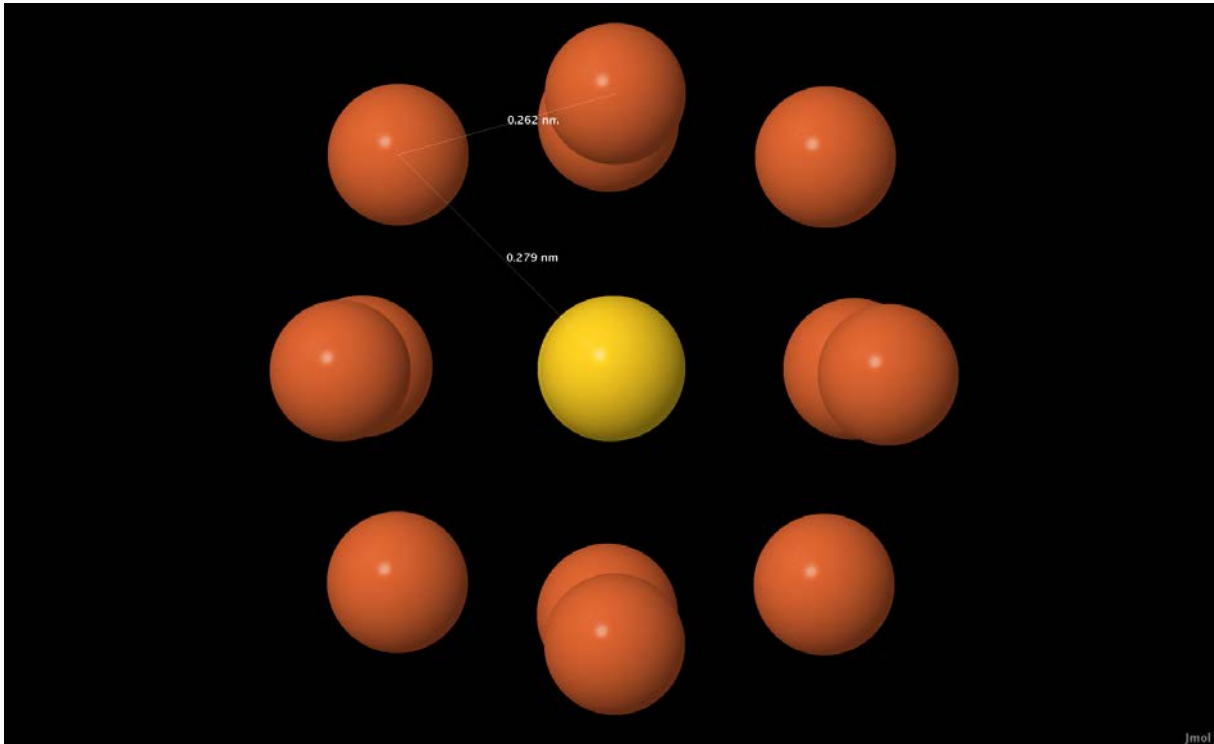


Figure 3 After SIA [100] interaction with ED in FCC Cu

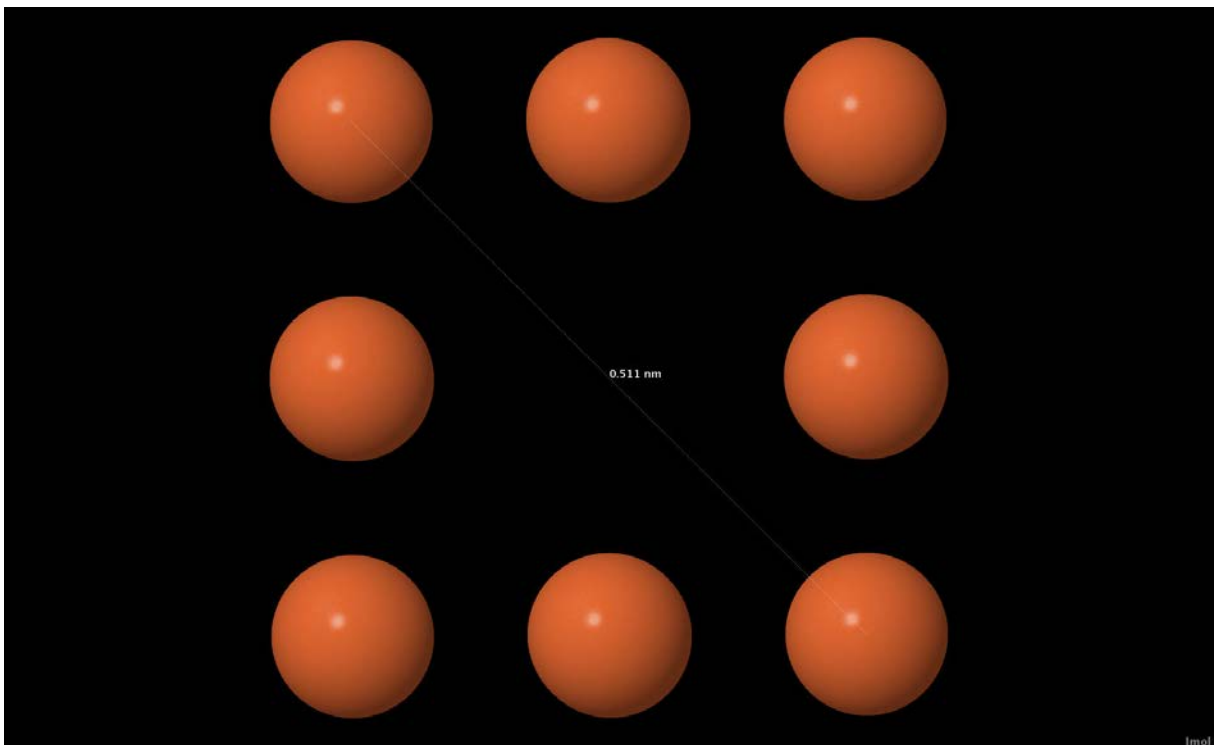


Figure 4 Perfect Vacancy in FCC Cu

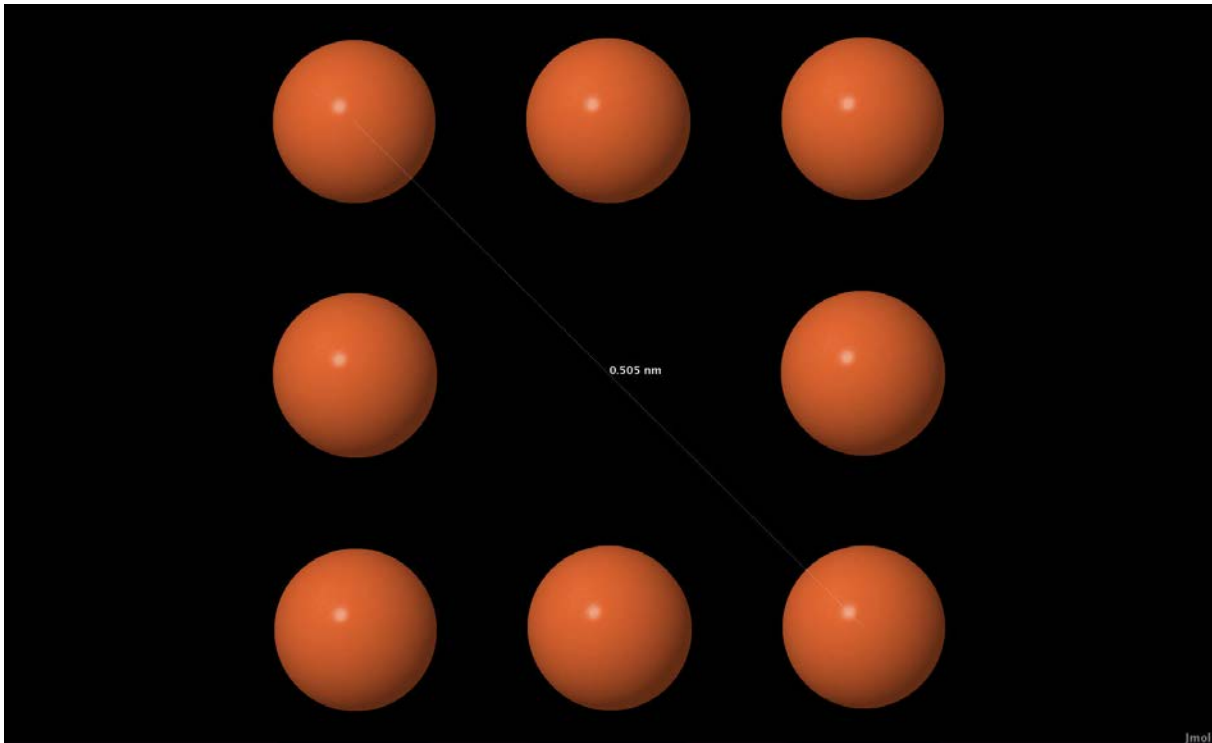


Figure 5 Vacancy after interaction with ED in FCC Cu

It is also worth noticing that the dumbbell SIAs in $\langle 100 \rangle$ directions under the strain field of dislocation stabilized into a near-octahedron position. This change is shown in snapshots Fig.6 and Fig.7. The dumbbell SIA which is closer to dislocation experiences a stronger attraction than the other one. Hence, after interaction the energy favourable configuration is no longer perfect $\langle 100 \rangle$ dumbbell. This structure change also gives the explanation of the SIA-ED interaction energy landscapes far away from dislocation core is converged around interaction energy = 0.09 eV instead of 0, since our interaction energy is defined by the differences of formation energy with and without dislocation.

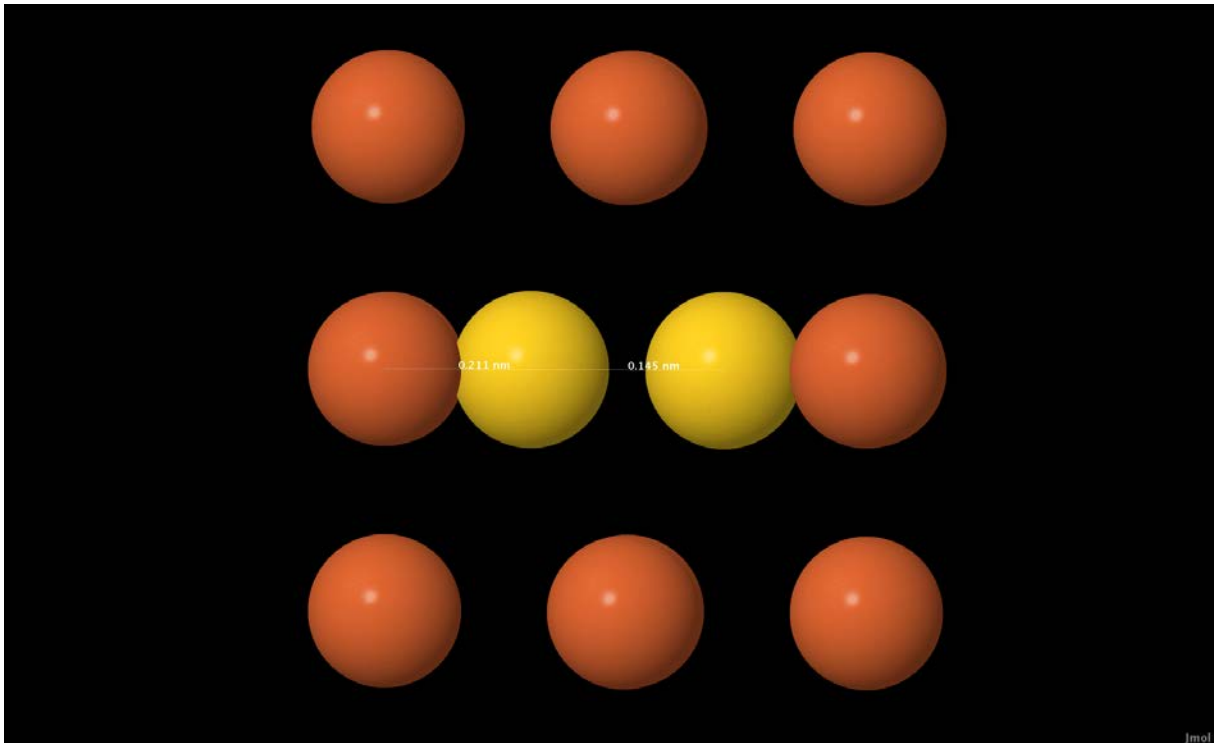


Figure 6 Before interaction, dumbbell in [100]

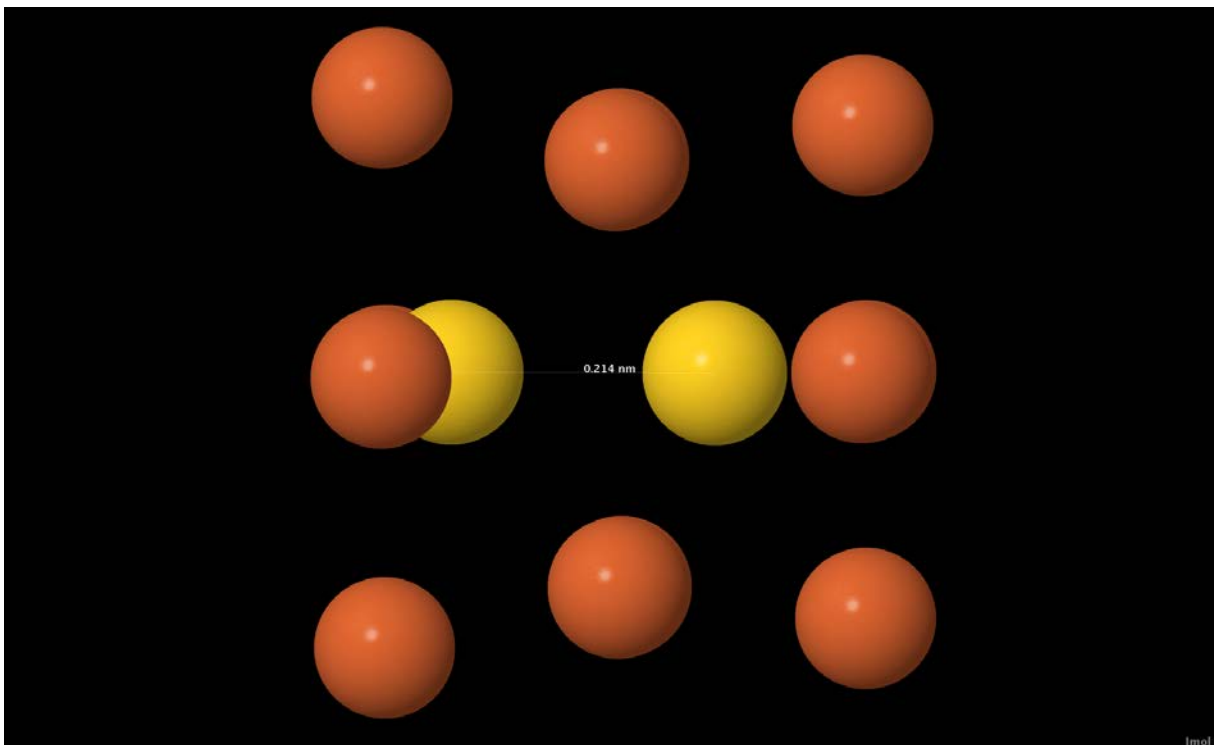


Figure 7 After interaction, octahedron position

In order to compare our results with analytical ones, we generate partial dislocation cores on analytical solution. Since the analytical solution was aimed at single core dislocation, the partial dislocation has been generated by superposing the same function on two different locations. The locations of partial cores and the distance between them are set to be the same as in our calculation model. With Eq.1 we use $v_{vac}=0.6\omega$ and $v_{SIA}=1.2\omega$ as the dilatation volumes of the PDs, where ω is the atomic volume. Fig.8 shows the analytical results. The vacancy has a smaller interaction range than SIA, which has also been shown in our atomistic calculations. However, comparing Fig.1 and

Fig.8, the absolute interaction range around the core is much larger than in atomistic results. The analytical results reaches theoretical limit when the dislocation core radius $r \approx b$. And also the interaction energy profiles around the core in our calculations show certain angles while it's perpendicular to x-axes in analytical results. Those differences can be explained by the fact that the assumptions that analytical results are based, such as interactions are isotropic; the PDs are seen as a spherical inclusion; and so on, could lead to invalid interactions especially around the core region. And also the construction of split cores is simple superposition of two single core dislocation, it might also have some impacts on the total interaction energy landscape.

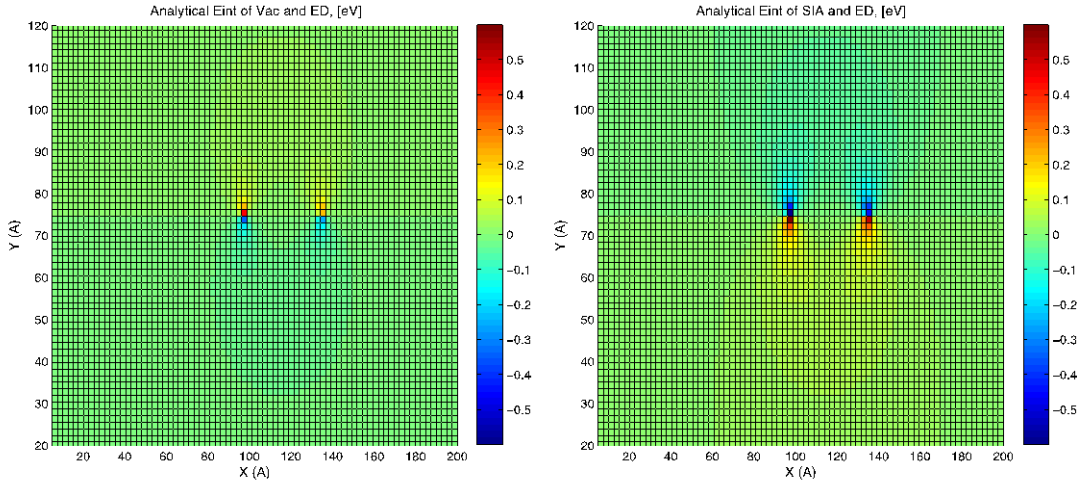


Figure 8 Analytical interaction energy profile

Conclusions and discussion

In order to compare with our calculated model, linear superposition is used on the origin analytical expression derived from Ham. This approach gives us the analytical expression for a system with two partial dislocation. Though it is not self-evidently reasonable. The assumption of isotropic system in Ham's analytical approach hindered the distinguishing of crystal direction. Hence the interactions from atomistic calculations reveal better physical pictures. The atomistic calculations give reasonable interaction energy landscape: they show the different nature of vacancy and SIAs interact with dislocation: SIAs have larger dilatation volume hence larger interaction values and ranges than vacancy.

We observe the dumbbell to octahedron transition change in the interaction of SIAs with dislocation.

We obtained reasonable interaction energy map for Bd calculation.

ACKNOWLEDGEMENTS

This work is funded by the national project on Generation IV reactor research and development (GENIUS). Thanks to SCK for cooperation. And Janne Wallenius for the help and support.

REFERENCES

¹ R Bullough and R C Newman, Reports on Progress in Physics 33 (1970), 101

² Frank S. Ham, Journal of Applied Physics 30 (1958), 915-926

³ Wolfer, W. G., L. K. Mansur, and J. A. Sprague. No. CONF-770641-7. Wisconsin Univ., Madison (USA). Dept. of Nuclear Engineering; Oak Ridge National Lab., TN (USA); Naval Research Lab., Washington, DC (USA), 1977

⁴ G.P. Walters, Journal of Nuclear Materials 136 (1985), 263-279

⁵ M.J. Makin and G.P. Walters and A.J.E. Foreman, Journal of Nuclear Materials 95 (1980), 155-170

⁶ Y. N. Osetsky and D. J. Bacon, Modelling Simul. Mater. Sci. Eng. 11 (2003), 427-446

⁷ C.S. Becquart, K.M. Decker, C. Domain, J. Ruste, Y.Souez, J.C. Turbatte, J.C. Van Duysen, in: Proceedings of the Third International Conference on Computer Simulation of Radiation Effects in Solids (COSIRES 1996), Rad.E.Def. Solids 142 (1997) 9.

⁸ Y. Mishin et al., Phys. Rev. B 63 (2001) 224106

Irradiation Experiment to Determine Effect of Long Term Low Dose Irradiation on FBTR Grid Plate Material

S. Murugan, V. Karthik, K. A. Gopal, Ran Vijay Kumar, Divakar Ramachandran, Jojo Joseph, T. Jayakumar

Metallurgy and Materials Group, Indira Gandhi Centre for Atomic Research, Kalpakkam, TN 603102, India.

Presented by Divakar Ramachandran

Abstract. The performance of the FBTR 316 SS grid plate which experiences a cumulative neutron dose of a few dpa at a temperature of about 350°C over its life time is one of the factors that could limit life of FBTR. While adequate data are available on austenitic stainless steels subjected to low doses, damage induced is a function of a number of parameters, some of which are unique to a reactor. An accelerated irradiation test was performed to characterize the mechanical property changes of 316 SS grid plate material subjected to neutron doses in the range ~1.0 - 2.5 dpa. The results show an increase in strength from un-irradiated values and a reduction in uniform elongation. Based on an extrapolation of this data, the limiting value of 10% on uniform elongation is estimated to be reached after 6.5 EFPY, at a dose of 4.4 dpa. Further irradiation experiments are planned to validate this extrapolation.

INTRODUCTION

Fast Breeder Test Reactor (FBTR) at Kalpakkam, India, is operating for more than 25 years [1]. Grid plate of FBTR (Fig. 1) is a permanent core structure supporting the core subassemblies and is subjected to low fluence neutron irradiation conditions over its life time. Type 316 stainless steel (SS) has been used in the fabrication of grid plate of FBTR. The irradiation induced changes in mechanical properties of the grid plate is one of the factors considered for extending the life of FBTR. Towards this, an accelerated irradiation test was performed in FBTR to characterize the mechanical property changes of 316 SS subjected to low dose irradiation. This paper describes the details of the irradiation experiment and the salient results obtained from the mechanical tests carried out on irradiated grid plate material.

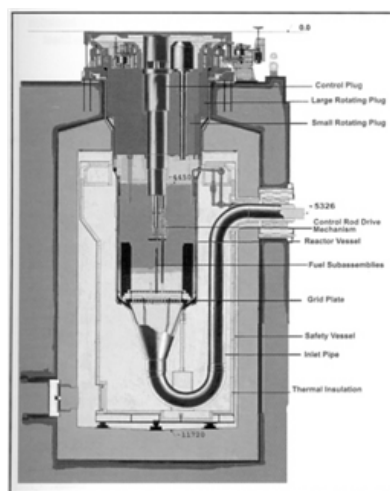


FIG. 1. A view of reactor assembly of FBTR

EXPERIMENTAL

1.1. Materials and Irradiation Experiment

The chemical composition of the type 316 SS (FBTR quality) grid plate material used in the present study was analyzed by spark emission spectrometer method (Table 1). Flat sub-size tensile specimens of dimensions shown in Fig. 2 and disc specimens (8.0 mm diameter and 1.0 mm thick) were machined from the available stock of FBTR grid plate material. A vented type irradiation capsule of 20 mm outer diameter and 18 mm inner diameter was fabricated with five compartments (C1 to C5) and loaded with 6 numbers of tensile & 6 numbers of disc specimens in each of the five compartments (Fig. 3). This irradiation capsule was locked in a special steel subassembly and loaded in FBTR for irradiation.

During irradiation, reactor sodium entered and surrounded the specimens through the holes made in the wall of irradiation capsule. The irradiation temperature of the specimens was 350 to 370° C. Duration of irradiation was 58.18 Equivalent Full Power Days (EFPDs). The neutron doses attained in the specimens in the five partitions from top to bottom were 1.08, 1.98, 2.57, 2.05, and 1.18 dpa (displacement per atom), respectively. After completion of irradiation, post irradiation examination of the specimens was carried out in radioactive hot cells.

Table 1. Chemical composition of type 316 SS (FBTR quality) (wt %)

Cr	Ni	Mn	Mo	C	Si	Cu	Co	Pb	Al	Sn	Ti
15.2 ± 0.5	12.3 ± 0.5	1.80 ± .05	2.06 ± .05	0.06 ± 0.01	0.76 ± .02	0.12 ± .02	0.22 ± .02	< .01	<.03	<.01	<0.08

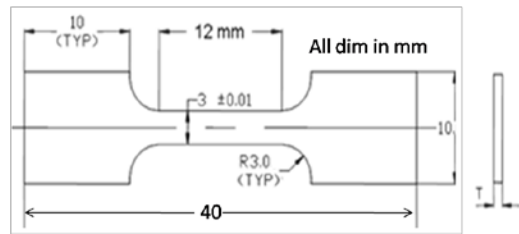


FIG. 2. Schematic of sub-size tensile test specimen

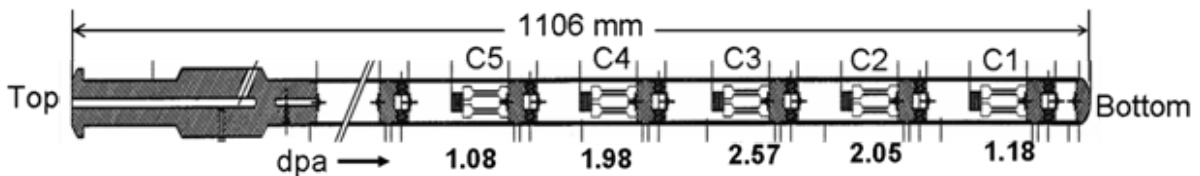


FIG. 3. Schematic of the irradiation capsule showing the tensile & disc specimens loaded in various compartments and the corresponding dpa values.

1.2. Post-irradiation examination

In the hot cells, the irradiation capsule was dismantled using a Laser system and uni-axial tensile tests were carried out on irradiated grid plate specimens retrieved from each partition. The remote tensile

tests were performed as per the ASTM E-8 and ASTM E-21 standards using a 2 ton capacity tensile test machine installed in the hot cells (Fig. 4). Custom made miniaturized wedge type grips were employed for gripping the sub-size tensile specimens during the tests. A resistance heating furnace was fitted to the machine to carry out the tensile tests at elevated temperatures. The tensile tests were performed at a nominal strain rate of 4×10^{-4} /s at temperatures of ambient (28°C), 350°C and 400°C. The test temperature was maintained within $\pm 2^\circ\text{C}$ of the required temperature using a PID controller.

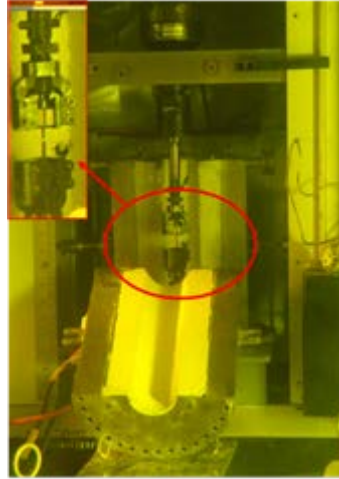


FIG. 4. Remote tensile testing machine inside the hot cells

RESULTS AND DISCUSSION

1.3. Analysis of tensile data

The load-crosshead displacement data recorded during the tensile tests was converted into stress-strain data using the original dimensions of the specimen measured prior to its loading in the capsule. The stress-strain plots of the tested specimens were analyzed to estimate the 0.2% offset yield strength (YS) and ultimate tensile strength (UTS). The ductility values were defined by the parameters Strain to Necking (STN) and Strain to Failure (STF). The STN was evaluated as the plastic strain from 0.2% yield offset to maximum load prior to onset of necking. The STF was evaluated as strain from 0.2% yield offset to failure load. The typical stress-strain curves for the various dpa conditions tested at 350°C and the trends in the YS, UTS and % STN are shown in Figs. 5a and 5b.

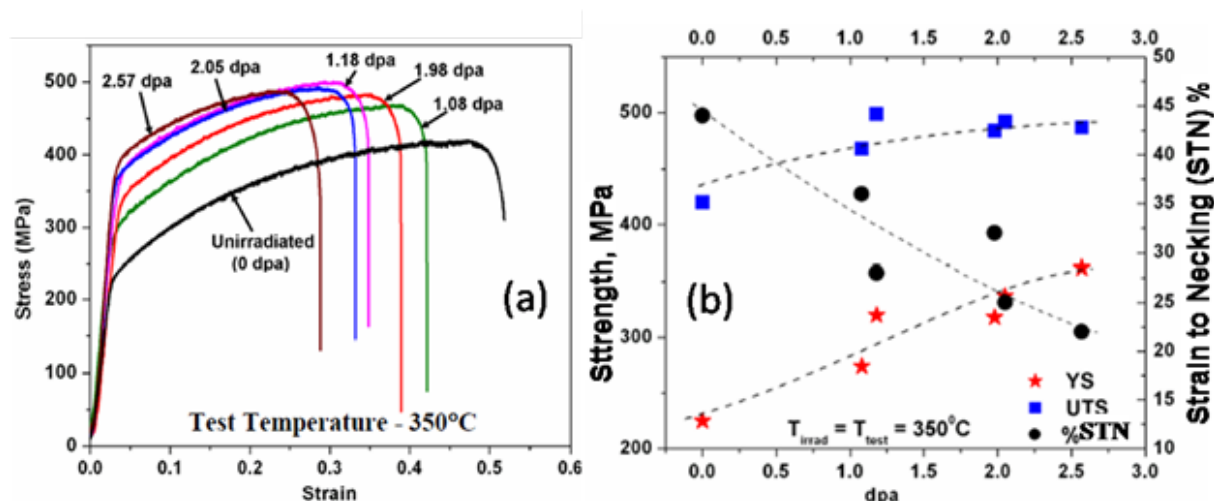


FIG. 5. (a) Stress-strain plots and (b) trends in UTS, YS and % STN of the irradiated grid plate specimens of various dpa tested at 350°C

It can be seen that the irradiated SS316 undergoes an increase in YS and UTS with respect to the unirradiated values for all the dpa conditions. The increase in YS is considerably higher than the increase in UTS (from the unirradiated values) for the irradiated specimens. The narrowing of the difference between YS and UTS with increase in dpa reduces the ability of the steel to work harden leading to the onset of plastic instability at lower strains. This resulted in the reduction in STN to about 22-32% for the specimens irradiated to 1.18 - 2.57 dpa from a value of about 45% for the unirradiated condition for tests conducted at 350°C. The trends of radiation hardening and loss of ductility in tensile tests carried out at 400°C (Fig. 6) and 28°C were similar to that of 350°C tests.

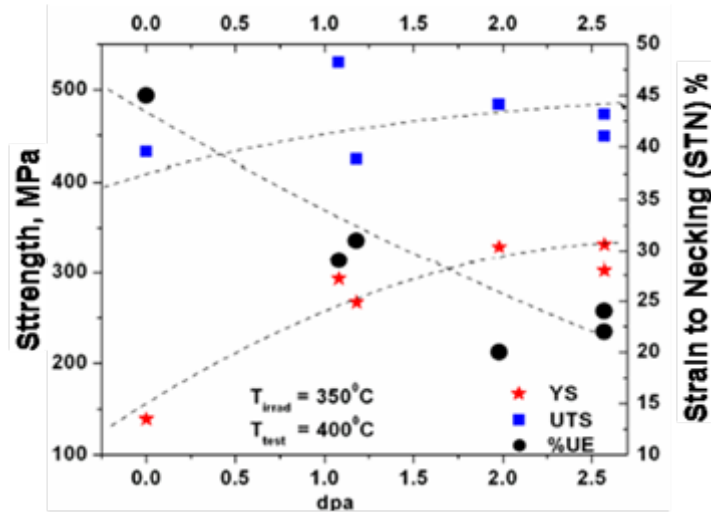


FIG. 6. Trends in UTS, YS and % STN of the irradiated grid plate specimens of various dpa tested at 400°C

1.4. Comparison with reported trends in literature

The trends in the mechanical properties of FBTR grid plate specimens after low dose irradiation are consistent with those reported in literature. The results of variation in tensile ductility of 316 SS irradiated at 425-475°C in RAPSODIE and tested at 350°C indicated a uniform elongation above 20% at 1.3 dpa [2]. Studies by Tavossoli et al. [3] on 316L irradiated at 400°C for dose between 4 to 5 dpa indicated a total elongation of about 30% at test temperatures of 350°C-400°C. The results of irradiation experiments conducted on J316 (composition close to SS 316 of FBTR grid plate) in Oak Ridge Research (ORR) Reactor at 330°C-400°C indicated a STN of more than 15% at a dose level of 3 dpa which declined to values <10% beyond 5 dpa [4].

1.5. Estimation of residual life from ductility criterion

The effect of low dose neutron irradiation on the material property is considered in the design standard of FBR structural materials by two approaches [5]. One is to establish the design standard directly based on the basic material property of the irradiated material/embrittled material, and the other is to set the design limit for accumulated neutron irradiation to maintain the ductility of the material. For all main reactor components irradiated to less than a few dpa through its operational period, the second approach is more realistic and in such cases the structural design standard based on unirradiated material data can be applied to the design evaluation. Based on the results of several studies [5], a design limit for fast accumulated neutron dose was set to maintain 10% fracture elongation. This criterion adopted using ASME code definition of ductile material as that which has more than 10% fracture elongation, was found to give the most conservative estimate of irradiation damage of FBR structural materials.

The residual ductility limit for the FBTR grid plate has been considered to be based on % STN instead of % STF, conservatively. A STN >20% at test temperatures of 28, 350 and 400°C indicated retention of adequate ductility in SS 316 grid plate of FBTR for an accumulated fast neutron dose of 2.57 dpa.

S. Murugan et al.

By extrapolating the experimental data of % STN and dpa at 400°C, it can be inferred that the limit of 10% STN will be reached at 4.37 dpa. Considering the present accumulated dose in the grid plate and the dose rate in dpa per equivalent full power year (EFPY) that the grid plate would be subjected to in future, it is estimated that it will take 6.5 EFPY to reach the residual ductility limit of 10%. Irradiation of further samples is planned to validate this extrapolation

CONCLUSIONS

An accelerated irradiation test was performed in FBTR to characterize the mechanical property changes of the type 316 SS grid plate material subjected to low dose irradiation. The 316 SS irradiated to neutron doses of 1.08-2.57 dpa showed an increase in YS and UTS from the unirradiated values. The increase in YS was more pronounced than increase in UTS and this resulted in a reduction of uniform elongation or strain to necking. These results are consistent with the results of irradiated SS316 reported in the literature. The 2.57 dpa specimen exhibiting a uniform elongation of above 20% at test temperatures of 28°C, 350°C and 400°C indicated retention of adequate residual ductility in SS 316 irradiated to this displacement damage. Based on an extrapolation of the experimental data, the limiting value of 10% on uniform elongation is estimated to be reached after 6.5 EFPY, at a dose of 4.37 dpa. Further irradiation experiments are planned to validate this extrapolation.

ACKNOWLEDGEMENTS

The contribution of Dr. C.P. Reddy, S. Varatharajan and G. Srinivasan of Reactor Operations and Maintenance Group (ROMG) of IGCAR in this experimental work is thankfully acknowledged. The authors wish to acknowledge the valuable contributions of a number of colleagues from Post-Irradiation Examination division, during the course of various examinations. The active interest and encouragement from Director, IGCAR is gratefully acknowledged.

REFERENCES

- [1] G. Srinivasan, K.V. Suresh Kumar, B. Rajendran, P.V. Ramalingam, The Fast Breeder Test Reactor- Design and Operating Experience-Nuclear Engineering and Design, Vol. 236, April 2006- pp 796-811.
- [2] A.A Tavassoli, "Effect of neutron irradiation on mechanical properties of permanent near core structure", Effect of Radiation on Materials, ASTM STP 1046, p 684.
- [3] A.A.Tavassoli, "Effect of neutron irradiation on mechanical properties of permanent near core structures", Effect of Radiation on Materials, ASTM STP 1046, p 684.
- [4] J.P. Robertson, I. Ioka, A.F. Rowcliffe, M. L. Grossbeck, S. Jitsukawa, in Effects of Radiation on Materials: ASTM STP 1325, R. K. Nanstad, M. L. Hamilton, F. A. Garner, and A. S. Kumar, Eds., American Society for Testing and Materials, Philadelphia, 1999, pp. 671-688
- [5] K.Aoto, Y.Wada, "Concept of design criteria of low dose irradiation for FBR structural materials", IAEA TEC DOC – 817. (1995) p.79.

Development of materials and fabrication technologies for sodium cooled fast reactor

T. Jayakumar, Divakar Ramachandran, M. D. Mathew, K. Laha, A. K. Bhaduri

Metallurgy and Materials Group, Indira Gandhi Centre for Atomic Research,
Kalpakkam, TN 603102, INDIA

Presented by Divakar Ramachandran

Abstract A comprehensive programme on materials development and fabrication technologies is being pursued at Indira Gandhi Centre for Atomic Research (IGCAR), Kalpakkam, India for improving the economic viability of fast nuclear power plants through extension of fuel burn-up and decreasing doubling time. IFAC-1, a modified version of Alloy D9 has been developed through optimisation of titanium, phosphorous and silicon contents for better swelling and creep resistances, allowing enhanced fuel burn-up. Manufacturing technology for oxide dispersion strengthened 9Cr-ferritic steel clad tube has been established, improving the creep resistance of an inherently void swelling resistant material. Studies on improved 9Cr-1Mo steel varieties for clad and wrapper applications for future metallic fuel reactors with reduced doubling times are under way. Other alloys developed include improved versions of 316LN SS as a structural material and type IV cracking resistant grade 91 steel for steam generator applications. These alloys require special welding consumables and procedures, technology for which has been indigenously developed. An overview of the work carried out at IGCAR will be presented.

INTRODUCTION

Sodium-cooled fast reactor (SFR) technology represents the second of the three stage nuclear programme envisioned for India, to make use of the large thorium reserves available. The difficulties in setting up of fossil fuel powered plants and the need for clean sources of electricity add to the importance of nuclear technology for India's development. In India, the Fast Breeder Test Reactor (FBTR) of 40 MW_t has been operating successfully for over 25 years at the Indira Gandhi Centre for Atomic Research, (IGCAR), Kalpakkam [1]. Based on this experience, a 500 MW_e Prototype Fast Breeder Reactor (PFBR) has been designed indigenously and is at an advanced stage of construction, even as the design is being further optimised for enhanced economy with respect to cost of electricity production, for use in future reactors. Currently, several programmes are under implementation for the development of new materials and fabrication technologies for higher fuel burn-up with higher linear power and lower doubling time, required for improved economy of future commercial fast reactors. This paper presents progress and challenges in the development of fast neutron fission reactor materials and associated fabrication technologies that are essential for a successful commercialisation of nuclear technology for electricity production through SFRs.

DEVELOPMENT OF MATERIALS FOR SODIUM-COOLED FAST REACTORS

1.1. Core Structural Materials

1.1.1. Austenitic stainless steels

Improvement in economics of operation of SFRs for commercial production of electricity is largely dependent on the performance of core structural materials, i.e., clad and wrapper materials of the fuel subassembly, which are subjected to intense neutron irradiation at high temperature during service. Under these operating conditions, materials problems such as void swelling, irradiation creep and helium embrittlement are of significance. The previous generation of materials for core structural

applications, type 316 austenitic stainless in 20 % cold work condition, used for clad and wrapper in FBTR have shown a residual ductility of around 1 % and extensive formation of voids leading to swelling at damage levels of around 80 *dpa* [2]. A continuous evolution of materials for fast reactor core components so as to improve fuel element performance has led to the development of radiation resistant 300 series austenitic stainless steels with increased nickel content and decreased chromium content in comparison to the standard versions. Austenitic stainless steel alloy D9 (15Cr-15Ni-Mo-Ti-C) with specifically tailored composition, especially with regard to carbon and titanium content, has improved void swelling resistance and this alloy in 20% cold worked condition has been chosen for the fuel clad and fuel subassembly wrapper tubes for PFBR. This alloy has been shown to have performed adequately, exhibiting lower swelling and retaining in excess of 3% residual ductility at a damage level of up to 62 *dpa* [3]. The improved performance of this alloy has been attributed to the preferential fine-scale precipitation of TiC at intragranular dislocations in the austenitic matrix contributing to higher rupture strength and lower creep rate compared to 316 SS. Development of this class of alloys has been further carried out at IGCAR. It is known that Si, Ti and P have a major influence on the void swelling behaviour [4]. In an effort to further optimize the alloy composition for higher void swelling and creep resistances, fifteen laboratory heats were produced with 0.025 and 0.04 wt% P, 0.75 and 0.95 wt.% Si and 0.16, 0.20, 0.24 and 0.30 wt.% Ti [5][6]. Influence of titanium on creep properties at 973 K showed a peak in rupture strength and a minimum in steady creep rate corresponding to Ti/C=6 in the heats containing phosphorus of 0.025 w. % and silicon of 0.75 wt % (Fig. 1). The alloys have been irradiated using 5 MeV Ni⁺ ions with 30 appm He pre-implanted, to a peak damage of 100 *dpa* at a damage rate of 7×10^{-3} *dpa/s* at various irradiation temperatures between 700 and 970 K. The void swelling was found to be lower for the sample containing higher amount of phosphorous and the swelling at peak temperature was 2.5 % (Fig. 2) with the reduction in swelling being more pronounced at temperatures > 523°C. Based on the above studies, an optimized alloy having Ti/C = 6 with 0.75 wt.% Si and 0.054 wt.% P, designated as IFAC-1, is proposed for fuel pin cladding and wrapper applications and is expected to allow safe operation up to 150 *dpa*.

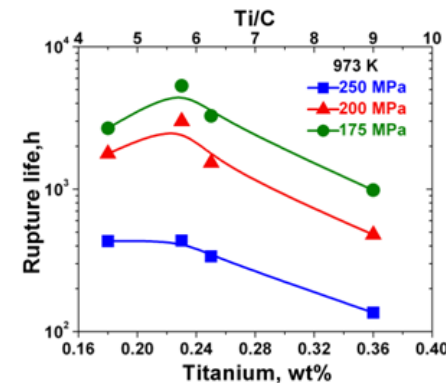


FIG. 1. Influence of titanium on creep rupture life of alloy D9 at 973 K. ($P = 0.025$ wt. %, $Si = 0.75$ wt. % and $C = 0.04$ wt. %).

1.1.2. Ferritic steels

High chromium (9-12 Wt. %) ferritic-martensitic steels are considered as the long-term solution for fast reactor core structural materials because of their inherent void swelling resistance [7][8] and lower shift in DBTT on neutron irradiation [9]. While several alloys in this class have excellent swelling resistance to doses even up to 200 *dpa* [7][8], their creep resistance decreases drastically above 550°C, making them unsuitable for clad tube applications. Another concern is the increase in ductile to brittle transition temperature (DBTT) due to irradiation. Consequently, extensive studies involving modification of the composition and initial heat treatments have been carried out to improve the fracture toughness of the ferritic-martensite 9-12 wt.% Cr steels. Presently used 9wt.% Cr ferritic/martensitic steels with low S and P were chosen on the basis of lowest increase in DBTT on irradiation [10][11]. Efforts have been made to further optimise this composition with particular regard to Si content. Variation of Charpy-V energy with temperature in three heats of 9Cr-1Mo steel with Si

in the range 0.24 – 0.6wt% of the steel (Fig. 8), shows that Si has no deleterious effect on DBTT. These materials are very promising for wrapper applications in fast reactors along with IFAC-1 as clad material with intended burn-up of more than 150 GWd/t.

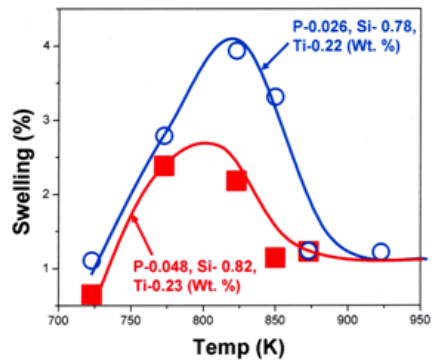


FIG. 2. Temperature dependence of void swelling measured by surface profilometry for the alloy D9 with two different phosphorous concentrations.

Target burn-up levels of up to 200 GWd/t set for the next generation of SFRs with higher operating temperatures would require development of oxide dispersion strengthened (ODS) ferritic martensitic steel with adequate creep strength for clad tube application [12][13][14]. Synthesis of this alloy necessitates a complex powder metallurgy route followed by hot and cold mechanical processes steps were adopted to produce the clad tubes. Pre-alloyed powders of the steel and nanosized Y_2O_3 particles are blended in a high energy simoloyer type of mill in argon atmosphere. The mixed powder is consolidated by canning in mild steel cans, degassing and sealing followed by upsetting to compact the powder into canned billet. The mild steel can is then removed by machining. The billets were hot extruded to produce rods. Mother tubes were prepared by concentrically drilling the extruded rods. Clad tubes were produced by cold drawing (pilgering) of the mother tube in several passes with intermediate softening heat-treatments. The clad tubes were finally subjected to normalizing and tempering heat treatments in inert atmosphere. Clad-tubes of composition Fe-0.11C-9Cr-2W-0.2Ti-0.27 Y_2O_3 , with outer diameter 6.6 mm, wall thickness 0.45 mm and up to 4500 mm length have been successfully produced. The dispersoid size distribution peaks around 10 nm [15] which results in the measured creep rupture strength at 700°C being comparable to that of the titanium-modified austenitic stainless steels (Fig. 3). This makes it a promising replacement for clad material which is likely to be used in the third stage fast reactors along with 9Cr-1Mo ferritic steel as wrapper material to increase the fuel burn-up to around 200 GWd/t.

1.2. Structural Materials

1.2.1. Austenitic Steels

Austenitic stainless steels of type 316 and its closely related variant 316L(N) are the preferred candidates for high temperature structural components of sodium cooled fast reactors (SFRs) due to their adequate high-temperature tensile and creep strengths, compatibility with liquid sodium coolant, ease of fabrication, weldability and commercial availability. A modified grade type 316 stainless steel has been used as the principal structural material for FBTR. This material differs from the conventional grade of type 316 stainless steel with respect to close control on composition to avoid scatter in mechanical properties. Understanding the microstructural changes, dislocation evolution and damage mechanisms during long-term deformation in this material [16][17] has enabled the development of robust creep life prediction models that can predict lives under service conditions that are not covered by laboratory testing [18].

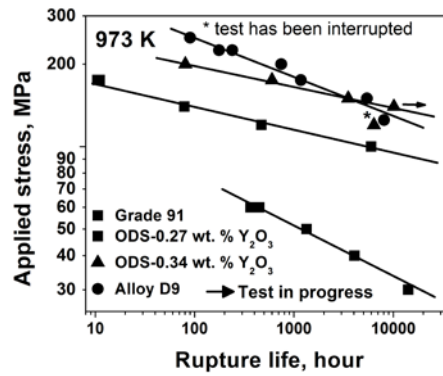


FIG. 3. Creep rupture strength of 9Cr-ODS steel and 973 K, compared with other steels.

1.2.2. Influence of Nitrogen on Creep Strength of 316L (N) Stainless Steel

In general, austenitic stainless steels have relatively poor resistance to intergranular stress-corrosion cracking (IGSCC) in chloride and caustic environments. Type 316 SS welds exposed to marine environments have been reported to fail by IGSCC in the heat-affected zone, due to the combined influence of sensitization and the presence of residual stresses introduced during welding. A nitrogen-alloyed low-carbon (0.03 wt.% maximum) version of this steel (316L (N) SS) has been chosen for the high-temperature structural components of PFBR. For PFBR, nitrogen is specified in the range of 0.06 to 0.08 wt% (as mentioned in RCC-MR design code), in order to compensate for the loss in solid-solution strengthening due to the reduced carbon content. This has the effect of substantial increase in rupture life (Fig. 4). The beneficial effects of nitrogen arise due to higher solubility of nitrogen in the matrix than the carbon, reduction in stacking fault energy of the matrix and introduction of strong elastic distortions into the crystal lattice, giving rise to strong solid solution hardening [19]. Nitrogen also effects the diffusivity of chromium in austenitic stainless steels leading to retardation in coarsening of $M_{23}C_6$ thereby retaining the beneficial effects of carbide precipitation to longer times [20][21].

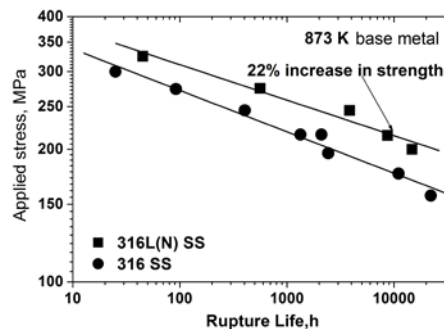


FIG. 4. Influence of nitrogen on creep properties of 316L(N) SS steel.

With a view to increasing the design life of structural components of future sodium cooled fast spectrum reactors from 40 years to 60 years and beyond, studies are being carried out to develop a nitrogen alloyed 316LN stainless steel with superior tensile, creep and low cycle fatigue properties as compared to 316L (N) stainless steel containing 0.07 wt.% nitrogen. The influence of nitrogen on the creep behaviour of 316LN stainless steel has been studied at nitrogen levels of 0.07, 0.11, 0.14 and 0.22 wt. % [22] by keeping the rest of the composition unaltered. The carbon content in these heats was 0.03 wt. %. Creep rupture strength increased substantially with increase in nitrogen content (Fig. 5) and this could be correlated to a decreasing tendency for sub-grain formation leading to a uniform distribution of dislocations in the steel with 0.22 wt% N.

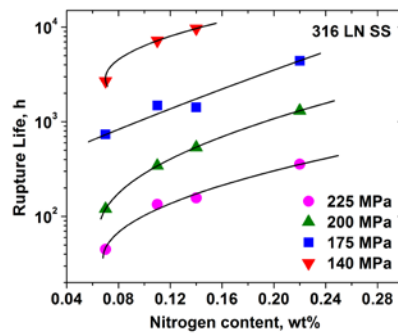


FIG. 5. Influence of nitrogen on creep properties of 316LN SS at 923 K.

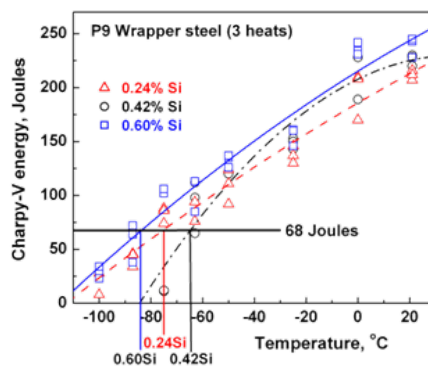


FIG. 6. Effect of silicon content on fracture toughness of grade 9 (9Cr-1Mo) steel.

1.3. Steam generator materials

Niobium stabilized 2.25Cr-1Mo steel is used in the steam generator of FBTR. Modified 9Cr-1Mo steel is being used in constructing steam generators of PFBR. Moderate creep strength coupled with high thermal conductivity, low thermal expansion coefficient and virtual immunity to stress corrosion cracking in chloride and aquatic mediums over those in austenitic stainless steel. Modified 9Cr-1Mo is used in the normalized and tempered condition that gives rise to tempered martensite structure. In this alloy, the additions of V, Nb and N ensure intragranular precipitation of highly stable V, Nb-carbonitrides (MX) particles on tempering and during creep exposure [23] to confer relatively high creep strength. The creep-rupture strength of indigenously developed modified 9Cr-1Mo steel in rolled, forged and tube product forms were found to be higher than the average strength values reported in RCC-MR design code [24]. Steel meeting stringent requirements was produced by electro slag refining process and the forged rounds were then converted into long seamless tubes. Strict quality control was carried out at all stages including development of innovative non-destructive testing techniques.

Creep strength of the fusion welded joint of the steel is considered to be a life limiting factor. In the actual structures fabricated by welding, a high percentage of the failures have been reported to occur in the heat affected zone (HAZ) [25][26]. The detailed microstructure in the HAZ of ferritic steels is extremely complex and is controlled by the interaction of thermal fields, produced by the heat input from the welding process, and the phase transformation and grain growth characteristics of the materials being welded [27]. Further modifications in microstructure can occur as a result of

tempering either during the later stages of welding and post-weld heat-treatment (PWHT) or during service. These microstructures which generally vary from wrought base material through transformed HAZs to cast weld metal, can have greatly different mechanical properties. As a consequence premature cracking occurs in the intercritical region of HAZ to reduce its creep rupture life, commonly termed as type IV failure. The joint of the steel possesses lower creep rupture life than the base steel. Chemical composition of modified 9Cr-1Mo steel has been altered with the control of nitrogen to less than 100 ppm and microalloying with boron. The steel exhibits better resistance to type IV cracking with less reduction of creep rupture strength of weld joint than the base metal (Fig. 7) [28].

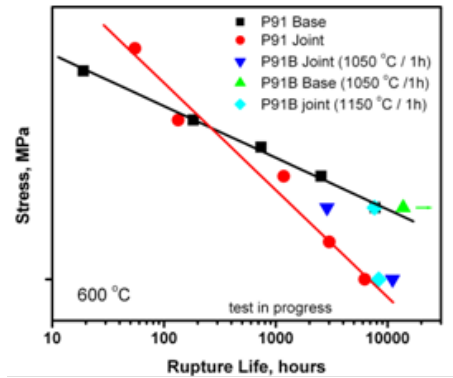


FIG. 7. Effect of boron on creep rupture life of modified 9Cr-1Mo steel and its weld joint.

DEVELOPMENT OF FABRICATION TECHNOLOGIES

1.4. Welding of end plug to clad tubes of improved / alternate materials

IFAC-1 fully austenitic stainless steel contains higher levels of low-melting eutectic phase-forming elements, such as phosphorus, which makes it particularly susceptible to solidification cracking. Extensive pulsed gas tungsten arc welding (GTAW) trials, with varied weld parameters, have been carried out for welding of 316LN SS end plug to IFAC-1 clad tubes to establish the feasibility of solidification-crack free welds. Based on these trials, defect free 316LN SS end plugs welded to IFAC-1 clad tubes have been qualified in helium leak testing and X-ray radiography. The optimum weld parameters have been established that provides confidence that defect-free welds of IFAC-1 clad tubes with 316LN SS end plugs can be produced repeatedly.

Solid-state welding of modified 9Cr-1Mo steel end plugs to 9Cr-1Mo-ODS steel clad tube is being pursued using two processes; viz. Pressure Resistance Welding (PRW) and Magnetic Pulse Welding. Procedure development trials have been carried out using the PRW process using two different end plug designs which have qualified non-destructive evaluations, with radiography revealing uniform weld joint with no detectable weld defect and acceptable helium leak tightness ($1.0 \cdot 10^{-11}$ atm.cc/sec against requirement of $1.0 \cdot 10^{-7}$ atm.cc/sec).

1.5. Development of special-purpose electrodes for welding of improved versions of structural materials

1.5.1. Electrodes for welding of nitrogen-enhanced of 316LN SS

The chemical composition of the weld metal for shielded metal arc welding (SMAW) of nitrogen-enhanced 316LN SS, containing 0.14%N, has been specified based on evaluation using the WRC-1992 diagram and experience gained during indigenous development of E316-15M electrodes as per PFBR specifications. Table 1 details the chemical composition and delta-ferrite content of E316-15 weld metal as per ASME, PFBR specifications, and the weld metal chemistry achieved with the

indigenous E316-15M electrodes for PFBR. To ensure ferritic mode of solidification and sufficient delta-ferrite for adequate resistance to hot-cracking, the chemical composition of the weld metal for the nitrogen-enhanced E316-15(N) electrodes, proposed for CFBR, has been suitably tailored as given in Table 1. Using the E316-15M PFBR specification as the basis, the content of three elements, C, N and Cr, were judiciously adjusted for the E316-15(N) CFBR specification, while also ensuring that the chemical composition is within the ASME specification window. To ensure adequate resistance to both hot cracking and elevated-temperature formation of sigma-phase, delta-ferrite content of 3-7 FN is specified for the E316-15(N) weld metal. Additionally, care is to be exercised during welding to avoid formation of nitrogen porosity. These modified E316-15(N) electrodes meeting the CFBR specifications have been successfully developed in collaboration with an Indian electrode manufacturer. The most challenging part of this development was to achieve the specified minimum toughness of 3.0 daJ/cm² after the 750°C/100h ageing heat treatment. This requirement is included to assess the susceptibility of the weld metal to embrittlement by sigma-phase formed during high-temperature exposure by transformation of the delta-ferrite, for which the Mo content has to be carefully controlled in the lower limit of the specification. Another challenge was to improve the slag detachability of the deposited weld metal. Poor slag detachability of the weld metal often necessitates extensive grinding and rework. Many trials batches were made to optimize both the composition of the weld metal and flux.

1.5.2. Electrodes for welding of modified 9Cr-1Mo steel

SMAW electrodes based on the stringent specifications (AWS classification E9016-B9 of ASME section II-C SFA-5.5 with modified/additional requirements) (Table 2), have also been developed with Indian electrode manufacturers. The weld metal of one of the synthetic electrodes, made from mild steel core wire, met the specification. Only the electrodes that are developed as per the composition requirements of the specifications possess minimum requirement of 45 J at 20°C after PWHT at 760°C for 3 h. Results of impact tests on the weld metals produced from these electrodes (Fig. 8) shows that most of the commercially available electrodes do not meet the toughness requirement as specified. For the weld metals that met the composition requirements as specified, Reference Temperature for Nil Ductility Transition (RTNDT) was determined from a combination of drop weight test (ASTM E 208) and impact test. For the weld metals of non-synthetic electrodes developed, this value was found to in range of -3 and -5°C. The recommended temperature for hydro-testing of the components is 33°C above the RTNDT determined for the material of construction for the component. This means, hydro-testing of the components fabricated using these consumable (in this case steam generators) can be conducted at ambient temperature (~30°C). It is interesting to note that the weld metal of a synthetic electrode had RTNDT much above the room temperature and hydro-testing of a component made using such welding consumable would require use of hot water.

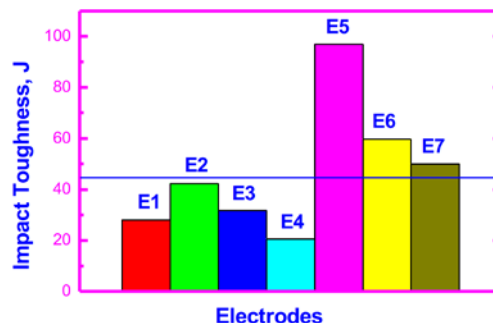


FIG. 8. Impact toughness of different welding electrodes

Table 1. Chemical composition (in wt-%) and delta-ferrite content of E316-15 weld metal as per ASME, PFBR and CFBR specifications

Element	C	Cr	Ni	Mo	N	Mn	Si	P	S	Ti+Nb+Ta	Cu	Co	B	FN
ASME	0.08 max	17-20	11-14	2-3	NS	0.5-2.5	0.9 max	0.04 max	0.03 max	NS	0.75 max	NS	NS	NS
PFBR (specified)	0.045-0.055	18-19	11-12	1.9-2.2	0.06-0.10	1.2-1.8	0.4-0.7	0.025 max	0.02 max	0.1 max	0.5 max	0.2 max	0.002 max	3-7
PFBR (achieved)	0.05	18.5	11.1	1.9	0.1	1.4	0.46	0.006	0.025	<0.1	<0.05	<0.05	0.001	3.0-3.9
CFBR (specified)	0.040-0.050	19.0-20.0	11.0-12.0	1.9-2.2	0.12-0.16	1.2-1.8	0.4-0.7	0.025 max	0.020 max	0.10 max	0.5 max	0.2 max	20 ppm max	3-7

Table 2. Chemical composition of grade 91 steel weld metals from SMAW electrodes

Elements	Specified	SMAW weld metals						
		E1	E2	E3	E4	E5	E6	E7
C	0.08–0.12	0.09	0.06	0.062	0.1	0.085	0.10	0.1
Cr	8.0–9.5	9.00	9.8	9.0	8.64	8.30	9.00	9.0
Mo	0.85–1.05	1.0	0.8	1.1	0.94	1.0	1.00	1.0
Mn	0.5 – 1.20	0.55	0.6	1.5	0.7	0.7	0.70	0.75
Si	0.15–0.30	0.20	0.35	0.3	0.25	0.28	0.24	0.32
S	0.01 max	0.007	0.015	0.01	0.01	0.015	0.012	0.008
P	0.01 max	0.015	0.015	<0.007	0.006	0.015	0.009	0.01
Ni	0.4–1.0	0.6	0.1	0.9	0.6	0.5	0.70	0.52
Nb	0.04–0.07	0.06	–	0.03	0.05	0.069	0.06	0.065
V	0.15–0.22	0.07	0.012	0.012	0.19	0.004	0.17	0.21
N	0.03–0.07	0.033	0.025	0.03	0.046	0.025	0.055	0.06
O	NS	0.07	0.05	0.04	--	--	0.068	0.08
Cu	0.25 max	0.05	0.05	< 0.05	0.03	0.05	<0.050	--
Al	0.04 max	0.034	0.034	–	0.003	–	<0.01	--

SUMMARY

Creep strength and void swelling resistance the most important properties for fast neutron reactor core structural material. Alloy D9 is being currently used for the clad and wrapper for PFBR, under construction at Kalpakkam. To enhance the fuel burn-up, composition of alloy F9 with respect to titanium, phosphorous and silicon has been optimized for void swelling and creep resistance to develop a modified alloy D9, referred as IFAC-1. The 9Cr-1Mo ferritic steel has been considered for wrapper application. The limit of silicon in the steel for toughness point of view has been established. The 9Cr-2W steel has been dispersed with yttria to increase its creep rupture strength as par with alloy D9 for its application as clad tube. Type IV cracking susceptibility in the weld joint of modified 9Cr-1Mo steel has been suppressed on microalloying the steel with boron and controlling the nitrogen content for steam generator application. Fabrication issues with these newer materials are being addressed through research and developmental activities. Special weld processes and consumables have been developed and qualified to enable use of the materials in future reactors.

ACKNOWLEDGEMENTS

The authors thank Mr. S. C. Chetal, Director, Indira Gandhi Centre for Atomic Research for his keen interest in this work. Research contributions from many colleagues from Metallurgy and Materials group are gratefully acknowledged.

REFERENCES

- [1] Srinivasan, G, et al., The Fast Breeder Test Reactor – Design and Operating Experience, Nucl. Engg. Design 236 (2006) 796.
- [2] Venkiteswaran, C. N, et al., Study of Microstructure and Property Changes in Irradiated SS316 Wrapper of Fast Breeder Test Reactor, J. ASTM Intl 6 (2009).
- [3] Joseph, Jojo, et al., Proceedings FR-13 (2012)
- [4] Was, G. S., Fundamentals of Radiation Materials Science: Metals and Alloys, Springer-Verlag Berlin Heidelberg, 2007.
- [5] Latha, S., et al., Thermal Creep Properties of Alloy D9 Stainless Steel and 316 Stainless Steel Fuel Clad Tubes Intl J Pressure Vessels and Piping, 85 (2008) 866.
- [6] Latha, S., et al., Effect of titanium on the creep deformation behaviour of 14Cr-15Ni-Ti stainless steel, J Nucl. Mater., 409 (2011) 214.
- [7] Dubuisson, P. *et al.*, Microstructural evolution of ferritic-martensitic steels irradiated in the fast breeder reactor Phénix, J. Nucl. Mater., 205 (1993) 178.
- [8] Klueh, R. L. and Harries, D. R. (eds.) High Chromium Ferritic and Martensitic Steels for Nuclear Applications, (2001), ASTM, Pa, pp 90.
- [9] Lindau, R. and Schirra, M., Fusion Engg. Design, 58-59 (2001) 781.
- [10] Kohyama, A. *et al.*, Low-activation ferritic and martensitic steels for fusion application. J. Nucl. Mater., 233-237 (1996) 138.
- [11] Harrelson, K. J. *et al.*, Impurity element effects on the toughness of 9Cr-1Mo steel, J. Nucl. Mater., 141-143 (1986) 508.
- [12] Ukai, S. *et al.*, Characterization of high temperature creep properties in recrystallized 12Cr-ODS ferritic steel claddings, J. Nucl. Sci. Technol., 39 (2002) 872.
- [13] Ukai, S. *et al.*, Development of 9Cr-ODS Martensitic steel claddings for fuel pins by means of ferrite to austenite phase transformation, J. Nucl. Sci. Technol., 39 (2002) 778.
- [14] Kaito, T. *et al.*, Progress in the R&D project on Oxide Dispersion Strengthened and Precipitation Hardened Ferritic Steels for Sodium Cooled Fast Breeder Reactor Fuels, GLOBAL 2007, Boise, Idaho, Sep. 9-13, 2007.
- [15] Dasgupta, A *et al.*, “Electron Microscopy Studies on Oxide Dispersion Strengthened Steels”, *Materials Challenges and Testing for Supply of Energy and Resources*, Thomas Bollinghaus, T. *et al.* (Eds.), Springer-Verlag (2012), 117–128.
- [16] Mathew, M. D. *et al.*, Creep Properties of Three Heats of Type 316 SS for Elevated Temperature Nuclear Applications, Nucl. Technol., 81 (1988) 114.
- [17] Mathew, M. D. *et al.*, Dislocation Substructure and Precipitation in Type 316 Stainless Steel Deformed in Creep, Mater. Trans. JIM 38 (1997) 37.
- [18] Wolf, H. *et al.*, Prediction of Creep Parameters of Type 316 Stainless Steel under Service Conditions using the Theta Projection Concept, Mater. Sci. Engg., A159 (1992) 199.
- [19] Shastry, G. *et al.*, Creep Deformation and Fracture Behaviour of Type 316L(N) Stainless Steel, Trans. IIM, 58 (2005) 275.
- [20] Sasikala, G. *et al.*, Creep damage and fracture behaviour of a type 316L(N) stainless steel and its weldment, Trans. IIM, 53 (2000) 223.
- [21] Sasikala, G. *et al.*, Creep Deformation and Fracture Behaviour of a Nitrogen Bearing Stainless Steel Weld Metal, J. Nucl. Mater., 273 (1999) 257.
- [22] Mathew, M. D. *et al.*, Improving creep strength of 316LN stainless steel by alloying with nitrogen, Mater. Sci. Engg., A535 (2012) 76.
- [23] Vitek, J. M. and Klueh, R. H., Metall. Trans. A, 14A (1983) 1047.
- [24] Raj, B. and Choudhary, B. K., A perspective on creep and fatigue issues in sodium cooled fast reactors, Trans. IIM., 63 (2010) 75.
- [25] Laha, K. *et al.*, Metall. Mater. Trans. A, 34A (2007) 58.
- [26] Brett, S. J., Advances in materials technology for fossil power plants (Eds. Viswanathan, R. *et al.*), University of Wales, Swansea (2001), 343–351.
- [27] Alberry, P. J. and Jones, W. K. C., Diagram for the prediction of weld heat-affected zone microstructure, Met. Technol. 4 (1977) 360.
- [28] Das, C. R. *et al.*, Characterization of Ferrite in Tempered Martensite of Modified 9Cr-1Mo Steel Using the Electron Backscattered Diffraction Technique, Metall. Mater. Trans. A,

Mechanical Properties of Cladding and Wrapper Materials for the ASTRID Fast-Reactor Project

P. Gavoille^a, A. Courcelle^a, J.L. Seran^a, X. Averty^a, B. Bourdilliau^a, O. Provitina^b, V. Garat^c, D. Verwaerde^d

^aNuclear Materials Department, Nuclear Energy Division, French Alternative Energies and Atomic Energy Commission, Gif sur Yvette, France

^bNuclear Fuel Department, Nuclear Energy Division, French Alternative Energies and Atomic Energy Commission, Saint-Paul-lez-Durance, France

^cAREVA NP, Lyon, France

^dEdF R&D, Clamart, France

Abstract. In the ASTRID fast-reactor project, the AIM1 (Austenitic Improved Material) is the reference material for fuel cladding. AIM1 is the result of optimization studies performed at CEA on titanium-stabilized austenitic alloys to minimize irradiation swelling and preserve good mechanical properties during reactor lifetime. For the wrapper, the choice has been made to use a 9Cr martensitic steel (EM10), which has been extensively characterized in Phenix. This type of steel offers an excellent resistance to irradiation induced void swelling and keeps a sufficient level of ductility after irradiation.

The first part of this paper gives an overview of fresh and irradiated AIM1 properties. A special emphasis is given to recent experimental data:

- New metrologies to determine cladding strain were performed on fuel pin irradiated in the PHENIX reactor at high dose : 130 dpa,
- Axial and ring tensile tests were also done at room temperature and irradiation temperature ($400^{\circ}\text{C} < T < 700^{\circ}\text{C}$). This complements older high-temperatures tests simulating transients conditions ($700^{\circ}\text{C} < T < 1200^{\circ}\text{C}$).

The recent work on AIM1 modeling is also described. Swelling and irradiation creep models were updated to include the latest measurements at higher dose. New mechanical models were developed to describe tensile and thermal creep properties.

In the second part, an overview of the mechanical properties obtained on irradiated EM10 material is given, with tensile tests and impact toughness results for doses over 100 dpa, and remaining topics for ongoing research are discussed.

The paper will conclude on the future work that remains to be done to achieve a satisfactory qualification of AIM1 and EM10 before the ASTRID startup.

1. Introduction

Stainless-steel cladding has to ensure the fuel-rod integrity until fuel discharge in normal operating conditions ($400^{\circ}\text{C} < T < 650^{\circ}\text{C}$) and when subject to incidental thermal transient. Hypothetical events studied in safety analysis consider temperatures as high as 1200°C . The main requirement of the cladding material is to limit swelling, irradiation creep and maintain sufficient mechanical strength and ductility during irradiation (limitation of irradiation embrittlement effects). At high temperature $T > 650^{\circ}\text{C}$, cladding strain from thermal creep should also be limited (cladding hoop stress can reach 100 MPa due to fission-gas pressure and possible fuel-cladding interaction). Other important aspects such as the chemical interaction with the fuel, corrosion with the sodium coolant and reprocessing issues have to be taken into account.

The wrapper, on the other hand, has to maintain the geometry of the fuel assembly, to allow for sodium to flow through it in order to ensure the heat exchange and acts as a structural element for the core. Operating conditions are similar to those of the cladding in terms of dose (100 dpa), and operating temperatures are close to the sodium temperature ($380^{\circ}\text{C} < T < 550^{\circ}\text{C}$). The main issues concerning the wrapper material are irradiation induced swelling and embrittlement, as well as mechanical resistance during incidental transients.

2. Cladding material

The first reference materials for cladding used in the French fast reactor Rapsodie and Phénix were made of unstabilized 316-type. Incubation dose for swelling was low (less than 50 dpa). Major improvements in swelling resistance have been made by stabilizing the steel with titanium and using cold work material (amount of cold work : 20%). Further adjustments of the chemical composition have led to a cold worked, stabilized titanium 15%Ni-15%Cr alloy with optimized minor elements contents (B, P, Si, Mo etc.) [1]. Minor elements known to affect weldability are kept to minimum.

For the first ASTRID core, the maximum dose will be about 110 dpa (NRT unit is used throughout the paper). The reference material of the cladding is the latest generation of cold worked 15-15Ti developed at CEA and named AIM1 (austenitic improved material).

In 2012, results from AIM1 neutron-irradiation programs launched in the 90's are not available. First examination of irradiated AIM1 is expected to start in 2013. For now, extrapolation of irradiation properties are based on previous versions of 15-15Ti whose specifications are very close to AIM1 (called in this paper 15-15Ti precursor and AIM1 precursor). Details of chemical composition are presented in Table 1. Experimental results suggest that some mechanical properties (elasto-plastic behavior, thermal creep, toughness) are not significantly sensitive to the small variation of minor elements (as long as irradiation swelling is low). In contrast, incubation dose for swelling is known to be very sensitive to chemical composition and fabrication process.

	C	Mn	Si	Cr	Ni	Mo	P	Ti	B
15-15 prec									
mini	0.08	1.0	0.3	14.0	14.0	1.0	<0.01	0.3	0.004
maxi	0.10	2.0	0.6	16.0	16.0	2.0		0.5	0.008
AIM1 prec									
mini	0.08	1.0	0.8	14.0	14.0	1.3	<0.01	0.3	0.004
maxi	0.10	2.0	1.0	16.0	16.0	1.7		0.5	0.008
AIM1									

Mini	0.08	1.0	0.7	14.0	14.0	1.3	0.03	0.3	0.004
Maxi	0.10	2.0	0.9	16.0	16.0	1.7	0.05	0.5	0.008

Table 1 : chemical composition of three generations of swelling resistant austenitic steel.

2.1. Swelling and irradiation creep

Swelling and irradiation creep properties are obtained by measuring the total strain profile of irradiated fuel pins. Additional density measurements quantify the swelling component. Figure 1 presents the results of three irradiation programs where fuel pin have been irradiated to 83 (black curve), 110 (blue curve) and 130 dpa (red curve) in Phenix. On Figure 1, dots are swelling strains from density measurements, the shaded area represents the adjustment of a swelling and irradiation creep model to the data. Note that density measurements are still not available for the 130 dpa irradiation.

Claddings made of AIM1 precursor differ from AIM1 by a lower P contents and higher Si content as shown in Table 1. Total strain measurement at 83 and 110 dpa have been published elsewhere [2] [3]. A new non-destructive examination of irradiated AIM1 precursor was performed at higher dose 130 dpa and shows two striking features:

- The presence of two peaks in the strain profile which was not seen at lower dose. Density measurements and TEM examinations planned in 2013 should give further insight.
- A significant strain is observed in the upper part of the cladding. Since thermal creep is negligible in the temperature range around 650°C, the deformation might arise from fuel-cladding mechanical or chemical interaction.

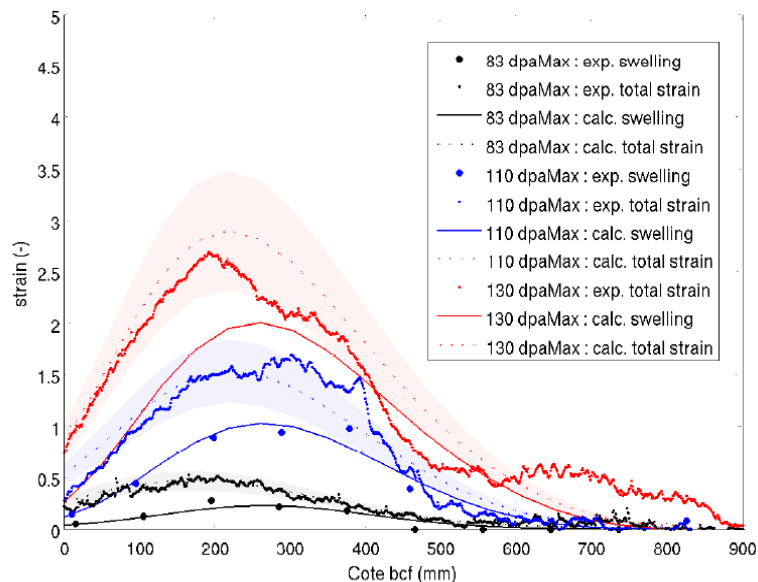


Figure 1: total and swelling strain versus axial position for three PHENIX irradiation programs.

Incubation dose for this AIM1 precursor is about 100 dpa. By extrapolation, it is expected that incubation dose of AIM1 will increase to 115 dpa using different Si and P contents. Note that AIM1 precursor claddings have been irradiated in Phenix up to 160 dpa to reach a total strain of 7%.

2.2. Thermal creep

Axial creep properties have been measured mainly on unirradiated 15-15Ti precursor above 500°C. Figure 2 shows minimum creep rates for several levels of stress and temperature. In order to compare creep performance of AIM1 with 15-15Ti precursor, creep tests have been performed on unirradiated AIM1 at 650°C. AIM1 measurements have been performed at 650°C (black curve). Dotted line are an adjustment of the data by a classic power-law creep. Results demonstrate the good consistency between 15-15Ti precursor and AIM1 secondary creep rate and confirm that small variations of Si and P contents do not produce a big change in creep properties.

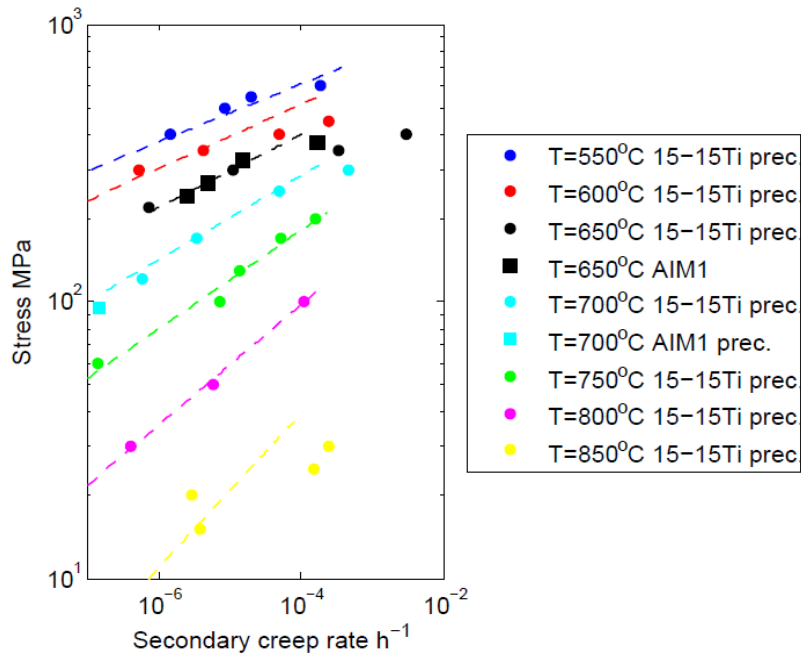


Figure 2 : Secondary creep rate measured in 15-15Ti precursor.

One remaining aspect that merits further investigation is the thermal creep properties after irradiation. Experimental data on 15-15Ti is scarce and most of the behavior laws are based on 316Ti feedback.

2.3. Tensile properties

Axial and hoop static tensile tests have been performed on unirradiated AIM1 in the temperature range 0 – 700°C with a standard strain rate of $3e-4$ s⁻¹. Tensile properties (Yield Strength, Ultimate tensile strength and uniform elongation, are displayed Figure 3. Results demonstrate a satisfactory behavior of AIM1 similar to the previous generation of 15-15Ti. SEM Fractographies after tensile test indicates a classic transgranular ductile fracture over the whole temperature range. In the range [100 – 500°C] stress-strain curve shows serration and presence of dynamic aging (Portevin-Le-Chatelier effect) arising from dynamic interaction between solute atoms and dislocation. Tensile tests are still underway to assess the dependence of tensile properties with strain rate and permit an identification of a reliable viscoplastic model.

Tensile test of irradiated AIM1 precursor are compared with unirradiated data in Figure 3 up to 110 dpa. Mechanical properties are rapidly saturated with the dose (after 20 dpa). Irradiation produces hardening below 550°C and softening above. The resistance to swelling prevents the occurrence of embrittlement and the degradation of mechanical properties as it was observed previously in 316Ti.

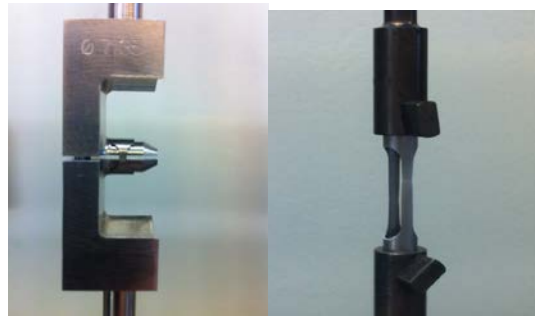
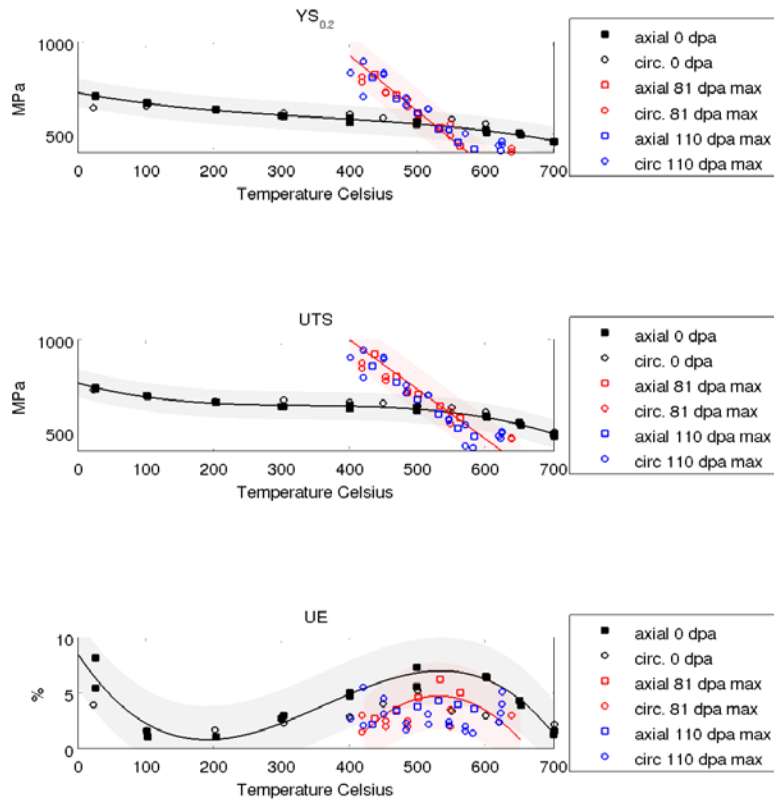


Figure 3 : Tensile properties : Yield Strength (YS), Uniform Tensile Stress (UTS), Uniform Elongation (UE) versus temperature for unirradiated (black color) and irradiated (blue and red color) 15-15Ti. Lower picture displays specimen cut from a cladding by electro discharge machining.

2.4. High temperature transient conditions

To assess the mechanical behavior in incidental and accidental conditions, dynamic tensile test were performed after fast temperature ramps. The rapid increase of temperature in the specimen was achieved by Joule effect. Experimental database is summarized in Table 2. Strain rate ranges from 10^{-3} s^{-1} to $10s^{-1}$ and heating rate were as high as $500^{\circ}C/s$ to simulate severe accidental situation.

Material	Number of tests	Temperature °C	strain rate s ⁻¹	Dose dpa
unirradiated : normal conditions				
AIM1	18SL+14ST	[20 - 700]	[10 ⁻⁵ - 3 10 ⁻⁴]	0
AIM1 prec.	27SL+24ST	[20 - 700]	[10 ⁻⁵ - 10 ⁻⁴]	0
unirradiated : acc./inc. conditions				
15-15Ti prec.	40 SL	[850 - 1250]	[10 ⁻¹ - 10]	0
15-15Ti prec.	56 SL	[650 - 950]	[10 ⁻³ - 1]	0
irradiated : normal conditions				
AIM1 prec.	5SL+24ST	[430 - 560]	[4.5 10 ⁻⁶ - 4.6 10 ⁻⁴]	[36 - 82]
AIM1 prec.	6SL+29ST	[420 - 625]	[4.5 10 ⁻⁶ - 4.5 10 ⁻⁴]	[48 - 111]
irradiated : inc./acc. conditions				
15-15Ti prec.	80 SL	[650 - 950]	[10 ⁻¹ - 1]	[40 - 95]
15-15Ti prec.	40 SL	[650 - 950]	[10 ⁻¹ - 10]	

Table 2 : Summary of the static and dynamic tensile tests performed on 15-15Ti. SL means axial loading (*Sens Long* in French) and ST means hoop loading (*Sens Travers*)

The main conclusions of this high temperature program were the following:

- Tensile properties are not very sensitive to the level of irradiation damage. Temperature rate and hold time after the temperature ramp does not influence YS, UTS or UE either.
- A sizeable effect of the strain rate was measured on UE and UTS as shown in Figure 4.

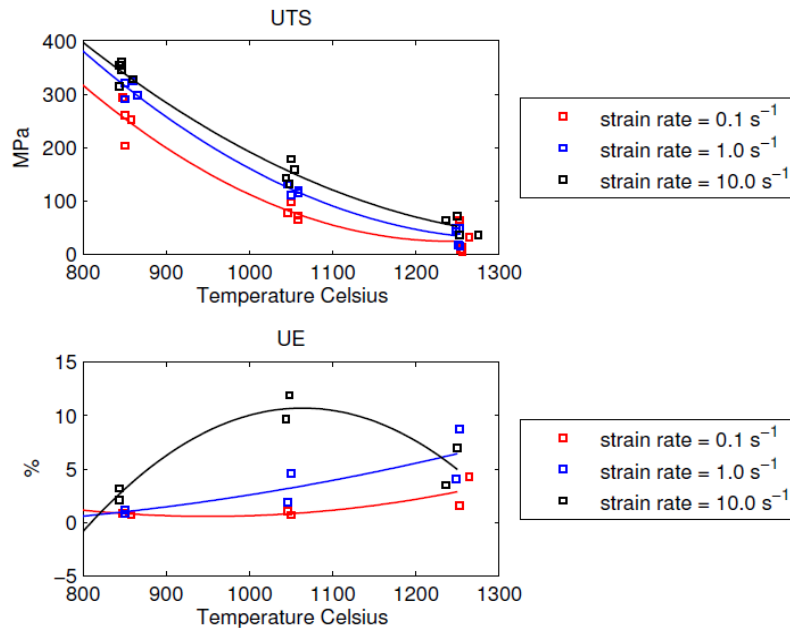


Figure 4 : ultimate tensile stress and uniform elongation versus final temperature measured after temperature ramps for several levels of strain rate.

3. Wrapper material

Developments for wrapper materials followed the same trend as for cladding materials: cold worked 316 alloys used for the first generation of wrappers were replaced by 316 Ti alloys to improve swelling resistance. The next step was the use of body centered cubic materials (ferritic and ferritic-martensitic materials) which have an intrinsically higher swelling resistance but exhibit a ductile to brittle transition at low temperatures, shifting to higher temperatures with irradiation.

The first bcc variant, named F17, a 17% Cr fully ferritic structure, presented important shifts of the Ductile to Brittle Transition Temperature (DBTT) under irradiation (reaching values of more than 200°C). It was later replaced by the EM10, an unstabilized 9% Cr fully tempered martensitic alloy, presenting much more limited irradiation embrittlement and excellent dimensionnal stability under irradiation. The EM10, extensively tested in the Phenix reactor, has proven suitable for use in sodium fast reactor conditions for doses higher than 100 dpa, and is the reference material for the ASTRID reactor.

3.1. Swelling resistance

The dimensionnal stability of the EM10 alloy has been studied through several experimental irradiations in Phenix : DOREMI 1 and DOREMI 1Bis, FERROFEU, SPHINX5 and finally BOITIX9, which allowed to verify that up to doses as high as 150 dpa, this alloy did not present levels of swelling higher than 0,5% in Phenix irradiation conditions (see Figure 5).

Moreover, dimensionnal measurements made directly on the full wrapper indicated only slight geometrical variations. Finally, TEM observations of the BOITIX9 samples have confirmed the low cavity density in the microstructure (Figure 5).

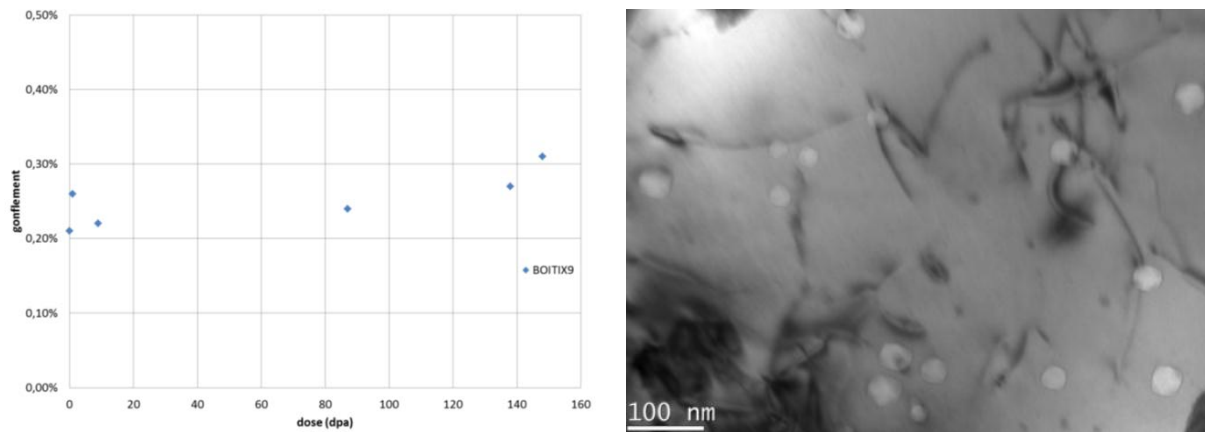


Figure 5. Swelling results from BOITIX9 and microstructure of a sample irradiated 155 dpa at 439°C.

3.2. Mechanical properties

As ferritic-martensitic materials present a DBTT, the evolution of the impact toughness has been studied after irradiation on such alloys. Results show an important embrittlement of the ferrite with irradiation, leading to a large shift of the DBTT for fully ferritic alloys (F17), and moderate shift for ferritic-martensitic alloys (such as the T91 alloy, a stabilised 9% Cr steel). The fully tempered martensitic structure of the EM10 leads to a much more moderate shift of the DBTT, which remains below 10°C even at high levels of dose (see figure 6).

Tensile test results confirm that the EM10 maintains a suitable mechanical resistance after irradiation, with a yield strength over 360 MPa in the 380-525°C temperature range, and levels of uniform elongation over 1%. Irradiation at low temperatures (380-440°C) leads to irradiation induced hardening, but at higher temperatures (440°C-525°C), the evolution of mechanical properties is much less important, and is more associated with thermal ageing.

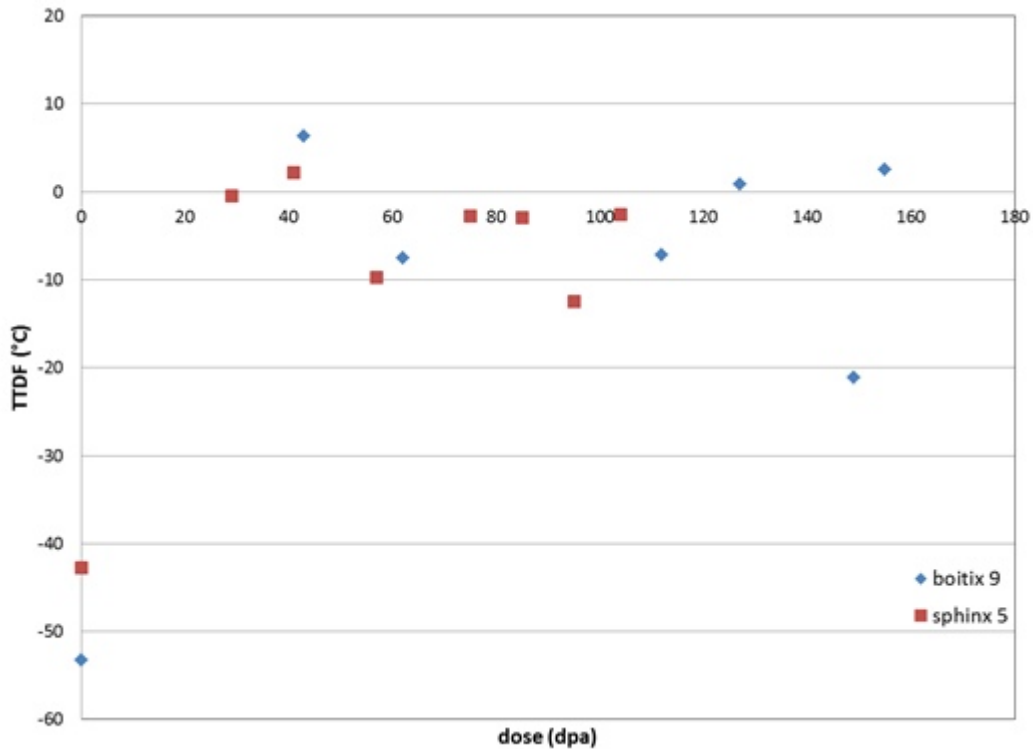


Figure 6. Evolution of the DBTT with increasing irradiation damage

4. Conclusion

AIM1 is the result of more than 30 years of R&D at CEA on swelling resistant austenitic and was chosen to be the reference cladding material of the future fast-reactor project ASTRID. Studies of AIM1 were reactivated at CEA to demonstrate its performance for the first ASTRID core up to 110 dpa. Assessment of AIM1 performance relies on a comprehensive database on previous version of 15-15Ti. CEA reactivated the qualification studies on AIM1 and the following studies are already planned:

- Investigation of the double peak seen in 130 dpa profile strain (density measurement and TEM examinations)
- Non-destructive and destructive examination of irradiated AIM1 up to 110 dpa
- Creep tests of irradiated AIM1 precursor at 130 dpa and AIM1 at 110 dpa
- Ions irradiation of AIM1 on the multi-ion beam irradiation platform JANNUS

Furthermore modeling efforts are in progress to set-up a viscoplastic model capable of reproducing tensile tests at various strain rates and creep tests for unirradiated and irradiated AIM1. Setting up a reliable swelling model in austenitic steel remains a challenging task. Promising cluster-dynamic models are currently tested.

If the properties of the EM10 wrapper material are well established for levels of dose exceeding 150 dpa in nominal conditions, further tests are on-going concerning the mechanical behavior of this alloy during incidental transients, which potentially involve phase transformation coupled with mechanical loadings.

REFERENCES

- [1] “The Swelling Behavior of Titanium-Stabilized Austenitic Steels Used as Structural Materials of Fissile Subassemblies in Phenix”. Seran, J-L, Touron, H, Maillard, A, Dubuisson, P, Hugot, J P, Le Boulbin, E, Blanchard, P, Pelletier, M, Effects of Radiation on Materials. Vol. II; Andover, Massachusetts; USA; 27-30 June 1988. pp. 739-752. 1990.

- [2] “Behavior Under Neutron Irradiation of the 15-15 Ti and EM 10 Steels Used as Standard Materials of the Phenix Fuel Subassembly”. JL Seran, V Levy, P Dubuisson, D Gilbon, A Maillard, A Fissolo, H Touron, R Cauvin, A Chalony. Effects of Radiation on Materials: 15th International Symposium; Nashville, Tennessee; USA; 19-21 June 1990. pp. 1209-1233. 1992.

- [3] “Swelling and Irradiation Creep of Neutron-Irradiated 316Ti and 15-15Ti Steels”. Maillard, A, Touron, H, Seran, J L, Chalony, A. Effects of Radiation on Materials: 16th International Symposium; Aurora, Colorado; USA; 23-25 June 1992. pp. 824-837. 1994.

Irradiation Performance of Oxide Dispersion Strengthened (ODS) Ferritic Steel Claddings for Fast Reactor Fuels

**Takeji Kaito^a, Satoshi Ohtsuka^a, Yasuhide Yano^a, Takashi Tanno^a,
Shinichiro Yamashita^a, Ryuichiro Ogawa^a, Kenya Tanaka^a**

^aJapan Atomic Energy Agency
4002, Narita-cho, Oarai-machi, Ibaraki 311-1393, Japan

Abstract. The oxide dispersion strengthened (ODS) ferritic steel claddings developed by Japan Atomic Energy Agency were irradiated in Joyo and BOR-60 in order to confirm their irradiation performance and thus judge their applicability to high burnup and high temperature fast reactor fuels. In Joyo, material irradiation tests up to 33 dpa were carried out at in the temperature range of 693 - 1108 K. The irradiation data were obtained concerning mainly mechanical properties and of microstructure stability. In BOR-60, fuel pin irradiation tests were conducted up to burnup of 11.9 at% and neutron dose of 51 dpa. The irradiation data were obtained concerning fuel-cladding chemical interaction, dimensional stability under irradiation and so on. These results showed the superior irradiation performance of the ODS ferritic steel claddings and their application possibility as fast reactor fuels. This paper describes the evaluation of the obtained irradiation data of ODS ferritic steel claddings.

1. Introduction

In Japan, the practical realization of the fast breeder reactor (FBR) cycle has been expected as an effective means to contribute to long-term stable energy supply and global warming countermeasures. In addition to ensuring safety, improvement of the economical performance is required to promote the FBR cycle technology. There are two important technological tasks to improve the economical performance: the development of high burn-up fuel to attain the average burn-up of 150 GWd/t and the development of a high temperature plant system to attain the coolant outlet temperature of 823 K [1]. This average burn-up is equivalent to 250 dpa for the maximum neutron dose, and the cladding temperature reaches approximately 973 K. The Japan Atomic Energy Agency (JAEA) has developed oxide dispersion strengthened (ODS) ferritic steels as the most promising cladding material to be used in such a severe environment [2-5]. It is important to confirm the irradiation behaviors for fuel pins to judge the applicability of ODS claddings. In material irradiation tests carried out in Joyo to the neutron dose of 33 dpa at irradiation temperatures between 693 and 1108 K, superior mechanical properties and microstructural stability of ODS claddings were obtained [6-10]. In addition, ODS cladding fuel pin irradiation tests in BOR-60 have been conducted under the framework of JAEA-Research Institute of Atomic Reactors (RIAR) collaborative work [11]. In these irradiation tests, the irradiation results up to burnup of 11.9 at% and neutron dose of 51 dpa were obtained, and superior properties of the ODS claddings concerning fuel compatibility, dimensional stability under irradiation and so on were confirmed [12, 13]. On the other hand, anomalous irradiation behaviors, fuel pin failure, and microstructure change involving coarse and irregular precipitates, occurred in a part of the ODS cladding fuel pins [13]. The combined effects of heterogeneity of matrix Cr composition (presence of metallic inclusions) and high-temperature irradiation caused the anomalous microstructure change, and they contributed to the fuel pin failure [14]. This paper gives an overview of the irradiation performance of the ODS claddings for fast reactor fuels.

2. Experimental

2.1. Materials irradiation tests in Joyo

2.1.1. Materials

The cladding materials provided for irradiation tests were 9Cr-ODS martensitic steel (manufacturing lot: M11, Mm14) and 12Cr-ODS ferritic steel (manufacturing lot: F14). Chemical compositions and manufacturing process of these ODS claddings are shown in **Table 1**. M11 and F14 were manufactured by the partial pre-alloy process. This manufacturing process used Ar-gas atomized alloy powder and Y_2O_3 powder with a small amount of elemental powder (Fe, C, Cr, W, Ti) for minor control of chemical composition. On the other hand, Mm14 was manufactured by the pre-mix process using the elemental powder and Y_2O_3 powder.

2.1.2. Irradiation tests

Materials irradiation tests were carried out in the experimental fast reactor Joyo using the core material irradiation rig (CMIR) [9, 10] and material testing rig with temperature control (MARICO) [8]. The ODS cladding specimens were loaded into stainless steel capsules, and were filled with coolant sodium. Irradiation temperatures were between 693 and 1108 K and neutron dose was up to 33 dpa. Irradiation conditions are shown in **Table 2**.

2.1.3. Post-irradiation examinations

The irradiated specimens were taken from stainless steel capsules, and first their appearance observation was carried out. Next, densimetry of irradiated specimens was done using an immersion density technique to evaluate the swelling behavior. Ring tensile tests were performed to examine irradiation effects on tensile properties. These tests were done in air using a screw-driven tensile testing machine at a constant crosshead speed of 1.67×10^{-3} mm/s. The test temperatures were from 693 to 1108 K corresponding to the irradiation temperature of each specimen. Microstructural observations for irradiated specimens were done by optical microscopy. In addition, transmission electron microscopy (TEM) examinations were conducted for evaluation of nano-scale microstructural evolution.

2.2. Fuel pins irradiation tests in BOR-60

2.2.1. Fuel pin design and fabrication

9Cr-ODS martensitic steel (Mm14) and 12Cr-ODS ferritic steel (F13) were provided as the fuel claddings. Chemical compositions of these ODS claddings are shown in **Table 1**. Mm14 was manufactured by the pre-mix process and F13 was manufactured by the partial pre-alloy process. These claddings were used on the fuel pins, in combination with vibro-packed MOX fuels. A schematic drawing of the ODS cladding fuel pin is shown in **Fig. 1** (a) and it was the wrapping wire type. Each pin had a length, outer diameter and cladding wall thickness of 1,050, 6.9 and 0.4 mm, respectively. The fuel column lengths differed for the 9Cr-ODS and 12Cr-ODS cladding fuel pins, and were 300 and 450 mm, respectively. These fuel pins were sealed by the pressurized resistance welding (PRW) method with an upper-end plug; this work was done by JAEA [15]. The lower end-plug was welded by the tungsten inert gas (TIG) end-face fusion method; this work was done by RIAR [11]. Vibro-packed MOX fuels with added 5 - 7 wt% U metal getter particles were used, and Pu content was set to 15 wt%. Details of the design, fabrication and inspection of ODS cladding fuel pins have been reported in Ref. [11].

2.2.2. Irradiation tests

The fabricated ODS fuel pins were loaded into two experimental fuel assemblies (EFAs), and were irradiated in the Russian experimental fast reactor BOR-60. A schematic drawing of an EFA is shown in **Fig. 1** (b). Each EFA had a bundle of 19 fuel pins which included four fuel pins with 9Cr-ODS cladding, two fuel pins with 12Cr-ODS cladding, and 13 fuel pins with Russian austenitic stainless steel ChS-68 (0.06C-16Cr-15Ni-2Mo-2Mn-Ti-V-B) cladding [16]. ChS-68 cladding, for which many actual use results have been obtained for the driver fuel pins in BOR-60 and BN-600, was used as a

reference for comparative evaluation of FCCI behavior. The irradiation test achieved the maximum peak burnup of 11.9 at% and neutron dose of 51 dpa. The irradiation temperature calculated by RIAR, based on BOR-60 actual operation conditions, was 973 K at a maximum and 943 K on average.

2.2.3. Post-irradiation examinations

EFAs were carried into the hot-cell after decreasing the decay heat and removing the residual sodium. After dismantling the EFAs, visual inspections of the fuel pin bundle were made and then the bundle was disassembled. After further detailed visual inspections, outer diameter measurements and gamma-scanning for each ODS cladding fuel pin were conducted. In addition, a puncturing test to evaluate the internal pressure due to fission product gases was conducted for some ODS cladding fuel pins. In order to evaluate the fuel-cladding chemical interaction (FCCI) and the outer surface corrosion of ODS claddings, metallographic observations were carried out.

3. Results

3.1. Dimensional stability

Results of densimetry of 9Cr-ODS and 12Cr-ODS cladding specimens irradiated in the CMIR showed that the volumetric swelling was less than 0.02 vol%. In addition, although a slight increase of the outer diameter was observed around part of fuel column in the 9Cr-ODS and 12Cr-ODS cladding fuel pins irradiated in BOR-60, those values were less than 0.5%. From these results, good dimensional stability of both 9Cr-ODS and 12Cr-ODS claddings was confirmed as expected.

3.2. Mechanical properties

Ultimate tensile strength (UTS) is shown in **Figs. 2** (a) and (b) as a function of test temperatures for 9Cr-ODS and 12Cr-ODS claddings irradiated in the CMIR. The relation between yield strength and test temperature was similar to that of UTS at all irradiation temperatures although there was a difference in each absolute value. As shown in **Fig. 2** (a), UTS of M11 was higher than Mm14 comparing with that of the as-received. When irradiation was done at a temperature below 923 K, UTS of the irradiated 9Cr-ODS claddings was almost the same level as the as-received specimen and no significant increase in UTS was observed. In the case of irradiation above 1023 K, a decrease in UTS was recognized. On the other hand, no change in UTS for 12Cr-ODS claddings was observed at all test temperatures except 673 K as shown in **Fig. 2** (b). In addition, the uniform elongation of the irradiated 9Cr-ODS and 12Cr-ODS claddings was more than 2% at all irradiation temperatures. The in-pile creep rupture strengths of 9Cr-ODS and 12Cr-ODS claddings obtained in the MARICO irradiation test are shown in **Figs. 3** (a) and (b). As shown in **Fig. 3** (a), the in-pile creep rupture data of 9Cr-ODS claddings up to the rupture times of 614 hours (≈ 2.0 dpa) at 973 K and 512 hours (≈ 3.1 dpa) at 998 K were obtained. Strength reduction due to the neutron irradiation was not observed for 9Cr-ODS claddings under these irradiation conditions. Similarly for 12Cr-ODS claddings, no in-pile creep rupture strength reduction due to the neutron irradiation was observed for the 12Cr-ODS claddings as shown in **Fig. 3** (b) though MARICO test provided only one rupture time of 611 hours (≈ 3.1 dpa) at 1023 K.

3.3. Microstructural stability

Figure 4 shows the optical microstructures of 9Cr-ODS and 12Cr-ODS claddings irradiated in the CMIR. As shown in **Figs. 4** (b) and (c), martensitic structures of 9Cr-ODS claddings were observed after irradiation below 900 K, which was similar to the microstructure of the as-received material. As seen from **Fig. 4** (d), some of the martensitic structures changed due to recovery during the irradiation above 1003 K. On the other hand, 12Cr-ODS claddings had large recrystallized-grains as shown in **Fig. 4** (e), and there was no significant change in microstructures of 12Cr-ODS claddings after irradiation at all irradiation temperatures as shown in **Figs. 4** (f) - (h).

As a result of TEM observation of 9Cr-ODS and 12Cr-ODS claddings irradiated in the CMIR, it was confirmed again that microstructures of all the 9Cr-ODS claddings consisted of fine tempered

martensitic structures, precipitates and dislocations structure and that no voids were induced by irradiation. On the other hand, all the 12Cr-ODS claddings had recrystallized ferritic structures with a low population of precipitates and dislocations. And no voids evolved in the irradiated structures. **Figure 5** presents the oxide particle distribution of the 9Cr-ODS claddings before (**Fig. 5** (a)) and after irradiation (**Figs. 5** (b) - (e)). Compared to the oxide dispersion before irradiation, the uniform distribution of fine oxide particles seemed to be totally unchanged even after irradiation at 1103 K (**Fig. 5** (e)). The same tendency was confirmed in the 12Cr-ODS claddings.

3.4. Fuel and sodium compatibility

In order to evaluate the FCCI and the outer surface corrosion of ODS claddings, metallographic observations were carried out for ODS cladding fuel pins irradiated in BOR-60. **Figure 6** shows optical micrographs (cross section) in the upper part of the fuel column of the 9Cr-ODS cladding fuel pin. Average cladding mid-wall temperature during the irradiation period, neutron dose and burn-up of this position were approximately 943 K, 28 dpa and 7.6 at%, respectively. As seen in these photographs, no significant FCCI was observed. On the other hand, a different reaction layer from the matrix in the range of about 60 μm from the cladding outer surface was observed. As a result of conducting a line analysis using an electron probe micro analyzer (EPMA), it was determined that Cr content in the reaction layer decreased to about half that in the matrix. Such a decrease in Cr content occurred only in the upper part of the fuel column irradiated at high temperature, and did not occur below the core center. Optical micrographs (cross section) obtained in the upper part of the fuel column are shown in **Fig. 7** for the 12Cr-ODS cladding fuel pin. The irradiation conditions were the same as for the 9Cr-ODS cladding fuel pin. FCCI to a depth of about 35 μm was observed clearly in the inner surface of the 12Cr-ODS cladding (**Fig. 7** (a)). And a different reaction layer, like that seen in the 9Cr-ODS cladding, was observed up to about 30 μm from the cladding outer surface.

3.5. Welded part integrity

The metallographic observation of the upper-end plug welded by the PRW method was carried out to confirm its integrity for ODS cladding fuel pins irradiated in BOR-60. As a representative example, optical micrographs (longitudinal section) of the 9Cr-ODS cladding fuel pin are shown in **Fig. 8**. Average temperatures during the irradiation period and neutron dose of this position were approximately 943 K and 1 dpa, respectively. As shown in these photographs, significant microstructure changes, cracking, etc. did not occur in that welded part. The integrity of the welded part was also confirmed for other 9Cr-ODS and 12Cr-ODS cladding fuel pins. These results show that the PRW method would be a very promising welding method for ODS claddings.

3.6. Anomalous irradiation behaviors

In one EFA, which was irradiated up to the peak burnup of 10.5 at% and neutron dose of 45 dpa in BOR-60, anomalous irradiation behaviors such as fuel pin failure and microstructure instability occurred in a part of the 9Cr-ODS cladding fuel pins [13]. The cause of these anomalous irradiation behaviors was concluded to be the combined effects of two factors: the matrix Cr heterogeneity in the 9Cr-ODS cladding and the irradiation temperature exceeding the designed one [14]. Especially, it was considered that the matrix Cr heterogeneity was caused by the pre-mix process used in manufacturing the 9Cr-ODS claddings, and it could be prevented by applying the pre-alloy process. Details from investigation of the cause of these anomalous irradiation behaviors are reported in Ref. [14].

4. Discussions

4.1. Relationship between mechanical properties and microstructure

The tensile properties of ODS claddings irradiated in Joyo were shown in Sec. 3.2. The change of irradiation hardening or softening is shown as the UTS ratio in **Fig. 9** with the present results for these ODS claddings, and previous results for ODS claddings [6] and conventional 11Cr-ferritic/martensitic steel (PNC-FMS) [17] irradiated in Joyo. There was no remarkable degradation in tensile strength in

the ODS claddings. On the other hand, the tensile strength of PNC-FMS claddings degraded due to neutron irradiation at high temperatures above 903 K, and it was suggested that such significant strength reduction was related to a drastic microstructural change during irradiation, especially recovery of martensitic structure and precipitation behavior [17].

Also, no in-pile creep rupture strength reduction was confirmed in the ODS claddings as described in Sec. 3.2. On the other hand, in the in-pile creep rupture test of 20 % cold-worked modified 316 stainless steel (PNC316) conducted using the material open test assembly (MOTA) in the fast flux test facility (FFTF), creep rupture strength reduction due to the neutron irradiation was observed even for the rupture time of 300 hours (≈ 2.5 dpa) at 878 K [18]. Such strength reduction in PNC316 could be mainly attributed to the earlier recovery of dislocation structures introduced by the cold-working. The coarsening of MC precipitates by the radiation-induced solute segregation may be indirectly associated with the early dislocation recovery. This result suggested that the dislocation recovery and the coarsening of MC precipitates would not influence the creep rupture strength of the ODS claddings, since the main factor governing high temperature strength in the ODS claddings is the stability of oxide particles. From TEM results described in Sec. 3.3, the oxide particles and microstructure of ODS claddings were confirmed to be stable during neutron irradiation. Thus, there was no significant reduction of tensile strength and creep rupture strength in ODS claddings because the oxide particles were stable under the irradiation conditions.

4.2. Fuel compatibility

The FCCI behavior of ODS claddings irradiated with vibro-packed MOX fuels in BOR-60 was shown in Sec. 3.4. Generally, it is thought that higher Cr content steel has superior corrosion resistance. However, as for FCCI behavior, the opposite tendency occurred only in the 12Cr-ODS cladding. Although it can be considered that non-uniformity of the microstructures in 12Cr-ODS cladding was the cause, it is necessary to perform a detailed evaluation. These results were summarized and compared with the data of PNC316 and PNC-FMS claddings, which were irradiated with pellet type MOX fuels. **Figures 10** (a) and (b) show the burn-up dependence and the temperature dependence of FCCI, respectively. From these figures, it was obvious that the FCCI of ODS claddings was below or equal to that of PNC316 and PNC-FMS claddings. In particular, at temperatures lower than 923 K in **Fig.10** (b), the FCCI of ODS claddings was not observed. Here, it is necessary to note that the oxygen-to-metal (O/M) ratio of ODS cladding fuel pins was low, i.e. about 1.93, as vibro-packed MOX fuels containing U metal getter particles were used whereas the O/M ratios of PNC316 and PNC-FMS cladding fuel pins were 1.95 - 1.99. The cladding inner surface corrosion is effectively prevented by the lower O/M ratio, because the low oxygen potential restricts the chemical reaction of the cladding material with fission products and fuel. In fact, it has been shown that the FCCI was surely restricted by lowering the O/M ratio of the fuels based on extensive irradiation tests of PNC316 and ChS-68 fuel pins [19, 20]. These results indicated that the inner corrosion of the ODS claddings by FCCI could be controlled by lowering the oxygen potential in the fuel pins using U metal getter, even in low Cr content cladding such as 9Cr-ODS steel.

5. Conclusions

Irradiation tests in Joyo and BOR-60 for the ODS claddings developed by JAEA were carried out in order to confirm the irradiation performance of the ODS claddings and thus judge their applicability to high burnup and high temperature fast reactor fuels. The main points of the tests are summarized as follows.

- 1) Valuable data indicating application prospects of the ODS claddings for high burnup fuels were obtained regarding superior dimensional stability and integrity of the upper end-plug welded by the PRW method.
- 2) No significant irradiation effect on mechanical properties of the ODS claddings was observed within the irradiation conditions in the Joyo material irradiation tests. The oxide particles and microstructures of ODS claddings were observed to be stable during neutron irradiation.
- 3) FCCI data for the ODS claddings were acquired within the irradiation conditions in the BOR-60 fuel pin irradiation tests, and it was shown that FCCI could be reduced by lowering oxygen potential in the fuel pins using U metal getter, even for low Cr content claddings such as 9Cr-ODS steel.

ACKNOWLEDGEMENTS

The execution of these irradiation tests required the active cooperation of many people in JAEA and RIAR, and we wish to gratefully acknowledge their support and encouragement.

REFERENCES

- [1] SHIMAKAWA, Y., KASAI, S., KONOMURA, M. and TODA, M., An innovative concept of a sodium-cooled reactor to pursue high economic competitiveness, *Nucl. Technol.*, 140, p.1 (2002).
- [2] UKAI, S. and FUJIWARA, M., Perspective of ODS alloys application in nuclear environments, *J. Nucl. Mater.*, 307-311, p.749 (2002).
- [3] UKAI, S., et al., Production and properties of nano-scale oxide dispersion strengthened (ODS) 9Cr martensitic steel claddings", *ISIJ International*, 43[12], p.2038 (2003).
- [4] OHTSUKA, S., UKAI, S., FUJIWARA, M., KAITO, T. and NARITA, T., Nano-structure control in ODS martensitic steels by means of selecting titanium and oxygen contents, *J. Phys. Chem. Solids.*, 66, p.571 (2005).
- [5] OHTSUKA, S., UKAI, S. and FUJIWARA, M., Nano-mesoscopic structural control in 9Cr-ODS ferritic/martensitic steels, *J. Nucl. Mater.*, 351, p.241 (2006).
- [6] YOSHITAKE, T., et al., Ring-tensile properties of irradiated oxide dispersion strengthened ferritic/martensitic steel claddings, *J. Nucl. Mater.*, 329–333, p.342 (2004).
- [7] YAMASHITA, S., YOSHITAKE, T., AKASAKA, N., UKAI, S. and KIMURA, A., Mechanical behavior of oxide dispersion strengthened steels irradiated in Joyo, *Materials Transactions*, 46 [3], p.493 (2005).
- [8] KAITO, T., et al., In-pile creep rupture properties of ODS ferritic steel claddings, *J. Nucl. Mater.*, 386-388, p.294 (2009).
- [9] YANO, Y., et al., Effects of neutron irradiation on tensile properties of oxide dispersion strengthened (ODS) steel claddings, *J. Nucl. Mater.*, 419, p.305 (2011).
- [10] YAMASHITA, S., et al., Irradiation behavior evaluation of oxide dispersion strengthened ferritic steel cladding tubes irradiated in Joyo, *J. Nucl. Mater.*, to be published.
- [11] UKAI, S., KAITO, T., SEKI, M., MAYORSHIN, A.A. and SHISHALOV, O.V., Oxide dispersion strengthened (ODS) fuel pins fabrication for BOR-60 irradiation test, *J. Nucl. Sci. Technol.*, 42[1], p.109 (2005).
- [12] KAITO, T., UKAI, S., POVSTYANKO, A.V., EFFIMOV, V.N., Fuel pin irradiation test at up to 5 at% burnup in BOR-60 for oxide-dispersion-strengthened ferritic steel claddings, *J. Nucl. Sci. Technol.*, 46[6], p.529 (2009).
- [13] KAITO, T., et al., ODS cladding fuel pins irradiation tests using BOR-60 reactor, *J. Nucl. Sci. Technol.*, to be published.
- [14] OHTSUKA, S., et al., Investigation to determine the cause of peculiar irradiation behavior of 9Cr-ODS steel in BOR-60 irradiation tests, *J. Nucl. Sci. Technol.*, to be published.
- [15] SEKI, M., et al., Pressurized resistance welding technology development in 9Cr-ODS martensitic steels, *J. Nucl. Mater.*, 329-333, p.1534 (2004).
- [16] POROLLO, S.I., KONOBEEV, Yu.V. and GARNER, F.A., Swelling and microstructure of austenitic stainless steel ChS-68 CW after high dose neutron irradiation, *J. Nucl. Mater.*, 393, p.61 (2009).
- [17] YANO, Y., et al., Mechanical properties and microstructural stability of 11Cr-ferritic/martensitic steel cladding under irradiation, *J. Nucl. Mater.*, 398, p.59 (2010).
- [18] UKAI, S., MIZUTA, S., KAITO, T. and OKADA, H., In-reactor creep rupture properties of 20 % CW modified 316 stainless steel, *J. Nucl. Mater.*, 278, p.320 (2000).
- [19] KASHIHARA, H., et al., Dimensional stability of FBR fuel pins with modified type 316 stainless steel cladding at high burn-up, *Proc. Int. Conf. On Fast Reactor Core and Fuel Structural Behaviour*, Inverness, UK, Jun. 4-6, 1990, 243 (1990).
- [20] HERBIG, R., RUDOLPH, K., LINDAU, B., SKIBA, O.V. and MAERSHIN, A.A., Vibrocompacted fuel for the liquid metal reactor BOR-60, *J. Nucl. Mater.*, 204, p.93 (1993).

Table 1 Chemical compositions and manufacturing process of ODS claddings

	(wt%)			
	9Cr-ODS martensitic steel		12Cr-ODS ferritic steel	
	M11	Mm14	F13	F14
C	0.13	0.13	0.03	0.044
Si	0.05	0.009	0.045	0.052
Mn	0.044	<0.01	0.07	0.09
P	0.002	<0.005	0.005	0.005
S	0.002	0.003	0.003	0.004
Ni	0.021	<0.01	0.03	0.08
Cr	9.00	8.8	11.5	11.39
W	1.95	2.0	1.9	1.87
Ti	0.20	0.20	0.27	0.26
Y	0.29	0.28	0.18	0.18
O	0.14	0.17	0.12	0.10
N	0.013	0.012	0.0094	0.010
Ar	0.025	0.054	0.055	0.0045
Y ₂ O ₃ ^{*1}	0.37	0.35	0.23	0.23
Ex.O ^{*2}	0.06	0.10	0.07	0.05
Manufacturing process	Partial pre-alloy	Pre-mix	Partial pre-alloy	Partial pre-alloy
Irradiation test	Joyo (CMIR)	Joyo (CMIR, MARICO), BOR-60	BOR-60	Joyo (CMIR, MARICO)

^{*1} Estimated from yttrium content with the assumption that yttrium exists as Y₂O₃

^{*2} Excess oxygen which is defined as the value obtained by subtracting oxygen concentration in Y₂O₃ from the total oxygen concentration in steel

Table 2 Irradiation conditions

	Joyo material irradiation test		BOR-60 fuel pin irradiation test
	CMIR	MARICO	
Temperature (K)	693 - 1108	723 - 1023	973/1043 ^{*2}
Neutron dose (dpa) ^{*1}	33	28	51
Burnup (at%) ^{*1}	-	-	11.9
Linear heat rate (w/cm) ^{*1}	-	-	442

^{*1} Peak value

^{*2} Peak value of ODS cladding fuel pin (Design value/Estimate value based on the PIE result)

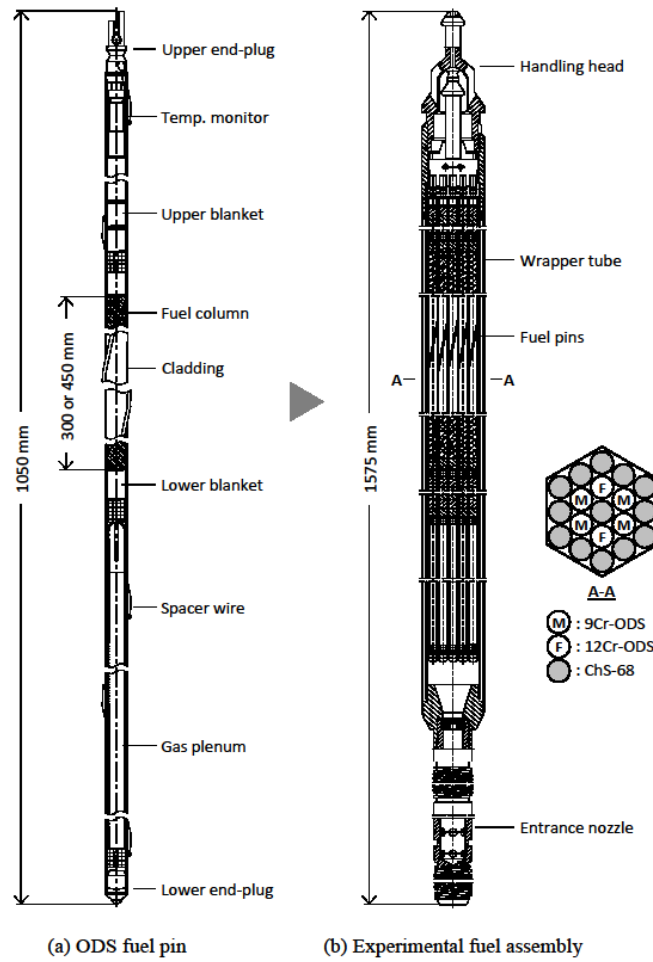


Fig. 1 Schematic drawings of (a) ODS cladding fuel pin and (b) experimental fuel assembly for BOR-60 fuel pin irradiation tests

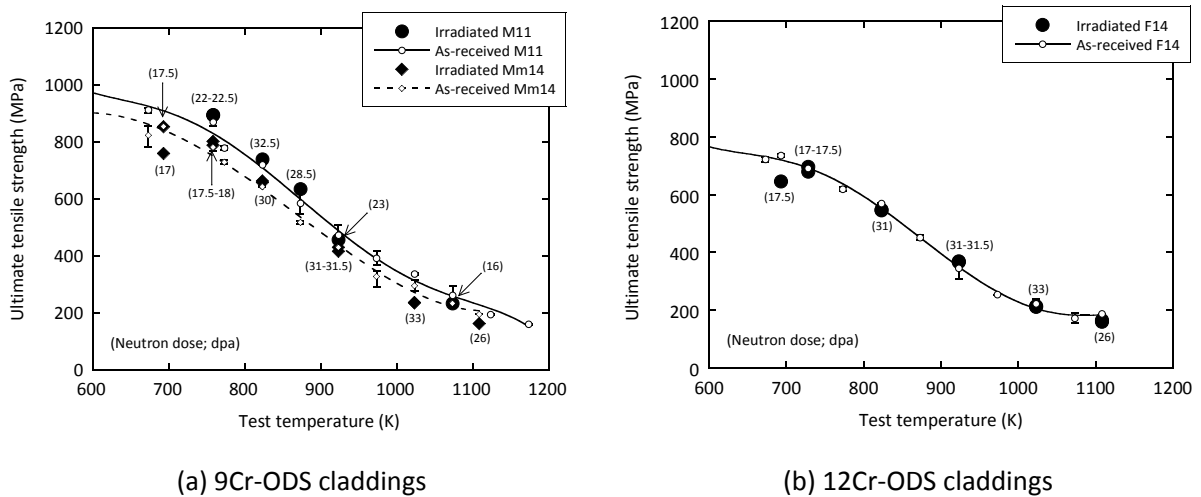


Fig. 2 Ultimate tensile strength of ODS claddings after irradiation in Joyo

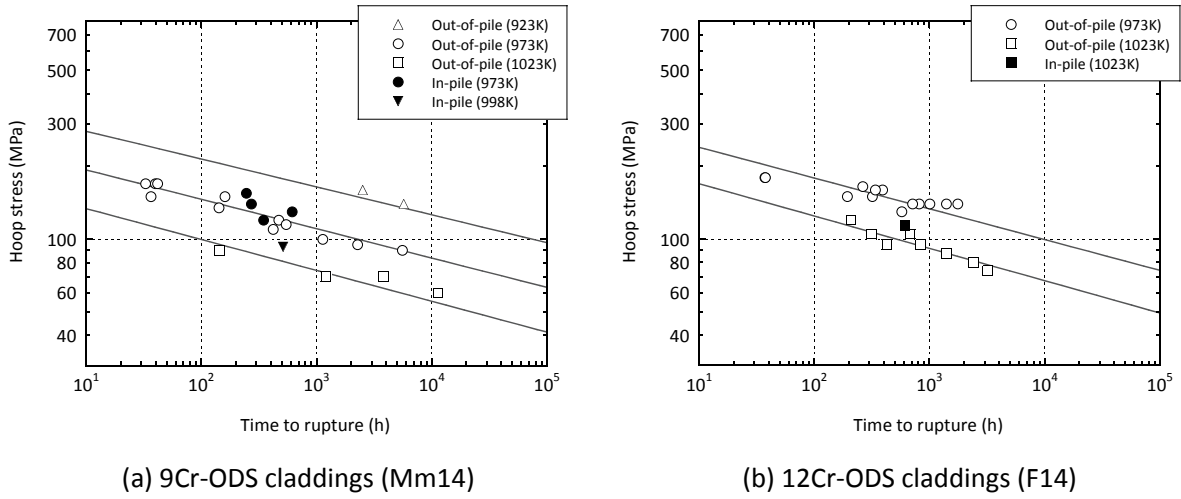


Fig. 3 In-pile and out-of-pile creep rupture strength of ODS claddings after irradiation in Joyo

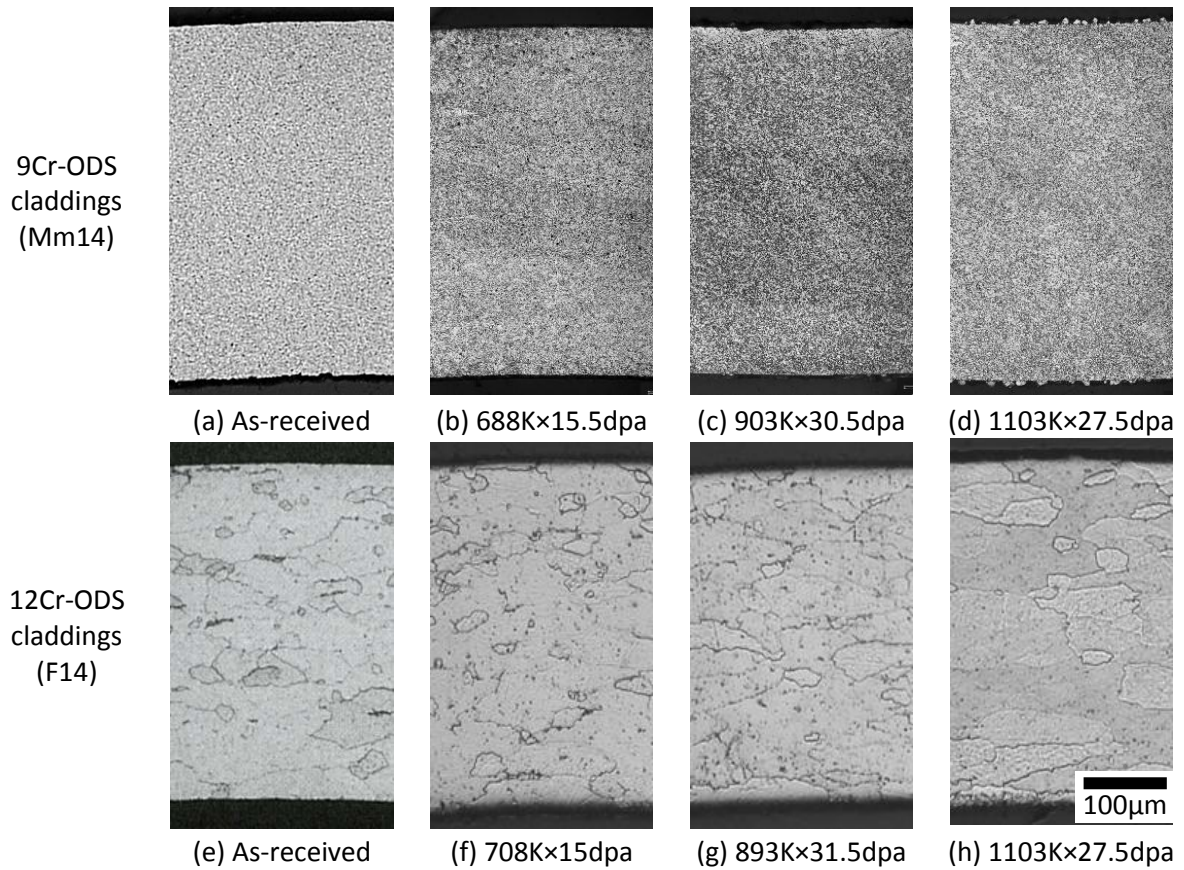


Fig. 4 Optical microstructure in the cross-sectional direction of ODS claddings after irradiation in Joyo

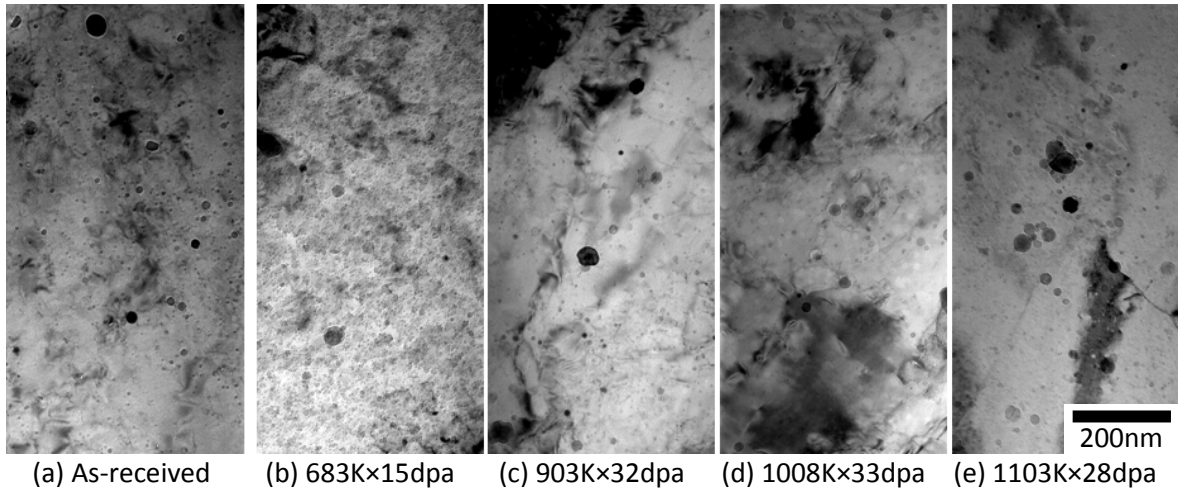


Fig. 5 Bright field micrographs exhibiting oxide particle distribution of 9Cr-ODS claddings after irradiation in Joyo

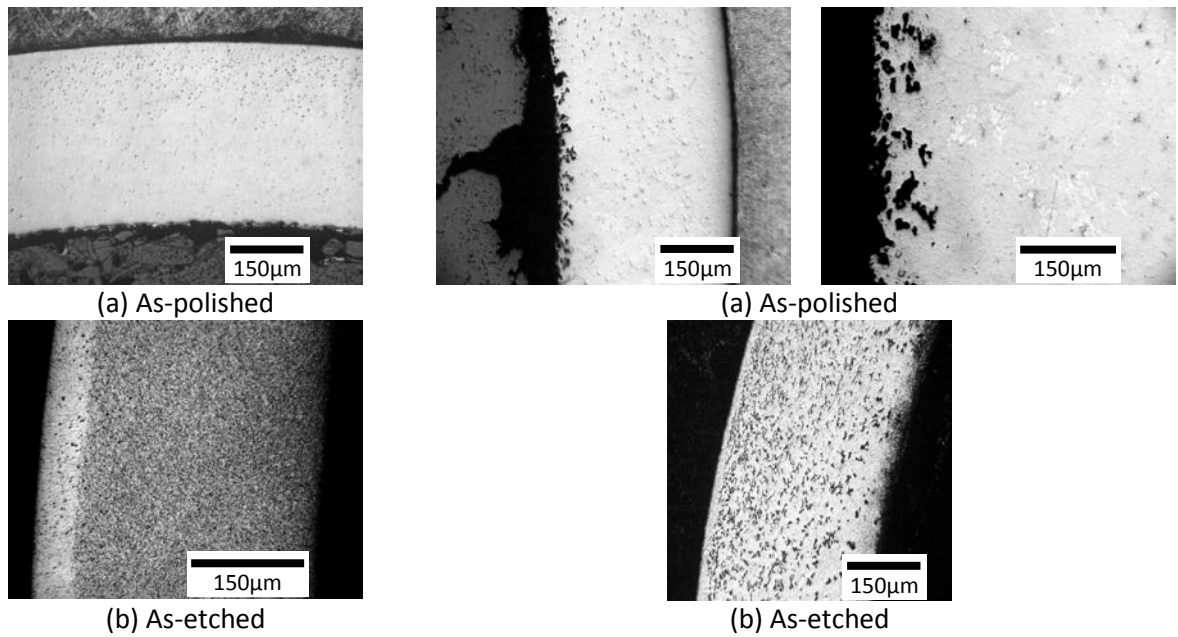


Fig. 6 Optical micrographs of 9Cr-ODS cladding fuel pin, after irradiation in BOR-60

Fig. 7 Optical micrographs of 12Cr-ODS cladding fuel pin, after irradiation in BOR-60

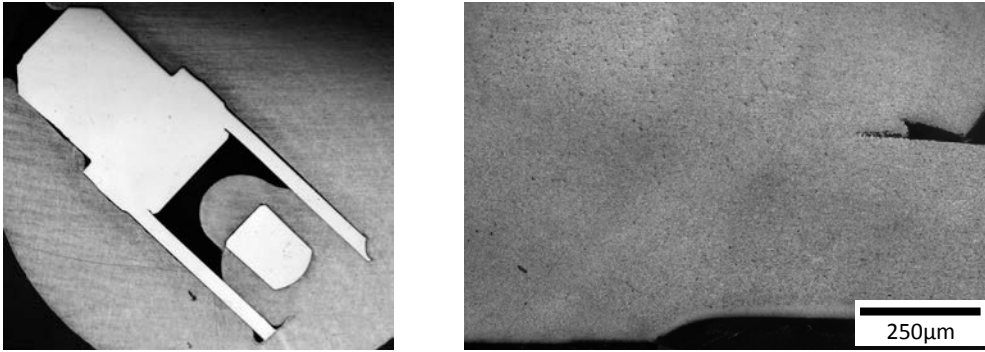


Fig. 8 Optical micrographs in the vicinity of the PRW part of the upper end-plug

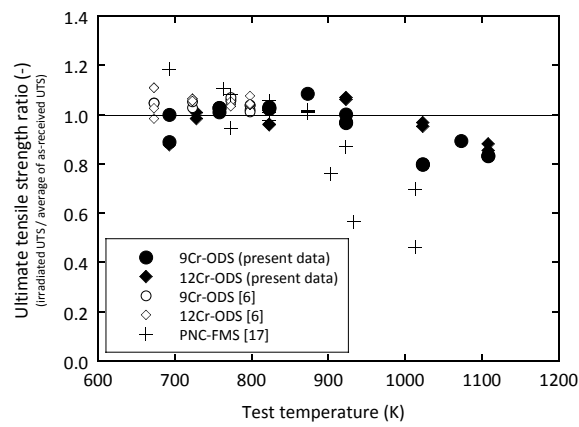


Fig. 9 Relationship between ultimate tensile strength ratio and irradiation temperature

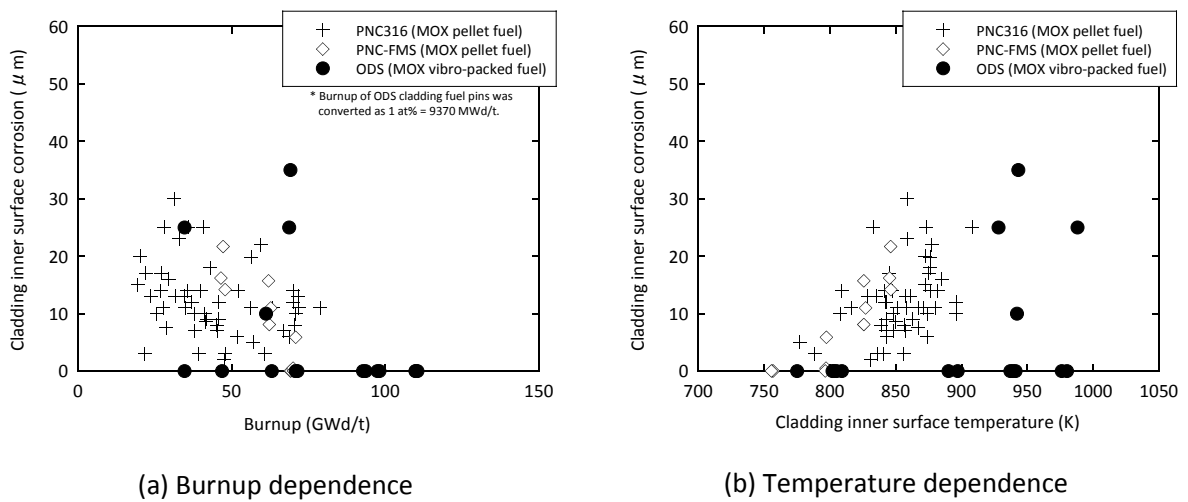


Fig.10 Comparison of FCCI of the irradiated ODS claddings and PNC316 and PNC-FMS claddings

Recovery of nuclear materials from Phénix to support the qualification of ASTRID design options

I. Munoz-Viallard^a, J.-M. Augem^b, M. Phélip^a, F. Dalle^c, M. Blat-Yrieix^d, Ch. Billey^e, N. Devictor^a, S. Dubiez-Le Goff^f, S. Pillon^e, M. Le Flem^c

^aCEA/DEN (DEC & DER), Cadarache, France

^bEDF SEPTEN, Villeurbanne, France

^cCEA/DEN (DMN), Saclay, France

^dEDF R&D, Ecuelles, France

^eCEA/DEN (DEIM & DTEC), Marcoule, France

^fAREVA, Lyon, France

Abstract. During its 35 years of operation, the PHENIX experimental reactor was connected to the electricity power grid and was subjected to representative constraints of Gen IV future sodium-cooled fast reactors (sodium environment, flux, materials and temperatures). During this time, more than 200 specific irradiation experiments were also conducted in the reactor. It is of primary interest to use all this knowledge and know-how as a lever to qualify the ASTRID prototype options and to meet modelling needs. A working group has been set up to select the relevant irradiated materials according to R&D needs and to propose future experimental examinations. This paper gives an overview of the approach and some illustrations of the valuable materials that will be recovered:

- Core materials: fuel sub-assemblies, control rods, neutron shielding, reflectors,
- Nuclear steam supply system (NSSS) materials: reactor vessels, diagrid (cold plenum of the reactor, with low irradiation dose), core cover plug,
- Circuit materials: sodium circuit, steam circuit
- Large components: intermediate heat exchangers, steam generators, pumps
- Instrumentation components.

1. Introduction

Prospective studies carried out by the CEA and industrial partners led France to elaborate a R&D strategy on future nuclear energy systems for the medium and the longer terms (> 2040); this strategy gives clear priority to fast neutron nuclear systems with a closed fuel cycle. The sodium-cooled fast reactor (SFR) is the reference option, while the gas-cooled fast reactor (GFR) remains a long-term option.

Along with the R&D, plans for ASTRID (for Advanced Sodium Technological Reactor for Industrial Demonstration) have been prepared [1]. This prototype aims at demonstrating technological advances of the Gen IV future sodium-cooled fast reactors up to an industrial scale. As an industrial prototype, it should be commissioned sometime around 2020.

ASTRID has to integrate operational feedback from past reactors like Phénix [2] and Superphénix. The shutdown of the Phénix reactor in 2009 and its current dismantling provides us with an

opportunity to lever our knowledge and know-how in support of the qualification of the ASTRID prototype and associated R&D needs.

A working group has been set up to select the relevant irradiated materials according to R&D needs and to propose future experimental examinations. This paper gives an overview of the approach and some illustrations of the valuable materials that will be recovered.

2. Relevance of Phénix feedback

The examination of materials from the Phenix plant gives us an excellent opportunity to consolidate our knowledge both on the ASTRID prototype and sodium-cooled fast reactors in general. Within the scope of developing SFRs by 2040, the structural materials [3] expected to be used to build these reactors must be qualified for a service life of 60 years.

This qualification involves two stages:

- Laboratory tests. Though they are not entirely representative of the real conditions of use, they nevertheless help us to understand the mechanisms involved, providing data that can be used to model the structural behaviour,
- Estimative calculations which must be checked and/or adjusted in relation to feedback and experience.

Within this context, the examination of materials having been used over a significant period of time under real load conditions (temperature, stress and irradiation) and in a representative environment (sodium, polluted sodium, water-steam, etc.) will provide valuable information. These examinations will preferably concern the Phenix plant which operated for 35 years, including 15 equivalent years at nominal power under conditions representative of the future Generation IV fast reactors (sodium environment, flux, materials and temperatures). Several additional examinations of materials from Superphénix (particularly on 800 Alloy and 316L(N), not used in Phénix) have been programmed, particularly on standard objects which were not used in Phénix (materials and fabrication processes, e.g. steam generator tubes made of the alloy 800).

It is assumed that the results of the creep and aging laboratory tests can be extrapolated over time by a factor of 3 without disrupting the degradation mode. For a reactor designed to operate 60 years with an average of 90% of availability, the different material characteristics must therefore be justified for periods of at least 18 years, i.e. 160,000 hours. This requires performing ageing programmes over such periods of time, as well as very long tests under moderate loading for certain characteristics (e.g. creep). These laboratory tests are very time-consuming, which can have a negative impact on the development schedule of a reactor technology. To gain access to data at a much faster rate and to reduce certain margins on the long-term extrapolations of behaviour laws, it is possible to use materials that have been pre-aged in the facility.

During its 35 years of operation, more than 200 specific irradiation experiments were also conducted in the Phénix reactor. A lot of these experiments have not been exploited, either because this was not their initial objective or because the R&D programmes had evolved over time. Within the scope of the ASTRID qualification studies, there is now renewed interest in some of these experiments.

3. “Phénix Treasures” approach

The “Phénix Treasures” approach was launched in late 2010 at the same time as the ASTRID pre-conceptual design studies and discussions on the core qualification programme. This involved setting up several working groups. This initially entailed compiling an inventory of all the relevant objects having been irradiated in Phénix and Superphénix which could be examined as part of the ASTRID R&D programme. A list of relevant examinations was also defined. This inventory was extended to

cover all of the subjects relevant to ASTRID R&D, i.e. fuel, absorbers, structural materials, safety, instrumentation, neutronics, thermohydraulics, transmutation and reprocessing.

A specific project team has been coordinating the requirements of the CEA and its industrial partners on these subjects since early 2012. It is responsible for updating requirements, defining an interim storage scenario for objects pending examination in the experimental laboratories, and organising the conditioning of these objects together with their transport. This approach is carried out in close collaboration with the Phénix dismantling project team, the Phénix Plant operator (especially the Phénix Irradiated Elements Cell in charge of dismantling sub-assemblies and experimental capsules), the departments in charge of transport, the nuclear facilities (INB) capable of storing and examining these objects, and the relevant R&D contributors.

The various examinations will provide information to support:

- Choice of design options for the ASTRID prototype, particularly for the core and instrumentation,
- Qualification studies and R&D on materials (both in-core and out-of-core structural material and absorbers),
- R&D on transmutation,
- Improvement of simulation codes.

3.1. Identified requirements

More than 200 types of objects of different interest have been identified for all the relevant subjects, including standard and non-standard in-core and out-of-core objects. They represent almost 600 different pieces on which one or several samples must be taken. Figure 1 shows the main categories of objects that will have to be examined. Several types of objects, components and sub-components have been inventoried for each category. The examinations have been prioritised according to their relevance with respect to SFR materials and techniques, particularly in terms of the current options for the ASTRID reactor [4].

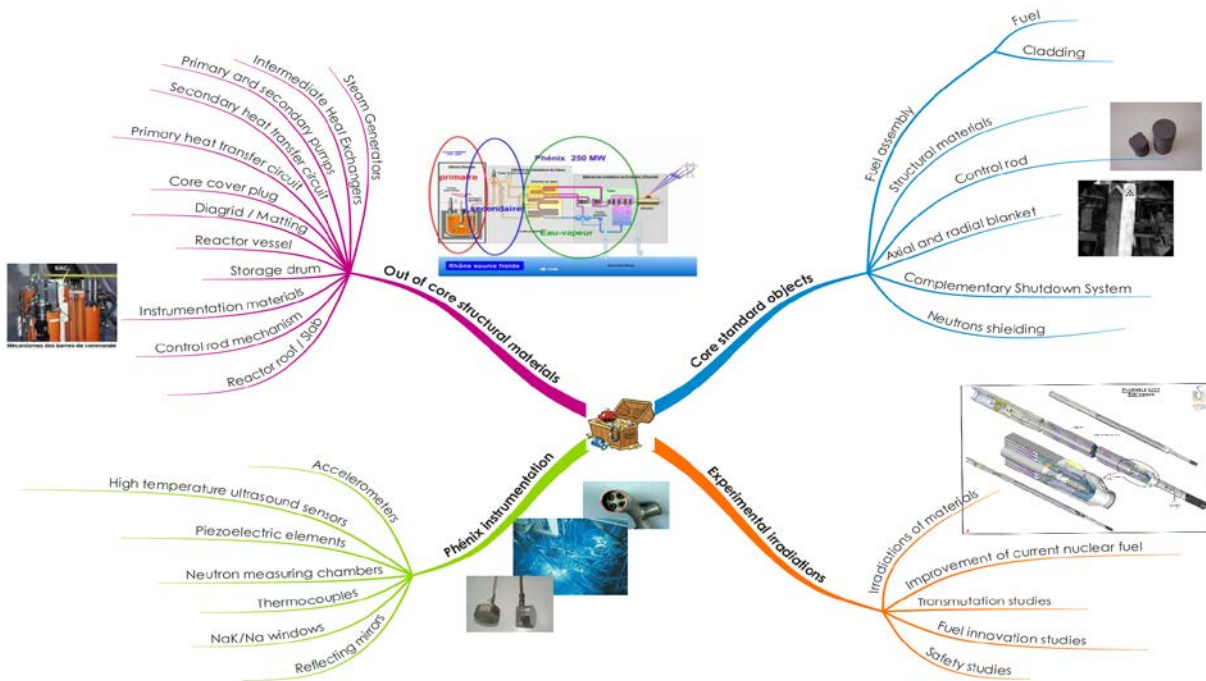


FIG. 1. Main categories of objects identified.

3.2. Project constraints

As the Phénix reactor is being dismantled, the availability of the components is closely related to:

- Reactor dismantling schedule which must integrate the sampling of the relevant components before they are treated as waste,
- Potential problem of sampling (no washing/decontamination to conserve the real condition of some samples, reaching the areas of interest, etc.),
- Dismantling rate of sub-assemblies and experimental capsules in the Phénix Irradiated Elements Cell, which determines the availability of objects, spread over several years or even decades.

Once the large components, the sub-assemblies and experimental capsules have been dismantled, the availability of objects for examination will also depend on:

- Availability of licensed nuclear facilities for interim storage and experimental laboratories,
- Availability of transport casks and authorisations.

The specific organisation in place prioritises the dismantling of objects that must first pass through the Phénix Irradiated Elements Cell, plans ahead and organises the different samples to be taken on site, and forestalls any transport and delivery issues at the nuclear facilities.

4. Exemples of valuable objects to recover

4.1. Various relevant objects to support fuel qualification

The major innovations in the previously identified fields of the ASTRID prototype must be qualified, particularly those in relation with safety and in-service operability [5]. The CEA is responsible for designing the ASTRID core. In late 2009, the CEA recommended the innovative CFV core (Figure 2) with a low void effect and the possibility of achieving a negative void coefficient, together with the potential advantage of reinforcing its natural behaviour in relation to past reactors. This design ensures a robust safety demonstration in terms of preventing and mitigating core meltdown. It was used as the reference core during the pre-conceptual design phase.

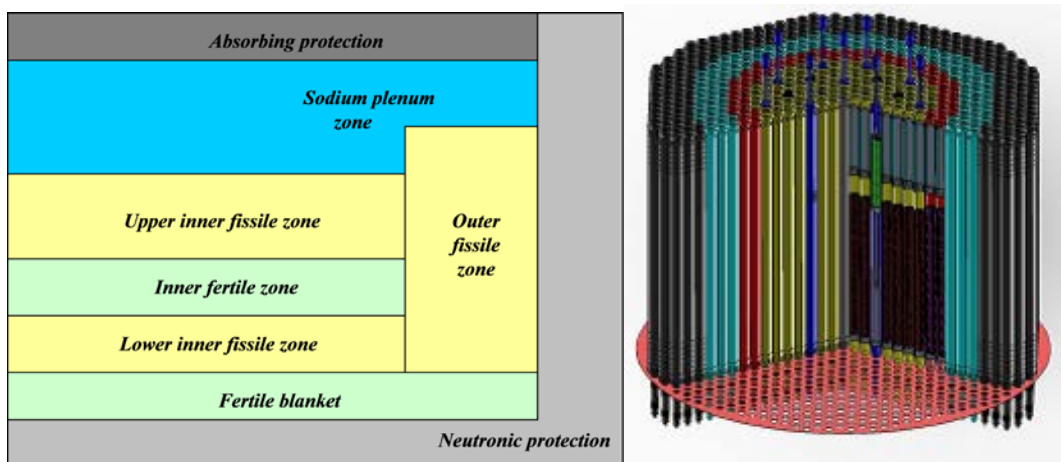


FIG. 2. CFV core.

The design is based on heterogeneous-type fuel pins forming a stack of fissile and fertile columns [6][7]. The main characteristics of the inner core fuel pins for the first loads are detailed in Table 1.

Once the design has been validated in terms of technical feasibility and performance, the qualification process for a nuclear fuel requires testing a prototype under representative conditions (representative pin or bundle geometry, representative materials, representative experimental conditions) before testing the industrial product during the last stage of the process. According to this process, the fuel designs currently under investigation must now be tested under representative conditions.

Table 1. Characteristics of inner core pins

Pins characteristics	ASTRID inner core pins	PAVIX experimental pins	ZEBRE 4 experimental pins
Pin length (mm)	~ 2000	1793	1793
Pin concept	Heterogeneous	Heterogeneous	Heterogeneous
Fertile zone height (mm)	~ 250	291/120	280/180
Fissile zone height (mm)	~ 300	360/370/50	300/200/180
Fuel type	(U,Pu)O ₂	(U,Pu)O ₂	(U,Pu)O ₂
Max. Linear power (W/cm)	300-450	270	425
Mean burn-up (GWj/t _{HM})	> 80	111	113
Clad material	15/15 Ti (AIM1)	15/15 Ti (AIM1)	316 Ti ε
Max. dose (dpa NRT)	~ 110	107	91

There are several experimental irradiations that have been completed but remain to be examined. These experiments may provide additional information for this qualification phase. For example, the PAVIX experimental irradiation in Phénix involved several sub-assemblies composed of heterogeneous fuel pins. The PAVIX fuel pins and a homogeneous pin are represented in Figure 3 and compared with a standard Phénix pin.

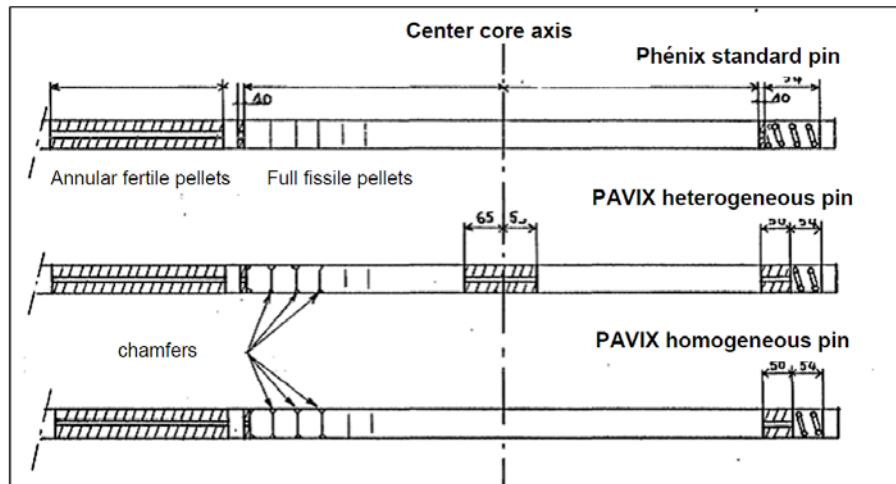


FIG. 3. PAVIX pin geometry compared to standard Phénix fuel pin.

Table 1 compares the PAVIX pins characteristics to those of reference fuel pins for the ASTRID inner core. Post-irradiation examinations (PIE) foreseen on this type of pin will provide additional information on the heterogeneous axial design and on the cladding material [8]. These PIE will complete the current database containing other experimental heterogeneous pins irradiated in Phénix. For instance, the ZEBRE 4 pins have already been examined, but under different irradiation conditions and with a less representative cladding (cold-drawn 316 Ti).

Information on creep and swelling of the reference cladding material in ASTRID will also be available and the positive impact of the fuel axial heterogeneity on the cladding internal corrosion (ROG/RIFF) should be confirmed. These examinations will complete the database for validating the GERMINAL code used for simulating the thermomechanical behaviour of the fuel. They also aim at reducing the calculation uncertainties of codes used to simulate radioelement composition variations under irradiation in the inner fertile plate. Lastly, they should make it possible to compare the dissolution behaviour of homogeneous and heterogeneous fuels.

4.2. Various relevant objects to support the qualification of absorber elements

At the end of the preliminary analyses for the ASTRID start-up core, the designers recommended to start with absorber element material and design solutions that have already been proven in Phénix. This approach must be validated and consolidated by a series of examinations on fresh and existing irradiated materials.

Available feedback is mainly based on the experimental irradiations conducted in Phénix, as well as on the control rods and the complementary shutdown systems in Phénix and Superphénix.

More specifically, this involves the experimental qualification of:

- Pin design for the complementary shutdown system in ASTRID (safety rods) [9],
- Shroud associated with the cladding of the absorber elements,
- Vent of the absorber elements,
- Behaviour of boron carbide [10].

The absorber pins for the complementary shutdown system in Phénix (Figure 4) are those which are the closest to the safety rod design.

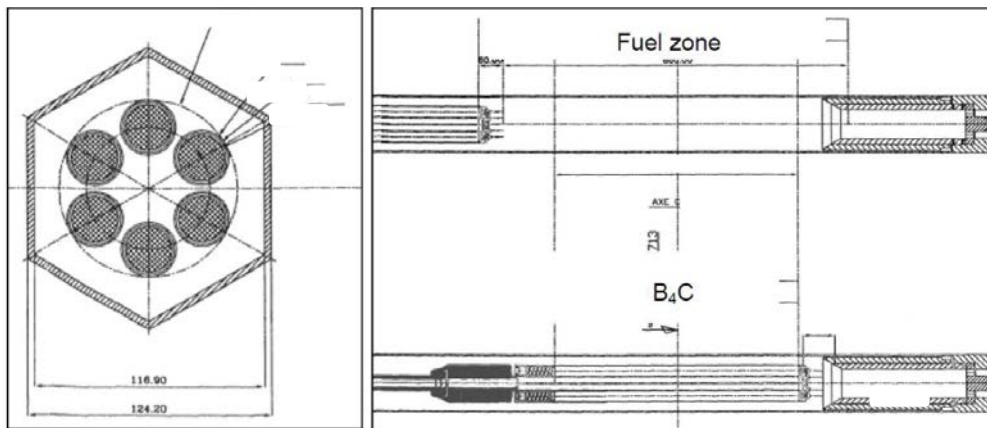


FIG. 4. Phénix complementary shutdown system.

Each pin in this sub-assembly includes a column of boron carbide made by magnesiothermic reduction and composed of a single stack. The boron carbide is enriched with boron-10. The pellets are sleeved in a austenitic steel shroud. The top vent comprises millimetric holes in the top plug. The absorber pin that underwent the most drops and the highest doses in the reactor was chosen for examination. The non-destructive post-irradiation examinations on these pins will allow to check their general behavior under irradiation and particularly that of the shroud. Destructive examinations will consolidate knowledge on the carburisation and boronisation of cladding in the presence of a shroud and on the shroud itself within the operating temperature upper range. Observation of the top of the absorber stack should provide information on the operation of the top vent which will be subjected to specific examinations. This type of shouldered column and this type of vent could be reused in the ASTRID start-up core.

4.3. *Objects for R&D and qualification of out-of-core structural materials*

The examinations on Phénix structural materials were divided into categories to meet the following technical and scientific objectives: effects of irradiation, thermal ageing, corrosion under stress, compatibility issues in sodium, resistance of coatings, excessive and progressive strain, thermal fatigue, fatigue-creep / stress relaxation cracking, and reasons for distress.

These examinations will allow significant progress in R&D thanks to the long time of operational experience which is difficult to reach at a laboratory scale. A microstructural and mechanical analysis of the 316L steam generators ties will be used to study the microstructural changes in this material over a significant period of time. There must be a very clean surface to analyse the layers of corrosion related to sodium: measuring rods are easy objects to handle and could provide information on long-term corrosion in sodium. Consequently, this type of examination should provide important experimental data required to validate models.

Other examinations will validate and improve the design rules, as well as quantifying damage assessed during the ‘lifetime extension’ project. Examination of welds subjected to stress in the intermediate heat exchangers will help to determine the conservative nature of the weld joint factors. The core cover plug in Phénix represents a unique source of information on irradiation at low doses, hardening and embrittlement by helium over 35 years. Operational feedback of coating materials used on the pumps (stellite® and colmonoy®) will influence design choices and contribute to the ASTRID qualification process. Lastly, other examinations will help to validate procedures, such as those used when performing ‘old-on-the-new’ repairs, or when washing, cleaning and putting components back into the sodium.

The following materials will be subjected to either on-site examinations or sampling for examination in a laboratory:

- Austenitic stainless steels (316 L, 304L and variants),
- Cast austenite-ferrite steels (secondary pump),
- Forged steels (secondary pump shafts),
- Steels for nuts and bolts,
- Unalloyed ferritic steels (drum and top structures of the reactor block),
- Ferritic steels with molybdenum chromium (steam generators and steam systems),
- Cobalt-based alloys, nickel-based alloys (Hard facing),
- Welding products for homogeneous, heterogeneous and bimetallic welds.

The next object to examine is a rod that has been available in a storage well since 2001. This rod served several purposes: measuring the position of the dummy diagrid support, and measuring the temperature in the hot collector and on the heater rod support. Over the entire operational period, the information covers 26 years in a sodium environment which includes 11 years' operation at full power, together with 400 start-up and shutdown transients. This rod is mainly composed of 304L stainless steel which is a relevant material for ASTRID.

Here below is the list of samplings and examinations that are either underway or pending:

- To study the long-term corrosion of 304L steel in a sodium environment, 5 pellets were cut (before decontamination) from different zones in terms of the environment, temperature, flux and sodium flow rate. Metallographic and SEM examinations will be performed to analyse the layers of corrosion and to compare the results obtained in relation to their sampling location.
- The zone corresponding to the free level of sodium is likely to reveal progressive strain which has never been evidenced before in a facility. A first series of measurements were performed in early 2012: a ruler resting on 4 generatrices of the rod where the sodium level fluctuated showed

a maximum difference in the radius of 0.5 mm (Figure 5). To confirm the existence of this strain and to quantify it, samples will be taken from this zone, more accurate strain profiles will be taken, and a strip will be sampled to take fine measurements using a micrometer.

- Lastly, fatigue-creep damage will also be investigated in this same area of fluctuation. Calculations performed in the past with this type of load and damage mode have revealed significant damage. Liquid penetration examinations will be performed to detect any surface cracks, as well as metallographic and SEM observations to visualise the cavities and eventually decide on the need and feasibility of conducting mechanical tests. Depending on the results, a broad programme of R&D and modelling could be launched to monitor this progressive strain coupled with fatigue-creep.

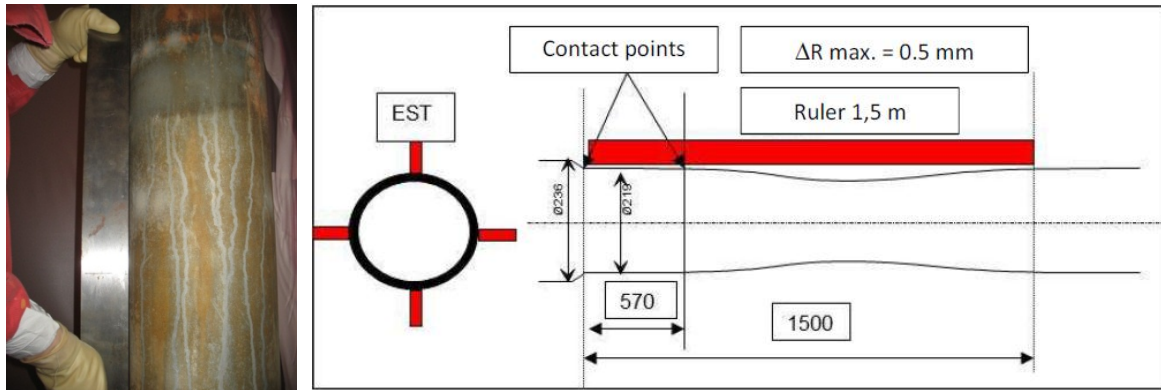


FIG. 5. Preliminary *in situ* measurements in the sodium fluctuation area of rod ML03-7.

5. Conclusion

This paper aims at giving a general overview of the approach undertaken by the CEA in collaboration with the industrial partners to fully benefit from the operational feedback of the Phénix reactor which is currently being dismantled. The very large number of examinations to be performed prevents us from providing in his paper an exhaustive list of the samples that have been identified as being relevant to the ASTRID project. This paper has therefore focused on several relevant objects and their examination which will support the ASTRID qualification process, particularly those of interest for the fuel elements, absorber elements and structural materials. The examinations will be conducted over a period of about twenty years and will be prioritised according to the availability of the components, the Phénix dismantling schedule, the qualification requirements related to the design and safety studies for the ASTRID prototype and PIE funding.

REFERENCES

- [1] P. Le Coz, E. Abonneau, J.F. Sauvage, J.M. Hamy, ASTRID Project : status and prospects, this conference.
- [2] L. Martin & al, Phénix : 35 Years Operation 1974-2009 evue Générale du Nucléaire (Janvier-Février 2009).
- [3] M. Le Flem, M. Blat-Yriex, V. Garat, J.L. Séran, French R&D materials for the core components of Sodium Fast Reactors, this conference.
- [4] F. Gauché, The French Fast Reactor Program – Innovations in support to higher standards, this conference.
- [5] F. Gauché, C. R. Physique, 13 (2012) 365-371.
- [6] E. Brunon, P. Jaekki, G. Mailhé, V. Garat, State-of-the-art of the conceptual design fuel-assembly for ASTRID, this conference.
- [7] M.C. Chenaud & al, Status of ASTRID core studies at the end of predesign phase 1, this conference.

I. Munoz-Viallard et al.

- [8] P. Gavaille, A. Courcelle, J.L. Séran, M. Le Flem, X. Averty, B. Bourdilliau, O. Provitina, Mechanical properties of Cladding and Wrapper Materials for ASTRID Fast-Reactor Project, this conference.
- [9] I. Guénot-Delahaie, D. Lorenzo, B. Valentin, J.-M. Esclaine, T. Helfer, State-of-the-art of the conceptual designs of control and shutdown rods for ASTRID this proceeding.
- [10] D. Gosset, J.M. Esclaine, A. Michaux, Neutron absorber materials in fast reactors :behavior under irradiation and perspectives, this conference.

Experimental and Theoretical Investigations of Ferro Boron as In-vessel Shield Material in FBRs

R. S. Keshavamurthy, S. Raju, S. Anthonysamy, S. Murugan, D. Sunil Kumar, V. Rajan Babu, S. C. Ravi Chandar, C. N. Venkiteswaran, S. C. Chetal

Indira Gandhi Centre for Atomic Research, Kalpakkam, 603102, Tamil Nadu, India

Abstract: The optimal design of shield materials with regard to their functional efficacy, volume, indigenous development and testing capability, besides overall cost economy is one of the major objectives of future FBRs (Fast Breeder Reactors) of India. In this connection, an alloy of boron and iron with tightly controlled amounts of impurities, herein referred to as Ferroboration (Fe-B), has been successfully developed as a potential alternate shield material for possible use in Commercial Fast Breeder Reactor (CFBR) planned in India. This paper summarises the important scientific, technological and testing aspects of the development of Fe-B as a viable shielding candidate. The summary includes: (a) Results of neutron attenuation experiments conducted in KAMINI reactor at IGCAR, (b) Neutron transport calculations and secondary sodium activation studies carried out with Fe-B as shield material in CFBR, (c) Results of high temperature clad and sodium compatibility studies, (d) Design and fabrication experience of Fe-B irradiation capsules. It is found that a configuration of 8 rows of Fe-B shields is sufficient to keep the secondary sodium activity to within the permissible limit and which contributes in a reduction of 145 shield assemblies. The reduction is an important incentive for reducing the reactor vessel size. Out-of-pile characterization of high temperature metallurgical compatibility with SS 304L clad has revealed that up to 1000 °C and for time period of 10,000 hours, the clad-attack depth did not exceed 250 microns. It is also found that Fe-B has good compatibility with liquid sodium for well over 5000 h, if oxygen concentration is kept below about 50 mass ppm. These encouraging out-of-pile results have further prompted the testing of Fe-B for obtaining useful in-pile experimental data, by the way of fabricating a suitable irradiation test capsule, which has currently undergone fast flux irradiation in Fast Breeder Test Reactor.

1. INTRODUCTION

It is well known that the leaking neutrons from core and blankets have energies that peak around 10-100 keV, and for this reason, the fuel and blankets are surrounded by a large quantity of shield materials, to the extent of 60-70 % of the core volume in fast reactors. In PFBR, there are 6 rows of stainless steel (SS) and 3 rows of B₄C shields consisting altogether in 609 SS+417 B₄C assemblies. In pool type of fast reactors, intermediate heat exchangers (IHXs), in which the primary sodium exchanges heat with the secondary sodium and pumps, are immersed in the pool of liquid sodium contained in the reactor vessel itself. Therefore, sodium becomes radioactive and as a result, the secondary sodium passing through IHXs also gets activated. It is obvious that without adequate shielding around the core, this activation can lead to an unacceptable large dose in the steam generator building. Therefore fast reactors are generally characterized by large in-vessel shields, which incidentally contributes to the reactor vessel size. Stainless steel was used as shielding material in a variety of fast reactors, such as RAPSODIE, JOYO, FBTR, BOR-60, FFTF and FERMI [1]. However, EBR-II used graphite and borated graphite, while SS/borated graphite was used in DFR. In PHENIX [2] Graphite/SS was used in the radial direction. In addition, B₄C was added in the axial direction because of the superior neutron absorption properties of boron. In SUPER PHENIX [3] too, B₄C shielding was provided in the axial direction. B₄C was also considered for radial shielding in the reactors SPX2, EFR and DFBR. The prototype fast breeder reactor (PFBR), presently under construction in India has been designed with 3 outermost rows of B₄C, in addition to 6 rows of SS. This is taken as the reference point, for evaluating alternate shielding options, the purpose of which is to realise adequate shielding capacity with compatible cheaper materials having lower neutron absorber atom densities (B¹⁰ in this case). It is clear that such an alternative, if realised, can lead to potential cost saving both due to a reduction in vessel size and in the number of shield assemblies.

It is with this design imperative, several probable candidates were considered to begin with and, subsequently, based on the neutron attenuation experiments in the KAMINI reactor, supplemented by the detailed reactor physics analyses and transport calculations, the choice of Fe-B containing about 17 wt.% of boron has been arrived at. A preliminary literature survey indicated that there is only limited information available from the open literature with regard to qualifying Fe-B as an alternate shield material. It soon emerged that some original science, technology and fabrication initiatives have to be made on an indigenous basis, if suitable grade of Fe-B satisfying stringent requirements with regard to chemical composition, high temperature clad and sodium compatibility for longer durations etc., were to be produced. Further, it is also mandatory to ensure that good out of pile compatibility is matched with the actual in reactor experience, under an irradiation test in FBTR. This naturally led to the fabrication of a Fe-B irradiation test capsule, confirming the required safety criteria of irradiation testing qualification. In what follows, a comprehensive description of IGCAR's experience in developing Fe-B is presented in various sections. For more elaborate details on physics and metallurgical aspects, attention is drawn to our published research reports [4-7].

2. NEUTRON SHIELDING PROPERTIES OF FERROBORON

2.1. General details

Commercial grade Ferro boron with density around 6.7 g/cc has been traditionally used as an alloy addition in steel industry. This Fe-B contains about 15-18 wt% boron, besides a lot of impurities like carbon, oxygen, silicon, phosphorous etc. (Table 1). The commercial material is generally available in lumps, granules and coarse powder forms with a price that is only about 10 % of boron carbide powder. However, it must be added that for nuclear Fe-B grades, there should be a tight control over free oxygen content (less than 50 ppm by mass). Further, the presence of unreacted 'boron' as such should be avoided, since it aggravates the SS clad attack at high temperatures (unbound boron diffuses fast into SS clad at temperatures exceeding 650 °C). The presence of carbon to the extent of 0.2 wt.% is not a serious issue in the current application, as SS 304L clad carburisation at typical operating temperatures is not a restricting factor, especially with twin type of containers planned for PFBR shield assemblies. On the other hand, boronization of SS clad needs to be investigated, if ferroboron with significant free boron content has to be used.

Table 1 Typical elemental composition of Ferro boron

Element	Boron	Silicon	Aluminium	Carbon	Sulphur	Phosphorous	Oxygen	Iron
Typical Composition (wt. %)	15-18	0.89	0.17	0.29	0.006	0.005	0.1	Balance

2.2. Attenuation experiments in KAMINI

Experiments were conducted in the southern end neutron beam (slit source of dimension 220mm x 7 mm) of KAMINI reactor with the ferro boron having a bulk density of ~ 4 g/cm³ with 11.8% and 15.2% natural boron. For comparison, experiments were also carried out with a natural boron carbide powder of density 2.4 g/cm³[6]. Shield material filled in rectangular aluminum boxes (of two different sizes 300mm x 150mm x50 mm and 300mm x 150mm x 60mm) was placed in front of the neutron beam. Provision of foil holders was made to keep the activation foils in front of the beam as well as in between aluminum boxes containing shield material. The foils were so selected that their combined sensitivities cover the energy spectrum from epithermal to fast neutron region.

The measured attenuation of thermal and epithermal fluxes are represented by reaction rates, ¹⁹⁷Au(n, γ) and ⁵⁵Mn(n, γ). It should be noted that ferro boron has 11.8 and 15.2% boron as compared to 78% in B₄C. Measured attenuation of fast flux is represented by threshold reaction rates, ¹¹⁵In(n, n') and ¹⁰⁵Rh(n,n'). With regard to the reaction rates representing fast fluxes, the thicknesses of B₄C and

Fe-B to achieve the same level of attenuation are approximately the same. The measured attenuation characteristics are illustrated in Figure 1.

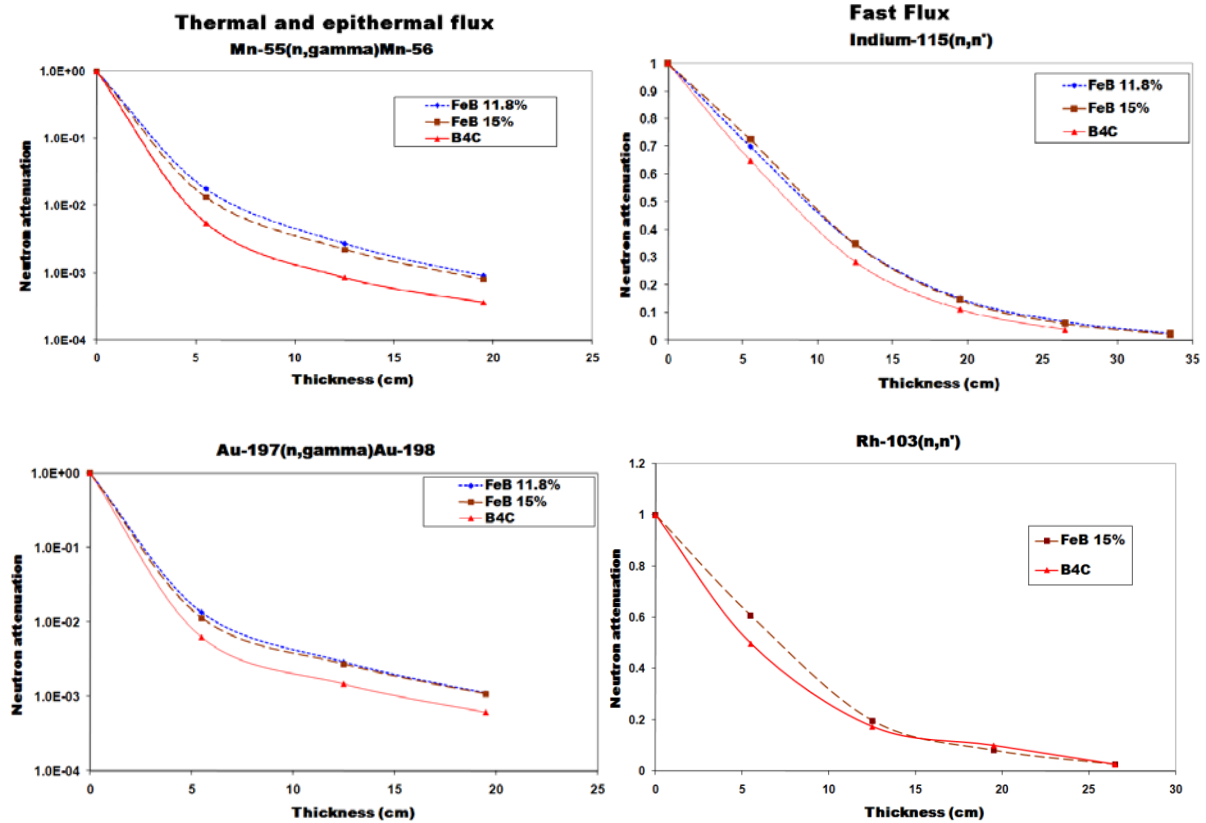


Fig.1 Measured neutron attenuation characteristics of Ferro boron as compared to Boron carbide.

2.3. Transport calculations using Ferroboron invessel shields

In CFBR, only 8 rows of radial ferro boron shield assemblies are considered in place of 6 SS+3 B₄C shield assemblies in PFBR [8]. The R-Z configuration with Fe-B shields is shown in Figure 2. Configuration used for calculations included full sodium and surrounding concrete. The cross section set IGC-S3 [9,10,11] is used in the calculations. The set is a 217- group coupled library based on ENDF/B-VI. It contains neutron cross section data in VITAMIN-J 175 group structure and 42-group gamma interaction data upto Legendre order 5. Calculations were performed by the 2 dimensional transport code DORT [12] and IGC-S3 cross section set.

Due to the elimination of one shield row with the use of Fe-B, there is a possibility of movement of IHX towards the core centre and hence its effects have been studied. Secondary sodium activity is the same as the reference value when IHX is moved by 70 mm towards the core. This is assuming that the shielding around IHX in CFBR is same as in PFBR. IHX can be moved further towards the core by providing additional shielding around IHX. Neutron transport calculations for optimization of the IHX shields to move IHX further towards the core have shown that the IHX can be moved by 18 cm with 8 mm boron carbide shielding around IHX. The neutron flux at the detector location remains the same as in PFBR. The use of Fe-B results in substantial cost and weight reduction by about 75 tonnes.

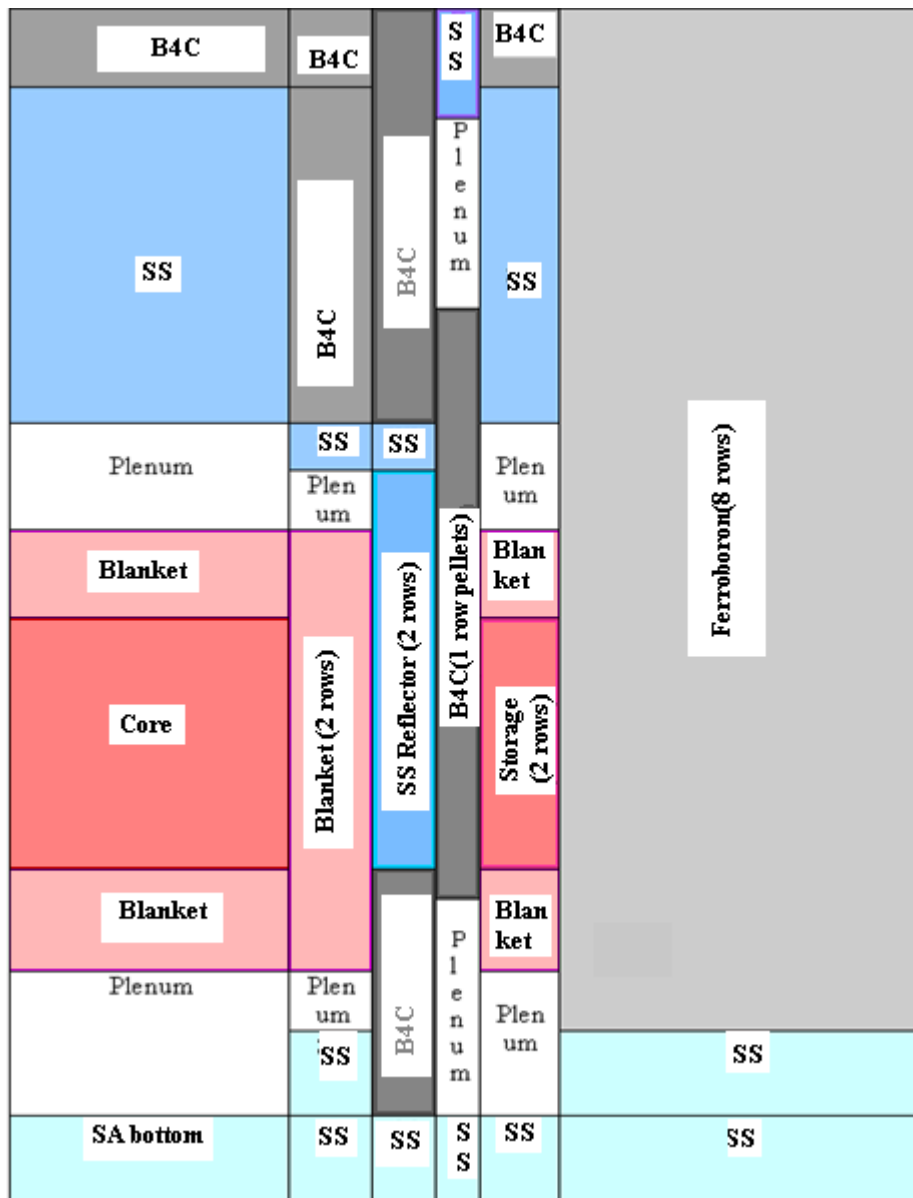


Fig. 2. R-Z model of CFBR with Fe-B shields

3. METALLURGICAL INVESTIGATIONS

Insufficient information is available in the open literature with regard to qualifying the metallurgical compatibility of Fe-B with austenitic stainless steels at high temperatures. In view of this a comprehensive metallurgical characterisation of the high temperature stability of Fe-B has been undertaken and in the following section a brief account of the major findings is given.

3.1. X-ray studies

The powder x-ray diffraction profile of Ferro boron [7] is presented in Fig. 3. As can be seen, the Fe-B contains a mixture of three intermetallic compounds, namely FeB, Fe₂B and Fe₃(B,C). It is noteworthy that no free iron or boron are highlighted; in other words the entire boron should be present in the combined form. The orthorhombic FeB constitutes the major phase, the other two being present in smaller volume fractions, especially the Fe₃(B,C) - boro cementite phase. This latter phase

is present due to the presence of carbon (0.3 wt.%), which together with boron forms the cementite phase [13]. According to the current assessed Fe-B binary phase diagram [14], the alloy with about 15 to 17 wt.% B should contain some amount of Fe_2B , the lower boride phase. However, this phase dissolves back into the FeB phase at high temperatures. In a similar manner, the $\text{Fe}_3(\text{B,C})$ boro cementite phase is also unstable at high temperatures, and it dissolves into the FeB and Fe_2B at high temperatures. Presently, reliable information on phase diagram features of boron rich Fe-B-C ternary is rather limited and does not cover the compositional range of our interest. Hence a detailed attempt has also been made to gather these useful basic data. This is briefly reported below.

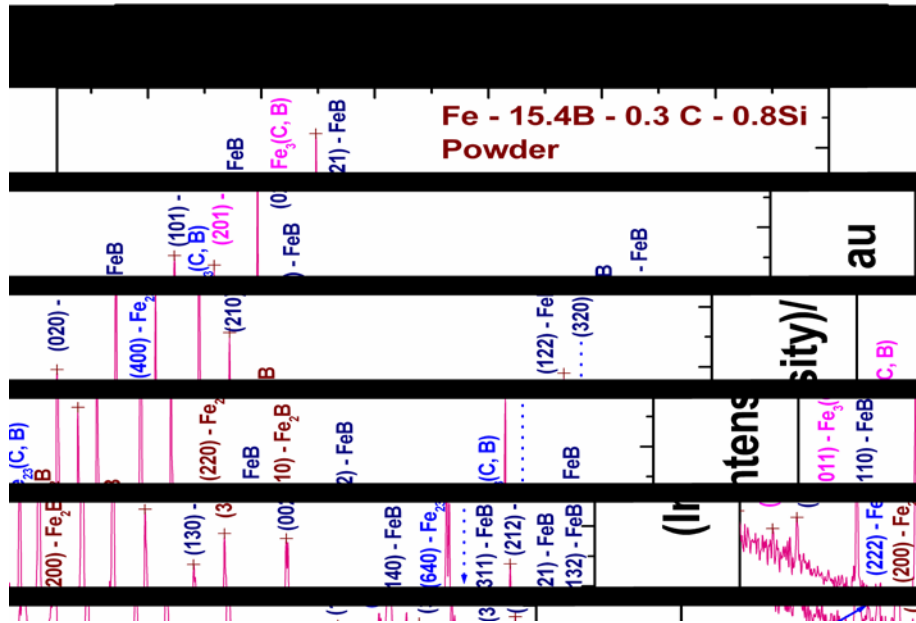


Fig.3. X-ray diffraction profile of Ferro boron

3.2. Thermal properties

The thermal stability of Fe-B powder was investigated [5] using differential thermal analysis (DTA) carried out in flowing pure argon (Iolar II grade) atmosphere. The corresponding DTA thermogram obtained during both heating and cooling cycle is shown in Figure 4 and the following major results obtained:

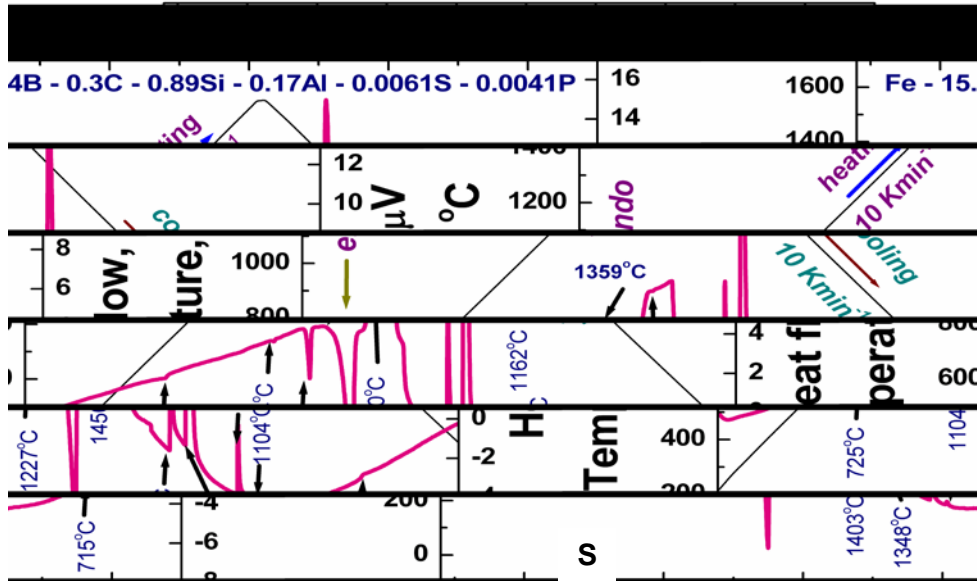


Fig. 4. DTA thermogram of Ferro boron powder recorded during heating and cooling.

- (i) the Curie temperature (T_c) was found to be 725 °C.
- (ii) The dissolution of boro cementite $Fe_3(B,C)$ occurs at about 1104 °C.
- (iii) The dissolution of Fe_2B in the γ -austenite phase was found to occur at 1227 °C.
- (iv) Finally, the melting of Fe-B begins at 1359 °C. It is found to be almost complete at 1450 °C. This later temperature may be taken as the melting point or the liquidus point of Ferro boron.

An estimate of the latent heat associated with the melting was made by making a comparison experiment under identical experimental conditions with pure iron and was found to be 356 kJ/kg. Fe-B releases a large quantity of heat of solidification as compared to other boron compounds.

3.3. Metallographic characterization

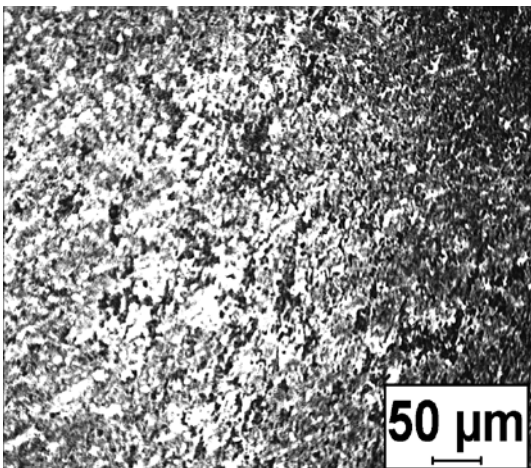


Fig. 5 (a). Microstructure of fine Ferro boron powder

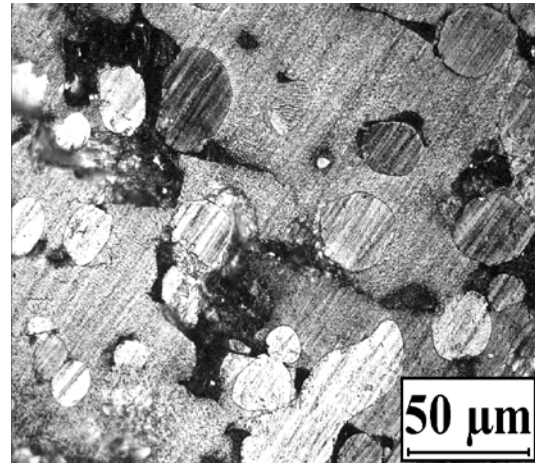


Fig. 5(b). Microstructure of bulk Ferro boron block

The optical and scanning electron microscopy investigations of Fe-B have also been carried out to support the results of thermal stability. The relevant results are shown in Fig. 5, and more details on metallographic constitution of Fe-B can be obtained from the published literature [5].

3.4. High temperature compatibility studies

The estimated life time of the shielding subassembly is about 60 years with the anticipated service temperature of 550°C. Accelerated tests for shorter time spans at successively higher

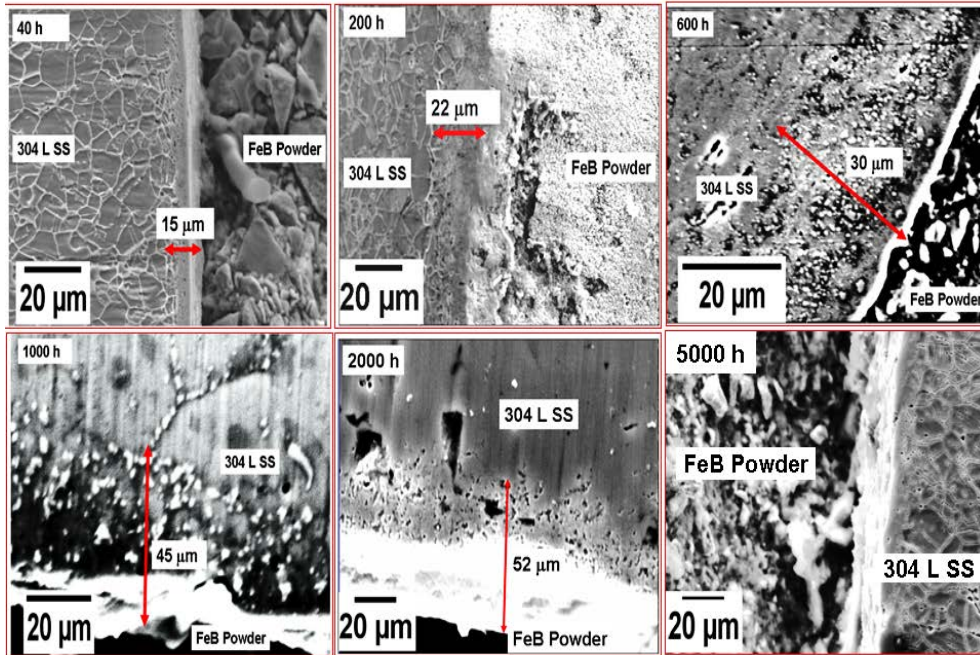


Fig.6 Clad –Ferroboron interaction at elevated temperature of 700 °C

temperatures, namely 550 °C, 600 °C, 700°C and 800°C, have been conducted for long time durations of up to 10000 h, for investigating the high temperature clad integrity in contact with Fe-B shield [7]. The results of metallographic characterization of Fe-B/304L reaction couples at 700 °C are presented in Figure 6. These investigations revealed that the loss of clad thickness due to boron diffusion induced attack is rather insignificant, as compared to clad thickness of 2150 microns. There is also an 5000 micron thick outer clad provided acting as an additional barrier. The estimated upper bound for clad attack thickness is about 250 microns over a period of 60 years at the design service temperature of 550°C. This is only about 12% of the primary clad thickness and 3.4% of total clad wall thickness and further, no loss of ductility of clad or cracking has been found at the end accelerated testing.

3.5. Chemical compatibility

Extensive chemical compatibility experiments were carried out by equilibrating Fe-B with SS304L in presence of sodium at various temperatures. SS 304L samples used for the chemical compatibility studies of ferroboron in sodium environment were analysed using SEM and EDX after several equilibration in sodium at 973 K for 1000, 2000, 3000, 4000 and 5000 h. Microhardness of the above specimens was also measured using a Vickers microhardness tester. It was observed that the reaction layer is clearly delineated (Figure 7). It is found that the zone of chemical interaction increased with time. The thickness of Ni depleted layer as a result of sodium corrosion also increases with time of exposure in sodium.

The clad thinning is seen to be around 250 microns at this elevated temperature of 973 K over 5000 h. It has been established that at the normal service temperatures, the general and in-sodium compatibility is good and do not pose constraints for the use of Fe-B up to about 1000 K. It must also be mentioned here that sodium is extremely unlikely to come into contact with the material as it is provided with double containment.

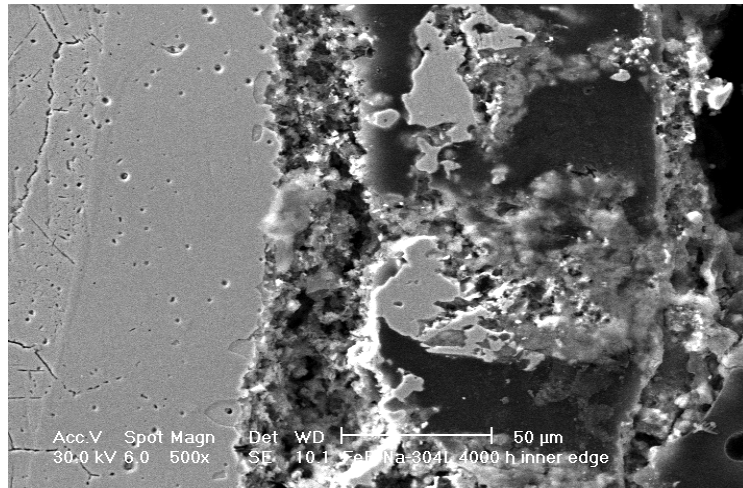


Fig.7. SEM image of clad interaction with hot sodium and Fe-B clearly delineated on the right.

4. FERROBORON IRRADIATION CAPSULES FABRICATION AND TESTING IN FBTR

In view of the good compatibility of Fe-B with SS clad and sodium in out of pile tests, design and fabrication of Fe-B irradiation test capsules was planned. Two types of Fe-B capsules were developed: one for conducting an irradiation test in FBTR and the other one being a 1:1 scale version of actual PFBR, as part of technology development.

4.1. Irradiation capsule

The irradiation test capsule (Fig. 8a) consists of an inner capsule with an outer diameter, OD, of 14 mm and an inner diameter, ID, of 12 mm containing fully vibropacked Fe-B granules under argon atmosphere in five separate partitions.

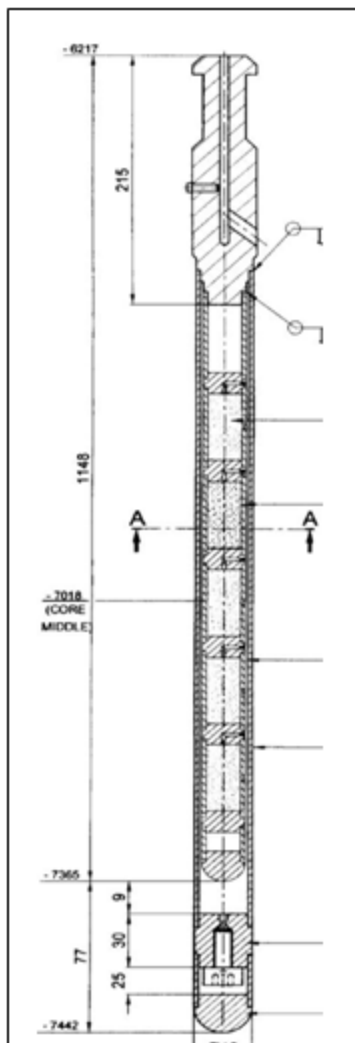


Fig.8(a) Capsule fabricated for Irradiation test in FBTR



Fig.8(b) Device to fill helium filling in secondary containment

There is an outer tube (OD: 16 mm and ID: 14.5 mm) serving as secondary containment for preventing the release of Fe-B powder into hot sodium, in the unlikely event of breach of the inner capsule. The central three partitions of irradiation capsule are in line with the fuel column of the driver fuel pins during irradiation in FBTR. The fabrication involved intricate thin section welds under argon glove box atmosphere, and suitable weld qualification procedures have been devised for ensuring proper quality of welds. The welding of the secondary containment was done at site in IGCAR followed by due quality

inspection protocols. High purity helium was filled in the annular gap between the inner capsule and the outer containment tube for ensuring good heat transfer characteristics.

For filling helium, an innovative helium filling arrangement was designed and fabricated. An intermediate plug was welded to the outer containment tube with provision to evacuate and fill the annular gap with helium and close the filling path. Leak-tight ring type containment with separate connections to vacuum pump and the helium gas cylinder was designed and fabricated to facilitate evacuation and gas filling operations (Fig. 8b). Neutron radiography of the capsule was carried out to get pre-irradiation data and as part of the qualification (Fig. 8c).

4.2. Irradiation in FBTR

The in-vessel shield in future FBRs will sustain 60 years of irradiation with an assumed load factor of 75 %. To simulate this, it was found necessary to load the capsule in the 4th ring location of FBTR and irradiate it for 45 effective full power days at a flux level of 1.0×10^{15} n/cm²/s. As part of pre-irradiation data, neutron radiography of the capsule was carried out using KAMINI neutron source reactor to measure the length of the Fe-B column for comparing the same with post irradiation data to evaluate the consolidation of stack if any. Irradiation of the capsule has been successfully completed. Post irradiation examination will be taken up shortly after discharging the capsule from the reactor.



Fig 8(c) Neutron radiograph of Fe-B capsule before irradiation

5. Conclusions

- I. Neutron attenuation characteristics of Fe-B has been investigated both theoretically and experimentally and Fe-B has been found to be favourable for use in FBRs.
- II. Its use will result in significant savings in cost, without impairing shielding capabilities.
- III. Extensive and in-depth out of pile characterization thermophysical properties and high temperature metallurgical compatibility tests with SS 304L clad were carried out. These, as well as studies of interaction of sodium and Fe-B together on clad at high temperature, show excellent compatibility with the clad.
- IV. The design of two types of Fe-B capsules was done, one type for conducting an irradiation test in FBTR simulating 60 years of neutron fluence in CFBR, and the other one consisting in a 1:1 scale FBR capsule as part of technology development. Fabrication of the capsules has been successfully carried out. The capsule was loaded in FBTR and the capsule has seen the intended 45 days of irradiation.
- V. Post irradiation examination will be carried out to look for any possible effect due to irradiation.

ACKNOWLEDGEMENTS

The authors sincerely thank the Minex Metallurgical Company for providing the Fe-B material. Vijayan Varier, D V Subramanian, Adish Haridas, Rajeev Ranjan Prasad, Arun Kumar Rai, K.Chandran, K. A. Gopal, Ananda Raj, V. Ganesan, Alok Saxena, R. Sudha and P. R. Reshmi are acknowledged for their help in the various stages of Fe-B development.

REFERENCES

- [1] INTERNATIONAL ATOMIC ENERGY AGENCY, Fast Reactor Database International Atomic Energy Agency, Vienna (Austria). Fast Reactor and Accelerator Driven System Knowledge Base. TECDOC-866, IAEA (1996).
- [2] CABRILLAT, J.C., CROUZET, J., MISRAKIS, J., SALVATORES, M., Shielding design methods for LMFBR validation on the PHENIX reactor. In: Proc. of the 6th Int. Conf. on Radiation Shielding. Japan, Vol. I (1983).
- [3] GOURDON, J., MESNAGE, B., VOITELLIER, J.,L., SUESCUN, M., An Overview of Superphenix Commissioning Tests. Nuclear Science and Engineering. 106, 1-10 (1990).
- [4] SUNIL KUMAR, D., KESHAVAMURTHY, R.S., MOHANAKRISHAN, P., CHETAL,S.C., Ferro-Boron As In-Core Shield Material in Fast Breeder Reactors: A Case Study, Nuclear Engineering Design, 240,10 (2972-2980).
- [5] ARUN KUMAR RAI, S. RAJU, B. JEYA GANESH, G. PANNEERSELVAM, M. VIJAYALAKSHMI, . T, JAYAKUMAR AND BALDEV RAJ, ,Investigation of high temperature phase stability, thermal properties and evaluation of metallurgical compatibility with 304L stainless steel, of indigenously developed ferrobore alternate shielding material for fast reactor applications, Nuclear Engineering and Design, 241, 2087-2801 (2011).
- [6] R.S. KESHAVAMURTHY, D. VENKATA SUBRAMANIAN, RAJEEV RANJAN PRASAD, ADISH HARIDAS, P. MOHANAKRISHNAN, AND S.C. CHETAL, Experimental Measurements of Neutron Attenuation in the Advanced Shield Material Ferro Boron in KAMINI Reactor, Energy Procedia 7, 273-278 (2011).
- [7] S. RAJU, ARUN KUMAR RAI, B. JEYAGANESH, M. VIJAYALAKSHMI, T. JAYAKUMAR AND BALDEV RAJ, Characterisation of High Temperature Phase Stability and Evaluation of Metallurgical Compatibility with SS 304L, of Indigenously Developed Alternate Shielding Material Ferro- Boron for Fast Reactor Applications, Conf. Proceedings on Asian Nuclear Prospects, Energy Procedia 7, 164-172 (2011).
- [8] SUNIL KUMAR, D., KESHAVAMURTHY, R.S., MOHANAKRISHAN, P., CHETAL,S.C., Axial and radial shield optimization for future pool type FBRs with Ferro-boron, IAEA Technical Meeting on Fast Reactor Physics and Technology, Kalpakkam, India (2011).
- [9] DEVAN, K., PANDIKUMAR, G., GOPALAKRISHNAN, V., MOHANAKRISHNAN, P., IGC-S3: A 217 Group (^{175}n , $^{42}\gamma$) coupled cross section set from ENDF/B-VI. Report RPD/NDS/99, Indira Gandhi Centre for Atomic Research, Kalpakkam, India (2002).
- [10] DEVAN, K., PANDIKUMAR, G., GOPALAKRISHNAN, V., MOHANAKRISHNAN, P., Effects of cross sections and quadrature orders on neutron fluxes and on secondary ^{24}Na activation rate of pool type 500 MWe FBR. Annals of Nuclear Energy. 30, 1181-1197 (2003).
- [11] SUNIL KUMAR, D., SUJOY SEN, KESHAVAMURTHY, R.S., MOHANAKRISHANAN, P., Comparison of FBTR hybrid Core and Mark-II (Carbide) core design and neutron irradiation in invessel shields. Annals of Nuclear Energy. 35, 937-946 (2008).
- [12] RHOADS, W.A., AND CHILDS, R.L., The DORT- Two Dimensional Discrete Ordinates Transport Code. Nucl. Sci. Engg. 99, 88 (1988).
- [13] OHTANI, H., HASEBE, M., ISHIDA, K., NISHIZAWA, T., Calculation of Fe-C-B ternary phase Diagram, Trans. ISIJ, Vol.. 28, 1043-1050 (1998).
- [14] OKAMOTO, H., Fe-B Phase Diagram- Supplementary literature Review, Journal of Phase Equilibria and Diffusion, 25, 297 (2004).

Fabrication and Evaluation of SFR Cladding Tubes

S.H. Kim, J.H. Baek, J.H. Kim, C.B. Lee

Korea Atomic Energy Research Institute, Daejeon, Republic of Korea

Abstract. Ferritic/martensitic steels are being considered as cladding materials for a Korean prototype SFR. Thus, thin wall tubes with FM steels for SFR cladding tubes were fabricated and evaluated. The cladding tubes were fabricated by drawing with intermediate heat treatments. The final heat treatment of the tubes implied normalizing at 1080°C and tempering at 750°C. The outer diameter and thickness of the cladding tubes were 7.4mm and 0.56mm, respectively. The burst test temperatures ranged from room temperature to 658°C. The ultimate hoop stress of the HT9 cladding tube at room temperature and 658°C was 1135MPa and 488MPa, respectively. The tensile tests were also carried out from room temperature to 700°C. The yield and ultimate tensile strength of the HT9 cladding tube at room temperature were 581MPa and 805MPa, respectively. Creep rupture tests of the cladding tubes were performed at 650°C. The HT9 cladding tube had a creep rupture strength consistent with literature.

1. Introduction

The environment of a SFR (sodium fast reactor) core is more severe than that of a PWR (pressurized water reactor) core. The peak cladding temperature is designed to be about 650°C and the neutron fluence should reach 200dpa. Thus, ferritic/martensitic (FM) steels have been receiving attention for application in SFR fuel cladding because of behavior under irradiation (e.g. excellent irradiation swelling resistance) [1][2][3][4][5][6]. Until now many out-of-pile and in-pile tests have been performed to apply FM steels (HT9 and PNC-FMS) to SFR cladding tubes. HT9 steels were irradiated in FFTF up to 200dpa, and PNC-FMS steels have been irradiated in JOYO. Among the FM steels, HT9 steel was selected as a candidate cladding material in Korea.

To achieve fuel cladding tube manufacturing technology in order to be consistent with the determined schedule in developing SFR fuel, KAERI has launched investigations to develop fuel cladding tubes in cooperation with a domestic steelmaking company. After the fabrication of medium-sized 1.0 ton of HT9 ingot, followed by multiple processes of hot and cold working, preliminary samples of HT9 seamless cladding tubes were fabricated. The objective in this study is to assess the mechanical properties of the HT9 cladding tubes as a part of the qualification process. An axial tension tests, a biaxial burst tests, and a pressurized creep tests of the cladding tubes were carried out to evaluate the mechanical properties of HT9 cladding tubes.

2. Experimental procedure

2.1. Fabrication of cladding tubes

Table 1 showd the chemical composition of the HT9 and Gr.92 cladding tubes. HT9 steel was manufactured as a 1.0 ton scale ingot using a vacuum induction melting method. The ingot was converted into the mother tube having a 19.05mm outer diameter, 1.24mm thickness, and 6m length by hot extrusion, cold pilgering, and a subsequent heat treatments. Manufactured mother tubes were

turned into the final form of seamless tubes having 7.4mm outer diameter, 0.56mm thickness, and 3m length by multiple processes of cold drawing and heat treatments. The cladding tube was finally heat-treated at 1038°C for 5 minutes as normalizing and 760°C for 30 minutes as tempering. A Gr.92 cladding tube as a reference was also fabricated and evaluated.

Table 1. Chemical composition of cladding tubes

Element	C	Mn	Si	Cr	Ni	Mo	W	Al	Nb	V	Cu	P	S
HT9	0.18	0.59	0.25	11.99	0.59	1.00	0.54	0.01	0.008	0.30	-	0.005	0.003
Gr.92	0.09	0.41	0.21	8.69	0.13	0.38	1.62	0.06	0.066	0.184	0.10	0.020	0.010

2.2. Microstructure observation and mechanical tests

The precipitates taken from the carbon extraction replicas were examined by a transmission electron microscope (TEM) with an energy dispersive spectroscope (EDS). The carbon extraction replicas were prepared by means of mechanical polishing, etching with a mixed solution (93 vol.% water, 5 vol.% nitric acid and 2 vol.% fluoric acid), carbon coating, and removing the replicas by electrochemical etching with a mixed solution (90 vol.% methanol and 10 vol.% hydrochloric acid).

A tension test was carried out in accordance with the ASTM E8 specification. The cladding was cut into a 200mm long sample and both ends were stuck by a mandrel to have a gauge length of 52~55mm. The strain rate was 0.005/min and tests were performed from room temperature to 700°C. The biaxial burst test was performed in accordance with the ASTM E764, E453 and B353 specifications. The pressure of argon gas was multiplied by 20 using a high-pressure compressor and the pressurization rate was controlled by a servo-type motor. The rate of pressurization was maintained to 14MPa/min during the test, and the test was conducted from room temperature to 658°C. A pressurized creep test of the HT9 tube was also performed. The cladding tube was sealed by welding and argon gas was injected to the desired pressure after the tube reached 650°C. The hoop stress was controlled in the range of 120 to 216MPa and its corresponding rupture time was measured.

3. Results and discussion

3.1. Microstructure of cladding tube

Figure 1 shows the microstructure of the HT9 cladding tube. The HT9 cladding tube exhibited a dual phase structure. The main structure was tempered martensite, and approximately 2% of the delta ferrite was contained inside the matrix. The Cr equivalent of HT9 steel was so high that the delta ferrite was formed after the final heat treatment. On the contrary, Cr equivalent of Gr.92 steel was not high, and thus the Gr.92 cladding tube exhibited a typical tempered martensite structure. Cr-rich $M_{23}C_6$ and Nb- and V-rich MX-type precipitates were observed in the HT9 steel. The Cr-rich $M_{23}C_6$ precipitates were the main particles. The $M_{23}C_6$ carbides were mainly detected in the prior austenite grain boundaries, but occasionally in the lath and lath boundaries. The MX precipitates were usually found in the lath and lath boundaries.

The outer diameter of the HT9 cladding tube was 7.427 ± 0.05 mm, and the thickness was 0.549mm. The inner wall of the HT9 cladding tube was observed by optical microscopy. No defect was detected. The surface roughness of outer and inner surfaces was 0.441 and 0.111 micrometer, respectively.

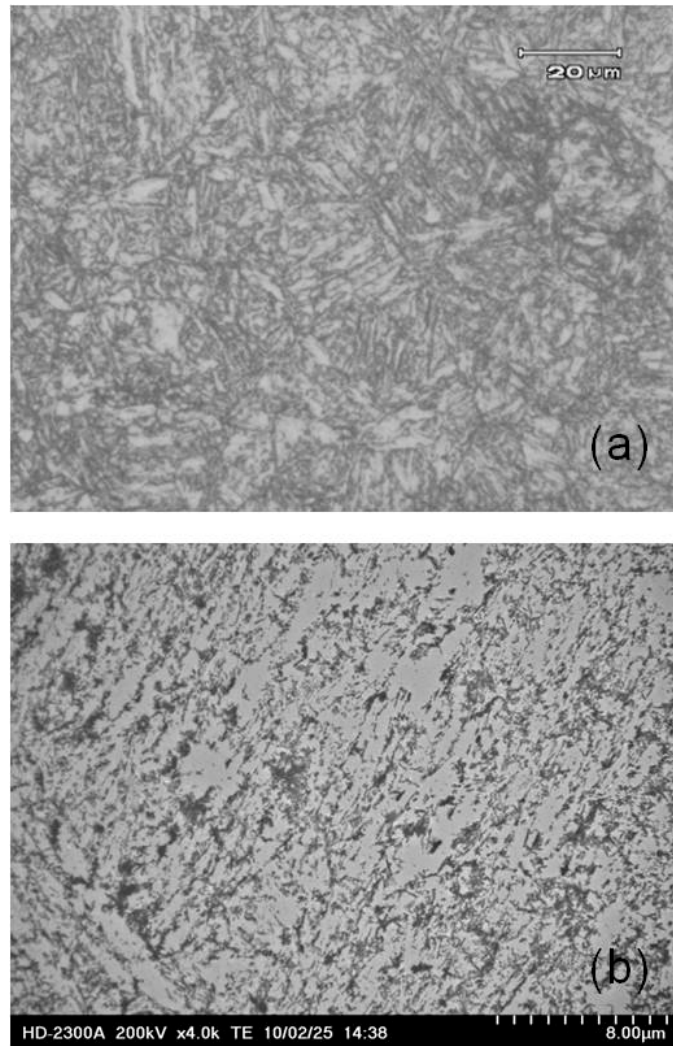


FIG. 1. Microstructures of the HT9 cladding (a) Optical microscope, (b) Scanning transmission electron microscopy of the carbon extracted replica.

3.2. Tensile properties of cladding tube

Figure 2 shows the stress-strain curve of the HT9 cladding tube. It reveals that plastic strain characterized by the work hardening mechanism governed the entire strain below 500°C. Above 550°C, softening caused by the void nucleation and associated to the coarsening process dominated the entire strain in the HT9 cladding, and resulted in a decrease of stress. Figure 3 and 4 show the uniaxial tensile properties of the HT9 and Gr.92 cladding with the test temperature. It indicates that dynamic strain aging characterized by the interaction between mobile dislocation and diffusion of solute atoms, such as carbon, took place around 400°C, so that the increase of the tensile stress, as well as the decrease of the elongation, occurs [7]. The yield and ultimate tensile strengths of the Gr.92 cladding tube were higher than those of the HT9 cladding tube. However, the Gr.92 cladding tube had a lower total elongation than the HT9 cladding tube. The examination of the fracture surface of the cladding tube showed that a typical ductile cup and cone fracture dominated at all temperatures.

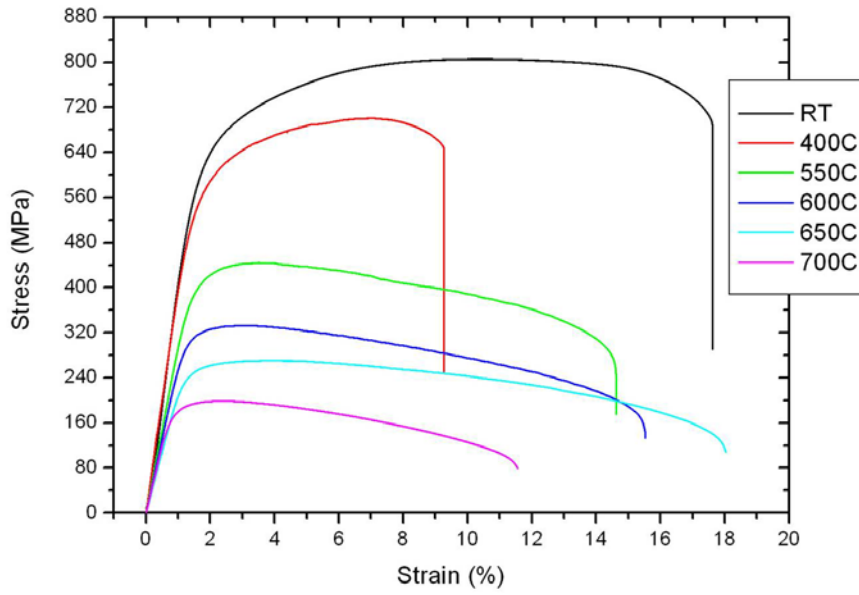


FIG. 2. Stress-strain curve of the HT9 cladding with temperature.

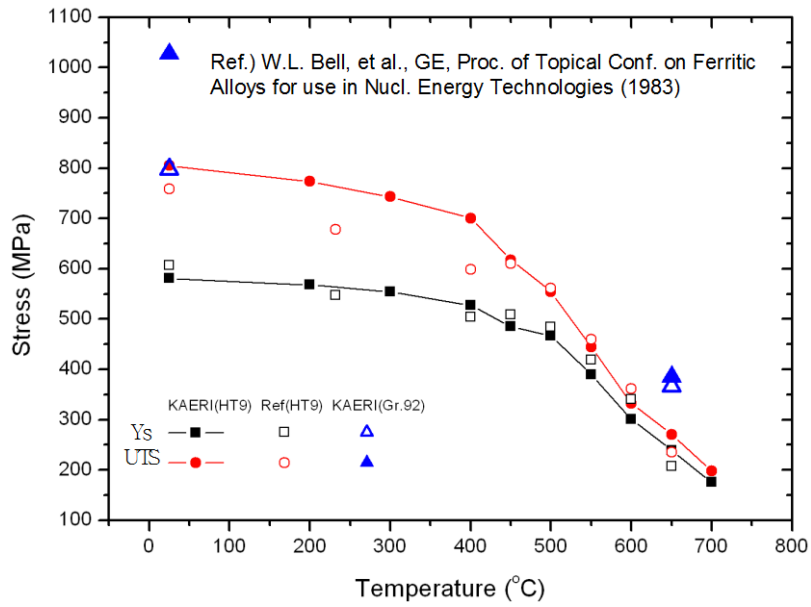


FIG. 3. Yield and tensile strengths of the HT9 and Gr.92 cladding tubes.

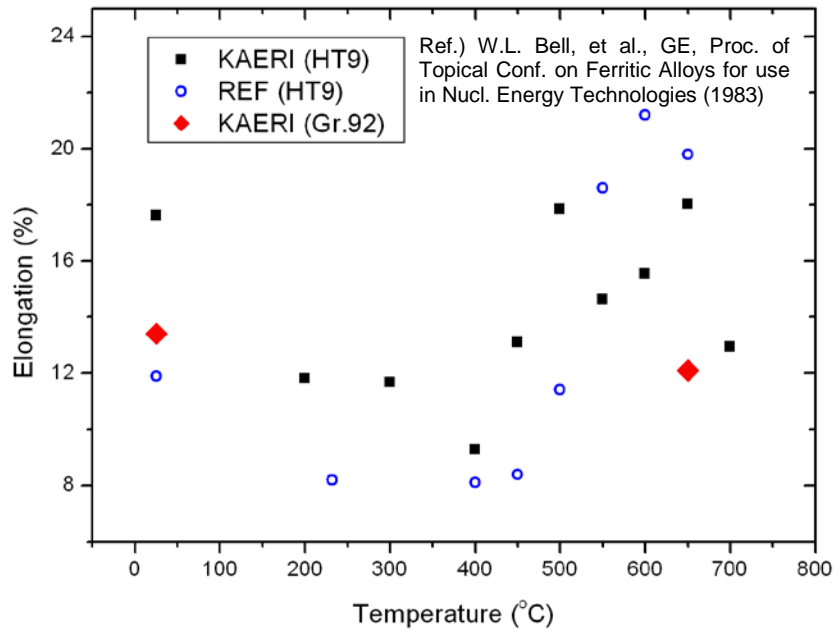


FIG. 4. Total elongation of the HT9 and Gr.92 cladding tubes.

3.3. Creep properties of the HT9 cladding tube

Figure 5 shows a stress-rupture diagram of the HT9 cladding tube tested at 650°C in air. From the result, a linear relationship was drawn under the log-log coordinate, where the comparison with the other results revealed a similar trend [8]. The linear regression of the given data showed that the relationship between the applied hoop stress (σ in MPa) and the cladding rupture time (t in hour) can be adjusted with the following relationship.

$$\log \sigma = 2.397 - 0.015 \log t$$

Further study of the long-term creep behavior of the HT9 cladding tube is going to be performed in the near future, together with . Creep testing of the Gr.92 cladding tube is also ongoing.

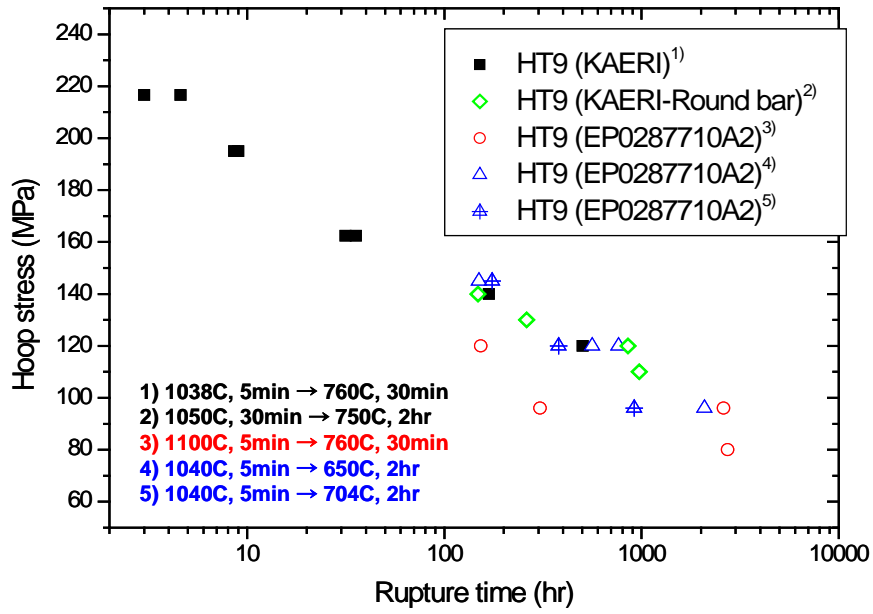


FIG. 5. Stress-rupture diagram of the HT9 cladding tube after biaxial creep test at 650°C.

3.4. Bursr properties of the HT9 cladding tube

Figure 6 shows the ultimate hoop stress of the HT9 cladding. Previous results obtained on the Gr.92 cladding were also plotted for a comparison. The ultimate hoop stress of the HT9 cladding tube was 1135MPa and 488MPa at room temperature and 658°C, respectively. At room temperature, the behavior of the HT9 was similar to that of Gr.92. The circumferential strains of the HT9 and Gr.92 cladding tubes were less than 1%, whatever the test temperature.

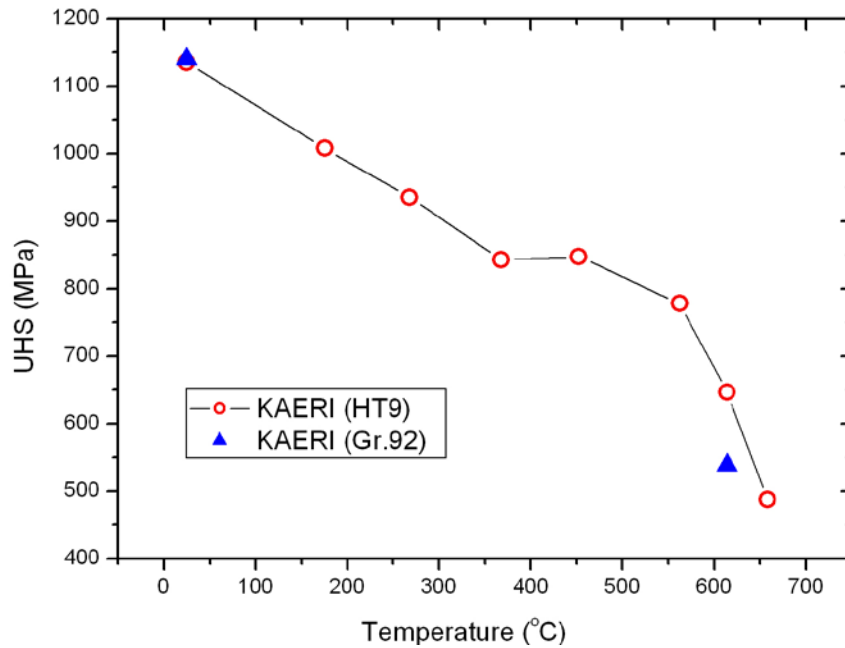


FIG. 6. Ultimate hoop stress of the FMS cladding tube.

4. Conclusions

As a part of developing fuel cladding for the SFR, KAERI has manufactured ferritic-martensitic cladding tubes (HT9 and Gr.92) in cooperation with a domestic steelmaking company. After ingot fabrication, followed by multiple processes of tube reduction and subsequent heat treatments, seamless FM cladding tubes with 7.4mm in outer diameter, 0.56mm in thickness, and 3,000mm in length could be manufactured. The objective of this study was to evaluate the mechanical properties of the FM cladding tubes for an assessment of quality inspection as well as for the validation of their material performance. An axial tensile tests, biaxial burst tests, and pressurized creep tests of the fuel cladding were carried out at various test temperatures. The HT9 cladding tubes fabricated in Korea exhibited mechanical properties similar to the data in the literature.

ACKNOWLEDGEMENTS

This study was supported by the NRF and the Korean Ministry of Education, Science and Technology, through the National Nuclear Technology Program.

REFERENCES

- [1] E.A. Little and D.A. Stow, Void-swelling in Irons and Ferritic Steels: An Experimental Survey of Materials Irradiation in a Fast Reactor, *J. Nucl. Mater.* **87** (1979) 25.
- [2] F.A. Garner, M.B. Tgoloczek, B.H. Sencer, Comparison of Swelling and Irradiation Creep Behavior of FCC-austenitic and BCC-ferritic/martensitic Alloys at High Neutron Exposure, *J. Nucl. Mater.* **276** (2000) 123.
- [3] D.S. Gelles, Microstructural Examination of Neutron-irradiated Simple Ferritic Alloys, *J. Nucl. Mater.* **108&109** (1982) 515.
- [4] Y. Dai, B. Long, Z.F. Tong, Tensile Properties of Ferritic/martensitic Steels irradiated in STIP-1, *J. Nucl. Mater.* **377** (2008) 115.

S.H. Kim et al.

- [5] S.H. Kim, W.S. Ryu, I.H. Kuk, Microstructure and Mechanical Properties of Cr-Mo Steels for Nuclear Industry Application, Nucl. Eng. Tech. **31** (1999) 561.
- [6] S.H. Kim, B.J. Song, W.S. Ryu, J.H. Hong, Creep Rupture Properties of Nitrogen Added 10Cr Ferritic/martensitic Steels, J. Nucl. Mater. **329-333** (2004) 299.
- [7] I. S. Kim, J. Kor. Inst. Met. & Mater., 17, 3 (1979).
- [8] D. S. Gelles, M. L. Hamilton and G. D. Johnson, European Patent, 0287710A2 (1988).

INNOVATIONS DURING SURFACE TREATMENT OF PFBR STEAM GENERATORS IN 91 GRADE MATERIAL

ARAVINDA PAI[†], TARUN KUMAR MITRA[‡], PRABHAT KUMAR[§]

Bharatiya Nabhikiya Vidyut Nigam Limited (BHAVINI)
Prototype Fast Breeder Reactor (PFBR) Project
Department of Atomic Energy
Kalpakkam - 603 102, India

Presented by ARAVINDA PAI

ABSTRACT

Prototype Fast Breeder Reactor (PFBR) is a 500MWe pool type, mixed oxide fuelled, sodium cooled nuclear reactor, which is in advanced stage of construction at Kalpakkam, India. The Steam Generator (SG) is a vertical, once through, shell & tube type heat exchanger with liquid sodium flowing in shell side and water/steam flowing in the tube side. Due to very high reactivity of sodium with water/steam, the boundaries of sodium to water/steam in SG must possess a high degree of integrity & reliability against failure. This is achieved by precise design, correct material selection and high standard quality control & quality assurance during manufacture. Modified 9Cr-1Mo material is selected as principal material of construction. Application of suitable corrosion protection technology is extremely important during fabrication for safe and reliable operation due to critical nature of component. After completion of manufacture of Steam Generators, degreasing, pickling and passivation is carried out on inside surfaces to ensure passive chromium oxide layer. Due to asymmetric shape, configuration and complex constructional features, the surface treatment of Steam Generators is extremely difficult & really challenging task. Huge quantity of nitric acid (HNO₃), HF and Demineralized (DM) water is used during surface treatment of each Steam Generators. Due to hazardous nature of acids, a closed loop of mini chemical plant is constructed for large scale circulation of pickling & passivation solution inside the Steam Generators. Enormous efforts were put and many trials were conducted and various innovations/new techniques were followed for the first time in the nuclear history for effective surface treatment of Steam Generators for 40 years design service life. This paper explains the challenges faced and experience gained during surface treatment on modified 9Cr-1Mo surfaces of PFBR Steam Generators in detail.

1. INTRODUCTION:

Prototype Fast Breeder Reactor has 3 heat transport circuits, viz primary sodium circuit, secondary sodium circuit and steam water circuit. There are 8 Steam Generator (figure-1) modules in PFBR with equal capacity arranged in two loops, each loop containing 4 steam generators. The main function of Steam Generator is to extract the reactor heat through secondary sodium system and convert the feed water into superheated steam. The SG is a vertical, once through, shell and tube type heat exchanger with liquid sodium flowing in shell side and water/steam flowing in the tube side.

Sodium enters the steam generator through a single inlet nozzle and flows upwards in the annular region, then flows down through top inlet plenum where it is evenly distributed before entering the tube bundle. Then sodium exits through the bottom outlet plenum and single outlet nozzle. Feed water enters the tube side at bottom, flows upwards through the orifice assembly which are threaded to the

[†] Scientific Officer (Long Range Planning and Strategies), BHAVINI, Kalpakkam, India

[‡] Director (Technical), BHAVINI, Kalpakkam, India

[§] Chairman and Managing Director, BHAVINI, Kalpakkam, India

tubesheet and then leaves as superheated steam from outlet of SG. Orifice assemblies are provided in each tube of SG from stability consideration.

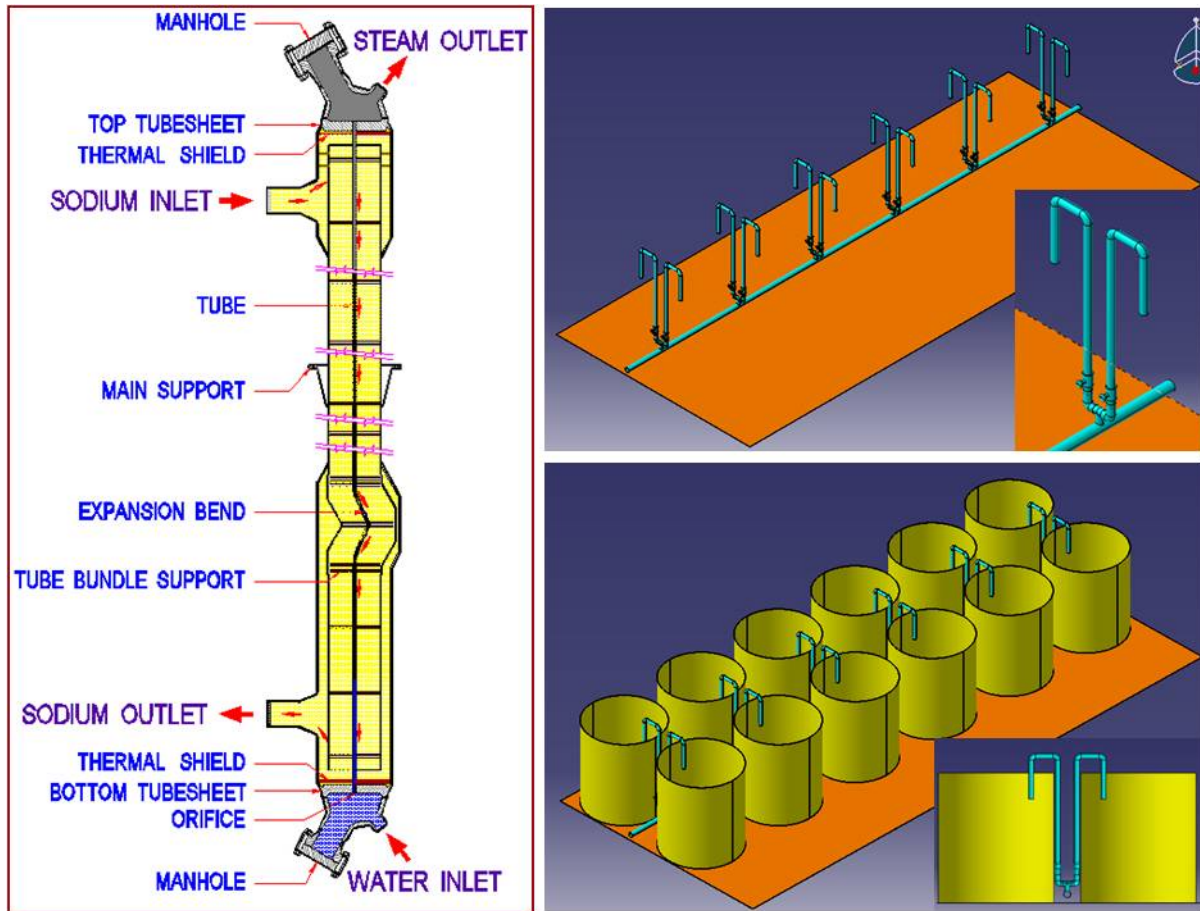


FIG. 1. Configuration of Steam Generator and Piping layout for surface treatment

The choice of steam generator design concept is one of the most critical issues the designers of LMFBRs (Liquid Metal cooled Fast Breeder Reactor) are faced with. The operating experience of SGs in other countries revealed that tube leakage affects the availability of plant, as sodium and water/steam are separated by a single wall tube in the SG. In case of crack/failure in tube, high pressure water/steam reacts with shell side sodium and results in an exothermic reaction with evolution of hydrogen, corrosive sodium hydroxide products and intense local heat. Therefore, Steam Generator is one of the critical key equipment in determining efficient running of the plant and demands high degree of integrity & reliability against failure to avoid extensive outage time. Integrity and reliability is achieved by choosing a correct material followed by an optimized design with high standard quality control & quality assurance during manufacture. The PFBR material specifications are stringent compared to specification of other industrial applications to enhance the reliability. Modified 9Cr-1Mo material is selected as principal material of construction for Steam Generators as this material has excellent high temperature mechanical properties and has high resistance to stress corrosion cracking in caustic & chloride environment in case of unforeseen events during reactor operation[1]. It has been reported that failure of this series of steels are mainly depends on atmospheric conditions and microstructures. During various stages of fabrication, storage & installation, the Steam Generators are exposed to corrosive atmosphere at ambient temperature, as fabrication place of SG and location of PFBR are in coastal site. The environmental conditions prevailing during these stages are different from those encountered during operation. Therefore, it is necessary that these materials are required to be highly resistive against general and localized corrosion[2]. Selection of appropriate material followed by application of suitable corrosion protection technology on surfaces of components plays a vital role for reliable service. As per PFBR specification, surface treatment by degreasing, pickling followed by passivation is a mandatory

requirement at the end of fabrication of Steam Generators. This paper highlights technological challenges and experience gained during surface treatment of PFBR Steam Generators in detail.

2. DESCRIPTION OF SURFACE TREATMENT ARRANGMENTS AND MAIN CONSIDERATIONS:

The PFBR Steam Generator is mainly consists of slender 12mm & 30mm thick cylindrical shell assemblies, tube bundle and dished ends made of modified 9Cr-1Mo steel, which are subjected to surface treatment at the end of fabrication. After completion of fabrication, Post Weld Heat Treatment (PWHT) of Steam Generator is carried out for the complete 26 meters length in a single charge at $760\pm 10^{\circ}\text{C}$ in a dedicated calibrated electrical furnace.

Surface treatment is carried out to remove organic and inorganic contaminates such as oil, grease, dirt, rust, oxide, mill scale etc. present on the surface which are inevitable during fabrication/heat treatment and storage. Failure to remove these foreign substances at the end of fabrication may lead to undesirable contamination of liquid sodium (shell side) and steam/water (tube side) during reactor operation. This leads to high load on the liquid sodium purification system. Surface treatment enhances the corrosion resistance of modified 9Cr-1Mo steel by forming uniform chromium oxide layer. Therefore, surface treatment is carried out for Steam Generators after completion of all fabrication activities which involves degreasing; pickling followed by passivation with water rinsing in between. Degreasing is carried out by circulation of DK 9.5 alkali solution. The pickling is carried out by circulation of mixture of HNO_3 and HF solution. Subsequently, passivation is carried out by circulation of HNO_3 .

Table 1. HOLDUP VOLUME FOR PIPING CIRCUIT AND EQUIPMENT

System	Volume
Temporary pipelines, m^3	$\sim 3 \text{ m}^3$
Solution preparation tank, m^3	$\sim 10 \text{ m}^3$
Tube side of SG	3 m^3
Shell side of SG	15 m^3

Due to hazardous nature of acids, a closed loop of mini chemical plant is constructed for circulation of pickling & passivation solution inside the SG during surface treatment. Table 1 indicates the holdup volume for surface treatment piping circuit and equipment. Only Stainless Steels (SS) make pumps, pipes and pipe fittings were used for circulation of acid solutions to avoid contaminations. The degreasing and chemical cleaning operation in presence of orifice assembly needs design of high pressure piping, procurement of high pressure pump with approximately $250\text{m}^3/\text{hr}$ discharge. Fabrication activities of mini piping plant majorly consists of erection of 34 nos. of tanks of 10,000 liters capacity, 425 meters of SS304 piping with ~ 300 nos. of pipe to pipe weld joints (dia. 2", 4" & 6"), 80 nos. of SS304 ball valves (dia. 2", 4" & 6") and connection activities of piping to acid storage tank/circulating tank/effluent storage tanks involving various in-situ welding activities. Complete pipeline and solution circulating tank in the temporary circuit is cleaned thoroughly by water flushing before taking up the surface treatment on actual job to ensure that dust/dirt which are existing inside the pipeline/tanks is not entering into the SG. The complete loop of piping is subjected to hydro test to ensure the leak tightness before feeding the acids into the piping circuit. Due to hazardous nature of acids, a stand by pump is always kept during the entire surface treatment operation to ensure that acids would not remain inside the critical equipment during unforeseen events. Huge quantity of HNO_3 , HF and demineralized (DM) water is used for surface treatment of each Steam Generators. The table-2 indicates PFBR specification requirements for DM water. The acids to the tune of 2.5 times than that calculated for the circulating volume is kept ready before initiating the treatment to avoid any kind of non-conformances due to shortage during actual circulation. Various control provisions are made in the piping circuit with appropriate valves to reverse the flow when desired for effective surface cleaning & passivation. Hazardous acid effluents generated after surface treatment of each Steam

Generators is punctually neutralized in Effluent Treatment Plant (ETP) before disposal as per the prevailing environmental norms.

Table 2. DM WATER QUALITY FOR SURFACE TREATMENT

Parameters	Unit	Acceptance Value
pH	-	6.5 to 7.5
Chloride	mg/l	< 1
Conductivity	μS/cm	<10

Due to asymmetric shape and configuration of Steam Generators, the surface treatment is extremely difficult and really challenging task. Enormous efforts were put for the effective surface treatment in a large scale for reliable 40 years long design service life expected from Steam Generators. As surface treatment is done in horizontal condition, air pockets are inevitable in the top surfaces of shell assemblies. Therefore, 26 meters length job was required to be rotated by 180 degree after completion of partial surface treatment and then balance surface treatment process is continued to ensure complete coverage and effectiveness of the process. Various test coupons made of tube and plate material were kept in the circulating tank during circulation of solution to ascertain the effectiveness and extent of cleaning on inaccessible inside surfaces of equipment. Monitoring of parameters such as pH, conductivity, chloride and iron content is carried out promptly at regular intervals. If surface treatment of shell side is carried out before tube side, then tube side is completely flushed with hot nitrogen and dried till dew point less than -40°C is achieved to avoid rusting if any on inside tube surfaces due to condensation during shell side cleaning process.

3. DEGREASING OPERATION AND INNOVATIONS:

Degreasing process is carried out to remove grease, oil and other organic matters by circulation of DK 9.5 solution, which is an indigenously developed proprietary alkali. During PWHT at high temperature, there was a concern of burning of traces of couplant/grease used during ultrasonic examination/Helium leak testing of welds, which may lead to formation of hard rust on modified 9Cr-1Mo surfaces, which is not desirable. Therefore, degreasing is carried out before PWHT for both tube side and shell side of Steam Generators. Hot nitrogen gas is purged on inside surfaces of shell side & tube side in counter flow direction during heat treatment to avoid oxidation at high temperature on inaccessible inside surfaces.

As per specification requirement, degreasing shall be carried out by circulating a solution consists of benzene, acetone and methyl alcohol in equal volumes at room temperature. As mixture of above degreasing solution is highly inflammable, circulation in large quantity is not insisted upon at the time of implementation due to industrial safety aspects.

Before degreasing operation on actual job, degreasing trials on 1"x1"x 12 mm thick modified 9Cr-1Mo coupons were carried out to check the effectiveness of process with different parameters. The various combinations of couplant and grease were made for the trials which were used during ultrasonic examinations/Helium leak test of Steam Generators. Initially, a trial was conducted with water solution containing lesser volume of DK 9.5 at $50\pm 5^{\circ}\text{C}$ to remove the couplant/grease available on trial coupons. This trial has not delivered satisfactory results. Subsequently, the volume of DK 9.5 was increased and temperature was increased to $55\pm 5^{\circ}\text{C}$. As trials conducted with these parameters have delivered outstanding results, it was decided to carry out degreasing on actual job with these process parameters.



FIG. 2. Piping arrangements for degreasing of Steam Generators

3.1. The sequence of degreasing operation:

Before starting the surface treatment, water flushing is done on forward and reverse direction to flush out the muck & loose adhered contaminations on equipment surface. DK 9.5 is prepared in water externally and transferred to cleaning circuit (figure-2). The solution is heated to 55 ± 5 °C and circulated in equipment. Since this is the very first operation involving utilization of hot fluid inside the system, temporary piping and equipment is allowed to expand freely. DK 9.5 solution emerges froth due to agitation and circulation. Periodic pH monitoring is carried out even though pH is neutral for this solution. After half an hour of circulation, one of the test coupon kept inside the circulation tank is taken out, rinsed with DM water and subjected to water break test. Circulation of degreasing solution is continued and water break test is conducted for every 30 minutes interval, till it passes. At the end of degreasing, the solution is cooled to less than 40°C and equipment/lines are drained and subsequently rinsed with DM water.

With Nitrogen filled condition at 1.5 kg/cm^2 pressure, the equipment is shifted to heat treatment furnace area for drying by heating in the furnace at about 150-200°C during which continuous nitrogen gas purging is done. Dryness is ensured by measuring dew point (less than -40 °C) of dry nitrogen at the outlet.

4. PICKLING OPERATION AND PROCESS DESCRIPTION:

After completion of PWHT, the pickling operation is carried out for both tube side and shell side of Steam Generators. Pickling solution comprise of mixture of HNO₃ and HF prepared in high quality DM water. Pickling solution is circulated in forward and reverse direction in steps of 15 minutes at ambient temperature. Iron content & pH of the solution is monitored regularly for every 10 minutes. Iron content of the pickling solution will increase with time and reach a stable value. During circulation, degreased and stress relieved coupons of tubes which were kept inside the circulation tank is taken out, rinsed in DM water and evaluated visually. The pickling process is continued till entire rust (brownish to blackish surface) is removed. Iron content reaching a stable value is also considered as alternate criteria for deciding the end of pickling operation. After pickling operation, acid solution is drained and equipment is rinsed with DM water till rinsed water reaches pH in the range of 6.5 to 7.5 (neutral).

5. PASSIVATION OPERATION AND PROCESS DESCRIPTION:

Passivation process is carried out immediately after pickling operation. Passivation solution contains HNO₃ prepared in DM water. The circulation process of passivation solution is similar to pickling

process at ambient temperature. During passivation, iron content is monitored in the solution for every 15 minutes. At the end of passivation, the test coupon surface should pass the cotton swab test and test coupon should be free from rust and surface shall have uniform greyish colour. After passivation, DM water rinsing is carried out till the pH of rinsed water is same as that of original water or pH is in range of 6.5 to 7.5. In addition, conductivity test, methyl orange test, Fe content test is carried out before discontinuing the water rinsing.

6. CHALLENGES AND DIFFICULTIES DURING FILLING, DRAINING AND DRYING OF EQUIPMENT:

The filling & draining of solution and drying of Steam Generator after surface treatment is complicated task due to its odd geometry and complex constructional features. The venting of air/gases from the equipment is essential during filling/circulation of solution to ensure positive contact between solution and surfaces to be treated. In order to ensure complete venting of air during initial filling, spilling of acid is not permitted to remove the air pockets due to hazardous nature of fluids involved. After surface treatment, about 40% solution can be taken to mixing tank & then transferred to effluent storage tank. Balance 60% of the solution in SG is required to be pumped through drain pipes connected to SG which requires about 60-90 minutes to complete. Higher size drain lines cannot be used as bent drain pipe cannot be negotiated within the available space between 12mm and 30mm thick shell assembly. If nozzles are kept in 12'O clock position during chemical cleaning, venting would be more effective but there would be no access to put fixed drain pipe till 6'O clock position due to existence of 12 mm thick shell assembly in between. In case, nozzles are oriented at 12'O clock position, small size flexible drain pipe can be used to negotiate upto the complete bottom portion of shell assembly, but there is a concern that flexible drain pipe may not reach till 6'O clock position inside the shell assembly. In addition, there are apprehensions that flexible drain pipe may not retain in the desired location due to forward and reverse flow of solutions during circulation. On the other hand, if nozzles are oriented at 6'O clock position, there would be no access to put fixed vent pipe till 12'O clock position due to existence of 12mm thick shells in between. In case, nozzles are oriented at 6'O clock position, flexible vent pipe is required to be used and the same will sag down and may not reach upto the top portion (12'O clock position) of the shell assembly (figure 3). Rotation of Steam Generator for filling & draining operation at surface treatment yard involves handling risks especially because of externals welded on outside surface and spilling of acid solution during rotation is a causing concern. In addition, flexible connecting piping arrangement for rotating the SGA during operation is not feasible considering the pressurized flow of hazardous fluids involved during surface treatment. After completion of surface treatment, elaborate arrangement of disconnection of piping for rotation to facilitate draining will expose SG to acid atmosphere for great duration of time, which is not desirable. Considering all these factors, it was decided to carry out chemical cleaning of SGA by keeping its nozzles in horizontal orientation (i.e. 3'O clock position). Due to all these limitations and complex geometry of Steam Generators, air pockets are inevitable during chemical cleaning operation.

During draining, drain valve is crack-opened to start with followed by gradual opening and drain valve is fully opened only after emptying about half of the equipment volume, so as to avoid acid jet during draining. Therefore, draining is a time consuming process. One no. 0.5" diameter vent pipe and 1.5" diameter drain pipe is provided in shell and tube side nozzles to remove air pockets at 12'O clock position and aid maximum draining at 6'O clock region respectively (figure 4).

The 26 meters length Steam Generator is lifted and rocking is done in horizontal condition to remove the water traces after completing all surface treatment operations. As drying by passing hot nitrogen gas (80⁰ C) was taking longer time to get less than -40⁰ C dew point at outlet, the more reliable evacuation method by vacuum is adapted for drying after surface treatment due to asymmetric shape & configuration of SG. The Steam Generator is presumed to be dry when 1mm of mercury vacuum is maintained for 30 minutes without pumping. Helium leak test is done after surface treatment which also ensures complete dryness of equipment, as test is done in vacuum mode.

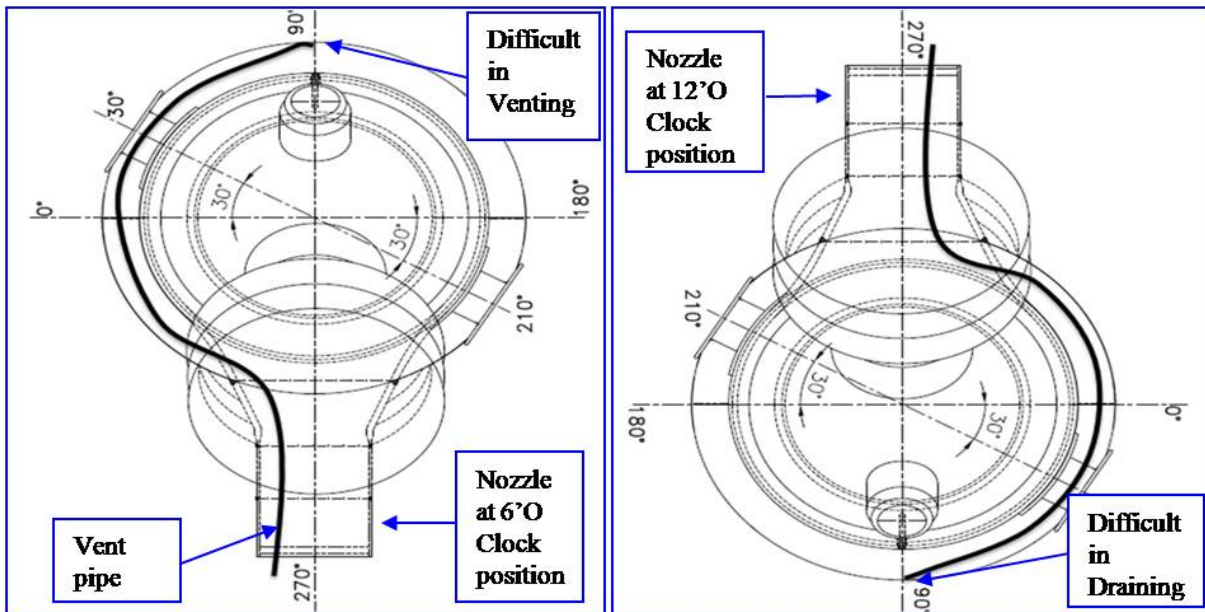


FIG. 3. Difficulties during draining and venting arrangement for surface treatment

The surface treatment is carried out immediately after hydro test subsequent to PWHT so as to ensure that no further operation is left which would affect on dryness until the equipment is taken for reactor commissioning.

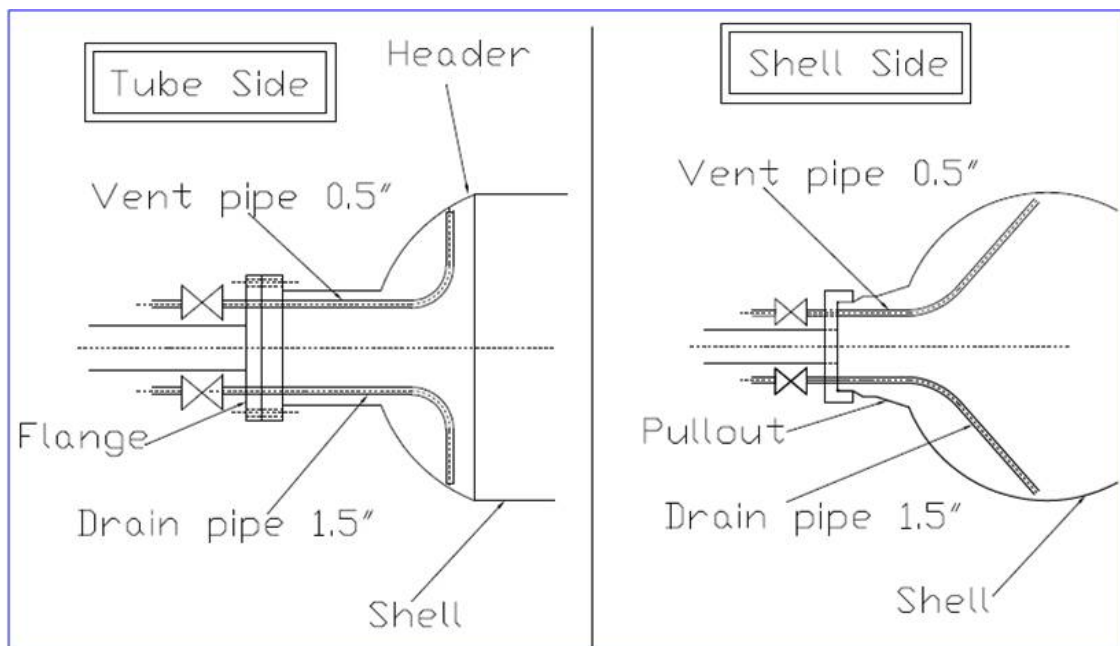


FIG. 4. Drain and Vent pipe arrangements for surface treatment

7. CHALLENGES AND PROBLEMS ENCOUNTERED DURING SURFACE TREATMENT OPERATION:

The figure-5 indicates various steps involved and layout for surface treatment of Steam Generators. The surface treatment inside the tube side is extremely difficult due to presence of orifice assemblies at bottom end of Steam Generator. Muck/loose particles formed due to metal/scale removal during degreasing, pickling and passivation may entrap in small diameter holes in the orifice assembly and may choke the fluid flow inside the tubes resulting in inefficient cleaning/passivation.

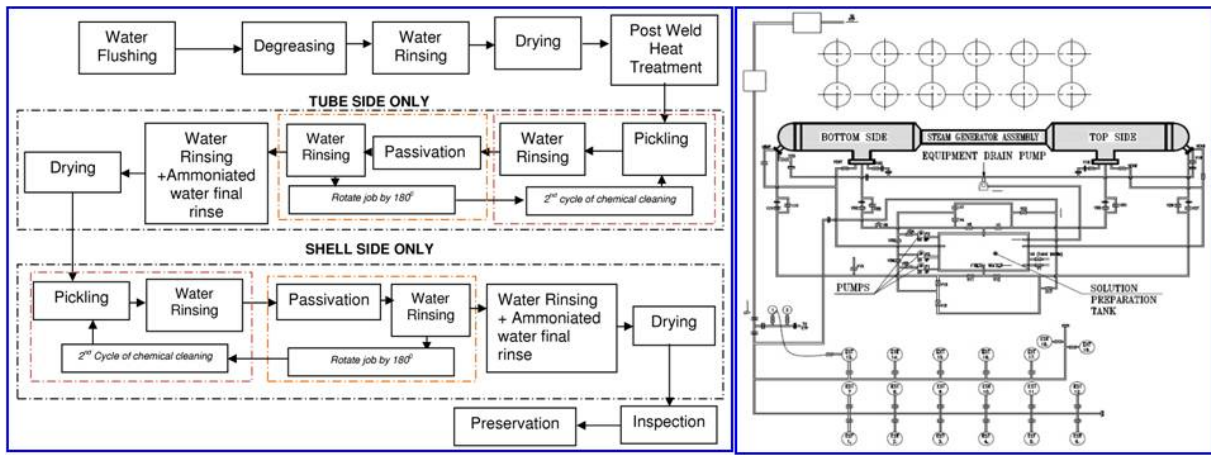


FIG. 5. Various steps involved and layout for surface treatment of Steam Generators

Therefore, a small scale mock up trial (figure 6) was conducted on 5 nos. of heat treated tubes with integrated orifice assemblies to check the apprehension of muck entrapment/choking in orifice assembly and to evaluate the effectiveness of circulation of acid solution in presence of orifice assembly. The temporary circuit for mock up trial includes 210 liters capacity tank for solution hold up and re-circulation, 15kg/cm² capacity SS304 pump, SS piping and valves. Huge quantity of muck which is more than expected during actual job cleaning was added externally during the trials. It was found that muck was not clogged inside the orifice assembly and presence of orifice assembly has not affected solution circulation inside the tubes during trial chemical cleaning operation. During trials, it was observed that surface treatment process is completely successful.

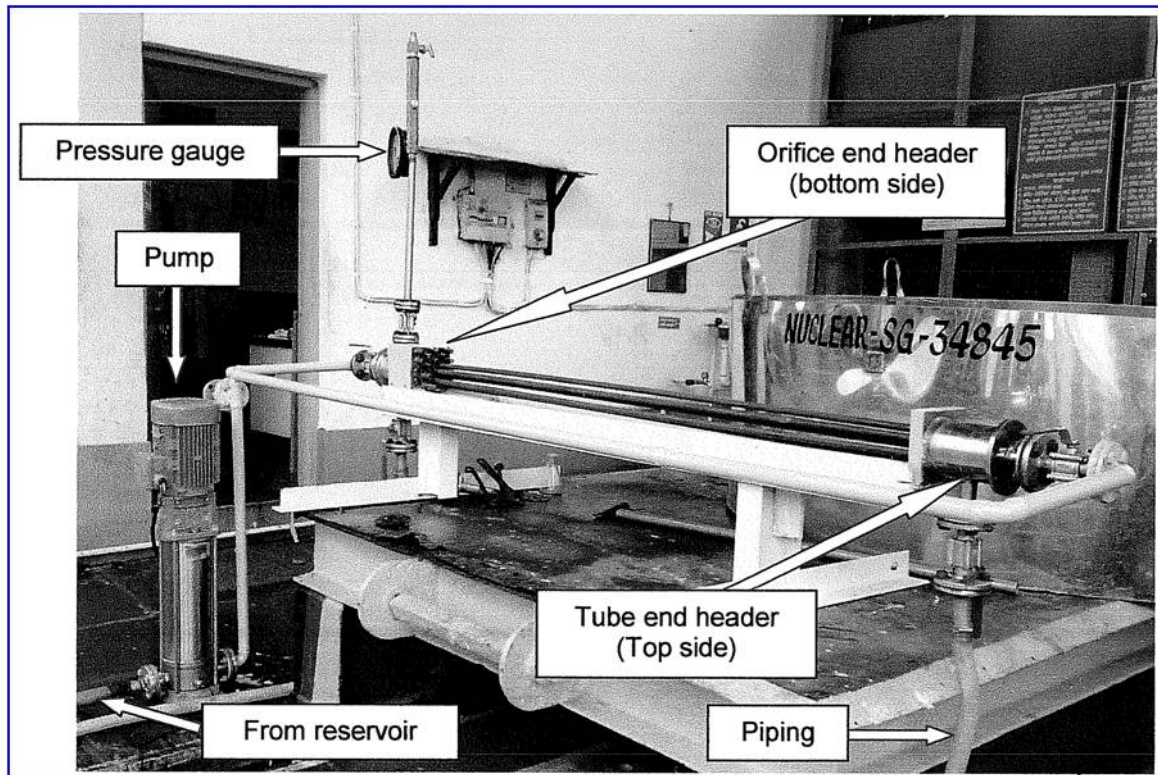


FIG. 6. Set up and arrangements for trial chemical cleaning operation

During initial stages of surface treatment of Steam Generators, ineffective cleaning is observed after pickling and passivation on inside surfaces of shell assembly at local portion on the top region (12'O clock position). In addition, muck/powdery substance at 6'O clock region are observed on shell

internal surface and surface treatment on inside surfaces of tubes were not fully satisfactory, which is presumed to be due to slow draining. It was thought that slight increase in HF in pickling solution would enhance the effectiveness of cleaning on top inside surfaces.

In addition, during initial stages, mixing of HF was carried out while HNO₃ is under circulation in the cleaning circuit. Hydrogen/Nitrous gas generated during this process was causing ineffective removal of rust/oxide layer, as these gases are assumed to be obstructing the effective contact between acid solution and inside surfaces. Based on these learning, it was decided to externally prepare the mixture of HNO₃ & HF and then transfer to the circulating tank. A separate hood is provided above the mixing tank, so that the gas/minor acid fumes generated during circulation are exhausted out to a safe place.

After above modifications and in spite of having temporary fixed vent pipe inserted at 12'O clock position, cleaning at 12'O clock position was not fully satisfactory, which was presumed to be due to stagnation of hydrogen/nitrous gas generated during circulation of acid solution. In addition, loose muck is observed at 6'O clock position, which is due to slow draining. Therefore, compressed nitrogen gas is purged inside the Steam Generator to create turbulence in solution during pickling, passivation and rinsing process in order to remove stagnation of gases at 12'o clock position and to remove loose muck at 6'O clock position. Even after all above modifications in the system and various trials, still there were uncleaned areas observed at 12'o clock position due to formation of air pockets. Therefore, finally it was decided to carry out 2nd time chemical cleaning for the complete shell side and tube side by rotating the job by 180° after removing the temporary attachment, so that uncleaned areas on both shell and tube side comes on bottom side. The observations after 2nd time chemical cleaning with this innovative technique was fully satisfactory and surface treatment process is completely effective. Figure-7 shows the surface appearance after initial surface treatment and subsequent to 2nd time surface treatment with rotation of equipment by 180°. In addition, minor oxide traces if any existing inside the inaccessible areas are expected to get cleaned by the liquid sodium during reactor operation as sodium possess good oxide removing properties at high temperature.

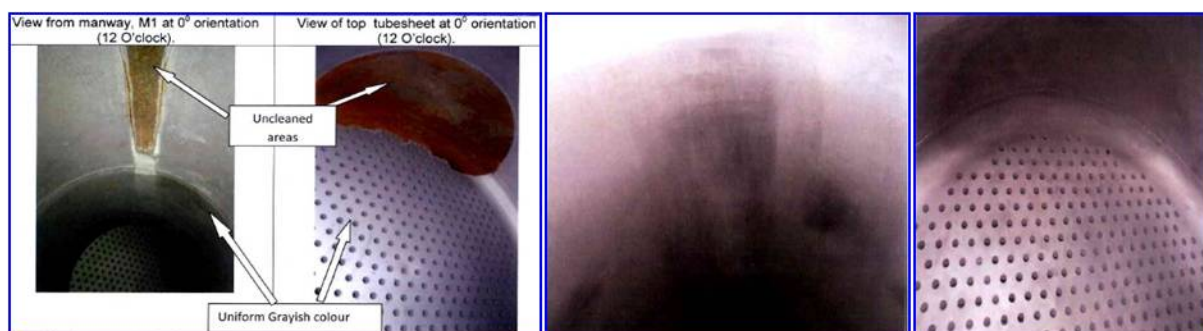


FIG. 7. Surface appearance before and after 2nd time surface treatment operation

There were concerns of crevice corrosion due to entrapped acid traces if any between orifice assembly and tubesheet hole during surface treatment of actual Steam Generators. Therefore, it was decided to soak DM water and create turbulence by purging compressed nitrogen gas to dilute the acid traces if any at the end of rinsing process. In addition, final rinsing using ammoniated DM water is carried out after second time surface treatment to increase the pH to ensure that cleaned surfaces and crevice areas are basic in nature. Ammoniated DM water is prepared in a separate tank having pH in the range of 9.2 to 9.6 with maximum conductivity of 65 μS/cm. Ammoniated DM water is circulated inside the Steam Generators for both tube side and shell side by reversing the flow after every 15 minutes. Before dispatch of Steam Generators, both tube side and shell side are filled with inert dry nitrogen gas at a pressure greater than 0.6 bar (gauge) to ensure that there is no foreign material contamination and atmospheric attack even during transportation from manufacturer place to the project site.

8. SHOT BLASTING AND PAINTING ON OUTSIDE SURFACES AFTER SURFACE TREATMENT:

After completion of surface treatment on inside surfaces, the shot blasting and painting is carried out using high temperature aluminium paint on outside surfaces. Initially, it was envisaged to carry out shot blasting using carbon steel shots. During shot blasting, there is a possibility of embedment of fine carbon steel shots inside the crevices between heating cable support strips and outside surfaces of Steam Generators. As potential difference between carbon steel shots and modified 9Cr-1Mo material is high, there were concerns about galvanic corrosion. Therefore, it was decided to carry out shot blasting using Alumina (Al_2O_3) grits to avoid galvanic corrosion.



FIG. 8. Surface appearance of SG after PWHT and after shot blasting & painting

Due to slender nature of component, it is inevitable to have many saddle supports at various locations for safe & smooth handling of Steam Generators in horizontal condition within manufacturer's site. Due to this reason, shot blasting and painting on complete surface cannot be done in a single stretch, as local outside surface which is supported at saddle locations are inaccessible for shot blasting and painting. Therefore, shot blasting and painting is also required to be done in two stages after rotating the equipment by 180° . Figure-8 shows the appearance of outside surface of Steam Generators after PWHT and after shot blasting & painting.

9. CONCLUSION:

The design and manufacture should employ proven techniques and it should be possible to conduct such analysis of design as may be necessary for the purpose of demonstrating adequate integrity at any specified time throughout the plant life. Very high standard quality control and quality assurance during raw material procurement, fabrication, surface treatment, inspection and testing has given confidence on trouble free service from PFBR Steam Generators for the design service life of 40 years. Understanding nature of materials, cause of the problem and a patient analysis to find the ways & means to counter the difficulties led this success.

ACKNOWLEDGEMENTS

The authors are thankful for the fruitful discussion provided by the project team at M/s L&T, Powai, Mumbai, India.

REFERENCES

- [1] M.G. Pujar, C.R. Das, S. Thirunavukkarasu, U. Kamachi Mudali, A.K. Bhaduri, J. Brijitta and B.V.R. Tata, Effect of boron addition on pitting corrosion resistance of modified 9Cr-1Mo steel: Application of electrochemical noise, Elsevier Publication, Materials Chemistry and Physics , 536– 547, 2011.
- [2] T.K.Mitra, Aravinda Pai and Prabhat Kumar, Challenges in manufacture of PFBR Steam Generators, Energy Procedia, Elsevier Publication, Pg 317-322, Volume 7, 2011.

Development of Welding and Hardfacing Technology: challenges for ASTRID project

T. Marlaud^a, D. Pierron^b, A-F. Bonnot^a, M. Blanc^c, L. Forest^c, M. Blat-Yrieix^d, J-P. Mathieu^d

^a AREVA NP, 69006 Lyon, France

^b AREVA NP, 71380 Saint Marcel, France

^c CEA Saclay, DEN/DANS/SEMT/LTA, 91191 Gif-sur-Yvette Cedex, France

^d EDF R&D, DMMC, Site des Renardières, 77818 Moret sur Loing, France

^e CEA Centre de Cadarache, 13108 Saint-Paul-Lez-Durance, France

Presented by A-F Bonnot

Abstract. The purpose of this article is to present the challenges for welding and hardfacing technology involved by sodium fast breeder reactors and by ASTRID specificities.

To meet with compromises between achieving good ductility properties (toughness, impact, elongation...) and room/high temperature mechanical resistance (creep, strength...) in welds, as ensuring metallurgical (solidification cracking) and process weldability, the development of specific welding filler consumables for materials used in the creep conditions is needed. The developments deal with the candidate materials (316L(N), Grade 91) and integrate a qualification approach to aim at achieving a robust manufacturing.

Contact zones in FBR sodium environment are subjected to various solicitations (high temperature, severe contact pressure, cycling...). When subjected to radiation, hardfacing alternatives to traditional cobalt base coatings depend on the application are required. The approach to evaluate the performance of alternative solutions, through an experimental program, will be presented.

1. Introduction

The reference concept chosen in France for the generation IV is the sodium Fast Breeder Reactors (FBR-Na) which benefit from 50 years of experience, notably through PHENIX (PHX) and SUPERPHENIX (SPX) reactors. For ASTRID (Advanced Sodium Technological Reactor for Industrial Demonstration), the materials choice results from the following requirements: good high temperature properties, low interaction with sodium, good corrosion resistance, an acceptable dimensionnal stability, a limited activation, and a good weldability. The purpose of this article is to present the challenges for welding and hardfacing technology involved in FBR-Na and ASTRID specificities.

To meet with compromises between achieving good ductility properties (toughness, impact, elongation...) and room/high temperature mechanical resistance (creep, strength...) in welds, as ensuring metallurgical (solidification cracking...) and process weldability, the development of specific welding filler consumables for materials used in the creep conditions is needed. These developments deal with the main candidate materials and integrate a qualification approach to aim at achieving a robust manufacturing. The austenitic stainless steel X2CrNiMo17-12-2 controlled nitrogen content (hereafter named "316L(N)") is the major structural material for ASTRID [1] (principal vessel, inner vessel, core support structure, secondary piping...), with an operating temperature up to 550°C. The X10CrMoVNb9-1 steel (hereafter named "grade 91") is a candidate for some design options of

ASTRID Steam Generators (SG) [1] and for the steam-water system, with operating conditions of 530°C-180 bars. Other structural materials as austenitic precipitation-hardened steels, low-alloyed steels, unalloyed steels, etc., candidates for other design options or in much smaller proportions in ASTRID than the major alloys mentioned above, will not be treated in this paper.

In previous French sodium Fast Breeder Reactors (FBR-Na), cobalt-base alloys have been used as hardfacing alloys for many contact and friction zones. Although they are perfectly reliable as protection against self-welding and wear damages for austenitic stainless steel in flowing sodium, cobalt-free alternatives have to be used in future FBR-Na in order to reach radioactivity aims (maintenance, decommissioning), when contact zones or wear products are subjected to radiation. The experimental program adopted to evaluate the alternative solutions' performance in sodium is presented.

2. Welding studies

2.1. Welding of 316L(N) (X2CrNiMo17-12-2 controlled nitrogen content)

Based on the 316L-SPH SS specified for SPX, but with a narrowed overall chemical composition to limit scatter in material properties, the 316L(N) (1S material of RCC-MRx) solidifies in a complete austenitic mode under conditions representatives of arc welding, as it could be shown on WRC-92 diagramm. Thus welding consumables specifications had led to the development of the austeno-ferritic 19Cr12Ni2Mo weld metal (hereafter named 19.12.2) in order to ensure good weldability and comparable properties of deposited metal to that of the base material in creep conditions. 19.12.2 weld metal benefits from the feedback of primary vessel of RAPSODIE, PHENIX and SUPERPHENIX (SPX) construction, which have led to the current deposited metal chemical composition of RCC-MRx code [2]. The deposited metal presents an adjusted composition to respond to the following influences: (i) the control of ferrite content to insure a good thermal aging behavior at 550°C and avoid hot cracking susceptibility in all welding positions, (ii) a chemical composition close to that of the base metal to limit dilution effects, (iii) a control of impurities (versus hot cracking, properties degradation...) (iv) a control of elements favouring sigma phase, (v) an optimised composition towards high temperature properties and sensitivisation to intergranular corrosion...

For ASTRID welding studies, it is proposed firstly to master again the experience on 19.12.2 grade throughout testing 19.12.2 electrodes not already marketed by the consumable suppliers for SPX construction. The requirements for test plate, given by the "Reference data sheet of filler materials" of RCC-MRx code, are described in Table 1. Characterizations on test plate are performed to check the absence of defects on deposited metal in flat position and to check, through only some mechanical characterizations, that the mechanical properties of the weldment belong to the dispersion band required from the standard codification rules. For example, it has been shown by an extent long-term R&D investigation, that on this grade an U-notch Impact Energy (K_{CU}) $\geq 3daJ/cm^2$ after an accelerate aging at 750°C 100h, ensure $K_{CU} \sim 3daJ/cm^2$ after 100 000 h at 550°C. Due to Standardization evolutions, the K_{CU} requirements in as weld and after accelerate aging conditions have been replaced by K_V requirements in RCC-MRx code.

Table 1. ASTRID main requirements for 19.12.2 electrodes acceptance test on test plate, flat position.

Charpy V-notch impact strength (J) at RT ; ind. value		Tensile properties at RT			Tensile properties at 550°C		
As weld	after 750°C 100h	0,2% YS (MPa)	UTS (MPa)	EI (L=5d)	0,2% YS (MPa)	UTS (MPa)	EI (L=5d)
≥ 60 J	≥ 25 J	≥ 350 MPa	≥ 550 MPa ; ≤ 800 MPa	≥ 35 %	Inf.	≥ 380 MPa	≥ 20 %
Creep test at 550°C; 260MPa - Time to rupture (h)				Creep test at 550°C; 230MPa - Time to rupture (h)			
700 h				2000 h			
Groove cracking test, Accelerated intergranular corrosion test							

Three electrodes have been tested (cf. Table 2). The chemical compositions of deposited metal for E1 and E3 meet with requirements. For E2, only the Mo content is a little too high. These welded metals, having a measured ferrite content between 3 and 7%, present a chemical composition close to the mean SPX composition.

Table 2. Chemical composition of the deposited weld metal from the three tested electrodes

Chemical composition (wt. %)			C	Si	Mn	Ni	Cr	Mo	N
RCC-MRx specifications	min		0.045	0.40	1.2	11	18	1.9	a
	max		0.055	0.70	1.8	12	19	2.2	
Mean SPX (test plate & qualification joints)			0.051	0.56	1.56	11.53	18.52	1.99	-
E1	Test plate ^b	Ø 3.15	0.056	0.627	1.79	11.89	18.53	2.09	0.0438
E2	Test plate ^b	Ø 3.2	0.051	0.51	1.67	11.53	18.19	2.26	0.027
E3	Test plate ^b	Ø 3.2	0.048	0.634	1.56	11.76	18.54	1.89	0.0304
Base Metal 316L(N)			0.027	0.39	1.63	12.14	17.58	2.54	0.065

^a for information

^b Test plate made in flat position

The tensile and impact notch properties are shown in FIG. 1 and compared with requirements of RCC-MRx and mean properties from SPX supply acceptance test. The given Charpy impact energies are the mean value of 3 Charpy samples. In order to place the results in relation with SPX experience, Charpy U-notch tests have been done for E1 and E3 on samples having undergone an accelerated aging heat treatment 750 °C-100 h, and compared to SPX requirements ($K_{CU} \geq 3daJ/cm^2$).

These results show that properties of deposited metal are close to SPX mean values, and almost all requirements are achieved for the three electrodes with reduced margin for elongation at RT. For E2 electrode, in consistency with its high composition in Mo which favours sigma phase, a poor toughness after accelerated aging is found, which reasserts the narrowed specification range. The accelerated creep test at 550°C, groove cracking test, and accelerated intergranular corrosion test are valid for the 3 tested electrodes. So E1 & E3 electrodes allow to deposit in flat position a welded metal comparable to SPX experience and responding to ASTRID requirements.

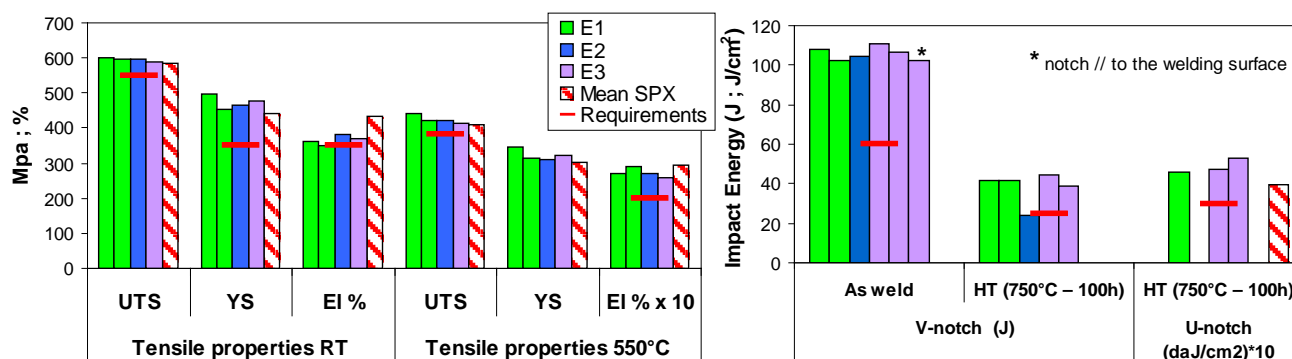


FIG. 1. Tensile and impact properties of E1, E2 & E3 deposited metal, comparison with SPX test plates mean values and RS2711.1 requirements

Further investigations will consist in characterization of joints performed in horizontal (PC/2G) & Vertical upwards progression (PF/3F) welding positions, which allow the characterization of joints (transversal properties...), ensure a good weldability (hot cracking susceptibility...) and an acceptable usability. The usability of these covered electrodes, having basic or rutile/basic coating, is indeed improvable in flat position, and could be a cause of defects during the manufacturing. The next step would be to insure an acceptable “usability” of electrodes through added specifications on the electrode

coating (like Basicity Index) and/or added technological tests like a slag detachability characterization test, as proposed by the reference [3].

In parallel with SMAW investigations, the development of solid wire for the automatic GTAW process is investigated. Based on 19.12.2 experience and on results from EFR program, with the aim of having a chemistry close to that of base metal, wires had been tested by achieving GTAW Narrow Gap (NG) joints. The undiluted chemistry of deposited weld metal is given in Table 3.

Table 3. Chemical composition of the automatic GTAW undiluted deposited metal from the tested wires

Wire	groove	Chemical composition of TIG deposited metal (wt%)					N ₂ analysis of TIG Wire (ppm)	Measured ferrite FN
		C	Ni	Cr	Mo	N ₂ (ppm)		
A	Narrow Gap U	0.025	11.83	18.17	1.95	636	470-552	4.5-5
B	Narrow Gap U	0.035	12.12	18.04	2.10	499	724-800	3
Base Metal 316L(N)		0.027	12.14	17.58	2.54	650	-	-

The characterization of this joint gives promising results, even if a narrowed chemistry composition range must be specified in comparison with 19.12.2 electrodes. The main challenge seems to be the control of chemistry modification between the wire and the deposited metal, like the evolutions of carbon or nitrogen, which are strong gamma-phase producing elements, influencing dramatically the ferrite in deposited weld metal. Further investigations are presently underway to test new welding products, with the aim to consolidate the chemical ranges, and to develop requirements and/or a technological test to insure the metallurgical weldability (like the crack test on joint made in vertical-up position for SMAW - RS 2536.5b and RS 9940 of RCC-MRx). In parallel, the mechanical behaviour of GTAW weld metals and weldments must be situated in relation to SMAW 19.12.2 grade.

2.2. Welding of Modified 9Cr-Mo Steel

Firstly developed for fast breeder reactor program, the grade 91 has wide applications in the power generation industry and more recently in petrochemical industry [5]. Mainly used for thin structures and with creep optimisation into consideration, the welding guidelines (EPRI, API recommendations [4][5]), conveying the manufacturer's practices, advice short PWHT (Post Welding Heat Treatment) at relative high temperature, typically 2h at 760°C.

For ASTRID, welds thicknesses are contained between 90 mm for steam-water circuit, 30 to 110 depending on SG design options. For these heavy or complex sections (with difference of thicknesses), a tolerance of $\pm 10^\circ\text{C}$ is necessary for monitoring the heat treatment, as illustrated by [5][6]. Furthermore, nuclear practice is to define two separate temperature ranges (Tempering/PWHT), and to perform mechanical characterizations after a Simulated PWHT including potential repairs, to ensure base metal non-affectation. With this approach, considering tempering temperature range of $770 \pm 10^\circ\text{C}$ for the base products and with 5°C of margin, a PWHT of $735\text{-}755^\circ\text{C}$ is considered as reference for ASTRID. So the range of $735\text{-}760^\circ\text{C}$ will be studied for long duration to include the accumulation of 2 minimum repairs.

During past R&D programs (EFR, HTR) [7][8], lots of filler products (SMAW, SAW & GTAW) had been characterized. From these investigations, preheat & interpass temperatures and welding parameters had been optimised, notably towards cold cracking risk. Concerning the filler metal composition, it is found that levels of Nb, V, N and Si must be maintained to relatively low levels with regard to toughness consideration. The addition of Ni and Mn is found to be beneficial for toughness, leading to choice of a range of Mn + Ni between 1.2 and 1.6.

Recently, it is observed a reduction of Mn+Ni content of commercial filler metals, due to a specification on an upper limit for Mn+Ni content: ≤ 1.5 from standards (EN ISO 21952, EN ISO 3580, SFA 5.28 and SFA-5.5 for SMAW and GTAW) and ≤ 1.2 or 1.0 from guideline recommendations [4][5]. Mn+Ni reduction is caused by problems on welding heat treatments, being

the main causes of premature weld failures in power plant industry, which are a non-complete austenite transformation to martensite before PWHT, or the exceeding of Ac1 temperature during PWHT, which leads to martensite formation during PWHT cooling.

As it is discussed hereafter, to obtain similar properties, and especially toughness and elongation, for the welded metal as for the base material, after a PWHT at 735°C in a reasonable time, Mn+Ni \geq 1.2 is found to be necessary. It should be noted that the margin between the higher PWHT temperature and Ac1 has yet to be measured.

The HTR program results [7][8] on 200 mm thick joint have shown the presence of microcracks about ~200µm long in melted zone of NG GTAW joint. These microcracks were attributed to hot cracking. After changing welding energy, tested several filler materials, either for direct welding of thick plates or for the welding of plates used for Vareststraint tests carried out in CEA, the following conclusions were drawn:

- Sulphur is an important parameter in the hot cracking phenomenon. This is confirmed by the presence of manganese sulphides along and inside the cracks. A filler material with very low sulphur content (a few ten of ppm) is needed to avoid cracking.
- Other parameters, like an important manganese to sulphur ratio and a chemical balance to allow a fully ferritic zone in the solidification path, seem to be favourable to avoid hot cracking.

Based on all these results, three wires have been characterized in GTAW, having similar Cr, Mo, Si, Nb, V, N levels, but with different C and Mn+Ni levels, as shown in Table 4. The only notable change in chemistry between the wire and the undiluted deposited metal of GTAW NG joints is a loss of C (~0.010%) and of Ni (~0.06%).

Table 4. Chemical composition of the automatic GTAW undiluted deposited metal from the 3 tested wires

	C	Mn+Ni	Cr	Mo	Si
Wire 1	0.08	1.74	8.92	0.89	0.23
Wire 2	0.127	1.41	8.91	0.94	0.23
Wire 3	0.144	1.28	8.85	0.98	0.24

The welded joints are characterized after different PHWT (t, T), and mechanical properties of the deposited metal are compared with the requirements of AWS A5.28 ER90S-B9 (in blue) and the requirements for base metal Grade 91 in RCC-MRx code (18AS material) (in red), as no "Reference data sheet of filler materials" is available. In addition to tensile properties and V-notch impact energy characterizations, a short creep test (175MPa – 550°C) has been done for concerned PWHT range, to accumulate data in order to be able in the future to specify a creep requirement.

Some of the measured properties (R_m and A% at 20°C, $R_{p0.2\%}$ at 550°C, creep rupture time under 175MPa-550°C, impact energy transition curves) are given in FIG. 2 for various PWHT through an time-temperature Hollomon-Jaffe parameter TP. These results show that about 10 hours of PWHT (at 735°C lowest temperature of PWHT range) are necessary to meet RCC-MRx base metal tensile requirements $R_m \leq 800$ MPa, A% $\geq 20\%$. Concerning A% $\geq 20\%$, a weak margin has been found even after PWHT of 10 h at 745°C. Margins are much higher with the requirements of standards (EN ISO 21952-CrMo91 & SFA-5.28-ER90S-B9) on deposited metal (A% $\geq 17\%$). The Charpy transition curves show a good toughness of GTAW deposited metal with a high upper shelf and a low transition temperature, giving a mean impact shock energy ≥ 40 J at -20°C for a PWHT 20 h at 750°C. But these data reveal a detrimental role of high carbon levels, leading to an increase in transition temperature and to a degradation of toughness for high (t,T) PWHT. It should be noted, that an optimisation of heat reaffected of pass n from the deposit of pass $n+1$, have an important role in transition temperature brittle/ductile [investigations in progress].

Finally these investigations show that the grade 91 welded metal from low carbon content wire presents acceptable properties for PWHT between [10 h-735°C to 40 h-760°C] (represent by the two vertical lines), even if the creep properties decline significantly for high (t,T) PWHT.

Through testing different filler batches of wire 1, the influence of sulphur on hot cracking is found again. Few microcracks in melted zone of a NG joint of 85 mm thick with a wire having 0.005 %S have been observed, whereas for lower content 0.003 %S no microcrack had been found. With the higher sulphur content (0.005 %S) representative of the lowest industrial specification for commercial filler products, a larger V-groove (chamfer angle of 15°, against 1° for NG) and pure argon as welding gas (against He-Ar for NG joint) no microcrack had been found, showing an important influence of welding conditions.

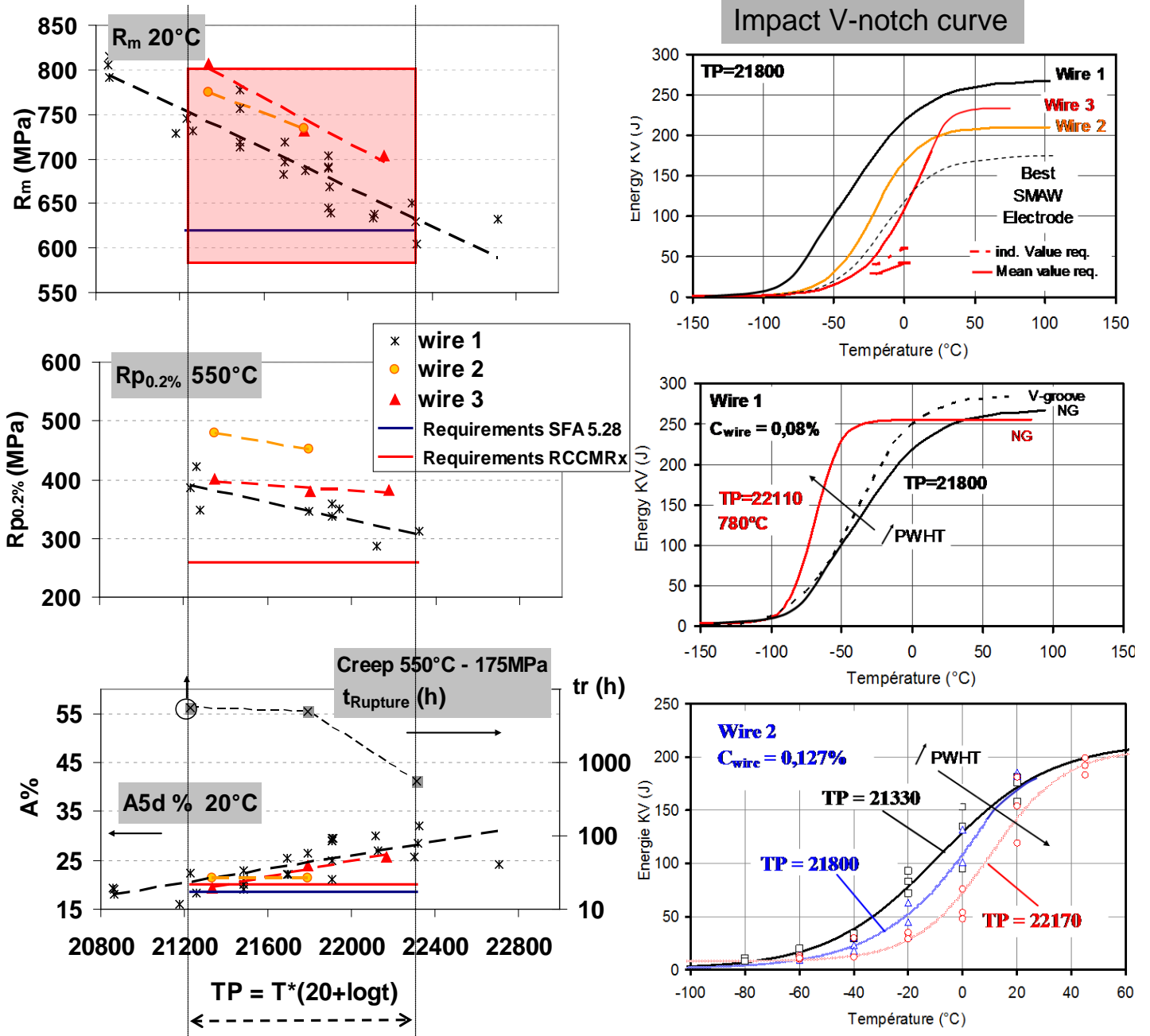


FIG. 2. R_m and $A\%$ at 20°C, $R_{p0.2\%}$ at 550°C, creep rupture time (550°C-175MPa), impact energy transition curves for various PWHT through an time-temperature Hollomon-Jaffe parameter TP – Comparison of the 3 wires

On impact transition curves in FIG. 2, the behavior of the best SMAW electrode is added, showing that due to an oxygen level higher in SMAW deposited metal (~500 ppm) than in GTAW deposited metal (≤ 40 ppm), a higher transition temperature and especially a weaker upper shelf energy are found. An extent work on SMAW optimisation have nevertheless permit to respect all tensile (at RT & 550°C) and toughness requirements, but leading to very narrowed composition ranges, and a

significant degradation of creep properties. So GTAW will be considered as reference process, even for welds repairs in manual mode.

3. Hardfacing challenges for in-sodium application

3.1. Evaluation program methodology

The experimental program initiated aims to evaluate the performance of alternatives to cobalt-base alloys when subjected to various solicitations in liquid sodium. Indeed contact and friction zones in FBR-Na might be subjected to high temperature, sodium corrosion, severe contact pressure, cycling, friction... depending on the considered zone. The solicitations applied during the various tests are chosen in accordance with the expected solicitations for different contact zones of ASTRID.

Functions of contact zones are very different when considering a zone or another one: guarantee of no self-welding, need for low friction coefficient, enabling thermal dilatations... Thus drastic changes of design and process are expected and it is foreseen that there is no universal solution for contact and friction zones. As a first step, only "thick" deposits of weldable alloys will be considered (from hundreds of μm to $\sim 2\text{ mm}$) in the experimental program. Surface treatments and thin deposits will potentially be subsequently added to the experimental program.

The challenging issue of the evaluation of alternatives lies in the fact that hardfacing performance relies on several aspects [9]: alloy composition, choice of the deposition process (and of its correct parameters set) and tribological system (and associated physical degradation mechanisms). This potentially leads to an infinity of solutions: we hereby present the strategy adopted by the workgroup to address this "choices" issue and to evaluate a reasonable set of them.

3.2. Hardfacing - processes and materials

After discussion and feedback study, only nickel-base grades are integrated to the experimental program. Indeed, iron-based and copper-based grades, that are also used as hardfacing materials for other industrial applications, can not be considered for contact zones in sodium as the minimum operating temperature is about 400°C .

For both deposition processes and materials, a distinction is made between industrially available options (sometimes already qualified for nuclear applications) and other ones that still require a substantial R&D effort. The focus will be initially on the first ones as relatively short-term applications are primarily aimed. Discussion within the workgroup and with potential providers led to the following choice:

- First studied Ni-base alloys:
 - Colmonoy® grade 5 type alloys that receives a subsequent feedback in sodium applications [10][12][13],
 - Tribaloy® 700 type alloys that were considered in the late R&D programs [10]-[13]
 - and Nucalloy® 453 type alloys that are nowadays considered for some cobalt-free applications.
- Plasma Transferred Arc Welding (PTAW) as a promising deposition process. Among weld hardfacing processes, PTAW has the advantage of a low dilution and an easy automation.

In addition, partners and laboratories will allow the evaluation of other medium-term options:

- Thermal or Cold spraying and Laser welding as innovative processes,
- Composite hardfacing of nickel metallic matrix (grades being commercially available or not) with carbides charges.

3.3. Samples description, procurements and fabrication monitoring

To make an easier comparison between samples, it was chosen to impose the substrate geometry and material. Plates of 316L(N) steel were prepared according to FIG.3. Providers were then asked to deposited hardfacing material on the plates at their convenience in order to reach a minimum deposit width of 2 mm after potential removing of the last layer and facing operations. In case more than one layer/pass is required to obtain this thickness and aimed final properties, they were asked to shift each

layer ending in order to allow further characterizations (including study of multi-pass reheating potential effect). This is illustrated in FIG.4, respectively for single and multi-pass deposits. Performance of hardfacing materials often being linked to the manufacturer, it has been decided to procure samples from several providers. Then a variation of welding/deposition parameters of provided samples is unavoidable since no process parameters were imposed. In order to compare characterization results with a reasonable understanding, a specific documentation effort is asked for the following steps in samples manufacturing:

- Plate preparation and cleaning;
- Raw Hard-facing materials sampling;
- Pre and post-heating characteristics;
- Operator and Machine identification;
- Welding procedure including machine adjustments, welding speeds (feeding, oscillations), layers geometries bead orders and directions;
- Recording of at least one temperature at any point of the substrate with thermocouple or pyrometer during the whole process including post and pre-heating.

A result of such a fabrication is presented in FIG.5, for Stellite© 6 alloy. Those samples will be used as the reference during sample characterizations.

Those data are expected to explain the differences in characteristics - should they occur - that could exist between samples of the same grades provided by different manufacturers. It could possibly also facilitate some numerical simulation of welding.

All the samples will be conventionally machined then grinded after deposition in order to reach a surface roughness of $0.4 \mu\text{m}$. To avoid any further differences between samples due to facing operation, all samples are machined and grinded at the same workshop with the same procedure.

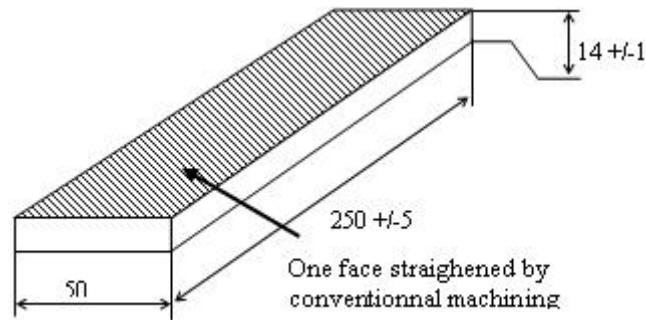


FIG. 3. Substrate geometry and preparation

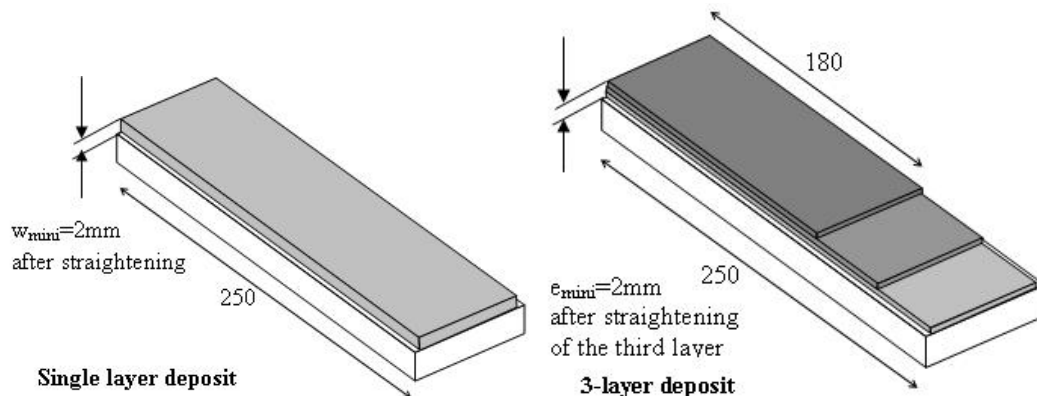


FIG. 4. Single layer and multi-layer deposit



FIG. 5. Stellite® 6 sample

3.4. Evaluation program samples - Initial characterization

To obtain a full understanding of tribological properties for hardfacing material, numerous tests are required; moreover, depending on the aimed application. Other properties as thermal shock resistance or mechanical shock resistance, which require the achievement of other different qualities. Thus, it was decided to split investigations in two separate phases.

The first phase should allow to discriminate promising solutions and to eliminate the least satisfactory ones. Many contact and friction applications involving use of structures during the reactor life, the study of thermal ageing at different temperatures (until 550°C) during different durations (up to 50 000 h) of the grinded sets is included in this first phase. Characterization of the as-grinded samples and thermal aged samples will consist in:

- Detailed metallographic examination and micro-hardness profiling to characterise structure, chemistry and quality of the hardfacing deposits;
- In-sodium corrosion tests in CORRONa testing device [14]. Corrosion tests temperatures and durations are chosen in order to understand long-term corrosion phenomena and their kinetics.
- In-sodium tribological tests in a specific module of CORRONa² testing device. Tests parameters will cover a large set of solicitations in order to evaluate performance for extreme service conditions: high pressure / small displacement, low pressure / large displacement...

At the end of this first phase, materials presenting unacceptable behaviour, in particular towards thermal aging, will be eliminated from the experimental program. Those with promising properties towards given solicitations will be associated with corresponding applications in ASTRID and further characterized.

3.5. Evaluation program on samples - Perspectives

Promising alternatives will then be subjected to a second phase of study in order to get other major properties as:

- Mechanical properties: flexion tests, toughness and impact tests, thermal shock resistance, mechanical shock resistance...
- Influence of welding parameters and facing operations on properties: a new set of experiments will be planned in order to determine the characteristics dependence according to process parameters.

Systematic in-sodium characterisation being constraining, the development of out-of-sodium tribological device is foreseen to facilitate the characterisation of numerous welding parameters and tribological parameters.

The ultimate step in the choice of an alternative to cobalt-base alloys for a given application will be to evaluate the performance of the planned alternative in representative conditions (environment and tribological system). Indeed, in this presented experimental program solicitations are considered independently from each other and manufacturing issues as dimensional tolerances and deformations are not studied. This last step will be the subject of a specific qualification program for each application.

4. Conclusion remarks

In the framework of ASTRID, developments of Welding and Hardfacing Technology are undertaken through the evaluation of different solutions (non commercial electrodes & experimental solid wires for 316L(N), experimental & commercial solid wires for grade 91, nickel-base hardfacings). Valuable experience gained from these technology developments will extend inputs to enable design engineers to define welding and hardfacing products specifications, to finalize design of components.... Further steps should integrate a qualification approach of products and processes, and should conduct industrial developments to solve manufacturing issues as the development of alternatives processes (EBW, GMAW...), parts alignment issues for Narrow Gap welding, specific developments for made-to-measure tube-to-tubesheet welding, chosen alternative hardfacing solutions for a given application, dimensional tolerances and deformations for alternative hardfacing.... In support of that work a large long-term R&D program on representative joints and hardfacing sollicitate under representative conditions (sollicitation, environment and reibological system...) will be conducted.

REFERENCES

- [1] M. Saez, S. Menou, B. Uzu, The pre-conceptual design of the nuclear island of ASTRID, Proceedings of ICAPP'12, Chicago, USA, June 24-28, 2012, Paper 12070
- [2] RCC-MRx 2012"Design and Construction Rules for Mechanical Components of Nuclear Installations", www.afcen.com.
- [3] S. Nagaraju et al., Novel method for quantative assessment slag detachability in austenitic stainless steels welds made by SMAW, Science and Technology of Welding and Joining, Vol 13 N°8 (2008) 739-743
- [4] EPRI Report 1023199 2011 - Guidelines and Specifications for High-Reliability Fossil Power Plants - Best Practice Guideline for Manufacturing and Construction of Grade 91 Steel Components
- [5] API Technical Report 938-B, Use of 9Cr-1Mo-V (Grade 91) Steel in Oil Refining Industry, first edition, June 2008
- [6] F. William & Newell JR., Welding and Postweld Heat Treatment of P91 Steels, Welding Journal April 2002, 33-36
- [7] Séran J.L. et al., Development of 9-12Cr martensitic steels for future nuclear systems: Weldability studies, mechanical characterizations and specification improvements, Proceedings HTR2006: 3rd International Topical Meeting on High Temperature Reactor Technology, Oct. 1-4, 2006, Johannesburg, South Africa
- [8] B. Riou, C. Escaravage, D. Hittner, D. Pierron, Issues in Reactor Pressure Vessel materials, 2nd International Topical Meeting on High Temp. Reactor Technology, Beijing, CHINA, Sept.r 22-24, 2004
- [9] P.H. Shipway, The range of surface coating methods, ch.3 in: Surface coating for protection against wear, Ed. B.G. Mellor, Woorhead Publishing in Materials
- [10] R.N. Johnson, Tribological coatings in liquid metal and irradiation environments, J. Materials for energy system, Vol 8, No1, 1986
- [11] R.N. Johnson, D.G. Farwick, Firction wear and corrosion of Laves-hardened nickel alloy hardsurfacing in sodium, Thin Solid Films, 53 (1978) 365-373
- [12] R. Bassani et al, Etude technico-economique sur le revêtement interne des chandelles de sommier d'un réacteur à neutrons rapides, Proceedings of the 4th international conference on liquid metal engineering and technology, Oct. 17-21, 1988, Avignon
- [13] Y. Depierre, J. Raffailhac, Characterizing the tribological behavior of fast breeder reactor materials, Proceedings of the 3rd international conference on liquid metal engineering and technology, April 9-13, 1984, Oxford
- [14] J.-L. Courouau, F. Balbaud-Célérier, V. Lorentz, T. Dufrenoy, Corrosion by liquid sodium of materials for sodium fast reactors: the CORRONa testing device, International Congress on Advances in Nuclear Power Plants (ICAPP 11), paper 11152, Nice, France, 2011

Qualification of the materials of ASTRID for 60 years lifetime

S. Dubiez-Le Goff^a, F. Dalle^b, M. Blat-Yrieix^d, J.-M. Augem^c

^a AREVA NP, Lyon, France

^b Commissariat à l'Energie atomique et aux Energies Alternatives, Saclay, France

^c EDF SEPTEN, Villeurbane, France

^d EDF R&D, Les Renardières, France

Abstract. An important issue of the qualification of the materials for the next generation of plants is the demonstration of their behavior up to 60 years. Representativeness of the experimental tests is one point to manage, using relevant ASTRID products and covering base metal and weldment characterization, including bimetallic junctions. The completion of the qualification of materials in representative conditions of a component operation is a key point.

From the design point of view, the final objective is to get the completion of the RCC-MRx database up to 60 years. This concerns the following properties:

- Creep rupture strength
- Creep strain laws
- Aging coefficient
- Toughness/RTNDT after aging (for modified 9Cr1Mo only)
- Fatigue curves, particularly for high cycles fatigue domain.
- Creep-fatigue interaction diagram (if changed)
- Weld coefficients.

1. Introduction

Sodium Fast Reactor (SFR) is considered in France as the most mature technology of the different Generation IV systems. In this context, the CEA is involved in a substantial effort on the ASTRID (Advanced Sodium Technological Reactor for Industrial Demonstration) pre-conceptual design mainly in cooperation with EDF, as experienced Sodium-cooled Fast Reactor (SFR) operator, and AREVA, as experienced SFR Nuclear Island and components engineering company.

In that frame, materials selection for the major components is a particular key point managed within a French Research and Development program launched by CEA, EDF and AREVA. Moreover previous SFRs were designed for 30 or 40 years lifetime. It is specified for ASTRID to have accurate data available for 40 years lifetimes before commissioning and to demonstrate during the reactor operation the possibility to reach 60 years of lifetime. The following chapters aim at identifying the materials items significantly affected by an extended lifetime up to 60 years: properties evolution and damages worsening.

2. Materials selection

2.1. Primary circuits

It is likely that the austenitic stainless steel X2CrNiMo17-12-2 with controlled nitrogen content, also called, “316L(N)” following the ASTM/ASME designation, will be the reference material for the vessels and internal components like (see Figure 1, [1]):

- Above Core Structure (ACS),
- Core support (diagrid and strongback)
- Decay Heat Removals (DHR);
- and the Intermediate Heat eXchangers (IHX).

A good confidence is acquired for this material thanks to the experience and large R&D database available from SUPERPHENIX. RCC-MRx Code [2], Tome 2, supplies therefore Reference Procurement specifications for forged parts as bars and plates, sheets and tubes in 316L(N) [3].

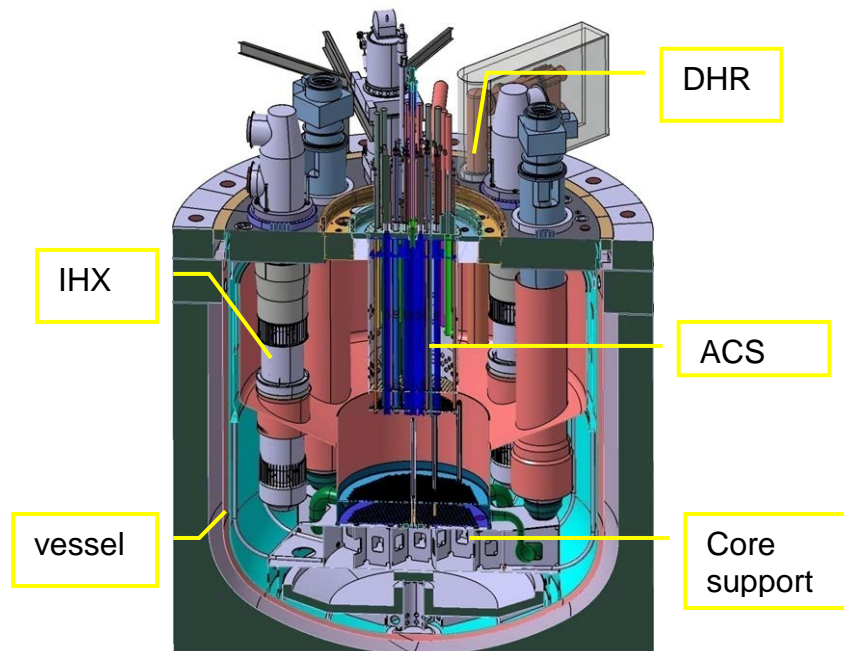


FIG. 1. Primary circuit architecture

ASTRID Project Business Confidential Information, CEA and AREVA NP property designs [1]

2.2. Steam generator

The choice of the material for the steam generator, with expected in-service temperatures range between 240°C and 530°C, is complex because various aspects shall be considered like mechanical and thermal properties, interaction with sodium on one side and water and steam on the other side, resistance to wastage, procurement, fabrication, weldability and ability for inspection and in-situ intervention. At this stage of ASTRID program, the following relevant options are kept, depending on the Steam Generator Unit (SGU) design (see Figure 2):

- For a helically-coiled SGU, the X5NiCrTiAl133-21 nickel-iron-chromium alloy after annealing heat treatment, also called Alloy 800 following ASTM/ASME designation, has been selected.

This choice arises from SUPERPHENIX feedback. RCC-MRx Code [2], Tome 2, supplies therefore Reference Procurement specifications dedicated to this application: tubes and bars (for the sleeves) in Alloy 800.

- For a straight tube SGU, the X10CrMoVNb9-1 ferritic-martensitic steel, also called 91 grade following ASTM/ASME designation, has been selected. This type of steam generator had been evaluated for the European Fast Reactor (EFR) project. This grade then benefits from a huge data base and RCC-MRx Code [2], Tome 2, supplies Reference Procurement specifications dedicated to this application: tubesheet, sheet and tubes grade 91.

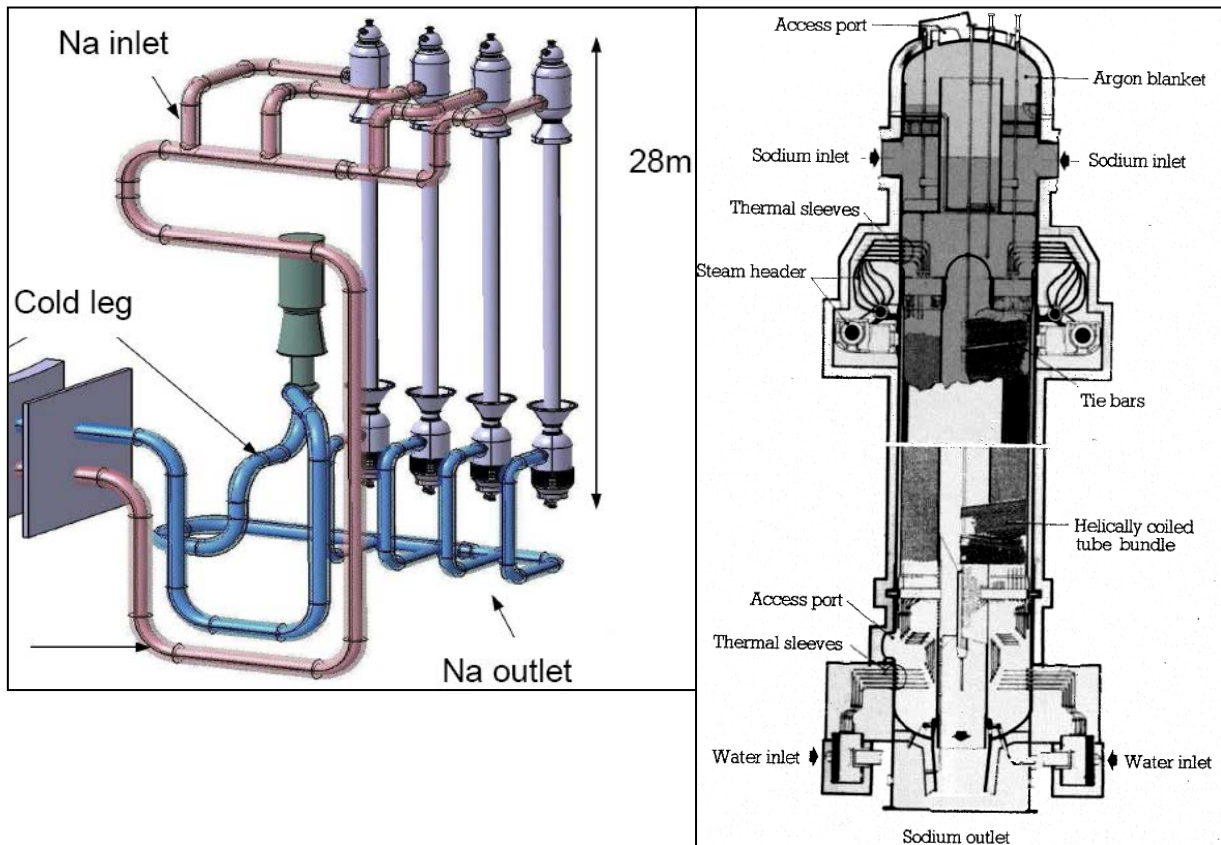


FIG. 2. Left - Straight tube in modified 9Cr1Mo ferritic steel, 125 MWth SGU concept;
Right - Helically-coiled SGU of SUPERPHENIX (Ref. 2)

It may be noticed that Gas Power Conversion Systems (GPCS) are also considered for ASTRID to suppress the sodium/water reaction which could occur in steam generators in case of tube failure. Those innovative systems will not be detailed in this paper, but a specific R&D and qualification material program is identified too.

3. Qualification program

The key point is that representative ASTRID products have to be tested to be compared with the current RCC-MRx [2] database:

For the 91 Grade:

- plates
- thick plate (for the tubesheets)

- vessels
- exchanger tubes
- welded joints: plate-plate, tubes-plate, thick plate–vessel, bimetallic weldments with sodium, water and steam circuits

For Alloy 800

- exchanger tubes
- bars (for steam generator thermal sleeves)
- welded joints: plate-plate, tube-bar, bimetallic weldments with sodium, water and steam circuits

For 316L(N)

- plates
- thick plate (for the tubesheets)
- vessel
- exchanger tubes
- welded joints

A huge program has already been launched to get supply of representative ASTRID products, it is particularly emphasized for those not already or partially covered by the RCC-MRx Code:

- tubesheet in 316L(N) (for IHX) and in 91 grade (straight tube SGU) thicker than in former SFRs
- seamless vessels in 316L(N) for some internals and in 91 grade for the straight tube SGU
- 316L(N) weldments with the austeno-ferritic 19Cr12Ni2Mo weld metal (19.12.2). The 19.12.2 electrode used for SMAW for former French SFRs construction is no more marketed and solid wire has to be developed for automatic GTAW process [4].
- 91 grade weldments with “nuclear grade quality ” has still to be developed. Recent data lead to considered GTAW has the reference process. The paper “IAEA-CN-199/348” of this Conference [4] details all the parameters to be managed to meet ASTRID requirements.
- Alloy 800 weldments with ERNiCr-3 weld metal: the feedback from SUPERPHENIX prompts to keep the same weld metal.
- All bimetallic weldments between the SGU and the steam/water circuits have to be qualified particularly for weldments in-service at temperature higher than 375°C.

These products are called “specific ASTRID products” hereafter.

3.1. In-service materials properties evolution

3.1.1. Creep rupture strength and creep strain laws

3.1.1.1. Current RCC-MRx data status

Creep rupture stress data are supplied by RCC-MRx (Section III – Tome 1 – Subsection Z – Appendix A3) up to:

- $3 \cdot 10^5$ h for the 91 grade and for the 316L(N).

— $2 \cdot 10^5$ h for the alloy 800 for temperatures covering the hottest parts of the SG.

These durations correspond respectively to 38 years and 25 years of operation with a reactor availability of 90%.

The presence of weldments is considered by corrective coefficients estimated by experimental tests and integrated in the structural analysis of structures supposed exempt of weld. The creep properties of welded joints have been defined in the RCC-MRx through Jr coefficients ($J_r < 1$) to be multiplied to creep rupture stress of base metal. Jr is currently supplied for some welded joints on 91 grade and 316L with controlled nitrogen, not for Alloy 800.

3.1.1.2. Qualification needs

As shown in the previous paragraph, the current creep to rupture data base has then to be extended to meet the ASTRID lifetime target. Two types of creep tests are foreseen:

- Very long term creep tests at in-service temperature, with time to rupture expected to reach approximately 1/3 of the target lifetime. This ratio is considered as a minimum to be able to extrapolate with good confidence an expected creep life; this recommendation leads to 12 years or 18 years of test and for respectively 40 or 60 years lifetime.
- Long term creep tests at temperature higher than the in-service temperature. Time-temperature equivalence allows indeed a compensation of the time increase by a rise of the testing temperature. This process is efficient if it can be guaranteed that the rise in temperature does not change the mechanisms of viscoplastic deformation and of damaging. An increase of 25°C must be considered as a maximum. As an example, at 550°C , a range of $+4,5^\circ\text{C}$ corresponds to a factor 1.5 on the time and to a variation of 5% on the stress level with the 91 grade parameters.

Huge data bases with long term tests are already available for grade 91, Alloy 800 and the 316L(N) base metals. For ASTRID the efforts of qualification lie in achieving creep results on the specific ASTRID products, particularly on weldments.

Besides the creep strain is acquired with extensometers during the whole test duration; this permits to fill in also the data base for creep strain laws definition.

3.1.2. Aging coefficient

3.1.2.1. Current RCC-MRx data status

In the RCC-MRx code, thermal aging is modeled through:

- thermal border lines
- aging factor,
- and toughness

Thermal aging effect is currently supplied for 316L(N) through the toughness data on weld metal (19Cr12Ni2Mo). It is not supplied for grade 91 and Alloy 800.

3.1.2.2. Qualification needs

Thermal aging is likely to affect base metal and welded joints: a discrepancy of the instantaneous properties is likely to appear between the beginning and the end of the components life and has to be evaluated. Indeed, above a certain operating temperature, those properties may display a sharper change than the creep characteristics, especially

- tensile strength,
- toughness
- and creep strength to rupture at short times (less than 1 000 h),

The qualification program is built to cover these properties on the specific ASTRID products.

For the 91 grade a particular point to check is the possible shift of the ductile brittle transition temperature. The final objective would be to define the same type of curve as available in RCC-M [5], see Figure 3, for low alloyed manganese-nickel-molybdenum steels, where the reference critical stress intensity factor (K_{IR}) is determined as a function of:

- The material temperature T at the point in time and the location in the structure for which fast fracture analysis is being performed,
- the reference transition temperature RT_{NDT} for the material under consideration

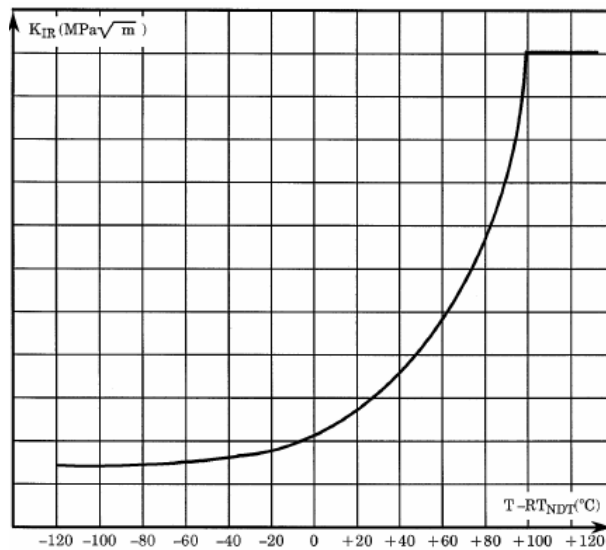


FIG. 3. Reference critical stress intensity factor K_{IR} as function of the temperature T and of the material transition temperature RT_{NDT}

3.2. Damages worsening by extended life time up to 60 years

3.2.1. Fatigue curves and creep-fatigue interaction diagram

3.2.1.1. Current RCC-MRx data status

RCC-MRx code provides cyclic curves, fatigue curves and creep-fatigue diagram for our three materials of interest. As represented in Figure 4, the creep fatigue interaction diagrams are bilinear and the intersecting point is (0.3-0.3) for all three in the RCC-MRx. For comparison, creep-fatigue diagrams in ASME are more severe than the diagram used in Europe for Alloy 800 and modified 9Cr1Mo: all are bilinear but the intersecting point is (0.12-0.12) for Alloy 800 and (0.1-0.01) for modified 9Cr1Mo according to the ASME, instead of (0.3-0.3) for stainless steels.

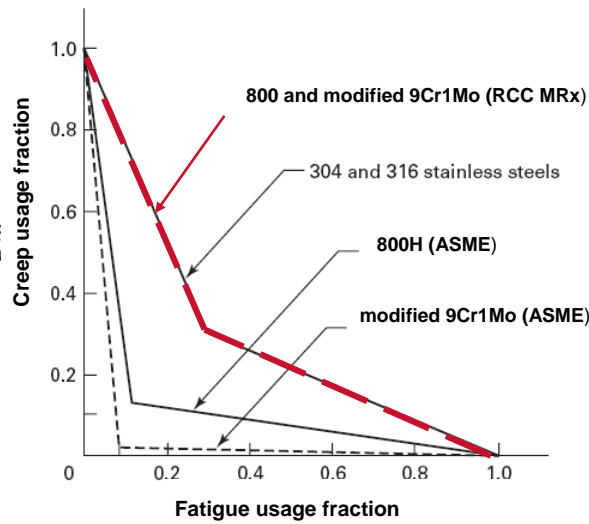


FIG. 4. Creep-fatigue interaction diagram according to Ref. [2] and[8]

3.2.1.2. Qualification needs

The conservatism of the fatigue curves and the creep-fatigue diagrams has to be confirmed with low strains and long hold time for creep-fatigue, which are representative of in-service conditions.

For the creep-fatigue damage, the 316L(N) is well known to be quite stable and there are a lot of data coming from creep fatigue tests. But the graphic on Figure 5 clearly demonstrates that

- low strains (solid line) are more damaging than large ones (dashed line)
- long hold times are more damaging than short ones

These kinds of tests have to be performed to increase confidence in relation with the extension of the design life, on Alloy 800 too.

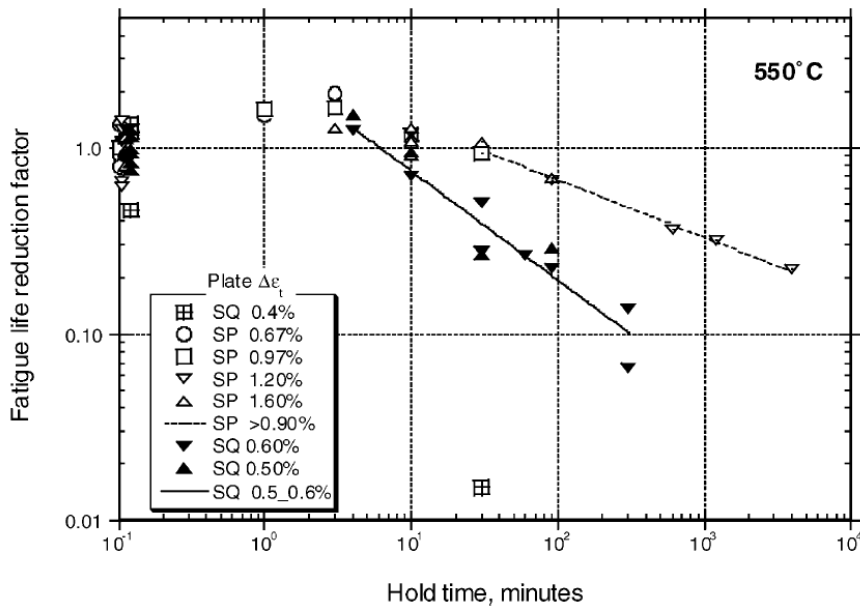


FIG. 5. Fatigue life reduction factor with respect to the hold time. Large and small strains, 550°C. The fatigue life reduction factors are defined as the ratios between the fatigue life measured for a given hold time and the fatigue life without hold time [6]

Problematic is different for grade 91 because ferritic-martensitic steels have opposite cyclic behaviour as compared with stainless steel: the former deconsolidates whereas the latter consolidates with cycles.

As shown in Figure 6, there is a significant increase of the creep rate measured during the creep maintain of the creep fatigue tests, as compared with the pure creep tests.

Creep fatigue tests are needed on specific ASTRID products to quantify the softening of the products as a function of representative in-service sollicitation of the SGU.

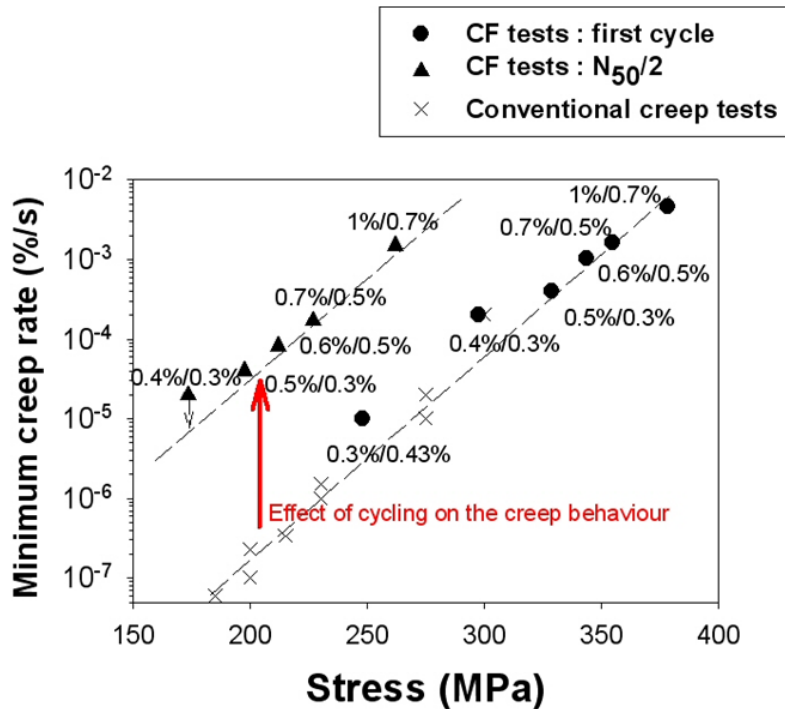


FIG. 6. Comparison between the minimum creep rates measured at the first cycles of creep fatigue tests, at $N_{50}/2$ of the same creep fatigue tests, and in conventional creep tests. The dashed lines schematize the relationship between the minimum creep rate and the applied stress. Each point corresponds to a creep fatigue test identified by the value $\Delta\epsilon_{fat}/\epsilon_{creep}$ [7]

3.2.2. Irradiation effects

3.2.2.1. Current RCC-MRx data status

Concerning the irradiation effects, it was shown in the past that the main vessel and internals were subjected to negligible irradiation. The life extension necessitates reconsidering the doses seen by the new structures: due to the more compact design, the closest structures to the core may be submitted to a higher neutron dose (i.e. ACS and diagrid). The consequences of such an irradiation, up to 60 years, shall be established and limited if needed.

Irradiation data are supplied in RCC-MRx for 316L(N) through border lines (negligible and maximal irradiation), tensile properties and toughness.

3.2.2.2. Qualification needs

To enrich the current data base, irradiation exposures are needed:

- At in service temperature (cold plenum for the diagrid and hot plenum for the ACS)

— At low dose

Particular needs are identified on welded joints due to their higher ferrite content, more sensitive to irradiation damage.

4. Conclusion

The completion of the qualification of materials in representative conditions of operation and on “specific ASTRID products” is a key point for ASTRID demonstrator. From the design point of view, the final objective is to get the completion of the RCC-MRx database up to 60 years.

ACRONYMS

ACS : Above Core Structure

DHR : Decay Heat Removal

EFR : European Fast Reactor

IHX : Intermediate Heat eXchanger

PCS: Gas Power Conversion Systems

SFR : Sodium Fast Reactor

SGU : Steam Generator Unit

REFERENCES

- [1] Manuel SAEZ et al, Status of ASTRID nuclear island pre-conceptual design, ‘International Conference on Fast Reactors and Related Fuel Cycles: Safe Technologies and Sustainable Scenarios’, Paris, France (March 2013)
- [2] RCC-MRx 2012 - AFCEN Code - Design and construction rules for mechanical components of nuclear installations
- [3] D. Bonne et al, Proceedings of the ASME 2010 Pressure Vessels & Piping Division, PVP2010, July 18-22, 2010, Bellevue, Washington, USA
- [4] T. Marlaud et al, Development of Welding and Hardfacing Technology: challenges for ASTRID project, ‘International Conference on Fast Reactors and Related Fuel Cycles: Safe Technologies and Sustainable Scenarios’, Paris, France (March 2013).
- [5] RCC-M, 2007 addenda 2010, Design and Conception Rules for Mechanical Components of PWR Nuclear Islands
- [6] M. Sauzay, et al, Creep-fatigue behaviour of an AISI stainless steel at 550 °C, Nuclear Engineering and Design 232 (2004) 219–236
- [7] B. Fournier et al, Creep-fatigue interactions in a 9 Pct Cr-1 Pct Mo martensitic steel: Part I. Mechanical test results, Metallurgical and materials transaction A, Volume 40A, February 2009-321
- [8] ASME Boiler and Pressure Vessel Code - 2010 Edition

OPTIMIZATION OF THE FABRICATION ROUTE OF FERRITIC/MARTENSITIC OXIDE DISPERSION STRENGTHENED CLADDING TUBES: METALLURGICAL APPROACH AND PILGERING NUMERICAL MODELING

L. Toualbi^a, E. Vanegas-Marquez^b, K. Mocellin^c, R. Logé^c, Y. Chastel^d, Y. de Carlan^e

^aNuclear Materials Department, Nuclear Energy Division, French Alternative Energies and Atomic Energy Commission, Gif sur Yvette, France, now ONERA, Châtillon, France

^bMines ParisTech, CEMEF, Sophia-Antipolis, France, now LISI Aerospace, Villefranche de Rouergues, France

^cMines ParisTech, CEMEF, Sophia-Antipolis, France

^dMines ParisTech, CEMEF, Sophia-Antipolis, France, now Renault, Guyancourt, France

^eNuclear Materials Department, Nuclear Energy Division, French Alternative Energies and Atomic Energy Commission, Gif sur Yvette, France

Abstract. Oxide Dispersion Strengthened ferritic / martensitic alloys are developed as prospective cladding materials for future Sodium-Cooled-Fast-Reactors (GEN IV). These advanced alloys exhibit a good resistance to irradiation and a high creep rupture strength due to a reinforcement by the homogeneous dispersion of hard nano-sized particles (such as Y_2O_3 or $YTiO$). ODS alloys are fabricated by powder metallurgy, consolidated by hot extrusion and manufactured into cladding tube using the pilger cold-rolling process. ODS alloys exhibit low ductility and high hardness at room temperature which implies intermediate softening heat treatments. Fabrication route optimization is needed to ensure a reliable manufacturing and reduce the cladding tube anisotropy. A better understanding of the deformation paths and of the constitutive laws is required and obtained by simulation of the HPTR cold pilgering process. The specific metallurgy of ODS materials has to be well known and controlled. This paper presents the combination of metallurgical and numerical approaches leading to the determination of the key points which should conduce to an optimization of the fabrication route of ODS cladding tubes.

1. Introduction

Among the various solutions available for consideration, for cladding purposes, with regard to fuel elements for the fourth-generation sodium-cooled fast reactors, ODS materials – i.e. oxide-dispersion strengthened materials – afford many benefits. Indeed, these high performance materials combine, at the same time, remarkable mechanical strength at elevated temperature, and outstanding irradiation behavior [1-7].

In order to enhance the neutronic performance of such reactors, the core design requires a closer-packed fuel-element bundle, i.e. one involving larger-diameter fuel pins and thinner spacer wires inserted between the cladding tubes, than those used in the Phénix (PX) or Superphénix (SPX) fast reactors (Figure 1).

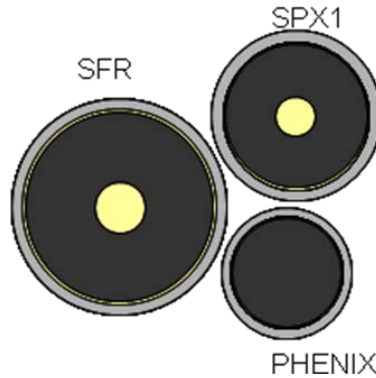


Figure 1: Sectional view of the fuel and cladding used for the Phénix and Superphénix fast reactors, and for the future SFR

To preclude any excessive deformation of the fuel pins, it is essential that the cladding material exhibit a limited swelling under irradiation. At the same time, in order to achieve optimization in economic terms, the target burnup would result in doses higher than those allowed for the cladding material used in Phénix, namely a 15–15 Ti austenitic steel. This, new alloys must be developed, e.g. ODS steel grades, exhibiting better performance levels than the last-generation austenitic steels designed for deployment in the Phénix, and Superphénix reactors (Figure 2) [1].

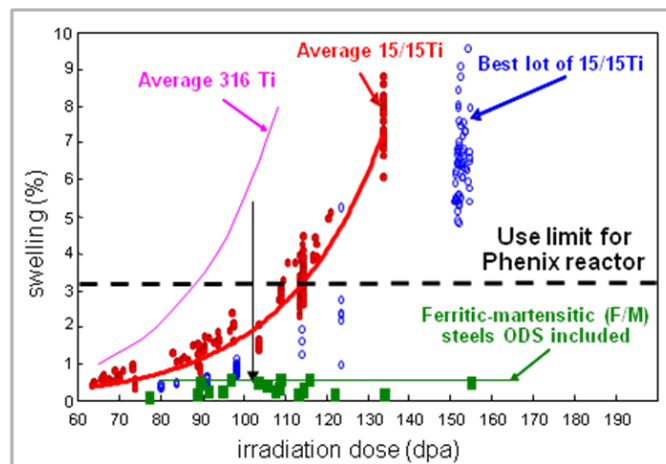


Figure 2: Irradiation induced swelling for different materials [1]

ODS materials afford not only negligible swelling under irradiation (Figure 2), owing to their body-centered cubic structure – by contrast to austenitic grades, which feature a face-centered cubic

structure – but equally outstanding creep properties, thanks to the nano reinforcements present in the matrix (Figure 3).

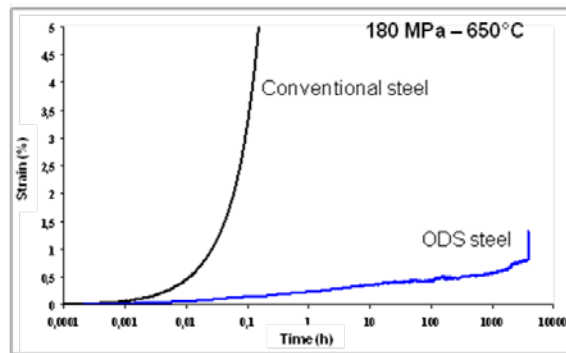


Figure 3: Creep curves of a conventional ferritic alloy, compared to that for a nano-reinforced 18Cr-ODS material

2. ODS metallurgy

Conventional metal forming techniques, involving processes of the melt type, followed by casting of the grade, do not allow materials containing fine oxide particles to be obtained. When oxides are introduced into the material at the molten stage, they either react with the furnace crucible or are no longer to be found after casting, or they coalesce within the liquid bath, yielding oxides that are too bulky to result in a reinforcement effect in the material.

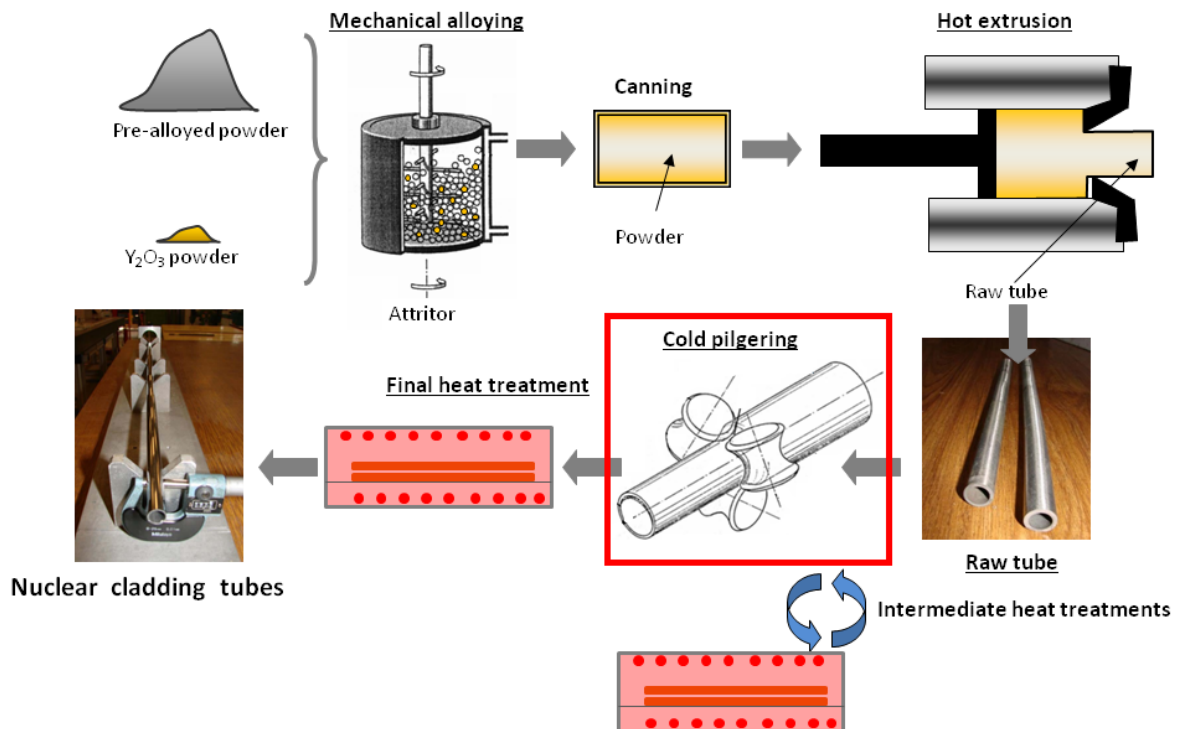


Figure 4: Standard fabrication sequences of ODS cladding tubes

It is thus necessary to go for mechanical synthesis, using a pathway hailing from powder metallurgy, commonly known as mechanical alloying. The standard fabrication sequence, for ODS materials, involves several steps (Figure 4). ODS materials are obtained by powder metallurgy, the first fabrication step involving cogrinding a metal powder together with yttrium oxide (Y_2O_3) powder. This mechanical alloying step yields to a powder which may be described, as a first approximation, as a metallic matrix, holding all of the alloying elements in a solid solution. Once the powder has been obtained, consolidation of the ODS materials is achieved either by hot extrusion, or by hot isostatic pressing. Subsequently, the cladding tube is cold formed by a sequence of cold pilger rolling passes with intermediate heat treatments, for stress relief purposes. It is on this last step that this work is focused.

Cold pilgering process

The HPTR (High Pressure Tube Reducer) cold pilgering process is a seamless tube forming operation where the tube is repeatedly rolled over a fixed cylindrical mandrel by three grooved dies. During this process the inner radius and wall thickness are both progressively reduced. After each back and forth movement (stroke) of the dies, the raw tube is advanced by a small distance and rotated around its axis. A material volume element undergoes typically several dozens of strokes before deformation is completed [8]. This complex mechanical history may lead to the nucleation of defects (longitudinal cracks) in low-cycle fatigue regime [9].

ODS specificity

It is now generally agreed that the mechanisms involved in the formation of nanophases, in ODS alloys, include the dissolution of yttrium oxides during grinding and a precipitation of nanophases (Y, Ti, O) during the hot consolidation step.

The nano precipitates giving their high mechanical properties to the ODS materials are thus present at the consolidation step. That is why ODS mother tubes exhibit, just after hot extrusion, low ductility and high hardness at room temperature which complicates their manufacturing. This low cold workability implies intermediate softening heat treatments during the fabrication route [7, 10-12]. Based on previous studies on ODS steels a hardness value below 400 HV1 is needed to avoid damage during manufacturing [12].

3. Fabrication route

The ODS fabrication route optimization studies have to combine both metallurgical understanding of the material behavior and numerical simulation of the process. Once the material behavior is investigated, the deformation path needs to be known and controlled.

Metallurgical approach

The fabrication route depends on the chemical composition. Two main alloy groups are studied at CEA: martensitic grades with a chromium content of 9%; and ferritic alloys containing more than 12% of chromium. This higher chromium content leads to better corrosion resistance, but as explained in details below, complicates the manufacturing.

In this study, two specific ODS grades are considered, a Fe-9Cr-1W-Ti- Y_2O_3 ODS martensitic steel and a Fe-14Cr-1W-Ti- Y_2O_3 ODS ferritic alloy.

9Cr-ODS martensitic steels

9Cr-ODS steels present a phase transformation from ferrite (α) to austenite (γ) which permits to release the hardening defects by a fully rearrangement of the microstructure [13-15]. The cold-rolled tube hardness is reduced during intermediate heat treatments performed into the austenitic domain.

The characteristic temperatures are respectively 850°C for starting point and 900°C for finishing point. Continuous Cooling Transformation (CCT) diagram permits to determine critical cooling rates: slow cooling rates lead to fully ferritic structure by contrast to fast cooling rates (above 1°C/s) which lead to martensitic structure [14]. Heat treatments control the metallurgical state of the 9Cr-ODS steel. Microstructure evolutions are followed during the fabrication route thanks to hardness measurements and Electron BackScatter Diffraction (EBSD) analysis of samples taken at different steps. Figure 5 presents the hardness change in the course of manufacturing.

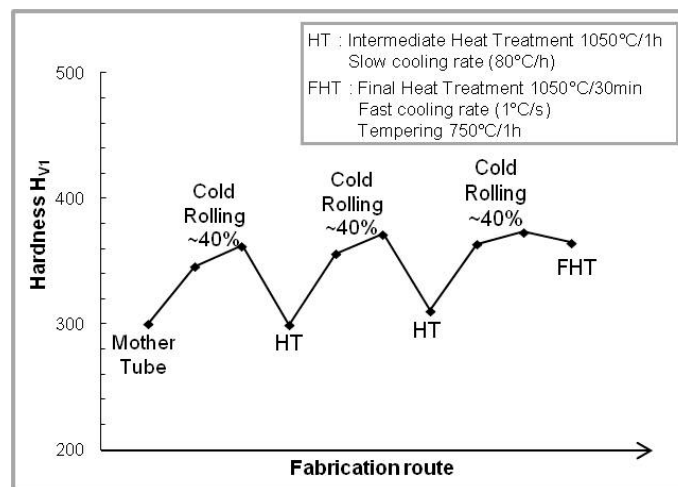


Figure 5: Hardness measurements during 9Cr-ODS cladding tube manufacturing

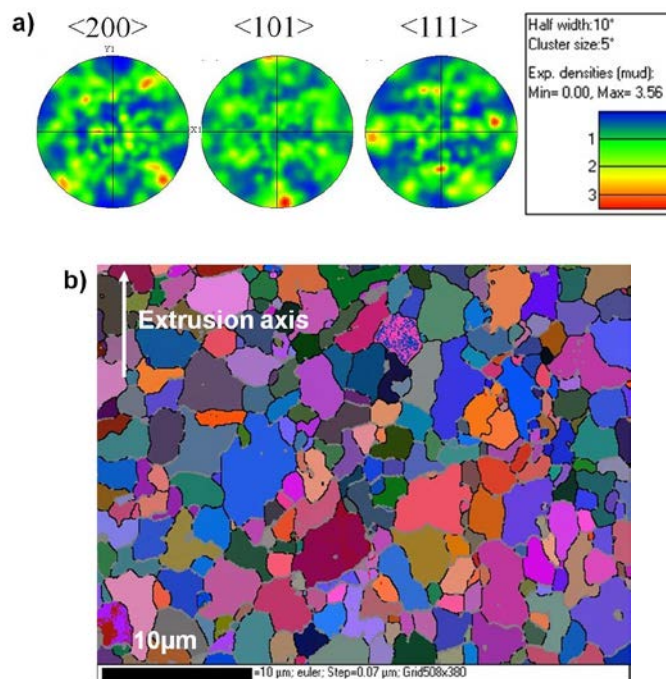


Figure 6: EBSD analysis of 9Cr-ODS mother tube after hot extrusion a) pole figures and b) EBSD map

EBSD analysis of the mother tube permits to observe both the morphological state and the crystallographic texture before cold rolling. After hot extrusion, which is made in the austenitic domain, 9Cr-ODS mother tube exhibits an equiaxial microstructure as illustrated by the EBSD map (Figure 6.b). The microstructure rearrangement due to the phase transformation permits to eliminate the crystallographic texture induced by the extrusion process as indicated by the pole figures (Figure 6.a).

The 9Cr-ODS mother tube is cold rolled under the softened ferrite phase which features a lower hardness level compared to the martensitic phase, low enough to ensure a safe manufacturing. After several rolling passes, the hardness measurements highlight an increase due to work hardening. EBSD map shows a microstructure made of fine grains, elongated in the cold rolling direction (Figure 7).

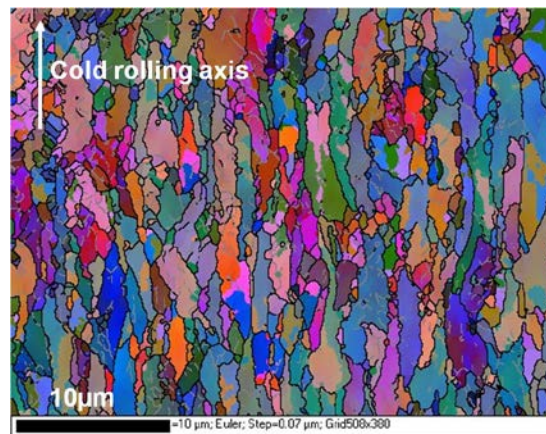


Figure 7: EBSD map of 9Cr-ODS cold rolled tube

Thanks to intermediate heat treatments performed in the austenitic domain at 1050°C during 1h, the microstructure is fully rearranged, which allows to efficiently release the hardening defects induced by the cold rolling passes. The slow cooling rates (80°C/h) permit to recover the initial softened ferritic microstructure, which features a low hardness (around 300 HV1) and can be easily cold worked (Figure 5). The anisotropic microstructure is replaced by an equiaxial grain structure during the heat treatment thanks to the (α) / (γ) phase transformation. The morphological anisotropy induced by pilger cold rolling process is efficiency destroyed (Figure 8).

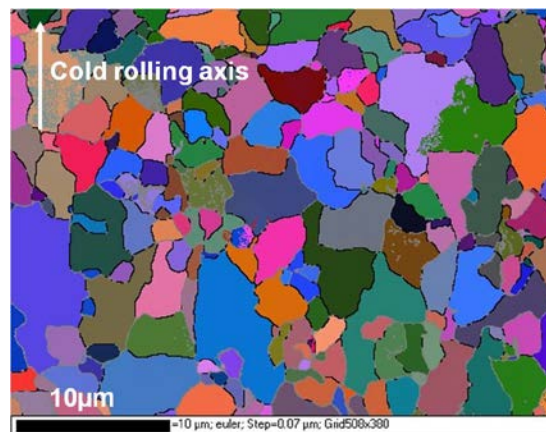


Figure 8: EBSD maps of 9Cr-ODS cold rolled tube after heat treatment (fully ferritic state)

Once the final geometry is reached, a final heat treatment is performed on the cladding tube in order to adjust the mechanical properties. An annealing at 1050°C during 30 minutes followed by a fast cooling (1°C/s) and a tempering at 750°C during 1h permits to obtain a tempered martensitic structure having high mechanical resistance.

In order to study the cold workability of this 9Cr-ODS grade, mechanical properties are determined in the circumferential direction by means of ring tensile specimens (Figure 9). Two metallurgical states are presented: a tempered martensitic structure and a softened ferritic structure which are respectively comparable to the final cladding tube and the softened raw tube during fabrication route. Tensile tests are performed at room temperature to be consistent with the cold rolling process.

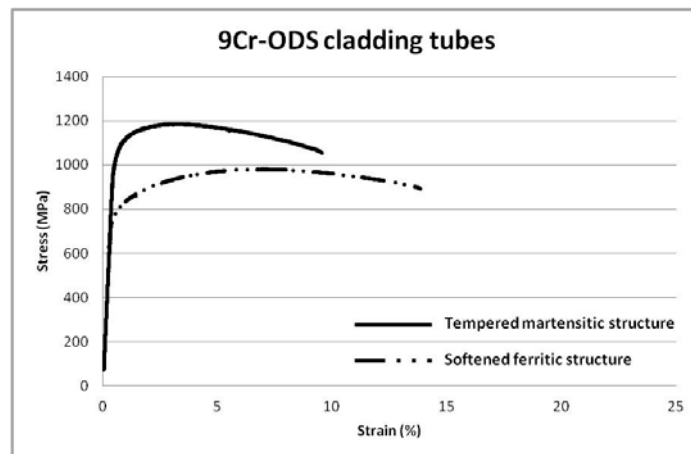


Figure 9: Stress-strain curves of 9Cr-ODS cladding tubes at 20°C (ferritic and martensitic structures)

One of the main differences between these two metallurgical states is the Ultimate Tensile Strength (UTS) value: the tempered martensitic structure exhibits a high UTS value of 1200 MPa whereas the softened ferritic structure has a UTS value around 1000 MPa. Since UTS values are directly linked to the hardness of the sample, the ferritic structure is favorable for cold manufacturing.

The Uniform Elongation (UE) values are also important results given by the tensile tests, because they can be linked to the ability of the material to be deformed before damage occurs. The softened ferritic structure is also favorable in terms of deformability at room temperature, because its UE value is twice as high as the one of the tempered martensitic structure.

These mechanical results prove the pertinence of the fabrication route performed with the softened ferritic structure. The fabrication optimization is linked to the phase transformation control during the heat treatments.

However, once the final cladding tube geometry is reached, the tempered martensitic structure is preferred because it represents a good compromise between high strength and ductility and fulfills the design requirements.

14Cr-ODS ferritic alloys

The microstructure control of 14Cr-ODS alloy, which does not exhibit a phase transformation, is more complex. Recrystallization treatments at very high temperature (above 1400°C) could be envisaged to

increase the cold workability and release the stresses induced by the manufacturing processes. However, abnormal grain growth was observed on recrystallized ODS ferritic alloys leading to reduced mechanical properties and a high brittle-to-ductile-temperature [16]. Thus, recrystallization conditions need to be both well known and controlled to obtain a favorable microstructure.

Performing recovery annealing, at temperature lower than the recrystallization temperature, is a good solution to avoid this abnormal grain growth and release a part of the internal stresses [17]. To manufacture the 14Cr-ODS CEA cladding tubes, no recrystallization treatments were performed. The microstructures described in this work are then either recovered fine grain structures or recovered coarse grain structures. At this time there is no reference fabrication route and various possibilities are being tested.

In the same manner, hardness measurements and EBSD analysis allow following the microstructural evolutions during the course of the manufacturing. 14Cr-ODS mother tubes exhibit a hardness level that is much higher than for 9Cr-ODS tubes. After hot extrusion, hardness measurements give a value around 500 HV1, which is too high to perform a reliable manufacturing. Heat treatments are needed and have to be done at very high temperature. In this example, the mother tube is treated at 1250°C during 30 minutes: the hardness is then low enough (close to 300 HV1) to avoid any damage during the cold rolling passes.

EBSD maps of Figures 10 and 11 illustrate the morphological evolution of the mother tube after the initial heat treatment (1250°C during 30 minutes). The difference is significant since the fine grains, elongated in the extrusion direction, observed on the extruded sample (Fig. 10.b) are replaced by a bimodal microstructure made of both coarse grains and fine elongated grains (Fig. 11.b).

The microstructure is less homogeneous than the one of the annealed 9Cr-ODS mother tube, but the hardness is reduced enough to perform cold rolling passes without any risk of damage.

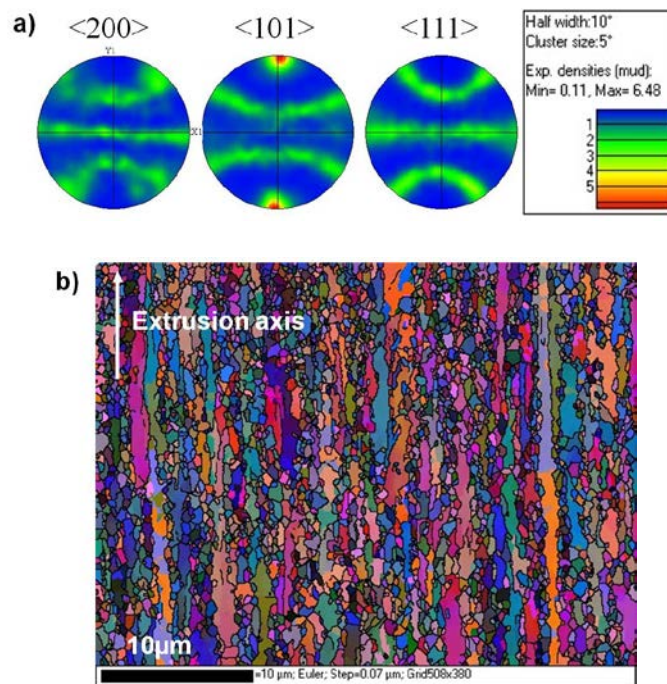


Figure 10: EBSD analysis of 14Cr-ODS mother tube before initial heat treatment a) pole figures, b) EBSD map

The comparison of Figures 6.a and 10.a indicates that the crystallographic evolution is strongly linked to the chemical composition. Indeed, the typical α -fiber orientation ($\langle 110 \rangle$ axis parallel to the extrusion axis) which is induced by the extrusion process is much stronger on the 14Cr-ODS mother tube (Fig. 10.a) than the one on the 9Cr-ODS tube (Fig. 6.a). Even after annealing at 1250°C during 30 minutes, the 14Cr-ODS mother tube is much more textured (Fig. 11.a).

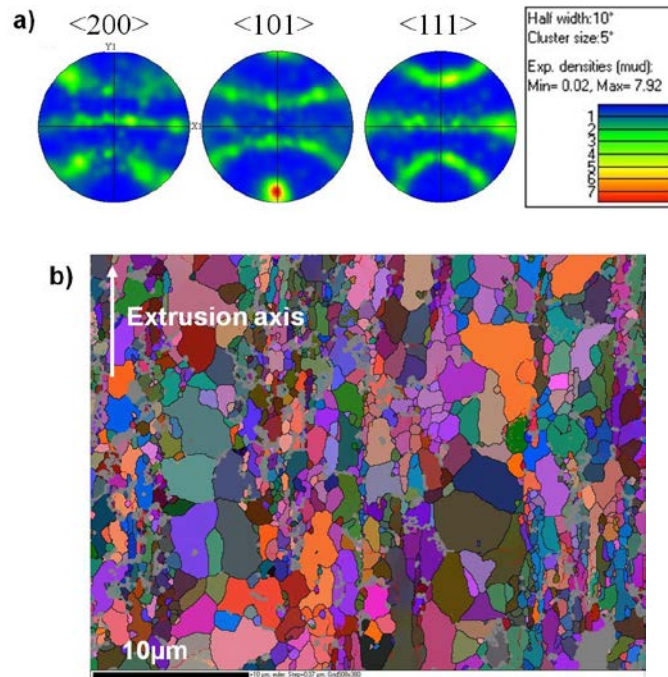


Figure 11: EBSD analysis of 14Cr-ODS mother tube after initial heat treatment (1250°C – 30 min) a) pole figures, b) EBSD map

These observations indicate that no microstructure rearrangement (such as phase transformation or recrystallization) happens during the heat treatment of the 14Cr-ODS mother tube: the microstructure control of the 14Cr-ODS ferritic alloy is much more difficult because of the lack of phase transformation. However heat treatments performed at high temperature allow to reduce enough the hardness of the mother tubes and to define reliable fabrication routes. Some 14Cr-ODS ferritic cladding tubes were manufactured, but optimization of processing conditions and heat treatments is needed to ensure mechanical properties which would be comparable to those of the 9Cr-ODS.

The metallurgical optimization of the fabrication route of ODS tubes is in progress and, in parallel, a numerical approach is conducted to improve the control of the deformation paths of ODS tubes.

4. Numerical approach

The current work focused on the mechanical analysis of a laboratory pilgering mill, HPTR (High Pressure Tube Reducer), at CEA. Nevertheless, the following numerical approach can be applied to the industrial mill, VMR (“Vertikaler Massenausgleich Ringwalzei”, or mill by offsetting vertical grooves of the masses).

The HPTR cold pilgering process could be improved by optimizing parameters such as tool kinematics, die profiles, lubricant, feed, rotation angle and Q factor (which is the ratio between the

wall reduction and the mean diameter reduction), etc. Optimization objectives may be related to cracking risks. Indeed, maximum hardness values have been identified, and these may be correlated to the calculated evolution of the material yield strength in the process. Consequently, deformation path should be identified using a numerical simulation because of the complexity of the kinematics. Moreover the constitutive law must be accurate enough to describe the pilgering mechanical loadings. The literature is mainly reporting monotonic laws, which are not expected to be suitable for cyclic conditions as those involved in pilgering. The full stroke numerical simulation of the cold pilgering process leads to the determination of the strain path undergone by a material point [18].

The optimization of the forming of ODS tubes is linked to the choice of an appropriated constitutive model [19]. Furthermore, FEM (finite element method) is quite successful to simulate metal forming processes, but accuracy depends both on (i) constitutive laws and (ii) material parameters identification. Consequently, this work aims to assess the impact of the choice of both simulation features and constitutive laws on cracking risk development in pilgering conditions. The final and robust numerical model aims to be accurate enough to be used as a design tool for process optimization.

Constitutive model

The macroscopic cyclic plasticity models are the most viable solutions when dealing with complex large scale forming operations, in order to avoid explosion of computing time and memory space. This work analyzes a numerical simulations of ODS tubes cold pilgering considering two constitutive laws, i.e. the monotonic and the cyclic behaviors. The influence of these constitutive laws on the mechanical history undergone by a material point during the process is assessed.

Monotonic constitutive model

A standard constitutive model to described monotonic loadings, tensile test in this work, is the elastic-visco-plastic Hansel-Spittel law given by:

$$\sigma_0(\bar{\varepsilon}) = A e^{m_1 T} T^{m_9} \bar{\varepsilon}^{m_2} e^{m_4 \bar{\varepsilon}} \left(1 + \bar{\varepsilon}^{m_5 T}\right) e^{m_7 \bar{\varepsilon}} \dot{\bar{\varepsilon}}^{m_3} \dot{\bar{\varepsilon}}^{m_8 T}$$

where $\bar{\varepsilon}$ is the equivalent deformation (total strain), $\dot{\bar{\varepsilon}}$ the equivalent deformation rate (total strain rate), T is the temperature and A, m_{1-9} are the regression coefficients. The tensile test is assumed isothermal (temperature T is constant) and without strain rate effects: parameters m_3 and m_8 are therefore set to zero.

Cyclic elastic–plastic constitutive model

The cyclic deformation induced by cold pilgering is fairly well approximated by a sequence of compression tests along two perpendicular directions [19]. The constitutive model considered in this study is therefore based on Chaboche for the cyclic behavior, it is denote as cyclic C/C. The latter utilizes multi-components forms of kinematic and isotropic hardening variables with non-linear evolutionary rules to describe the hysteresis loops and the transient behavior of the material.

The formulation chosen here is the following [20]. The elastic domain is defined by:

$$f = J_2 \left(\underline{\sigma} - \sum_i \underline{X}_i \right) - \sum_i R_i - \sigma_y \leq 0$$

In the previous equation σ_y is the initial yield surface size. \underline{X} is the kinematic internal stress tensor or back stress tensor and R is the isotropic hardening. The formulation of the kinematic hardening tensor is based on the non-linear Chaboche kinematic model:

$$\dot{\underline{X}}_i = \frac{2}{3} C_i \underline{\dot{\epsilon}}^p - \gamma_i \underline{X}_i \dot{p}$$

C_i and γ_i are constant material parameters. $\underline{\dot{\epsilon}}^p$ is the plastic strain increment tensor. \dot{p} is the plastic strain rate.

The isotropic hardening variable is introduced to describe the cyclic hardening phenomenon (increase of strength) or the cyclic softening (decrease). Its evolution is governed by the accumulated plastic strain and the stabilized state is reached when R gets its asymptotic value Q :

$$R_i = Q_i (1 - \exp(-b_i p))$$

Where Q_i and b_i are constants. Similarly to [21] a good compromise was found with a model using two kinematic variables (\underline{X}_1 and \underline{X}_2) and two isotropic variables (R_1 and R_2). This model was implemented within the FE (finite element) code.

Identification methodology of the model parameters

Because of the reduced amount of ODS material usually available for mechanical testing, the behavior of Fe-14Cr-1W-Ti ODS is studied using only two specimens, one with a uniaxial tensile test, and another one with a compression-compression strategy, alternating uniaxial compressions along two perpendicular axes. The latter test leads to loading paths similar to those encountered in cladding tubes pilgering. In this test, strain amplitude changes are included in the loading sequence (see [19]).

Chaboche model parameters for the compression-compression test have been identified using a semi-automatic identification process proposed by [19]. An inverse analysis method is used to fit the parameters A , m_1 , m_2 , m_4 , m_5 , m_7 of the Hansel-Spittel behavior law. The main interest of these methods is to identify parameters which are uneasy to estimate by manual fitting

Simulation set up

Optimizing numerically the whole process with a long tube is simply not feasible at the time being, because of the huge computation time involved. Consequently, a *short* tube approach is used [18,22].

A sensitivity analysis on the mesh sizes, time step, type of mesh and length of the tube was performed in order to assess the accuracy of the current calculations. An optimal set of numerical parameters was chosen: unstructured anisotropic mesh (4 elements over the thickness, 60 elements over the length and 100 elements over the circumference), tube length of 20 mm, time step of 0.001s. This configuration exhibits the best accuracy-computation time compromise. Tools are assumed to be rigid.

Coulomb friction is assumed with $\mu = 0.1$. The pass 3 of the fabrication route (pass deformation close to 25%) is simulated. The process total time is 98s. The tube is turned 39° and moved forward (feed) 1.7 mm after each stroke. A material point takes 120 strokes to pass through the working zone.

Initial position of the simulated systems is displayed in Figure 12.



Figure 12: FEM simulation set-up.

Lagrangian numerical sensors have been placed at the mid-length of the tube at various angles (0° - 19.5° - 39° - 90° - 180° - 270°) (Fig. 13) to avoid edge effects. Four sensors are placed over the thickness at the Gauss point as illustrated in *Figure 6*. In order to analyze the process over the circumference 6 sensors rows are placed in the $r(\theta)$ cross-section plane. Each row (called R) leads to four sensors (called S). Thus, R1 contains S1-4 counted from the external surface to the internal surface; R2 contains S5-8 and so on.

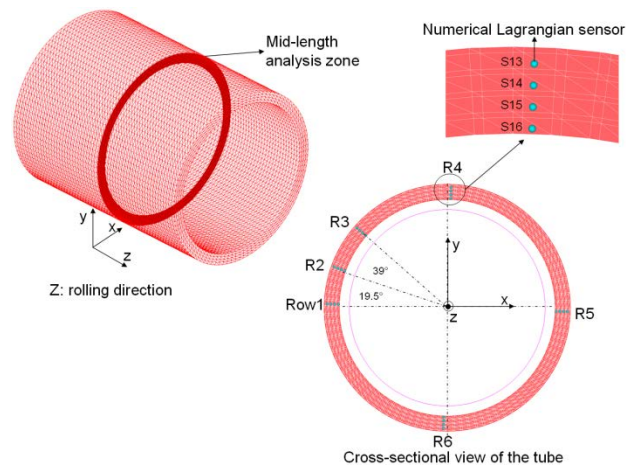


Figure 13: Lagrangian numerical sensors placed at the mid-length of the tube at different angles (0° - 19° - 39° - 90° - 180° - 270°).

Numerical results

The sensor S2 stress history is monitored and is illustrated in *Figure 14*. The axial stress is tensile when the material is located in the side relief and compressive over the die shoulder. A material point will experience cycles of tension and compression, potentially inducing fatigue phenomena during the pilgering process. The 120 positive (tensile) and negative (compressive) peaks appear in *Figure 14*; in the compressive case, high and low peaks alternate, because the material point varies, depending on the successive rotations. The largest stress is experienced in the last cycles because the thickness reduction is larger and the material is strongly work-hardened.

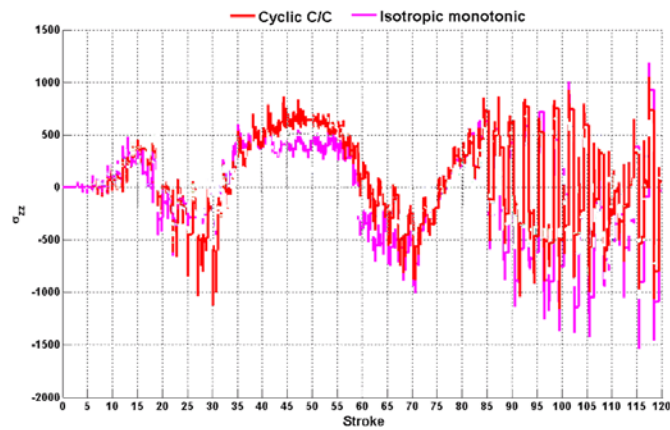


Figure 14: Sensor S2 longitudinal stress (in MPa) history for different ferritic ODS constitutive laws.

Figure 15 displays the dies and tube position when the longitudinal stress is maximum according to *Figure 14*, using the cyclic C/C constitutive law. In the deformation zone under the die, the longitudinal stress σ_{zz} is tensile in the side relief area, and compressive in the groove bottom (*Figure 15*).

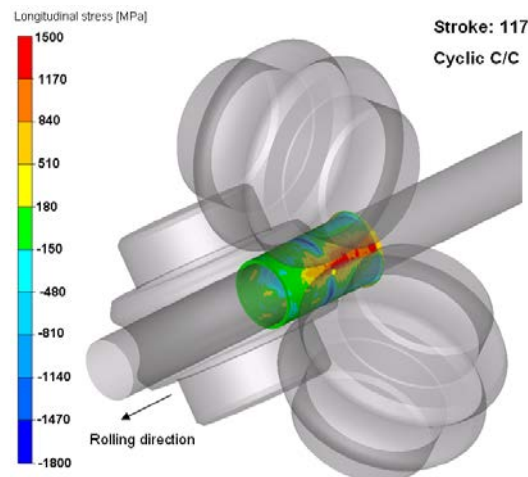


Figure 15: Longitudinal stress isovalues (in MPa) showing the high compression in the groove bottom and the high tensile material state in the side relief when using the cyclic C/C constitutive law. Stroke 117 corresponds to the moment when the tensile stresses are the highest for the Cyclic C/C constitutive law.

Now, when comparing the flow stress σ_0 value experimentally and numerically identified (at the external surface of the tube wall thickness, see *Figure 16*), it is observed that the monotonic constitutive law does not manage to model the final state of the ferritic ODS tube. On the other hand, the cyclic C/C constitutive law is much closer. In *Figure 16*, the initial yield stress (960 MPa) identified from the compression-compression test is however lower than measured (1238 MPa). The tube has indeed already undergone two forming passes and a subsequent heat treatment (without any recrystallization).

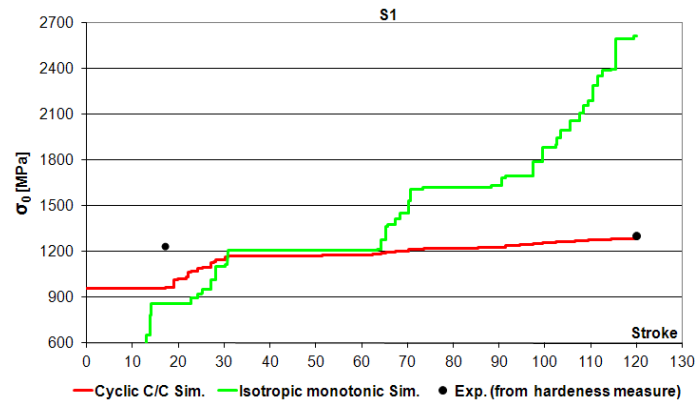


Figure 16: Sensor 1: stress σ_0 (in MPa) numerical and experimental response comparison for different constitutive laws.

5. Conclusions

Several tubes were successfully fabricated in both ODS grades. Mechanical properties and further microstructure analysis are in progress. The fabrication route of 9Cr-ODS alloys is well controlled. The ferrite to austenitic phase transformation allows controlling the hardness level by working under the softened ferrite phase. Work hardening and both morphological and crystallographic textures are efficiently reduced. On the contrary, the 14Cr-ODS fabrication route can be optimized by controlling the grain growth with heat treatments performed at high temperature. A better metallurgical understanding appears critical to govern the microstructure evolutions of ODS ferritic alloys. The accurate modeling of the material constitutive behavior is one of the most important features needed in order to predict the material behavior and simulate the process properly. This study assessed the impact of the constitutive law choice on the prediction of the mechanical history undergone by a material point during pilgering. A Chaboche-type constitutive model, identified with a specific compression/compression procedure, leads to better results in terms of stresses than a monotonic constitutive law, identified with a classical tensile test. Measurements performed before and after pilgering have shown that the ferritic ODS tube undergoes hardening. Experimental and “cyclic C/C predicted” stress results are in good agreement. In a future work, a systematic analysis of all strokes will help defining which stroke should mainly contribute to the oligocyclic fatigue of the material. Moreover the full scale numerical simulation of the cold pilgering process will allow analyzing the conditions for which cracking may develop and recrystallization may take place upon heat treatment. The cold pilgering process could be optimized looking at process parameters such as tools kinematics, die profiles, lubricant, feed, rotation angle and Q factor.

This work focused on the laboratory HPTR mill available at CEA/Saclay. The proposed constitutive law identified from alternated compressions could be used as well to model the industrial VMR mill, and lead to an optimization with objectives similar to those described for the HPTR process. This study shows that combining metallurgical and numerical approaches leads to a better understanding of both the material behavior and the mechanical path during the manufacturing process. It should allow to improve successfully the fabrication route of ODS tubes.

Acknowledgements

The authors gratefully acknowledge Elodie Rouesne, Didier Bossu, Patrick Olier and Cyril Cayron for their technical and scientific support. This research was supported by ANR (The French National Research Agency) in the context of the STRATOTUBE Project.

REFERENCES

- [1] P. Yvon, F. Carré, J. Nucl. Mater. 385 (2009) 217–222.
- [2] Y. de Carlan, J.-L. Béchade, P. Dubuisson, J.-L. Seran, P. Billot, A. Bougault, T. Cozzika, S. Doriot, D. Hamon, J. Henry, M. Ratti, N. Lochet, D. Nunes, P. Olier, T. Leblond, M.-H. Mathon, J. Nucl. Mater. 386–388 (2009) 430–432..
- [3] R. Lindau, A. Möslang, M. Rieth, M. Klimiankou, E. Materna-Morris, A. Alamo, A.-A.F. Tavassoli, C. Cayron, A.-M. Lancha, P. Fernandez, N. Baluc, R. Schäublin, E. Diegele, G. Filacchioni, J.W. Rensmanh, B.v.d. Schaaf, E. Lucon, W. Dietz, Fusion Eng. Des 75–79 (2005) 989–996.
- [4] A. Kimura, H.S. Cho, N. Toda, R. Kasada, K. Yutani, H. Kishimoto, N. Iwata, S. Ukai, M. Fujiwara, J. Nucl. Sci. Technol. 44 (3) (2007) 323–328.
- [5] A.A. Nikitina, V.S. Ageev, A.P. Chukanov, V.V. Tselev, N.P. Porezanov, O.A. Kruglov, Proceedings of DIANA I workshop “Dispersion Strengthened steels for advanced nuclear applications”, Aussois (France) April 4-8, 2011, J. Nucl. Mater., 2011
- [6] J. Alinger, G.R. Odette, D.T. Hoelzer, J. Nucl. Mater. 329–333 (2004) 382–386.
- [7] P. Dubuisson, Y. de Carlan, V. Garat, M. Blat, *ODS Ferritic/martensitic alloys for Sodium Fast Reactor fuel pin cladding*, Journal of Nuclear Materials, Volume 428, Issues 1–3, September 2012, Pages 6-12.
- [8] P. Montmitonnet, J.-L. Aubin, *Formage des tubes métalliques*, Techniques de l’ingénieur Doc M 3 068, 2008. In french.
- [9] P. Montmitonnet, R. Logé, M. Hamery, Y. Chastel, J.-L. Doudoux, J.-L. Aubin, Journal of Materials Processing Technology 125-126, pp.814 - 820, 2002..
- [10] S. Ukai, M. Fujiwara, J. Nucl. Mater. 307–311 (2002) 749–757.
- [11] S. Ukai, S. Ohnuki, S. Hayashi, T. Kaito, M. Inoue, A. Kimura, T. Fujisawa, T. Okuda, F. Abe, Proceedings of ICAPP ‘09, Paper 9232, Tokyo, Japan, May 10–14, 2009.
- [22] M. Inoue, T. Kaito, S. Ohtsuka, *Materials for Generation IV Nuclear Reactors*, Cargese, Corsica, 2007.
- [13] S. Ukai, T. Narita, A. Alamo, P. Parmentier, Journal of Nuclear Materials 329–333 (2004) 356–361
- [14] L. Toualbi, C. Cayron, P. Olier, J. Malaplate, M. Praud, M.-H. Mathon, D. Bossu, E. Rouesne, A. Montani, R. Logé, Y. de Carlan, *Assessment of a new fabrication route for Fe–9Cr–1W ODS cladding tubes*, Proceedings of DIANA I workshop “Dispersion Strengthened steels for advanced nuclear applications”, Aussois (France) April 4–8, 2011, Journal of Nuclear Materials, Volume 428, Issues 1–3, September 2012, Pages 47-53.

P. Gavaille et al.

- [15] S. Ukai, S. Mizuta, M. Fujiwara, T. Okuda and T. Kobayashi, *Journal of Nuclear Science and Technology*, Vol. 39, No. 7, p. 778–788 (July 2002)
- [16] A. Alamo, V. Lambard, X. Averty, M.H. Mathon *J. Nucl. Mater.* 329–333 (2004) 333–337.
- [17] T. Narita, S. Ukai, T. Kaito, S. Ohtsuka and T. Kobayashi, *Journal of Nuclear Science and Technology*, Vol. 41, No. 10, p. 1008–1012 (October 2004)
- [18] E. Vanegas, K. Mocellin, Y. de Carlan, R. Logé, acte de congrès CM-03-0479, *MATERIAUX 2010*, Nantes, France, 18-22 octobre 2010.
- [19] E. Vanegas-Marquez, K. Mocellin, L. Toualbi, Y. de Carlan, R.E. Logé, *Journal of Nuclear Materials* 420 (2012) 479–490.
- [20] J.-L. Chaboche, *International Journal of Plasticity* 5, pp.247 - 302, 1989.

Materials for ALFRED and ELFR – selection and challenges

A. Weisenburger^a, A. Gessi^b, A. Jianu^a, M. Del Giacco^a, R. Fetzner^a, A. Heinzl^a, G. Müller^a, P. Agostini^b

^aKarlsruhe Institute of Technology, Karlsruhe, Germany

^bENEA, Brasimone, Italy

Presented by A. Weisenburger

Abstract. Materials are one of the challenging issues for all future GENIV reactors. Several EU funded projects, e.g. ELSY and LEADER, aimed to design Pb cooled nuclear systems including the European lead cooled reactor ELFR and the demonstrator ALFRED. The selection of the structural materials determines the design and the design has to consider the properties and the availability of the materials. Beside general requirements for material properties that are common for all fast reactor types specific issues arise from coolant compatibility. The high solubility of steel alloying elements in liquid Pb at reactor relevant temperatures is clearly detrimental. Therefore, all steels that are considered as structural materials have to be protected by dissolution barriers. The common barriers for all steels under consideration are oxide scales that form in situ during operation. However, increasing the temperature above 500 °C will result either in dissolution attack or in enhanced oxidation. For higher temperatures additional barriers like alumina forming surface alloys are discussed and investigated. Mechanical loads like creep stress and fretting will act on the steels. These mechanical loads will interact with the coolant and can increase the negative effects.

For ALFRED austenitic steels (316 and 15-15Ti) are selected for most in core components. The 15-15Ti is the choice for the fuel cladding of ALFRED and the ferritic martensitic steel T91 was selected as fuel clad material of the ELFR. T91 is in both designs the material to be used for the heat exchanger. Surface alloying with alumina forming alloys is considered to assure material functionality at higher temperatures and is therefore selected for fuel cladding of the ELFR and the heat exchanger tubes.

1. Introduction

Climate change, peak oil and the growing dependency on states outside EU can't be answered only employing renewable energy sources like wind and solar. Especially the base load electricity production can not be guaranteed only considering such kind of electricity production methods. Nuclear energy using Fast GenIV reactors can fulfil the demands concerning CO₂ free, base load capability and sustainability. One of the most promising coolants especially due to its high thermal inertia and through that its long grace times in case of accidents is the HLM Pb. Since several years researches all over the world investigate this coolant and its impact on the reactor design and by that on the materials to be selected. In several EU funded project design, safety and some technological aspects of lead (Pb) cooled fast reactors were investigated. The LEADER [1] project, a follow up of ELSY, aims to design a prototypical demonstrator ALFRED and to continue with several design related aspects of the ELFR reactor. The demonstrator ALFRED should be available in the short and medium term and therefore material selection is beside safety aspects also triggered by the actual availability and the status of licencing. As a demonstrator the criteria for material selection are somewhat different to a commercial type like the ELFR. Material selection for ELFR of course considers all the aspects relevant for ALFRED plus the targeted burn up and the expected total dpa related damage especially of the fuel pins.

A. Weisenburger et al.

In the past, compatibility of structural material (steels like 316L, T91 and 15-15Ti (1.4970)) that can be employed for Pb cooled fast nuclear reactors were investigated in several EU projects like EUROTRANS [2][3][4] and projects world wide [5][6]. Solubility of steel alloying elements like Ni, Fe, Cr is the driving force for the reduced corrosion resistance in contact with Pb. In-situ oxidation is the acknowledged measure to protect steels in Pb up to certain temperatures that are material dependent. Based on experiments and the derived temperature limits the average core outlet temperatures of ALFRED and the ELFR are set to 480°C. The most challenging conditions with respect to temperature are at the fuel assembly and the heat exchangers. For both, thin protective oxide scales with negligible reduction in heat transfer are the additionally requested material and compatibility property. One very specific design issue, the spiral heat exchanger for the ELFR [7] was also considered in the material discussion.

This presentation will give an overview on the selected materials for ALFRED and ELFR considering, beside pure compatibility, the influence of mechanical interaction like creep and fretting.

2. Material Selection

The operating temperatures of the different reactor components are identical for both of the discussed nuclear reactors, ALFRED and the ELFR (Table 1). Therefore, most of the materials selected to manufacture the components like reactor and inner vessel and refueling equipment are identical for both concepts. One major difference between ALFRED and the ELFR is the expected maximum irradiation damage of the fuel assemblies. The ALFRED design foresees 100 dpa, what allows the use of the 15-15Ti stabilized austenitic steel also employed in the French Phenix reactor [8]. This steel is already licensed for application in nuclear reactors, which is an additional important aspect for material selection for ALFRED. The fuel assembly of the ELFR needs to withstand a maximum radiation damage of 200 dpa that is too high for the best available 15-15Ti stabilized steel [9]. The class of steels that can tolerate such high radiation damage are the ferritic/martensitic (f/m) steels, like T91 or specific ODS types.

Table 1. Materials and conditions for the different reactor components of ALFRED and ELFR

Components	Material	Min./Max Temp. Normal Operation (°C)	Max. Lead velocity (m/s)	Max. Radiation damage (dpa/y)	Max. Radiation damage (dpa)
Reactor Vessel	AISI316L	380÷430	0.1	< 10 ⁻⁵	0.0002
Inner Vessel	AISI316L	380÷480	0.2	0.1	2.1
Steam Generator	T91/AISI316L	380÷480	0.6	< 10 ⁻⁵	0.0001
Primary Pumps	MAXTHAL (Ti ₃ SiC ₂) Coated T91 or SS (Aluminized, Ta)	380÷480	10	< 10 ⁻⁵	0.0001
FA Clad	15-15Ti/T91	380÷550	1	-	100/200
FA Structures	Aluminized	380÷530	2	-	100/200
Dummy Assemblies	T91	380÷480	0.01	-	100/200
Refueling Equipment	AISI316L	380÷480	0.2	0.02	0.3
DHR Heat Exchanger	T91	380÷430	0.2	< 10 ⁻⁵	0.0001

Besides improved irradiation stability, the heat conductivity of the f/m steels is almost a factor of two higher compared to austenitic steels like 316L and 15-15Ti stabilized [10]. Therefore, T91 is also discussed as structural material for heat exchangers and steam generator (SG) components. The thermally most loaded components like fuel claddings and steam generators or heat exchangers, where coolant temperatures of 550°C can be reached, with cladding wall temperatures even 20K higher, might require surface aluminized steels to be operated. For most components, beside the pump impeller, the maximum Pb velocity of 2m/s does not require specific attention [11]. Due to the high local velocities that will occur at the pump impeller and the lack of corresponding experimental investigations, material selection for this component can not be done at the time. Several alternatives like ceramics (SiSiC, Maxthal) or coatings (Ta) are under consideration.

The main objective of any commercial reactor like the ELFR is highest possible safety and most efficient production of electricity. A spiral steam generator [7] is one of the design specifics of an ELFR to meet this requirement. Therefore, surface aluminization as one proposed material solution for thermally high loaded parts has to be tested regarding the manufacturability of a spiral SG.

3. Compatibility of selected materials with Pb

Compatibility of materials with Pb is mainly driven by the temperature dependant solubility of the alloying elements in the liquid Pb. Ni, Mn, Al and Si have substantial solubility of up to some wt% at 550°C [4]. The main elements of steel, Fe and Cr, are less soluble but still some 10⁻⁵wt% can not be neglected. Practically insoluble are refractory alloys like W, Mo and Ta and most ceramics. Therefore Ni containing metals like austenitic steels suffer more from dissolution attack than Ni free f/m steels like T91. To mitigate dissolution, any direct contact between the steel and the liquid Pb should be avoided. The most appropriate method is the in-situ oxidation by dissolved oxygen [12]. The oxygen concentration range is determined by the operating temperature range of the reactor. The lower operating temperature of 380°C, to consider some safety margin 325°C (T_{melt} of Pb), ascertains the upper limit of 10⁻⁴wt% oxygen to avoid PbO formation and any related coolant channel blockage. The highest achievable temperature at normal operation (550°C fuel clad) determines the lower limit of dissolved oxygen of 10⁻⁷wt% required to prevent or at least mitigate dissolution attack. Such formed oxide scales act as diffusion barrier and can prevent the dissolution. However, especially in case of f/m steels the growth of oxide scales can, at least after longer exposure times, result in severe reduction of the heat conductivity.

3.1. Austenitic steels – 316L, 15-15Ti (1.4970):

The operating range for the austenitic steel 316L is, as depicted in table 1, between 380 and 480 °C. The 15-15Ti that should be employed as fuel assembly material can reach temperatures up to 550°C or even higher due to reduced heat transfer properties by the formation and growth of oxide scales. The upper limits are due to limitations by the material compatibility and might be altered if suitable solutions are available. In previous national and international projects, Ni containing austenitic steels were mainly tested in Pb Bi eutectic (LBE) [3]. Due to the higher solubility of alloying elements in LBE than in Pb, a direct transfer of the attained knowledge is not simple. The general mechanism, the dissolution of Ni accompanied by penetration of Pb into the steel matrix, is equivalent for both coolants. However, the rate of dissolution and the resulting temperature and oxygen concentration limits might differ. Below 430°C, the maximum temperature of the reactor vessel, even in LBE, no dissolution attack was observed as long as the oxygen content is sufficient high for the formation of oxide scales. In Pb a better behaviour of the steels can be expected. However, if the oxygen concentration drops to low values even at this temperature dissolution attack will become an issue. Tests with 316L steel showed that at 450 °C in LBE with low oxygen content dissolution attack already starts after 2000h (Fig 1a)[3]. In LBE at a temperature of 500°C dissolution attack is observed after about 10000h. In Pb with the same oxygen content but at even higher temperature of 550°C oxide scales still protect the steel (Fig. 1b). The usability of the steel 316L up to the selected upper temperature limit of 480°C at “normal” operating conditions seems obvious if the oxygen is controlled within the given limits.

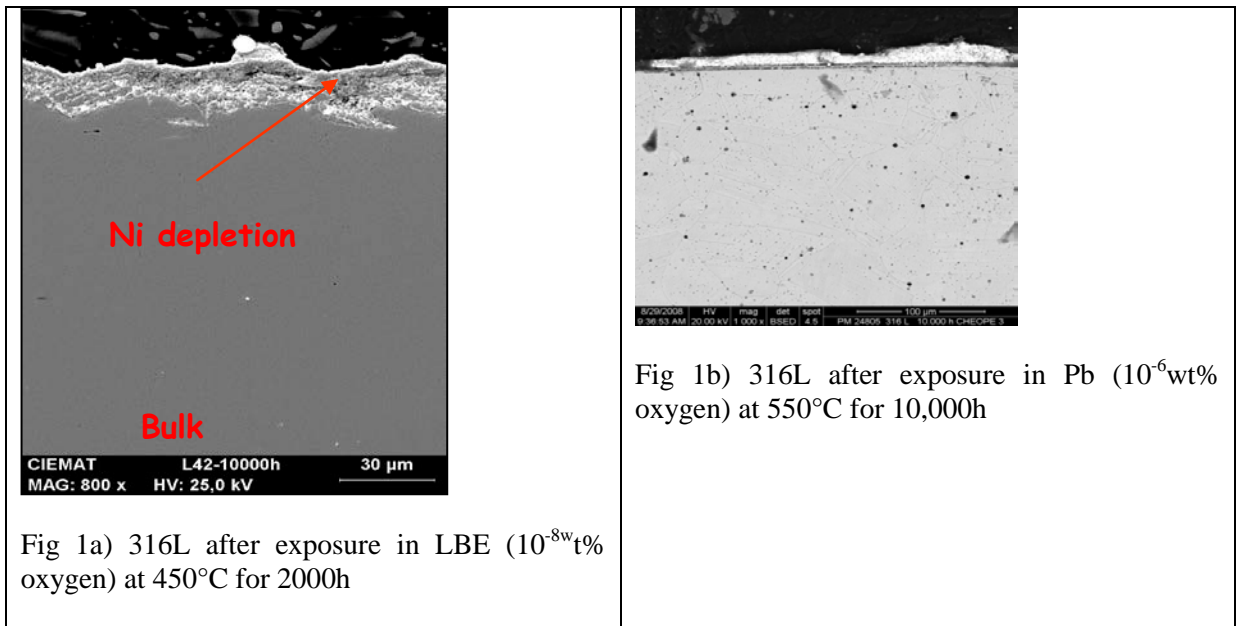


FIG. 1.

The 15-15 Ti stabilized steel (1.4970), foreseen as fuel cladding material, has to be stable up to 550°C or even 570°C. In LBE, this temperature is clearly above the operating range for this steel [3][13]. Local deep dissolution attack starting with leaching of Ni and later Cr will not allow the use of the 15-15Ti in LBE. But, in Pb, this steel showed in experiments at same temperature and oxygen activity the formation of protective oxide scales at least in the first 3000h of exposure [14][15]. Based on the experience with extrapolation of corrosion data from short to long term experiments, it is unlikely or at least uncertain whether this steel can be operated in Pb at 550°C for longer times. One difficulty that arised during the experimental work is the so called incubation time for the dissolution attack. At 500°C e.g with 10⁻⁸wt% oxygen, a typical oxide scale develops during exposure for 2000h [Fig 2a]. However, after 5000h dissolution attack was observed. One possible mechanism is the enrichment of the high soluble elements like Ni and Mn beneath the outer oxide scale [Fig. 2b]. These enriched phases are located in the spinel layer and can reach almost the interface to the outwards growing magnetite scale. The magnetite scale is rarely a dense and compact layer and quite frequently penetrated by the liquid metal. Therefore, the Ni and Mn enriched phases might act during prolonged exposure as a starting point for the dissolution attack if they reach the original metal surface and come in interaction with the liquid metal. Therefore all short term tests (<5000h exposure) must be carefully analyzed on any sign of local enrichment that can possibly predict the onset or starting of a dissolution attack in future exposure times.

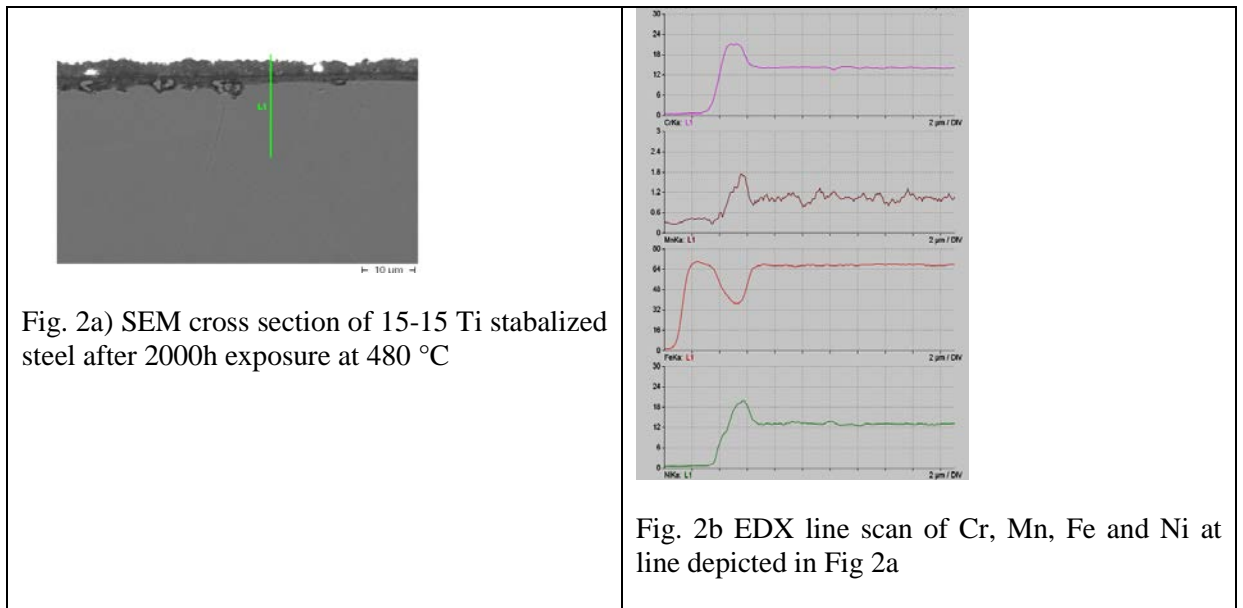


FIG. 2.

3.2. f/m Steel T91:

The operating temperature range for the f/m steel T91 is similar to that of the austenitic steel between 380 and 550°C. Again, the upper limit is not design but material driven and might be increased if adequate solutions are available. The f/m steel T91 does not contain Ni. Therefore, the susceptibility for dissolution attack is reduced compared to the austenitic steels. For the entire foreseen range of temperatures no dissolution attack of T91 steel is expected also for long exposure times if oxygen concentration is kept under control at nominal values [3]. The formation of oxide scales, which is the prevailing mechanism for Ni free f/m steels, is mainly independent of whether the medium in contact is pure Pb or LBE. The oxidation potential as the driving force and the diffusion constants in the steel, both determine the oxidation behaviour, are anyway similar for both coolants. Above 480°C typically three layered oxide scales that grow significantly with time are formed (Fig. 3a). One average 30µm thick scales grow after 6700h. Assuming parabolic growth, oxide scales of about 40µm thickness are formed after 15,000h. At 550°C oxidation is accelerated and the scatter of the measured data becomes significant (Fig. 3b). The average thickness of the spinel scale grows up to almost 60 µm after 15,000h assuming parabolic oxidation. The large scatter makes long term prediction difficult.

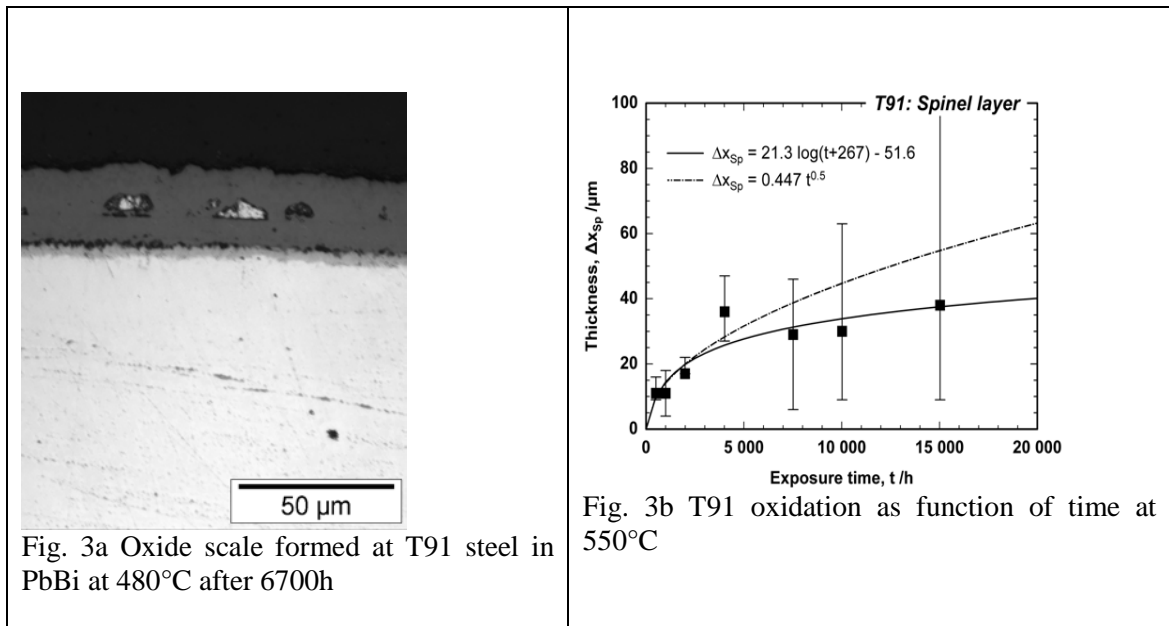


FIG. 3.

Besides the lack of precise and reliable data for long term, the observed oxidation becomes an issue regarding heat removal through fuel claddings and SG and HX tubes. Temperature increase of cladding tubes due to the reduced heat conductivity of the oxide scale and the reduced efficiency of the SG and HX must be considered during design or answered by a different solution like aluminizing of the steel. Besides, oxygen supply has to consider this effect too.

4. Alternative materials:

For the impeller of the pump the temperature range is between 380 and 480 °C. Regarding solely corrosion, both classes of steels, 316 type and T91 type, can be used. But, the expected local velocities of up to 10m/s or even higher might be problematic for the use of the materials described above. Localized high velocity flow pattern can severely damage steels as observed in corrosion experiments at IPPE and CIEMAT [3]. 316L steel was heavily eroded in such flow field at temperature and oxygen conditions that are suitable to form protective oxide scales at nominal flow velocities.

The materials discussed at the time are Maxthal, SiSiC or coatings (Ta).

Maxthal: Tests with Maxthal in Pb up to 750°C revealed its excellent compatibility with the liquid metal. The protective oxide scale, depicted in Fig. 4a, is quite thin and composed of TiO₂, SiO₂ and mixed oxides [16]. This material is discussed as pump impeller material and has to withstand high local velocities. Sofar no experiments are conducted that show either the suitability or non suitability of this material for the selected application. Experiments are planned and will give answers soon.

SiSiC: SiSiC was also tested in Pb up to 600°C and did not show any incompatibility with the liquid metal. Like for the Maxthal no specific test at high flow velocities was performed so far, but due to the known wear resistance of this material beneficial behaviour is expected.

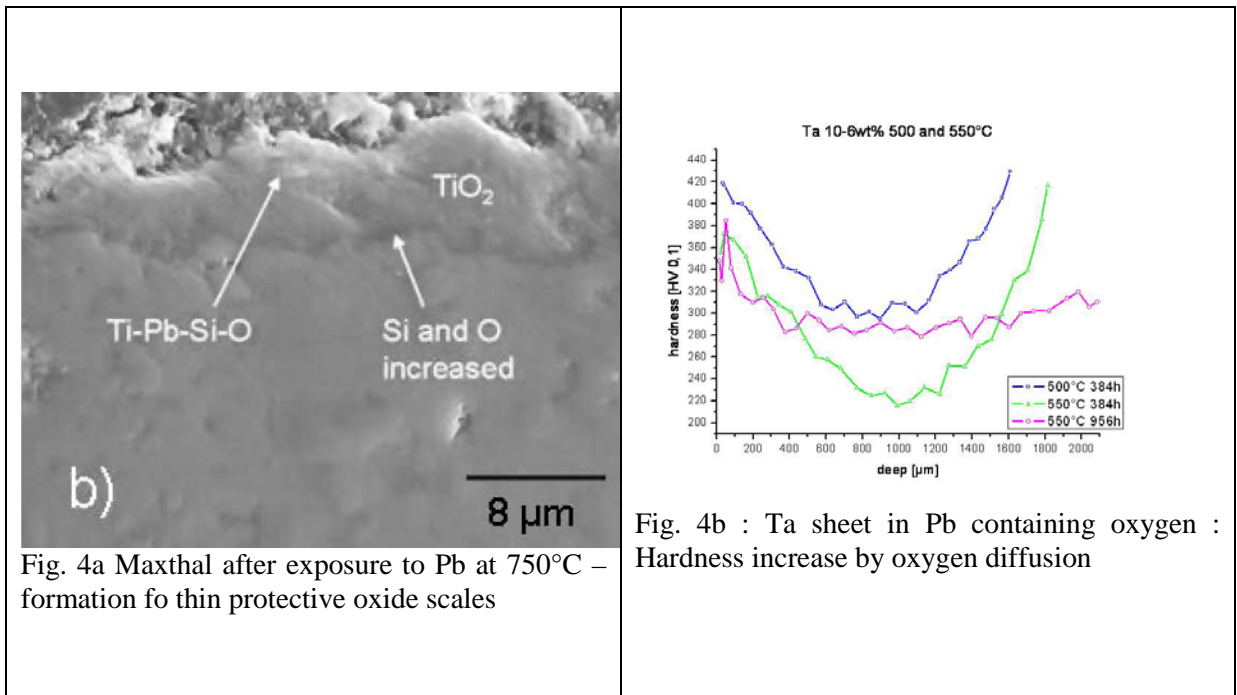


FIG. 4.

Ta Coating: Ta as refractory metal has no solubility in Pb. Therefore coating of an impeller was discussed as an other alternative solution. Basic exposure tests in Pb showed the expected incompatibility of the Ta with oxygen containing Pb at higher temperatures. At temperatures above 400°C the oxygen diffuses into the Ta and embrittles the material, as seen in the hardness increase of Ta exposed at 500 and 550°C in Fig. 4b. For longer times and higher oxygen contents even entire oxidation of Ta sheets (200μm thick) were observed. The simultaneous use of Ta and oxygen in Pb does not seem to be a suitable option for material protection in a Pb cooled nuclear reactor. Tests with a Ta coated steel impeller pump in oxygen reduced Pb are at the time under preparation. If successful the same impeller will be tested also in oxygen containing Pb at 480 °C to monitor whether the oxygen uptake and through that the embrittlement is significantly slowed down at this lower temperature.

5. Surface protection

Fuel claddings are operated up to 550°C. The use of 15-15Ti stabilized steel for the ALFRED cladding is doubtful or at least critical at this elevated temperature due to expected dissolution. The cladding material of the commercial ELFR, the f/m steel T91, will not suffer from dissolution, but oxidation becomes a severe problem. Therefore, surface protection barriers are required to ensure safe operation of Pb cooled fast reactors at the envisaged temperatures. Dense, stable and slowly growing oxide scales that are formed in-situ are the preferential protection barrier. Alumina, which is employed for protection of stationary gas turbines [17], but at higher temperatures, is one option. Surface aluminizing can be used to enrich a base steel (either 316 or T91 type steel) with aluminum resulting in the potential to form alumina scales during use [18]. One applicable method is the surface alloying of deposited coatings using pulsed electron beams [19]. By that, a surface graded material having the target Al concentration in the outer surface region can be manufactured [Fig. 5a]. Such scales showed their potential to protect steels up to 600°C even in LBE for more than 10,000h. To ensure the formation of such protective scales over the temperature range of 380 to 550°C an optimized FeCrAl composition was explored experimentally [20]. An Al content of 6wt% with 16wt% Cr was effective to form thin Al-rich scales between 400 and 600°C in Pb [Fig. 5b].

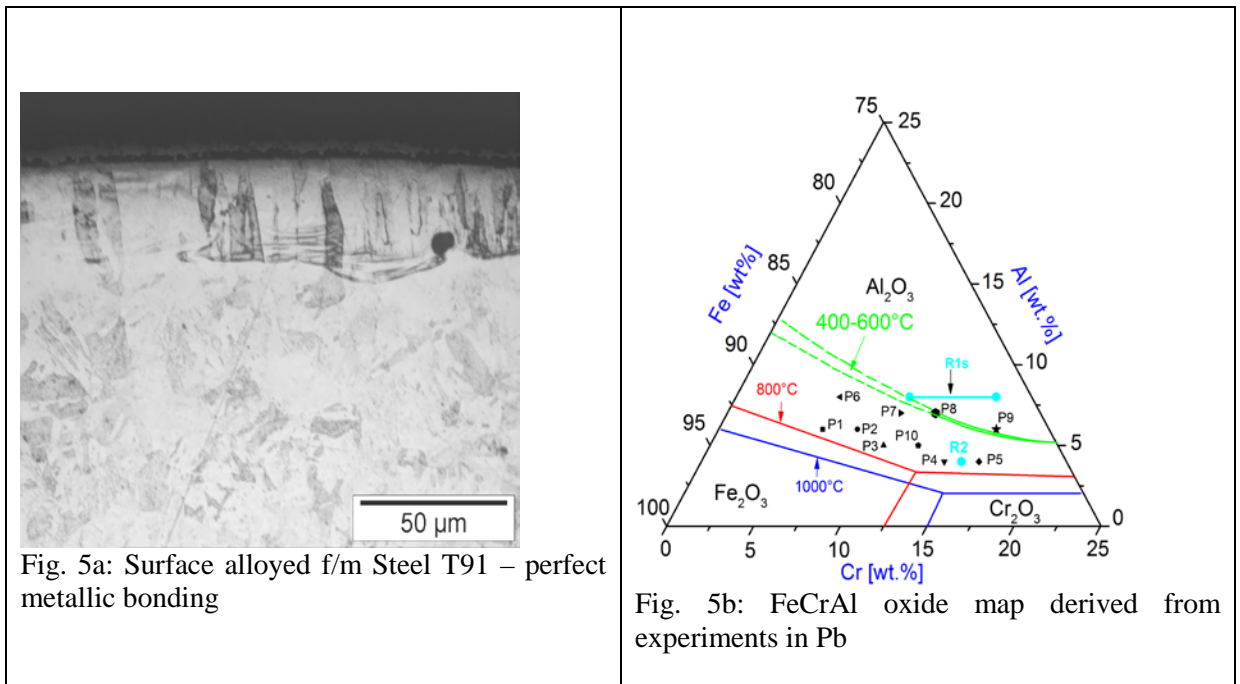


FIG. 5.

As mentioned in the introduction, a spiral steam generator [7] was specifically designed for a commercial Pb cooled fast reactor. Therefore, surface aluminized steels (T91 and 316 type) were tested to evaluate the allowable bending radius or strain before surface cracking occurs. At room temperature, a strain of 10%, that is sufficient for manufacturing a spiral SG, was reached with surface aluminized steel having about 6wt% of Al. This is the minimal required Al content for the formation of thin protective scales. Therefore, the potential of reactive elements like Y, Ce, Zr and others to lower the required Al content will be investigated in future.

6. Mechanical property degradation

Besides simple corrosion also mechanical properties like creep strength and wear resistance might be affected by the contact with the liquid metal coolant. It was shown [21][22][23] that liquid Pb has a deteriorating effect on mechanical properties if it comes in direct contact with the steel. Oxide scales that prevent the direct interaction will, as long as they stay intact, mitigate any effect of the Pb. The creep rupture strength e.g. of f/m steel T91 is reduced remarkably due to the contact with the liquid metal [21]. The influence of the coolant was negligible in case of surface aluminized T91. There, the thin alumina scale was able to catch the deformations of the steel without cracking. Detailed evaluation allowed to define a threshold stress of about 120 MPa, below which, mainly due to the reduced strain that does not result in oxide scale cracking, the influence of Pb becomes negligible [Fig. 6a]. 316L type steels in contrast does not show such pronounced effects at all.

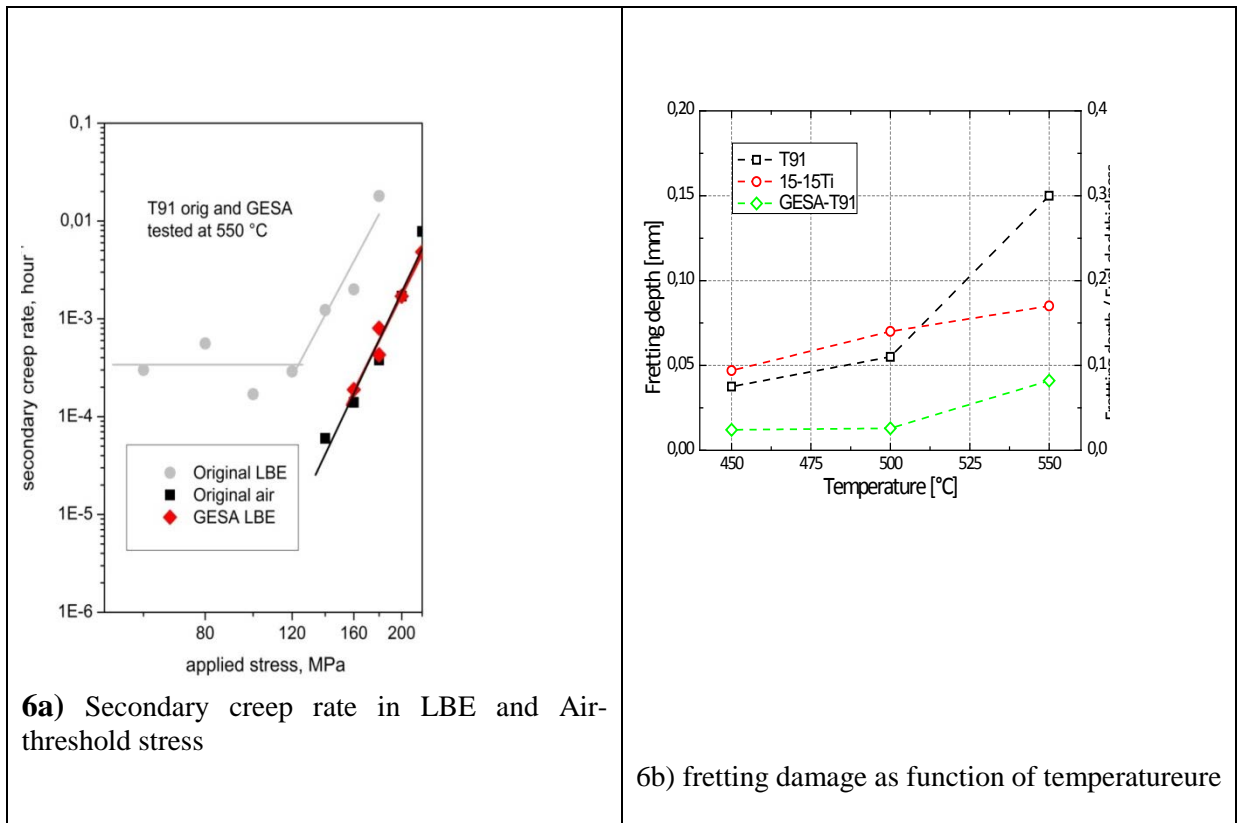


FIG. 6.a Secondary creep rate in LBE and Air- threshold stress 6b: fretting damage

Another interesting phenomena is fretting in Pb, which is a specific type of wear occurring at fuel claddings and heat exchanger tubes. Small amplitudes (<200 μ m) can lead to severe damage. Tests were done at harsh, accelerated conditions to evaluate the possible influence on the life time of the related components [24]. Steel T91 and the 15-15Ti stabilized steel and surface aluminized T91 were explored. Fretting wear can lead to fuel clad penetration at the T91 and 15-15Ti steel of more than 10% of wall thickness depending on the relevant parameters like amplitude load and temperature already after 150 h at a frequency of 10 Hz (Fig. 6b). Both steels show in addition a strongly increased wear with increasing temperature. The austenitic steel exhibits at 450 $^{\circ}$ C dissolution attack already after 600h, which was never observed even for more than 10,000h at 500 $^{\circ}$ C in Pb. The surface aluminized T91 steel has the highest resistance against fretting wear. Post examination based on the construction of fretting maps allowed to predict the parameters that allow safe operation of fuel cladding regarding fretting damage. Loads above 75N and amplitudes below 15 μ m combined with surface aluminizing are safe parameters.

7. Summary and Conclusion

- Solubility, oxygen potential, dissolution and oxidation kinetics are key parameters for material compatibility in Pb or LBE
- All components made from 316L can be used at the envisaged temperature range up to 480 $^{\circ}$ C
- Fuel claddings, both for ALFRED (15-15 Ti) and ELFR (T91) require surface protection most suitable based on surface alloying processes.
- Oxidation of f/m steel T91 above 450 $^{\circ}$ C \rightarrow insufficient heat transfer capability – might require surface protection at SG or HX tubes

A. Weisenburger et al.

- Higher flow velocities (alternative materials for impeller) and turbulent flow pattern → severe erosion requires further investigation
- Surface aluminizing can mitigate corrosion and deteriorating effects of coolant on mechanical properties
- Fretting needs to be considered – Surface aluminizing combined with high contact load and small amplitude are needed

ACKNOWLEDGEMENTS

The work presented was mainly performed with funding supplied under the EU contract of LEADER

REFERENCES

- [1] LEADER Lead – cooled European advanced demonstration reactor FP7-249661
- [2] EUROTANS, European Research programme for the transmutation of high active level nuclear waste in an accelerator driven system, FI6W-CT-2004-516520
- [3] WEISENBURGER, A., SCHROER, C., JIANU, A., HEINZEL, A., KONYS, J. STEINER, H., MÜLLER, G., FAZIO, C., GESSI, A., BABYAN, S., KOBZOVA, A., MARTINELLI, L. GINESTAR, K., BALBAUD-CELERIER, F., MARTIN-MUNOZ, F.J., SOLER CRESPO, L. Long term corrosion on T91 and AISI 316L steel in flowing lead alloy and corrosion protection barrier development: Experiments and models, J. Nucl. Mat. 415, 3, 31 (2011), 260
- [4] OECD-NEA, Handbook on Lead-bismuth Eutectic Alloy and Lead Properties, Materials Compatibility, Thermal-hydraulics and Technologies, OECD-NEA 6195, 2007
- [5] HOSEMANN, P., KABRA, S., STERGAR, E., CAPPILO, M.J., MALOY, S.A., Micro-structural characterization of laboratory heats of the Ferric/Martensitic steels HT-9 and T91 J. Nucl. Mat. 403,1-3, (2010)
- [6] KURATA, Y., Corrosion experiments and materials developed for the Japanese HLM systems, J. Nucl. Mat. 415, 3, 31 (2011), 254
- [7] CINOTTI, L., SMITH, C.F., SEKIMOTO, H., MANSANI, L., REALE, M., SIENICKI, J. Lead-cooled system design and challenges in the frame of Generation IV International Forum, J. Nucl. Mat. 415, 3, 31 (2011), 245
- [8] INTERNATIONAL ATOMIC ENERGY AGENCY, Fast Reactor database – <http://www-pub.iaea.org/books/iaeabooks/7581/fast-reactor-database-2006-update>
- [9] YVON, P., CARRE, F., Structural materials challenges for advanced reactor systems, J. Nucl. Mat. 385, 2, (2009), 217
- [10] COUTSOURDIS, D., Materials for Advanced Power Engineering, Part 1 361 Kluwer Academic Publishing Dordrecht 1994
- [11] ALEMBERTI, A., CARLSSON, J., MALAMBU, E., ORDEN, A., CINOTTI, L.,

A. Weisenburger et al.

- STRUWE, D., AGOSTINI, P., European lead- cooled fast reactor, in: FISA 2009, Prague, 22
- [12] MÜLLER, G., HEINZEL, A., SCHUMACHER, G., WEISENBURGER, A., Control of oxygen concentration in liquid lead and lead–bismuth J. Nucl. Mat.321, 2–3, (2003), 256
- [13] SCHROER,C., WEDEMEYER, O. KONYS, J., Aspects of minimizing steel corrosion in liquid lead-alloys by addition of oxygen, Nucl. Eng.and Design, 241, (2011), 4913
- [14] MÜLLER, G, SCHUMACHER, G., ZIMMERMANN, F., Investigation on oxygen controlled liquid lead corrosion of surface treated steels, J. Nuc. Mat., 278, 1, (2000) 85
- [15] GLASBRENNER, H., KONYS, J., MUELLER, G., RUSANOV,A., Corrosion investigations of steels in flowing lead at 400°C and 550°C, J. Nuc. Mat., 296, 1-3, (2001) 237
- [16] HEINZEL, H., MÜLLER, G., WEISENBURGER, A., Compatibility of Ti3SiC2 with liquid Pb and PbBi containing oxygen J. Nucl. Mater. 392, 2, (2009) 255
- [17] STRAUSS, D., MÜLLER, G., SCHUMACHER, G., ENGELK, V., STAMM, W., CLEMENS, D., QUADDAKERS, W.J., Surface and coatings Technology 135 (2001) 196–201
- [18] WEISENBURGER, A., HEINZEL, A., MÜLLER, G., MUSCHER, H., ROUSANOV, A., T91 cladding tubes with and without modified FeCrAlY coatings exposed in LBE at different flow, stress and temperature conditions, J. Nucl. Mat., 376, 3, (2008) 274
- [19] ENGELKO, V., YATSENKO, B., MUELLER, G., BLUHM, H., Pulsed electron beam facility (GESA) for surface treatment of materials, Vacuum 62 (2001) 211
- [20] JIANU, A. et. Investigation of oxide scales formed on FeCrAl alloys exposed to heavy liquid metals
- [21] JIANU, A., MÜLLER, G., WEISENBURGER, A., HEINZEL, A., FAZIO, C., MARKOV, V.G., KASHTANOV, A.D., Creep-to-rupture tests of T91 steel in flowing Pb–Bi eutectic melt at 550 °C J. Nucl. Mat., 394, 1, (2009) 102
- [22] WEISENBURGER, A., JIANU, A., AN, W., FETZER, R., DEL GIACCO, M., HEINZEL, A., MÜLLER, MARKOV, V.G., KASHTANOV, A.D., Creep, creep-rupture tests of Al-surface-alloyed T91 steel in liquid lead bismuth at 500 and 550 °C, J. Nucl. Mat., 431, 1–3, (2012) 77
- [23] VAN DEN BOSCH, J., BOSCH, R.W., SAPUNDJIEV, D., ALMAZOUZI, A., Liquid metal embrittlement susceptibility of ferritic–martensitic steel in liquid lead alloys, J. Nucl. Mat., 376, 3, (2008) 322
- [24] DEL GIACCO, M., WEISENBURGER, A., MUELLER, G., Fretting corrosion in liquid lead of structural steels for lead-cooled nuclear systems: Preliminary study of the influence of temperature and time, J. Nucl. Mat., 423, 1–3, (2012) 79

Synthesis of R&D results on 9%Cr steels for Steam Generators of Sodium Fast Reactors

F. Dalle^a, M. Blat-Yrieix^b, C. Cabet^a, S. Dubiez-LeGoff^c, Ph. Dubuisson^a, L. Forest^a, L. Martinelli^a, M. Sauzay^a, C. Desgranges^a, K. Ginestar^a

^aCEA Saclay, DEN/DANS, 91191 Gif-sur-Yvette Cedex, France

^bEDF R&D, MMC, Site des Renardières, 77818 Moret sur Loing, France

^cAREVA NP, 69006 Lyon, France

Abstract. Because of their favorable thermal and mechanical properties, 9%Cr ferritic-martensitic steels are relevant candidates for structural applications in Sodium Fast Reactors. Their specifications are more precisely dedicated to different designs of Steam Generators. This is why they have been extensively studied in the past decade by the French nuclear community. Key R&D points are thick products availability and properties, homogeneous and heterogeneous welding, long term creep evolution, creep-fatigue softening, steam oxidation, sodium corrosion, wastage, hydrogen embrittlement, caustic cracking under stress, etc. This paper proposes some R&D results obtained recently about homogeneous welding, mechanical and microstructural evolutions during cyclic loading and corrosion by steam/water environment. Finally, the importance of each subject is discussed considering Steam Generator applications.

1. Introduction

Sodium Fast Reactor (SFR) is considered in France as the most mature technology of the different Generation IV systems. Material selection for the major components of ASTRID (Advanced Sodium Technological Reactor for Industrial Demonstration) is a key point of the French Research and Development program launched by CEA, EDF and AREVA. The choice of materials for the Steam Generator (SG), with expected in-service temperature range between 240 and 530°C, is complex, depending on many aspects: thermal and mechanical properties, manufacturing, weldability, sodium interactions on one side and steam/water on the other side, resistance to wastage [1]...

Because of their favorable thermal properties, 9%Cr steels are relevant candidates for different designs of SGs.. The purpose of this article is to present some recent advances made by CEA, EDF and AREVA in various R&D programs, in order to improve the use and understanding of these materials. The importance of each R&D subject is discussed according to the SG specifications.

2. 9%Cr Steam Generator specifications

Different SG technologies have been chosen in the frame of the ASTRID project and several of them use 9%Cr steel parts. These different designs are the following:

- Steam Generator with straight tubes and expansion loops
- Steam Generator with straight tubes and an expansion compensator
- Reverse Steam Generator with sodium flowing inside the tubes and steam/water outside.

Table 1 gives some dimensions and operating conditions in order to compare the 9%Cr performance with SG specifications. The specific grade considered here is the ferritic-martensitic X10CrMoVNb9-1 steel following RCC-MRx designation [2], also called “grade 91” following ASME designation.

Table 1. ASTRID main requirements for 9%Cr Steam Generators (straight tubes and expansion loops)

<i>Envelope - External diameter (mm)</i>	1040
<i>Thick plate – Thickness (mm)</i>	250 (initial forging ~ 450 mm)
<i>Tube – External diameter (mm)</i>	15.6
<i>Tube – Thickness (mm)</i>	2.5
<i>Tube – Length (m)</i>	26.1
<i>Welds – Maximum thickness (mm)</i>	85
<i>Sodium temperature (°C)</i>	345 < 525
<i>Steam/Water temperature (°C)</i>	240 < 490
<i>Pressure (bars)</i>	~ 190
<i>Potential damages</i>	Excessive deformation, Creep fatigue, Ratcheting, Sodium corrosion, Steam oxidation, Caustic cracking under stress, Wastage, etc.

3. Recent advances on 9%Cr steels R&D

To meet the SG specifications, several R&D projects have been initiated some years ago by the French partners. Recent advances are described in the paragraphs below about homogeneous welding, mechanical and microstructural evolutions during cyclic loading, and corrosion by steam/water environment.

3.1. Welding

Currently, no weld metal has been specified for 9%Cr steels in the RCC-MRx code [2]. But welded joints must fulfil some requirements imposed by the Order of 12 December 2005 relative to nuclear pressure equipment (ESPN) [3]. In the case of ferritic steels, the weld metal tensile elongation A_{5d} at ambient temperature must be above 20% in the weld zone in case of “N1_{ESPN}” level. The feedback from literature, from industrial knowhow, and from several experiments carried out by the french partners indicates how difficult it is to ensure such a mandatory requirement for 9%Cr steels. This is why a parametric study was carried out on some welding conditions to find a way to improve the welded joint mechanical properties. Many joints have been elaborated by automatic TIG process with different commercial filler metals and different welding conditions: pulse or continuous welding current, deposition rate, post-weld heat treatment temperature (between 740 and 760°C), etc. The resulting microstructure, impact test, and tensile properties were studied.

The welding current type – pulsed or continuous – does not have a great influence on the welded joint microstructural and mechanical properties. On the contrary, the results depend on the deposition rate of filler metal and on the post-weld heat treatment temperature. Figure 1 shows the impact energy curves for three different deposition rates: 0.2, 0.75, and 1.89 g/cm, without any variation in the other parameters. The smaller the deposition rate per run is, the lower the ductile-to-brittle transition temperature is. The weld zone related to the lower deposition rate (0.2 g/cm) is characterized by a fine fully reaffected grain microstructure, a lower density of precipitates, and a lower hardness. These promising results clearly need to be completed with tensile tests and measurements of the weld metal elongation. It is also necessary to check the stability of these properties after ageing treatments. This work is currently in progress, through the elaboration of an additional joint with the identified optimized parameters.

As to the post-weld heat treatment temperature, it is well known that 9%Cr steels are very sensitive to heat treatments and that temperatures have to be closely controlled during all steps of nuclear

fabrication and assembly processes. The present study confirms that the post-weld heat treatment needs to be carried out within narrow temperature ranges to ensure the fulfillment of tensile and impact property requirements. More precisely, the French partners have taken a position on a reference temperature: $745 \pm 10^\circ\text{C}$, to separate the tempering temperature range (after austenitization) from the post-weld heat treatment range. The $\pm 10^\circ\text{C}$ margin is narrower than the usual $\pm 15^\circ\text{C}$ margin used for other industrial applications, but it seems achievable with early prescriptions at the design step of the project.

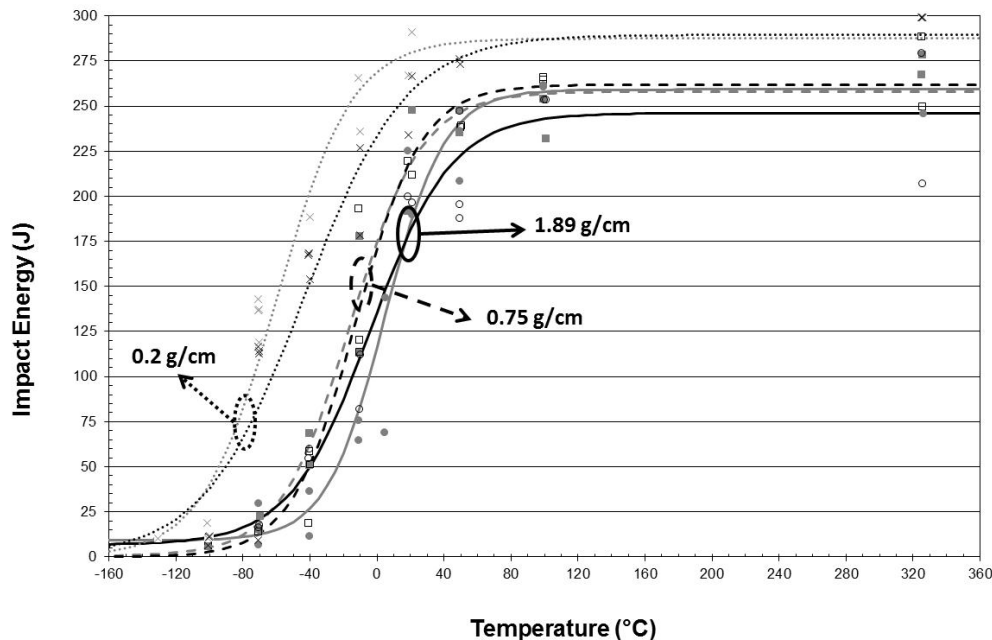


FIG. 1. Influence of deposition rate on the weld zone toughness properties ($55 \times 10 \times 10 \text{ mm}^3$ Charpy V-notch samples)

3.2. Cyclic softening

The cyclic softening of 9%Cr steel has been extensively studied in the past few years because it represents a major issue for nuclear applications. Because of its importance, several experimental and numerical studies have been undertaken by the French partners. Recently, a micromechanical model has been proposed for predicting both the microstructure evolution and the macroscopic softening of 9%Cr steels [4]. This model based on the self-consistent Kröner homogenization model [5] is suitable for elastic-plastic constitutive laws. Each martensite block is successively regarded as an inclusion within the matrix made of other blocks. The behavior of the polycrystal is then calculated by an average process over all the blocks. Based on the identified mechanisms of microstructure evolution determined by TEM observations [6], two different softening mechanisms are taken into account: the decrease in dislocation densities inside the subgrains and the subgrain size growth. The subgrain size growth is mostly due to the disappearance of Low Angle Boundary dislocations. The final model is based on some physical parameters mainly determined from literature or by microstructural observations and only depends on two adjustable parameters. These two parameters are volume and energy of activation and they are adjusted from the loading data of the first fatigue loop. Finally, the homogenization modeling gives good predictions of the cycling softening for two different strain rates (Fig. 2a). It also gives reasonable predictions of the evolution of the subgrain size during cycling with a quick increase at the beginning and then a continuous but slower evolution (Fig. 2b).

The predictions have been shown to be only weakly dependent on the main material parameters provided they belong to a physically-based range of variation. Further work is in progress to take into account other dislocation movements such as climb, to improve the predictions at high temperature. A localization law adapted from the approach of Molinari et al. [7] will also be implemented to better

approximate the viscoplastic behavior of these steels. With only two adjustable parameters, this micromechanical model is an important step forward to predict the real softening of 9%Cr steels in service conditions. It also allows a useful benchmark with phenomenological models used to design components.

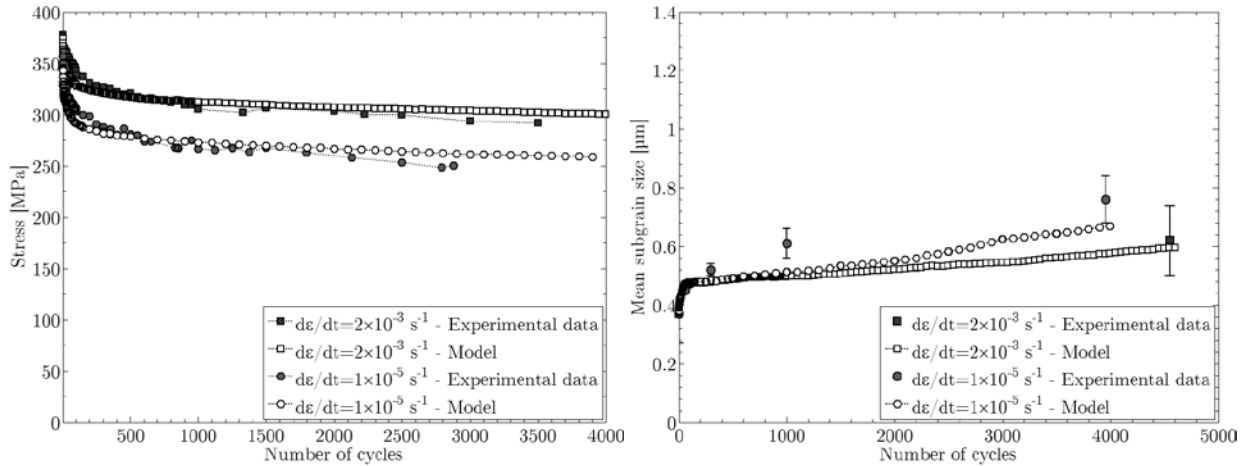


FIG. 2. Predictions of the pure fatigue behavior for two different strain rates: (a) cyclic softening and (b) sub-grain size evolution (b)

3.3. Steam oxidation

The oxidation of 9%Cr steels in water environments is also known to be a major issue for Steam Generator applications. It is necessary to estimate the metal loss by oxidation to make sure the initial thickness of the tubes is sufficient for the expected lifetime. In other words, the prediction of the total oxide thickness for a given lifetime is essential right from the design step of the project. According to the literature [8] and to the French partners experiments [9], the oxidation of martensitic steels above 400°C is characterized by the growth of a duplex layer composed of a Fe-Cr spinel ($\text{Fe}_{3-x}\text{Cr}_x\text{O}_4$, $0 < x < 2$) layer at the metal/oxide interface and a magnetite (Fe_3O_4) layer in contact with the steam. In most cases, a layer of hematite, formed by oxidation of the magnetite, is observed on top of the magnetite layer. An average parabolic law can be derived from the numerous experiments on 9%Cr steels oxidation to describe their oxidation kinetics. Nevertheless there is a significant scatter in the results (Fig. 3e) on the one hand and spalling of the scale may happen leading to a possible acceleration of oxidation on the other hand. Consequently it is necessary to improve the understanding of the different phenomena and their modeling, in order to give valid predictions of the oxide thickness but also to plan cleaning operations during service.

A dedicated device was developed to perform oxidation experiments in pure water vapour with a circulation loop. The tests are carried out at 550°C, in a low steam flow at atmospheric pressure, up to 5000 h on grade 91 specimens. The obtained oxidation kinetics is parabolic and its parabolic constant is consistent with literature results as observed on Fig. 3e. A precise TEM study of the three oxide layers was carried out on a sample oxidized during 48h in this device (Fig. 3a). In particular the spinel oxide is composed of a large quantity of small equiaxial grains with an average stoichiometry $\text{Fe}_{2.4}\text{Cr}_{0.6}\text{O}_4$. But at a finer scale near the base metal, a series of alternatively Fe-rich and Cr-rich grains is noticeable. This observation is in good agreement with the oxidation mechanism proposed to describe the oxidation process [10]. Oxygen is brought to the metal/spinel interface in molecular form (water molecule). The anionic growth of the internal scale is controlled by the space made available by the metal loss due to formation, by cationic flux, of the external magnetite scale. This mechanism could explain the alternative Fe- and Cr-enrichment during the spinel growth.

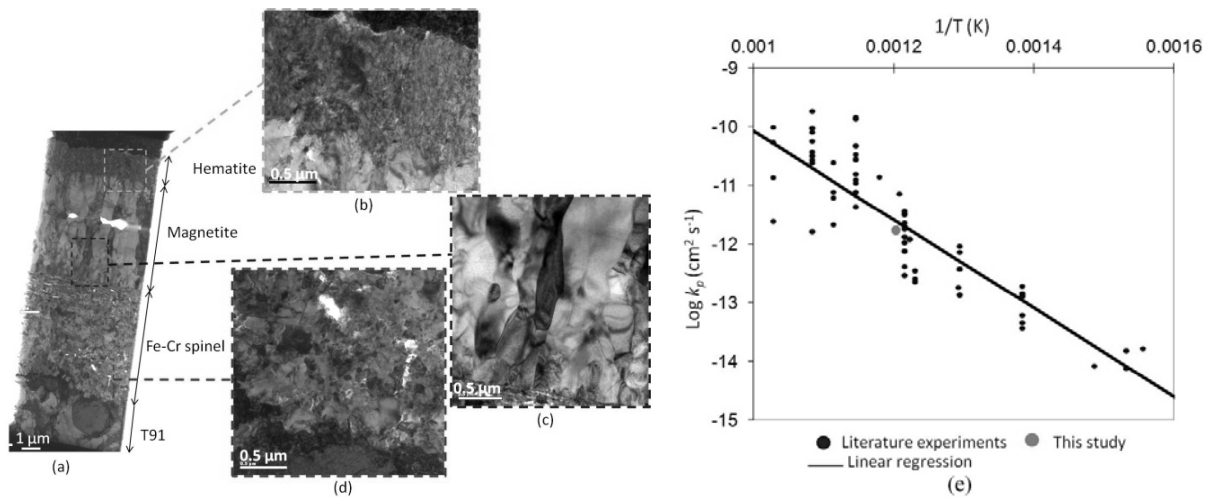


FIG. 3. Oxidation of 9%Cr steels in pure water: (a) Transmission Electron Microscopy picture of the cross section of a T91 sample oxidized during 48h, (b) zoom on the hematite layer, (c) zoom on the magnetite layer, (d) zoom on the Fe-Cr spinel layer, (e) parabolic constants versus temperature

4. Priorities of the R&D program on 9%Cr steels for ASTRID

Following the recent advances in such fields as weldability, mechanical behaviour or corrosion by environments, the R&D program on 9%Cr steels have been reassessed for the next step of the ASTRID project. This section briefly describes the R&D priorities as well as some qualification needs to be taken into account.

— Safety requirements [3] depending on applied heat treatments

It is well known that 9%Cr steels are very sensitive to heat treatments and that temperatures have to be closely controlled during fabrication and assembly processes. It is particularly difficult to meet the weld tensile elongation requirement ($A_{5d} > 20\%$) if the post-weld heat treatment is not carried out within narrow temperature range. Improvement of the weld metal chemical composition and optimization of the assembly process (see section 3.1 on deposition rate per run) are currently in progress to improve the welded joint mechanical properties. In addition, a study is needed to test different heat treatments simulating repair operations and in-situ re-heating during the SG life: a range between 735°C/10h and 760°C/40h should be explored.

— Long term tests on welded joints: thermal ageing, creep and creep-fatigue

Weld metals and deposit conditions are under development. When qualified welded joints are available, thermal ageing, creep, and creep-fatigue tests will be launched. It is critical to start long-term data acquisition as soon as possible, in order to guarantee SG lifetime.

— Steam oxidation

Some predictions of the total oxide thickness were made with the following hypotheses: the parabolic law is valid during the SG lifetime, oxide spallation and cleaning phases occur with given frequencies. This study shows that steam oxidation may be a critical issue if ASTRID SG lifetime is to be 60 years. It is obviously far less critical if the SG is replaced during operation: satisfactory estimations have been made for a 30 years lifetime. However, R&D studies are needed on the consequences of oxide scaling and the influence of water chemistry.

— Cyclic softening

Cyclic softening also influences the SG lifetime. As seen before (section 3.2), a polycrystalline plasticity model is currently being improved: it can enable predictions of the mechanical properties of 9%Cr steel after 30 to 60 years of service conditions.

— *Leak propagation – wastage*

As far as the sodium/water reaction is concerned, the 9%Cr steels were shown to be more prone to wastage than other SG materials (Alloy 800). Their overall resistance is deduced from austenitic steel performances by an extrapolation factor. It has been improved in some conditions, based on recent experiments in collaboration with IGCAR. Further experimental and numerical program is in progress to give better predictions of this phenomenon and to compare the kinetics of leak propagation to the kinetics of leak detection.

— *Thick plate supply*

Some thick forgings were obtained by AREVA, which is an important step to demonstrate the industrial capacity to produce ~250 mm thick plate (Table 1). Nevertheless the microstructural and mechanical properties of such products need to be checked, as well as their volume controllability.

— *Improvement of RCC-MRx rules*

SG designers use RCC-MRx rules, which are mainly based on experimental data about austenitic steels [2]. Since the physical and mechanical properties of 9%Cr steels are very different from austenitic steels, some rules need to be changed and adapted to softening materials. For example traction-torsion tests were recently carried out and they clearly showed that the “efficiency diagram” used by designers to limit ratcheting is unsuitable for 9%Cr steels. A short-term work is necessary to sort out this kind of difficulties.

— *Sodium corrosion*

Even if 9%Cr steels corrode more than austenitic steels in sodium, this phenomenon is not likely to be a critical item for SG applications. Results obtained after 5000 h in the corrosion loop CORRONa [9] need to be confirmed by long-term tests. Some predictions of the total oxidized thickness will then be available. Oxide and corrosion layers are expected to be significantly thinner than on the steam side of the SG tubes.

— *Heterogeneous welding*

With the guidance from RCC-MRx code, some know-how has been regained by the French partners on the 316L(N)/9%Cr heterogeneous welding. A Ni-based filler metal was used to fabricate several joints with automatic TIG process but softened areas were detected in the thermally affected zone. Some new filler metals should be tested in the near future.

— *Long term creep evolution*

A transition in deformation mechanisms is expected between high stress and low stress creep regime, with higher strain rates at low stress. Some work is currently in progress to determine this transition at 550°C.

— *Hydrogen embrittlement at low temperature*

The susceptibility of 9%Cr steels to hydrogen embrittlement in the SG conditions was estimated by the French partners in the past few years. Grade 91 in the normalized and tempered state was studied, following RCC-MRx specifications. For example simple tensile tests were carried out under severe SG conditions: low temperature, liquid water with high hydrogen content, weldment microstructure, holding time, etc. No degradation of mechanical properties was observed. This should soon be confirmed with some additional experiments.

— *Caustic cracking*

The susceptibility of 9%Cr steels to stress corrosion cracking by formation of caustic soda was recently estimated by the French partners. An experimental program was launched at low temperature, with holding times in various soda environments. The results showed little sensitivity of grade 91 to caustic cracking when compared to 2¼%Cr steels. Validation is planned in the near future.

5. Concluding remarks

Several designs were proposed for the Steam Generator of ASTRID: a technology based on straight tubes with either an expansion loop or an expansion compensator and a “reversed” technology with sodium flowing inside the tubes. This paper proposes an overview of the R&D actions initiated by CEA, EDF and AREVA about grade 91 for Steam Generators: the main subjects are manufacturing, RCC-MRx fulfillment, welding, mechanical behaviour, corrosion by environments, risks in service, etc. A status is given on recent R&D results about homogeneous welding, prediction of in service cyclic softening, and analysis of steam oxidation. An optimization of the deposited quantity of filler metal per run and of the post-weld heat treatment is currently in progress to improve the 9%Cr welded joint properties, in particular their tensile elongation. Cyclic softening during pure fatigue tests is well predicted by a polycrystalline model. Predictions under service conditions should be obtained soon. Steam oxidation was studied in pure water vapour: over long time range, the observed spinel, magnetite and hematite layers are in good agreement with literature data but understanding and modeling must be improved for mid-term oxidation kinetics. Finally, the priorities for the further program are reviewed, considering the need for SG applications and the recent R&D advances.

ACKNOWLEDGEMENTS

For their important contributions to the R&D on 9%Cr steels, the authors thank A.F. Bonnot, V. Grabon, T. Marlaud from AREVA, F. Delabrouille, A. Lina, D. Renaud from EDF and O. Ancelet, F. Beauchamp, J.L. Courouau, Y. Lejeail, L. Marchetti, P. Matheron, E. Pluyette, R. Robin, S. Vincent from CEA.

REFERENCES

- [1] S. Dubiez-Le Goff, S. Garnier, O. G lineau, F. Dalle, M. Blat-Yrieix, J.M. Augem, Proceedings of ICAPP'12, Chicago, USA, June 24-28, 2012, Paper 12053
- [2] RCC-MRx 2012 "Design and Construction Rules for Mechanical Components of Nuclear Installations", www.afcen.com.
- [3] Order of 12 December 2005 relative to nuclear pressure equipment. The ESPN (Equipements Sous Pression Nucl aires) Order covers the design, manufacturing and use of equipment specially designed for nuclear applications, and whose failure could result in radioactive emissions.
- [4] P.F. Giroux, F. Dalle, M. Sauzay, C.Ca s, B. Fournier, T. Morgeneyer, A.F. Gourgues-Lorenzon, Proc. Eng. 2 (2010) 3984-3993
- [5] E. Kr ner, Acta Metall. 9 (1961) 155
- [6] M.F. Giordana, P.F. Giroux, I. Alvarez-Armas, M. Sauzay, A. Armas, T. Kruml, Materials Science and Engineering A 550 (2012) 103-111
- [7] A.Molinari, S. Ahzi, R. Kouddane, Mech.Mater. 26 (1997) 43-62
- [8] I.G. Wright, R.B. Dooley, International Materials Reviews, 55 (2010), 3, 129
- [9] L. Martinelli, N. El Hassan, K. Guillot, C. Desgranges, submitted to Corrosion Science
- [10] L. Martinelli, F. Balbaud-C l rier, A. Terlain, S. Bosonnet, G. Picard, G. Santarini, Corrosion Science 50 (2008) 2537
- [11] J.-L. Courouau, F. Balbaud-C l rier, V. Lorentz, T. Dufrenoy, International Congress on Advances in Nuclear Power Plants (ICAPP 11), paper 11152, Nice, France, 2011

French R&D on materials for the core components of Sodium Fast Reactors

M. Le Flem^a, M. Blat-Yrieix^b, V. Garat^c and J.L. Séran^a

^aCEA, DEN, DMN, Gif sur Yvette, France

^bEDF, Moret sur Loing, France

^cAREVA, AREVA NP, Lyon, France

Abstract. The Sodium Fast Reactor (SFR) has been chosen as the reference type in France and the prototype construction, ASTRID, is planned within 2023. The starting core components of ASTRID should be fabricated with previous well documented reference materials such as 15/15Ti-like austenitic steels for the cladding tubes or 9Cr/1Mo-like martensitic steels for the wrapper tubes. However, additional R&D is welcomed to get an accurate description of best grades, their behavior at high temperature and their stability under irradiation. For the production reactors, the performances are expected to increase via the use of advanced materials exhibiting improved properties. ODS steels are the reference candidates for high burn-ups: they could sustain doses of 180 dpa at least with limited swelling and should not be sensitive to significant deformation by thermal creep. In addition, a long-term R&D program is also necessary to recommend new materials with superior performance such as, vanadium alloys or SiC/SiC composite, potential candidates for the wrapper tube because of its refractoriness and dimensional stability. The present work gives an overview of the investigation led for short-, middle- and long-term SFRs.

1. Introduction

Among the six reactor concepts investigated in the scope of Generation IV forum, the Sodium Fast Reactor (SFR) has been chosen as the reference type in France. The prototype, ASTRID, construction, is planned within the next decade. ASTRID will demonstrate the main options and qualify the technological choices for the commercial reactor, SFR. Based on the large feedback from previous French sodium reactors (Rapsodie, Phénix, SuperPhénix), the starting core components of ASTRID should be fabricated with previous well documented reference materials such as 15/15Ti-like austenitic steels for the cladding tubes or 9Cr/1Mo-like martensitic steels for the wrapper tubes, etc. Specific qualification of these materials for their use in ASTRID [1] is however needed in order to improve their description. In addition, various solutions regarding materials for absorbers, reflectors and shielding are also investigated in order to update the current database and behaviour modelling and to develop new designs.

Besides, the performance of the SFR core is expected to be highly impacted via the use of advanced materials exhibiting improved properties. Indeed, the main requirements for the structural materials to be used in these reactor systems are dimensional stability up to a maximum irradiation damage levels of ~180-200 dpa and limited deformation by creep. ODS steels (Oxide Dispersion Strengthened materials) with a ferritic and/or martensitic matrix are the candidates for the fuel cladding of production SFRs.

Finally, breakthrough materials must also be investigated to prepare the reactors of the very future such as advanced SFRs exhibiting enhanced margin in terms of safety, and GFRs working at high temperature (up to 850°C in service). According to these challenging requirements, most of the conventional nuclear materials exhibit limitations and refractory metals, such as vanadium, or ceramics, such as carbides, should be evaluated. In particular, SiC/SiC composites are promising due to the high refractoriness, limited deformation and low activation under neutron flux.

The program presently led in France (CEA, AREVA, EDF) to develop materials and to improve their in-pile behavior description in normal and accidental conditions is presented.

2. Reference materials for the core of ASTRID

The short-term construction of ASTRID demonstrator requires the use of well referenced and almost qualified materials, experienced in the past in the former french sodium reactors. Evolution is then preferred to innovation: for the core components, this means launching an R&D program to address qualification related to the specificity of the core and achieve a better description of the materials mainly in terms of swelling and mechanical properties under irradiation.

2.1. Austenitic 15-15 Ti for the cladding (AIM1)

The AIM1 specification (Austenitic Improved Material # 1) is relevant of the knowledge earned up to now to decrease the swelling of the austenitic steels of 316 grade (solution annealed 316, cold worked 316 Ti) and of 15/15Ti type: it deals both with optimization of the chemical composition (optimization of the Ti/C ratio, narrow specifications of swelling inhibitors such as Si, P, C and Ti) and with a better description of the fabrication route at the industrial scale (specific heat treatments to create an appropriate microstructure which is optimized in terms of resistance to swelling). These have been highlighted based on the feedback from many experimental irradiations of fissile pins in Phénix subassemblies or specimens irradiated in capsule made of advanced 15-15 Ti grades which have led to AIM1.

This feedback on 15/15 Ti is relevant to the predictions presently used for the ASTRID conception since the AIM1 grade should behave much better. In particular, the first target dose of 110 dpa could soon be revised upwards after the complete examination of AIM1 pins irradiated in the very last core of Phénix [2]: characterization of the pins of the experimental irradiation OLIPHANT1bis has begun in order to consolidate the design procedures. Recently, the OLIPHANT1bis experiment enabled the prediction of pin deformation by updating both swelling and thermal creep correlations (Figure 1) [3].

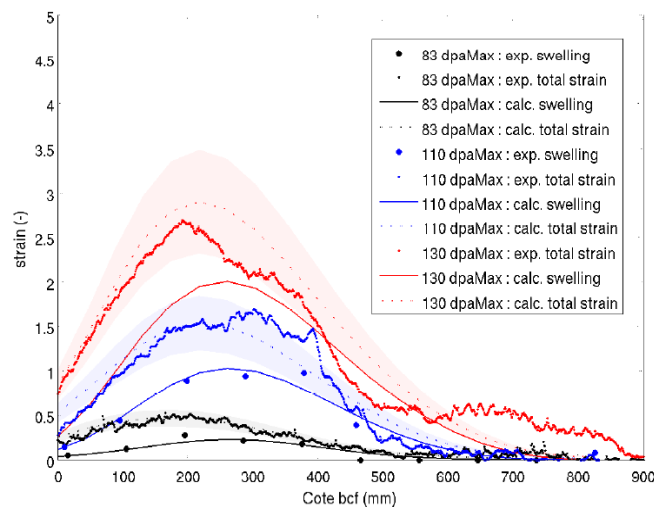


Figure 1: Total strain and swelling strain of 15/15Ti versus axial position for three irradiation experiments led in PHENIX reactor.

These correlations will be further improved, especially by refining the phenomenological description consisting of physical parameters determined by post-irradiation characterizations. This is true not only for the irradiation swelling but also for the creep strain (viscoplastic modeling). This work will finally contribute to enhance the austenitic alloy performance: an R&D program on advanced grades aims to tailor the properties and to determine the next generation of improved austenitic cladding materials, AIM2, specifications (Cr/Ni <1, etc.).

To support the pins manufacturing, spacing wires, and end-plugs (grade to specify according to ASTRID features) at the industrial scale, the fabrication routes are being examined. Joining procedures are also to be updated in line with recent progress made on the processes. These will confirm the specifications and help qualifying the final objects.

2.2. Martensitic 9Cr steel for the wrapper tube (EM10)

The major questionable point about the wrapper tube is the swelling induced by irradiation which results in a loss of mechanical strength (drop of toughness), embrittlement, and performance of the component in case of incidental or accidental event. In normal operations, thermal gradients and material swelling could lead to fuel assembly bow which can increase fuel handling forces. The present reference consists of taking advantages of materials with a body centered cubic crystal structure which has a good intrinsic resistance to irradiation swelling. Thus, ferritic steels or ferritic/martensitic steels are preferred to austenitic steels presented above. However, the ferritic/martensitic class of steels exhibits a ductile to brittle transition (DBTT) at low temperature without irradiation to higher temperatures upon irradiation.

The martensitic steel EM10 (9Cr-1Mo) is well described in terms of behaviour in nominal conditions. The BOITIX9 experiment does confirm the very good behaviour of this material up to 155 dpa [3], which lies in the higher range of ASTRID target:

- Swelling below 0.5%,
- Limited dimension change,
- Moderate shift of the DBTT under irradiation with regards to ferritic or partially ferritic steels (the DBTT remains below 10°C),
- Remaining ductility higher than 1% in the 380-525°C temperature range,
- Hardening in the 380-440°C range but limited change above 440°C compared to the non-irradiated material.

Because the ferritic/martensitic steels exhibit a phase transition (to austenite) in the 850-950°C domain, their mechanical strength significantly drops in this temperature range, which could be encountered in some of the accidental situations. To improve this, stabilised grades such as T91 and T92 grades have been assessed: they offer a slight improvement in mechanical strength at high temperature but exhibit a more pronounced embrittlement under irradiation together with a significant decrease in ductility above 900°C. Consequently, the EM10 grade remains the reference material for the wrapper tube. The modeling of its mechanical behaviour in the case of temperature excursion must be related to the modeling of its microstructure in this temperature range.

Just as for the cladding tube in AIM1, the wrapper tube fabrication route and joining are being investigated with respect to the large feedback from the previous manufacturing.

2.3. Absorbers and shielding materials

The reference absorber material for the control rods of ASTRID is B₄C, chosen because of appropriate neutron properties, good refractoriness and economical considerations. Regarding the qualification of

the B₄C in the scope of ASTRID construction, the main challenge deals with relaunching the characterization line of irradiated materials to study the absorber assemblies used in Phenix [2] in order to update the design procedures and to have a more accurate description of the materials and their chemical compatibility (e.g. B₄C with cladding).

Then, a R&D program is launched to optimize the fabrication route (powder quality, sintering process and parameters, microstructure control) and consolidate the understanding of the properties: this includes generic and uncommon fabrication tools together with basic research, such as, irradiation damage occurrence and its consequences [4].

Besides, some materials seem interesting but challenging. Hafnium, a refractory metal, has a good absorption cross section and is widely available but its use requires significant improvement from the metallurgical point of view (choice of the appropriate grade, improvement in fabrication). Besides, borides, e.g. HfB₂, are also refractory materials and, due to their metallic feature, they exhibit a high thermal conductivity which is almost not impacted by irradiation. Nevertheless, cracking could be a limitation.

Regarding neutronic shielding, several material and design solutions are investigated in order to optimize the shielding efficiency (mainly to minimize the activation of secondary sodium) and the number of shielding rows [1]. The candidate materials remain open at the present stage of the studies. For the reflector sub-assemblies, SiC, MgO, MgAl₂O₃ or ¹¹B₄C are investigated. For the lateral neutron shielding, natural B₄C or alternative materials on a hafnium or steel base are suggested. As the materials for reflectors and shielding are defined, an R&D program will be launched to define a fabrication route and to assess their physical and mechanical properties.

3. Reference materials to reach the very high challenging burn-up of future SFR cores: the ODS steels

According to the planned production SFRs, ODS steels are the reference materials to sustain high burn up. They exhibit a high dimensional stability (limited swelling under irradiation, almost no deformation by thermal creep) which is suitable to increase the life of the claddings up to 180-200 dpa. ASTRID will enable to test the best grades of ODS alloys and to qualify them for their use in future reactors.

Since 2007, three main ODS grades have been studied:

- one martensitic grade: 9% Cr - Fe-9Cr 1WTi Y₂O₃,
- two ferritic grades: 14% and 18% Cr – Fe-14/18Cr 1WTi Y₂O₃.

Because there is no french ODS manufacturer left, CEA had to develop and perform its own fabrication to supply the alloys for the R&D studies: first, bars were made to master the metallurgical aspects, and, in a second step, tubes were manufactured, which is more complex to handle [5]. At each fabrication step (mechanical alloying, hot processing, cold processing), parameters are optimized via microstructural characterizations (grain morphology, texture, recrystallization) [6,5], and appropriate modeling [7,8].

The Fe-9Cr-1W martensitic grade is the more examined one and exhibits very satisfactory tensile properties at high temperature compared to results reported in literature. The fabrication process is robust and tolerant. Besides, it could be necessary to increase the chromium content up to 12% to enhance the corrosion resistance towards sodium and fuel and to improve the reprocessing. This means using ferritic ODS: this solution is more complicated to achieve, the fabrication of the tubes and their resulting anisotropic microstructure are not optimized yet but improvements are feasible.

At high temperature, these ODS steels basically exhibit a sudden rupture characterized by almost no tertiary creep stage and a very limited deformation. The origin of this specific feature was evaluated

by microstructural observations by SEM and by in-situ TEM examinations [9]: the intragranular plasticity is actually very restricted and the deformation occurs by intergranular mode and debonding. Currently, the creep tests reported in literature suggest the CEA grades to be among the best ones (Figure 2 [10,11]). Now, tubes with optimized microstructure are needed to assess the ferritic and martensitic ODS steels.

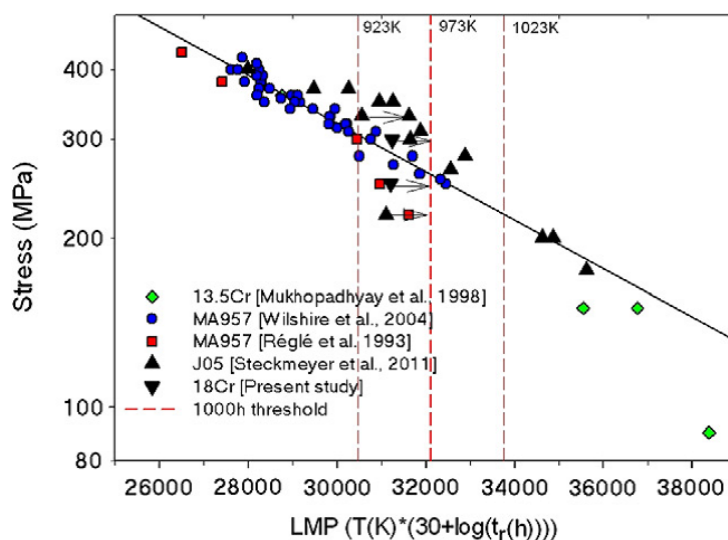


Figure 2: Creep lifetimes of CEA grades 14Cr ODS and 18Cr ODS (triangles) compared to literature data on 14Cr ODS steels.

The microstructural stability of the most recent ODS grades (oxide dispersion) has been highlighted by TEM observations of samples irradiated in Phénix as well as samples irradiated with charged particles. The French experiment TIRAMISU, launched in the Russian experimental fast reactor BOR60, will allow us to characterize up to 80 dpa the behaviour of CEA objects, especially the mechanical characteristics of 9Cr and 14Cr tubes. This will be essential to guide the choice of the reference grade, especially in terms of acceptable Cr content and corresponding hardening/embrittlement.

Finally, the welding ability of ODS is being assessed and corrosion phenomena (cladding/fuel, cladding/Na) are being investigated [12].

4. Forward-looking materials for advanced fast reactor cores

4.1. Vanadium alloys

Because of the limitation in irradiation dose for the austenitic steels (threshold dose before swelling) and the questionable fabrication behavior of high chromium ODS, the assessment of non-Fe base alloys was investigated, among them, the vanadium base alloys which exhibit a good compromise between mechanical strength up to 750°C, neutron compatibility (limited activation) and irradiation resistance (limited embrittlement above 400°C). The V-4Cr-4Ti alloy in particular has been developed with a very low swelling under irradiation and it benefits from a large feedback from fusion reactor programs. At the moderate temperature of the SFRs, meaning limited deformation by thermal creep, the thermal-mechanical evaluations made at CEA confirmed that V-4Cr-4Ti was promising as a cladding material.

The manufacturing of a V-4Cr-4Ti CEA-grade was then launched to implement an experimental program devoted to evaluate vanadium alloys (Figure 3). The resulting microstructure and mechanical properties are consistent with previous results and the chemical composition is well controlled [13]. Nevertheless, vanadium is very sensitive to impurities such as O, C, N and H, which easily diffuse in the bulk and induce embrittlement. This is an issue both for the processing at high temperature (e.g. extrusion) and for operating in Na because of the unacceptable hardening and embrittlement of V by

impurities in the coolant. This led to consideration of outer protection for the vanadium cladding: Si-based coatings proved to be efficient against corrosion by interstitial impurities [14], and using high chromium steel liner was also proposed through the fabrication of a triplex tube by co-extrusion (steel/V/steel) [15].

Then, the advantages of vanadium alloys are numerous but contamination must be avoided, which requires a significant R&D program.



Figure 3: Plates of V-4Cr-4Ti CEA grade (manufactured by GfE Metalle und Materialien GmbH, Nuremberg, Germany) after cold rolling and machining [13].

4.2. SiC/SiC composites

The SiC/SiC composites, ceramic matrix reinforced by high-strength ceramic fibers, are probably the most breakthrough materials because they are very different from metals: specific fabrication process, no conventional ductility but a damageable elastic behaviour, anisotropy, etc. The potential advantages in terms of target temperature (1000°C), chemical and dimensional stability (small deformation levels) justified the R&D led at CEA, first in the scope of GFRs and, second, in the present scope of future SFRs.

CEA has developed and patented a tubular sandwich concept (metallic liner inserted between two SiC/SiC layers) [16,17]) with proved gas tightness even when advanced cracking occurs in the composite. End-plugging of this sandwich cladding have been proposed and further enhancement of mechanical properties are achievable. The progress made in the field of architecture tailoring and infiltration mastering, led to an excellent control of the dimensions.

These first learnings are presently used to develop SiC/SiC hexagonal tubes for SFRs. Prototype versions are being fabricated and characterized in terms of mechanical and thermal properties. The transposition to relevant components is not so challenging and should be demonstrated soon. Besides, even if a good behaviour of SiC/SiC under irradiation is expected, this will be validated for relevant conditions of SFRs in the TIRAMISU experiment.

5. Conclusions and prospects

The reference materials envisaged for the core components of ASTRID benefit from the large feedback from the french sodium cooled reactors and do not exhibit any strong issue at the present time. Nevertheless, this involves launching a program devoted to answer to the specificities of this core, providing data for the design studies and giving assistance to the fabrication of components at the industrial scale.

The R&D program on ODS is led in the scope of the commercial SFR. The fabrication route of the cladding tubes must be optimized and approved and their mechanical behavior must be accurately determined together with the updated criteria for the design. ASTRID will enable testing of ODS bundles to confirm the selected grade and qualify the ODS cladding.

Finally, ASTRID should also give the opportunity to qualify new innovative materials, in particular the SiC/SiC wrapper tubes for very future SFR or SiC/SiC sandwich pins for the GFR.

ACKNOWLEDGMENTS

Authors would like to thank Pierre Gavaille, Aurore Michaux, Yann de Carlan, Laurent Chaffron and Cédric Gourdin (CEA Saclay) for their help in the writing of this paper.

REFERENCES

- [1] “Status of the ASTRID core at the end of the pre-conceptual design phase 1”. Chenaud, M.S., Devictor, N., Mignot, G., Varaine, F., Vénard, C., Martin, L., Phelip, M., Brunon, E., Lorenzo, D., Serre, F., Bertrand, F., Richard, P., Le Flem, M., Gavaille, P., Lavastre R., these proceedings.
- [2] “Recovery of materials from Phénix to support the qualification of ASTRID design options”. Munoz-Viallard, I., Augem, J.M., Phélip, M., Dalle, F., Blat-Yrieix, M., Billey, Ch., Devictor, N., Dubiez-Legoff, S., Pillon-Eymard, S., Le Flem, M., these proceedings.
- [3] “Mechanical Properties of Cladding and Wrapper Materials for the ASTRID Fast-Reactor Project”. Gavaille, P., Courcelle, A., Séran, J.L., Averty, X., Bourdilliau, B., Provitina, O., Garat, V., Verwaerde, D., these proceedings
- [4] “Neutron absorber materials in fast reactors: behavior under irradiation and perspectives”. Gosset, D., Esclaine, J.M., Michaux, A., these proceedings
- [5] “Assessment of a new fabrication route for Fe–9Cr–1W ODS cladding tubes”. Toualbi, L., Cayron, C., Olier, P., Malaplate, J., Praud, M., Mathon, M.H., Bossu, D., Rouesne, E., Montani, A., Logé, R., de Carlan, Y., *Journal of Nuclear Materials*, Volume 428, pp. 47-53. 2012
- [6] “CEA developments of new ferritic ODS alloys for nuclear applications” . de Carlan, Y., Béchade, J.L., Dubuisson, P., Seran, J.L., Billot, P. , Bougault, A., Cozzika, T., Doriot, S., Hamon, D., Henry, J., Ratti, M., Lochet, N., Nunes, D., Olier, P., Leblond, T., Mathon, M.H., *Journal of Nuclear Materials*, Volumes 386–388, pp. 430-432. 2009
- [7] “Numerical simulation of hot extrusion consolidation of PM ferritic ODS stainless steels”. Sornin, D., Couvrat, M., *Proceedings of the World PM2010 Conference– EPMA*, Florence, 10th - 14th October. 2010.
- [8] “A simple approach for the modeling of an ODS steel mechanical behavior in pilgering conditions”. Vanegas-Márquez, E., Mocellin, K., Toualbi, L., de Carlan, Y., Logé, R.E., *Journal of Nuclear Materials*, Volume 420, pp. 479-490. 2012
- [9] “Study of the deformation mechanisms in a Fe–14% Cr ODS alloy”. Praud, M., Momprou, F., Malaplate, J., Caillard, D., Garnier, J., Steckmeyer, A., Fournier, B., *Journal of Nuclear Materials*, Volume 428, pp. 90-97. 2012
- [10] “Mechanical behaviour of ferritic ODS steels – Temperature dependancy and anisotropy”. Fournier, B., Steckmeyer, A., Rouffié, A.L., Malaplate, J., Garnier, J., Ratti, M., Wident,

P. Gavoille et al.

P., Ziolk, L., Tournié, I., Rabeau, V., Gentzbittel, J.M., Kruml, T., Kubena, I., Journal of Nuclear Materials, Volume 430, pp. 142-149. 2012

- [11] “Tensile properties and deformation mechanisms of a 14Cr ODS ferritic steel”. Steckmeyer, A., Praud, M., Fournier, B., Malaplate, J., Garnier, J., Béchade, J.L., Tournié, I., Tancray, A., Bougault, A., Bonnaille, P., Journal of Nuclear Materials, Volume 405, pp. 95-100. 2012
- [12] “Corrosion by slightly oxidizing and carburizing liquid sodium at 550°C of materials for sodium fast reactors”. Courouau, J.L., Lorentz, V., Tabarant, M., Bosonnet, S., Balbaud, F., these proceedings
- [13] “French investigation of a new V-4Cr-4Ti grade: CEA-J57 - Fabrication and Microstructure”. Duquesnes, V., Guilbert, T., Le Flem, M., Journal of Nuclear Materials, Volume 426, pp. 96-101. 2012
- [14] “Multi-layered silicides coating for vanadium alloys for generation IV reactors”. Mathieu, S., Chaia, N., Le Flem, M., Vilasi, M., Surface and Coatings Technology, Volume 206, pp. 4594-4600. 2012
- [15] “Development of vanadium fuel cladding for Sodium Fast Reactors”. Le Flem, M., Gentzbittel, J.M., Wident, P., Rouillard, F., Guéneau, C., Sornin, D., these proceedings
- [16] “Overview of CEA's R&D on GFR fuel element design: from challenges to solutions”, Zabiégo, M., Sauder, C., David, P., Guéneau, C., Briottet, L., Ingremeau, J.J., Ravenet, A., Lorrette, C., Chaffron, L., Guédeney, P., Le Flem, M., Séran, J.L., these proceedings
- [17] “SiC/SiC composite materials for fast reactor applications”., Chaffron, L., Sauder, C., Lorrette, C., Michaux, A., Gélébart, L., Coupé, A., Séran, J.L., Le Flem, M., these proceedings

Neutron absorber materials in fast reactors: behavior under irradiation and perspectives

D. Gosset^{a†}, J.M. Esclaine^b, A. Michaux^c

^aDEN-DMN-SRMA-LA2M, CEA, Saclay (France)

^bDEN-DEC-SESC-LLCC, CEA Cadarache (France)

^cDEN-DMN-SEMI-LPCMI, CEA-Saclay (France)

Abstract. Neutron absorbers are one of the key components in a reactor core. Different components are then designed able to face normal and incidental conditions. In nearly all past, present and project fast neutron reactors, those systems use boron carbide as neutron absorber material. This material has been chosen for a good neutron absorption cross section, refractivity and easy absorption efficiency tuning, but its brittle properties lead to quick fragmentation due to helium retention and high thermal stresses, leading to a reduced lifetime. In this paper, we first describe the behavior of boron carbide under irradiation and present some recent results regarding its thermal conductivity and microstructural evolution and recovery. We then propose some perspectives aimed at developing new materials able to get over those limitations and a program to analyze irradiated materials in order to improve the behavior laws of the material.

1. Introduction

Delivering a sustainable energy taking into account the climate modification hazards needs to consider every possible production source. In that frame, nuclear energy is to play an important role. The known uranium resource, if used in the present or the planned generation-III nuclear plants, cannot reach the potential demand. As a consequence, new concepts are required. The Generation IV International Forum aims at developing such innovative systems [1]. Among them, France is currently developing the fast neutron reactor, sodium cooled ASTRID (Advanced Sodium Technological Reactor for Industrial Demonstration) project. This reactor is planned to reach the highest safety standards. In particular, special cares are taken regarding the out-of-core neutron protection and the control systems.

In nearly all past, present and planned fast neutron reactors, neutron absorption in the control systems is obtained with a single material, namely boron carbide. As a result, the main features of the behavior of boron carbide under neutron irradiation have been for long identified [2,3,4]. This has led to significant improvement of the materials and the regulation systems. However, some limitations still remain leading to actual lifetime much shorter than estimated from the only efficiency parameter [5,6]. In this paper, we first remind the structure and behavior of boron carbide under neutron irradiation. We then present some recent results regarding first the evolution of microstructural properties of boron carbide under neutron irradiation then the development of improved materials. As a conclusion, a possible PIE program is presented aiming at the elaboration of an improved data base for the ASTRID project.

[†] corresponding author: dominique.gosset@cea.fr

2. Neutron irradiation of boron carbide

Boron carbide is a refractory, brittle, hard, low density material [7]. For nuclear applications such as neutron absorber elements, it is most often used as high density cylindrical pellets obtained by hot-pressing small grain-size powders. Natural boron contains 2 isotopes, ^{10}B and ^{11}B , with 19.8 at.% ^{10}B . ^{10}B has a high neutron absorption cross section on the whole neutron energy range with no resonance (this leading to easy efficiency calculations: Figure 1). The ^{10}B content can easily be tuned in a wide range, from less than 0.5 ^{10}B at.% (this making B_4C one of the best neutron moderator) to more than 95 ^{10}B at. % (for highly efficient neutron absorbers). Boron carbide is a semi-conductor, with a low thermal conductivity (around 30 W/m.K at room temperature) with a $1/T$ variation at high temperature. Boron carbide exists over a wide composition range, from circa 9 at.% C to 20 at.%. The formula of the carbon-rich limit of the phase is then usually considered as B_4C . In the monophasic domain, most of properties present an extremum at the composition 13.3 at.% C, i.e. B_{13}C_2 . The crystal structure is build with nearly regular icosahedra connected first, by their polar atoms, this defining a rhombohedral cell, similar to the β -boron structure, second, by the equatorial atoms via a central motif, with highly covalent bondings this conferring its mechanical properties. Modifications of the composition of these elements, icosahedron and central motif, allow describing the whole composition range [8]. At the carbon-rich limit, most of studies lead to a B_{11}C formula for the icosahedra and CBC for the central motif, here a linear chain, then a B_4C composition. Some authors [9] consider a possible CBC and CBB mixed-composition for the central chain, leading to a $\text{B}_{4,3}\text{C}$ carbon-rich formula. The boron-rich compositions are obtained first by substituting boron to carbon in the icosahedra, leading to the $\text{B}_{11}\text{C-CBC}$, i.e. B_{13}C_2 composition, which corresponds to some extrema properties, then modifications of the composition of the central motif (carbon depletion, boron substitution,... with still some uncertainties), up to a composition close to B_{10}C .

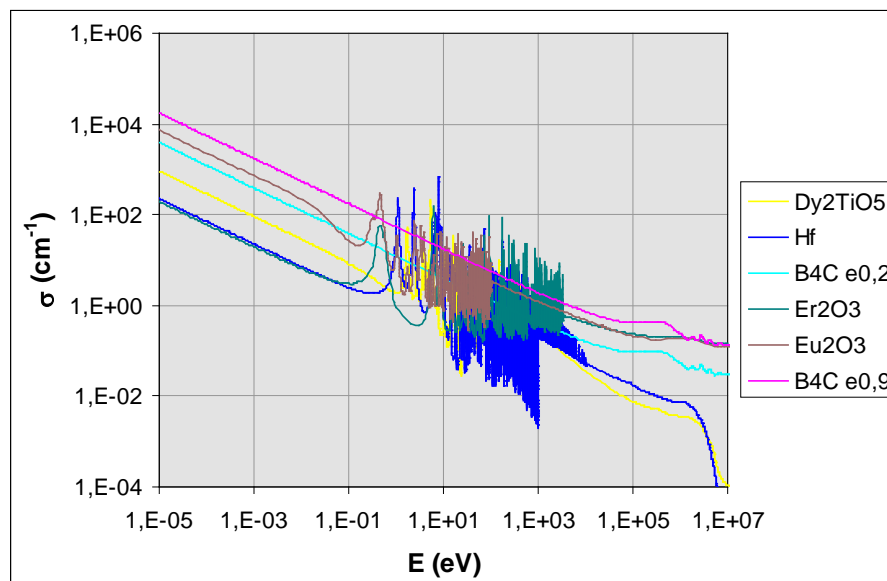
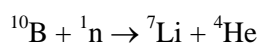


Figure 1. neutron absorption cross section of some usual materials, from [6]. Boron carbide B_4C is reported for two ^{10}B enrichment, e0.2 for natural (19.8 at.%), e0.9 for 90 at.%.

Neutron irradiation has huge effects on boron carbide. The neutron absorption reaction is:



releasing a high energy, around 2.6 MeV per fission, the actual value depending on Li activation and neutron energy.

As mentioned above, the thermal conductivity of boron carbide is low. Moreover, it strongly degrades under neutron irradiation (Figure 2, from measurements performed on B_4C pellets irradiated in the Phenix French reactor). Boron carbide is most often used as high relative density cylindrical pellets piled in metallic claddings. In sodium-cooled reactors, porous plugs allow sodium to flow into the gap

between the pellets and the cladding. The high energy release of the absorption reaction then leads to intense radial thermal gradients, comparable to the fuel ones, i.e. up to 500 °C/cm. The resulting thermal stresses exceed the material yield, leading to radial breaking of the pellets at the very beginning of their life.

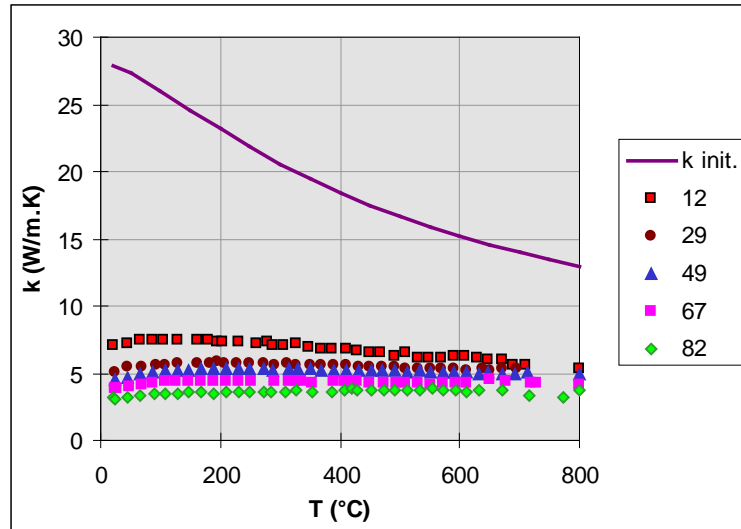


Figure 2 . Thermal conductivity of boron carbide irradiated in Phenix reactor, as a function of ^{10}B burnup (in $10^{20}/\text{cm}^3$; with $10^{20}/\text{cm}^3 \sim 0.1\%$ total boron). $k_{\text{init.}}$: thermal conductivity of non-irradiated B_4C .

On the other hand, most of produced helium is trapped in the material. Helium partially segregates at the grain boundaries as bubbles, lowering the grain boundaries strength. Most of helium remains in the grains. In the temperature range in fast neutron reactors, i.e. around 500-1200°C, helium is trapped in penny-shaped bubbles under very high pressure [10,4]. The bubbles are all parallel to the equatorial planes of the icosahedra. This leads to a very anisotropic swelling, mainly perpendicular to the bubbles plane then along the main diagonal of the rhombohedra. This results in high shear stresses between adjacent grains of different orientations. The conjunction of those two effects, grain boundary damage and anisotropic swelling, results in grain boundary embrittlement then intergranular cracking and increased helium release at burnups around $2 \cdot 10^{21}/\text{cm}^3$ [4]. At higher burnups, around $5 \cdot 10^{21}/\text{cm}^3$, intragranular bubbles connect, leading to intragranular cracking and subsequent increased helium release.

High thermal conductivity decrease then arises, which results from the dense intergranular cracking network, the helium bubbles dynamics but also from the damages induced by atomic displacements, inducing a change of the conduction mechanisms, from a $1/T$ phonon mode to a disordered mode, nearly constant thermal conductivity over a large temperature range (Figure 2). Each of these terms will depend on the irradiations conditions which in turn induce quite different temperature levels and thermal gradients. Those three components can be evidenced when performing annealing of an irradiated materials then thermal conductivity together with structural analyses [11, 12, 13]. From analyses we recently performed on B_4C samples irradiated in Phenix French reactor, different stages appear that could tentatively be attributed to different mechanisms, defects annealing and fission products (He, Li) migration, bubbles mobility and relaxation, brittle to ductile transition (Figure 3). Although lithium is known to diffuse at low temperature [14], no clear role such as segregation at grain boundaries or lithiated compounds or defects aggregates formation has been evidenced.

Last but not least, it is worth noting that most of available post-irradiation analyses have been performed on materials irradiated as neutron absorber elements in reactors, this preventing any accurate estimation of the actual temperature of the material. As a result, most of published results are temperature independent, although most of involved mechanisms are fundamentally temperature dependant.

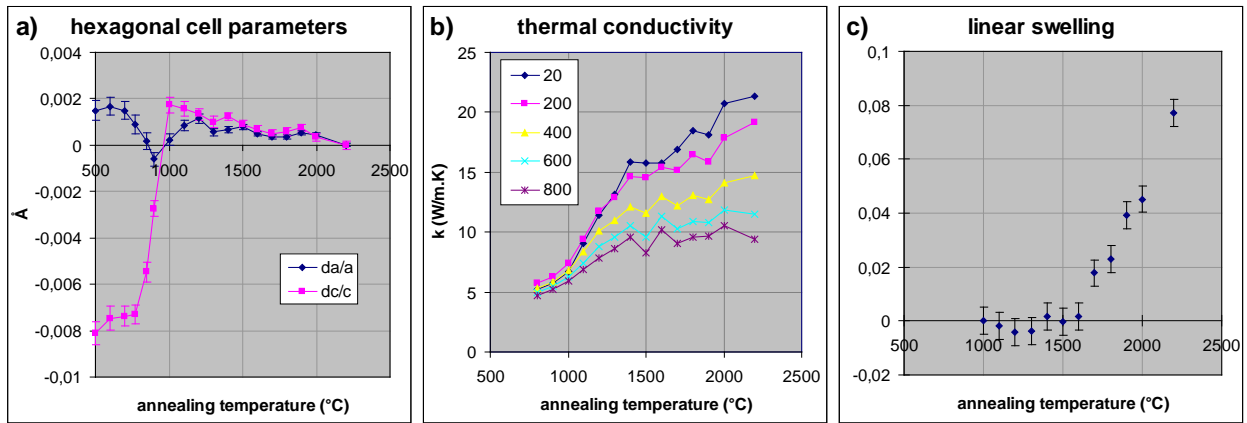


Figure 3. Evolution of some properties of a B₄C sample (density 95 %, ¹⁰B enrichment 48%) irradiated in Phenix reactor (burnup $2.5 \cdot 10^{21}$ ¹⁰B/cm³, irradiation temperature ~600°C, 70 efpd duration) during post-irradiation isochronal annealings.

a: relative change of the a and c parameters of the unit cell (hexagonal representation) as obtained from X-ray diffraction analysis, showing drastic modification around 800°C (lithium desorption, defects annealing).

b: thermal conductivity at different temperatures (reported in the block), showing the conduction mechanism change, from disordered (k vs. T nearly constant) to the 1/T classical mode.

c: swelling of the analyzed sample, evidencing the brittle-ductile transition around 1500°C then helium bubbles relaxation.

Regarding the behavior of the absorber element, the conjunction of pellets cracking and B₄C swelling leads to an accelerated filling of the absorber-cladding gap and to high mechanical stresses on the cladding (Figure 4). A second effect leads to a drastic limitation of the lifetime of the absorber elements. As mentioned above, sodium is allowed to flow inside the cladding, in order to allow helium release and cooling of the absorber. But this also leads to an efficient carbon transfer from boron-depleted (due to boron burning) boron carbide to the cladding, resulting in carburization then embrittlement of the metal. As a result, the lifetime of the absorber elements is much shorter than expected from the only neutron absorption efficiency.

3. Improving the absorber elements

Different routes have then been developed in order to overcome those limitations.

First, the initial absorber pin design has been deeply improved [15]. The material specifications have been refined: impurities, grain size distribution, density, this leading to optimized thermo-mechanical properties. On the other hand, the design of the absorber element has been drastically modified. The B₄C pellet diameter has been reduced, in order to lower the temperature gradients. Lower ¹⁰B-enriched material is used at the bottom of the absorber pins, leading to locally reduce the heat power. Most importantly, a metallic shroud has been introduced between the absorber and the cladding, aiming first at supporting the B₄C fragments then protecting the sodium-filled gap and second at limiting the cladding carburization. This has led to substantial improvement of the potential lifetime of the absorber elements (Figure 4).

Further improvements of the absorber elements performance require substantial material evolution. Different routes have been considered to overcome the main drawbacks of boron carbide. First, the thermo-mechanical and chemical properties could be highly improved with materials such as hafnium diboride: this material is highly refractory, do not contain carbon and is a metal-like thermal conductor, this conferring high thermal conductivity. Moreover, hafnium has a good neutron absorption cross-section (Figure 1) and neutron radiation damage in HfB₂ is metal-like (dislocation loops) and quasi-isotropic [16]. Second, we have shown extensive cracking can be controlled in cer-cer or cer-met composites [17], in that case a mechanical integrity of the absorber pellets can be preserved (Figure 5).

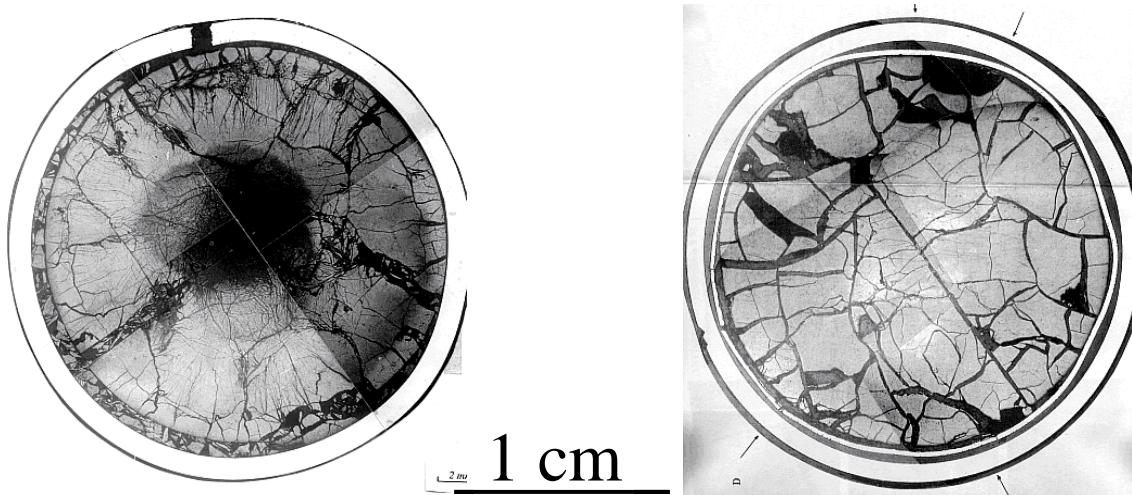


Figure 4: influence of the shroud on the absorber-cladding mechanical interaction (Phenix experimental pins), from [5]. Left: 140 efpd, $1.4 \cdot 10^{22} \text{ }^{10}\text{B}/\text{cm}^3$, $270 \text{ W}/\text{cm}^3$, showing gap filling with B_4C fragments and subsequent clad failure and extensive core damage (the hole at the center of the pellet results from post-irradiation machining). Right: 657 efpd, $2.5 \cdot 10^{22} \text{ }^{10}\text{B}/\text{cm}^3$, $180 \text{ W}/\text{cm}^3$ showing shroud cracking but remaining gap.

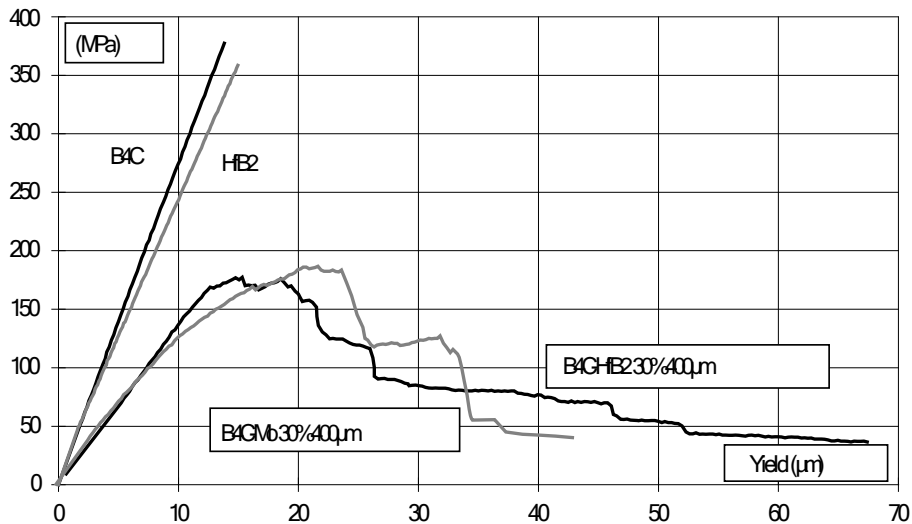


Figure 5. Yield strength of advanced absorber materials at room temperature, obtained with biaxial bending, as compared to B_4C boron carbide [17, 18]. HfB₂: pure hafnium diboride; B₄C-Mo, B₄C-HfB₂: heterogeneous boron carbide – molybdenum ceramic-metal and boron carbide – hafnium diboride ceramic-ceramic composites.

4. Conclusion

In nearly all past, present and planned fast neutron reactors, boron carbide has been used and considered as the only neutron absorber material. Its behavior under irradiation is well known, showing high efficiency but important issues resulting from low thermo-mechanical properties and the formation of high quantities of helium. Different directions have been explored to overcome those limitations, design modifications and material improvements. However, much has still to be made, in particular regarding the formulation of behavior laws to be used for the design of a future reactor. The major issue is that the actual irradiation temperature of the material is generally not known.

An ambitious program has then to be launched, including post-examination in hot-cells of absorber elements irradiated in the French Phenix reactor, fundamental studies of boron carbide aiming at obtaining accurate description of its behavior and the development of improved materials and components. In that frame, the ASTRID project constitutes an exciting challenge.

5. References

-
- [1] P. Yvon, F. Carré, Structural materials challenges for advanced reactor systems, *J. Nucl. Mat.* **385** (2009) 217–222
 - [2] C.W. Tucker, Jr and P. Senio, X-ray Scattering, by Neutron-Irradiated Single Crystals of Boron Carbide. I, *Acta Cryst.* (1955). **8**, 371
 - [3] R. G. Gray and L. R. Lynam, Irradiation behavior of bulb B₄C and SiC burnable poison plates, WAPD-261 (1963)
 - [4] G.W. Hollenberg and W.V. Cummings, Effect of Fast Neutron Irradiation on the Structure of Boron Carbide, *J. Am. Cer. Soc.* **60-11-12** (1977) 520-525
 - [5] D. Gosset, Absorber materials, in Dan Gabriel Cacuci (ed.), *Handbook of Nuclear Engineering*, **21.5.3**, Springer (2010)
 - [6] D. Gosset, M. Colin, Matériaux absorbants neutroniques pour le pilotage des réacteurs, *Techniques de l'Ingénieur*, B3720 (2006)
 - [7] F. Thévenot, Boron Carbide, a Comprehensive Review, *J Eur. Cer. Soc.* **6** (1990) 205-225
 - [8] V. Domnich, S. Reynaud, R.A. Haber, M. Chhowalla, Boron Carbide: Structure, Properties, and Stability under Stress, *J. Am. Cer. Soc.*, **94-11** 3605–3628 (2011)
 - [9] H. Werheit and U. Kuhlmann, Is the established structure of β -rhombohedral boron correct? Comparative study of IR-active phonons with B₆O, B_{4.3}C and β -rhombohedral boron, *J. Phys.: Condens. Matter* **24** (2012) 305401
 - [10] Zuppiroli, D. Lesueur, Modelling the swelling and microcracking of boron carbide under neutron irradiation, *Phil. Mag.*, **60-5**, 539 (1989)
 - [11] D. Gosset, D. Simeone, D. Quirion, Damage in boron carbide by neutron irradiation : X-ray diffraction estimation; RX 99 Colloque Rayons X et Matière No3, Strasbourg , France (07/12/1999), *J. Phys. IV* (2000), **10-10**, Pr10.55-10.63
 - [12] Y. Morohashi et al., Neutron Irradiation Effect on Isotopically Tailored ¹¹B₄C, *J. Nucl. Sci. Tech. Jpn*, **45-9**, 867–872 (2008)
 - [13] V. P. Tarasikov, Electron microscopy investigation of boron carbide irradiated in fast reactor, *Atomic Energy*, **106-3**, 220 (2009)
 - [14] X. Deschanel, D. Simeone, J.P. Bonal, Determination of the lithium diffusion coefficient in irradiated boron carbide pellets, *J. Nucl. Mat.* **265** (1999) 321-324
 - [15] B. Kryger, D. Gosset, J.M. Esclaine, Irradiation performance of the Superphenix-type absorber element, Technical Committee Meeting, Obninsk, 3-7 July 1995, IAEA-TECDOC-884 (1995)
 - [16] P. Cheminant-Coatanlem, L. Boulanger, X. Deschanel, A. Thorel, Microstructure and nanohardness of hafnium diboride after ion irradiations, *J. Nucl. Mat.*, **256** (1998) 180-188
 - [17] G.M. Decroix, D. Gosset, B. Kryger, Neutron absorber material and method of manufacture, US patent 5590393 (1996)
 - [18] G.M. Decroix, B. Provot, D. Gosset, X. Deschanel, Y. Frasin, CEA internal reports

Results and Prospects of Development of Works on Structural Core Materials for Russian Fast Reactors

A.A. Nikitina[†], V.S. Ageev, M.V. Leontyeva-Smirnova, N.M. Mitrofanova,

A.V. Tselishchev

Open Joint Stock Company

“A.A. Bochvar All-Russia Research Institute of Inorganic Materials” (VNIINM),
Moscow, Russian Federation

Abstract. The strategy of development of atomic energy in Russia in the first half of XXI century contemplates construction and putting in operation of fast reactors of new generation with different types of coolant: sodium (BN-800, BN-1200, MBIR), lead (BREST-OD-300) and lead-bismuth eutectic (SVBR-100).

For assurance of the working capacity of reactors that are under construction and achievement of economically reasonable burn-up of nuclear fuel the structural core materials with necessary level of radiation resistance, heat resistance, corrosion resistance to products of fuel fission, corrosion resistance in coolant and in water must be developed and justified.

For sodium cooled reactors the key challenge is creation of radiation resistant and heat resistant cladding materials, which must ensure the achievement of damage doses at least 140 dpa.

The solution of this problem is provided by phased use as cladding materials of austenitic steels ChS68 and EK164 (maximum damage doses ~ 92 and ~110-115 dpa, respectively), precipitation-hardening heat resistant ferritic-martensitic steels EK181 and ChS139 (maximum damage dose ~140 dpa) and oxide dispersion strengthened (ODS) steels (maximum damage dose more than 140 dpa).

For development of core materials for reactors with lead and lead-bismuth eutectic coolants the most serious challenge is corrosion resistance of materials in coolant. Therefore at present time a very wide range of works on study of corrosion resistance of candidate materials is carrying out. As the basic material for the cladding tubes is considered a ferritic-martensitic steel EP823 with high silicon content.

In this report the main results of works on justification of the working capacity of materials of different classes in respect to use it in cores of operating and prospective fast reactors with different types of coolant and prospects of further development of works are presented.

Introduction

The strategy of development of atomic energy in Russia in the first half of XXI century contemplates construction and putting in operation of fast reactors of new generation with different types of coolant: sodium (BN-800, BN-1200, MBIR), lead (BREST-OD-300) and lead-bismuth eutectic (SVBR-100).

For assurance of the working capacity of reactors that are under construction and achievement of economically reasonable burn-up of nuclear fuel the structural core materials

[†] Present address: Open Joint Stock Company

“A.A. Bochvar All-Russia Research Institute of Inorganic Materials” (VNIINM)
Moscow, Russia Federation nikitina@bochvar.ru, nikitina-2a@yandex.ru

with necessary level of radiation resistance, heat resistance, corrosion resistance to products of fuel fission, corrosion resistance in coolant and in water of cooling pond must be developed and justified.

In this report the main results of works on justification of the working capacity of materials of different classes in respect to use it in cores of operating and prospective fast reactors with different types of coolant and prospects of further development of works are presented.

1. Structural core materials of fast reactors with sodium coolant

At present time, in accordance with requirements of the chief designer of fast reactors, as prospective cladding materials for phased increase of the fuel burn-up are considered steels of austenitic (ChS68 and EK164), ferritic-martensitic (EK181 and ChS139) classes and steels, produced by the method of powder metallurgy (ODS steels).

1.1 Austenitic steels ChS68 and EK164 for cladding

In 1987 it was decided to use austenitic steel ChS68 as standard cladding material and to use ferritic-martensitic steel EP450 as standard material for wrapper tubes of reactor BN-600 [1].

The chemical compositions of these steels are shown in Table 1.

Steels that were designed reliably ensured the failure-free operation of BN-600 reactor at the burn-up of 11,2 % h.a. and the damage dose of 82 dpa. The same materials are accepted for cladding and wrapper tubes of reactor BN-800.

Table 1. Chemical compositions of steels ChS68 and EP450

Material	Content of elements, wt. %										
	C	Si	Mn	Cr	Ni	Mo	Nb	Ti	V	B	P
ChS68	0,05-0,08	0,3-0,6	1,3-2,0	15,5-17,0	14,0-15,5	1,9-2,5	–	0,2-0,5	0,1-0,3	0,002-0,005	≤ 0,015
EP450	0,10-0,15	≤ 0,5	≤ 1,0	11,0-13,5	0,05-0,30	1,5-2,0	0,15-0,40	–	0,1-0,3	0,005-0,015	≤ 0,025

Analysis of the profilometry data of cladding tubes from steel ChS68 on different stages of development of this material showed that all data split into two arrays (Figure 1). Array 1 was received on experimental fuel assemblies. Array 2 was received on standard fuel assemblies and shows significantly higher rate of swelling [2].

During the whole period of production of cladding tubes from steel ChS68 three manufacturing plants were changed. Equipment for rolling and heat treatment, as well as schemes of production of tubes on manufacturing plants are different.

To improve the quality of tubes from steel ChS68 it was decided:

- to optimize the chemical composition of steel ChS68;
- to use operation of diffusion annealing on tube;
- to increase the temperature of intermediate austenization annealing with use of the forced heating installation;
- to use the scheme of short mandrel drawing for creation of the final cold-worked condition.

The main requirement for fuel pin claddings on the stage of out-of-pile investigations is assurance of high long-term strength and ductility. For comparative tests on heat resistance were used specimens of cladding tubes from steel ChS68 with different technological variants of production.

Curves of long-term strength of tubes from steel ChS68 are shown in Figure 2 [2]. As it can be seen from the data, the maximal long-term strength at 700 °C is observed for tubes that were produced with use of diffusion annealing (DA), optimized regimes of austenization annealing and short mandrel drawing.

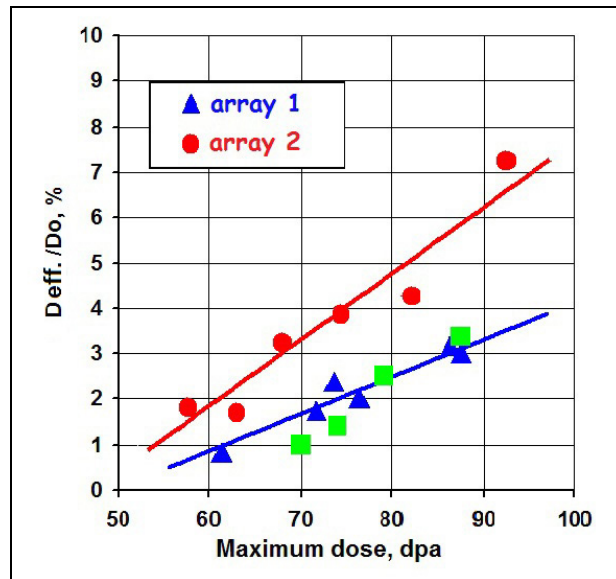


FIG 1. Form change of the fuel pin claddings from steel ChS68 as a function of the damage dose

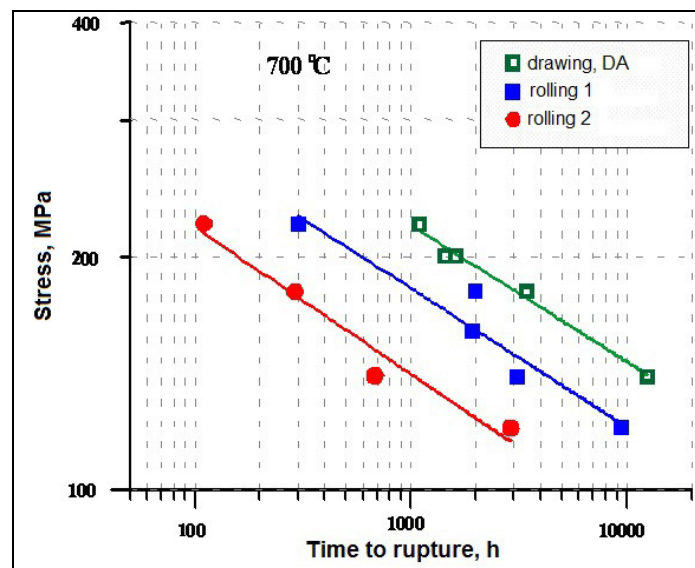


FIG. 2 Long-term strength at uniaxial tension of tubes $\varnothing 6,9 \times 0,4$ mm from steel ChS68

It was necessary to confirm experimentally the efficiency of the proposed methods of optimization of structure of cladding tubes from steel ChS68 after irradiation of reference and standard fuel assemblies. The results of post-irradiation investigations showed that cladding tubes from steel ChS68 manufactured by advanced technology have an average 1,5 times smaller form change than cladding tubes that were supplied earlier. At a dose of 87 dpa average $\Delta D / D$ is $3,3 \pm 0,4\%$. A characteristic feature of fuel pin claddings from steel ChS68

manufactured by advanced technology is a relatively small spread of swelling at high damage dose (Figure 3).

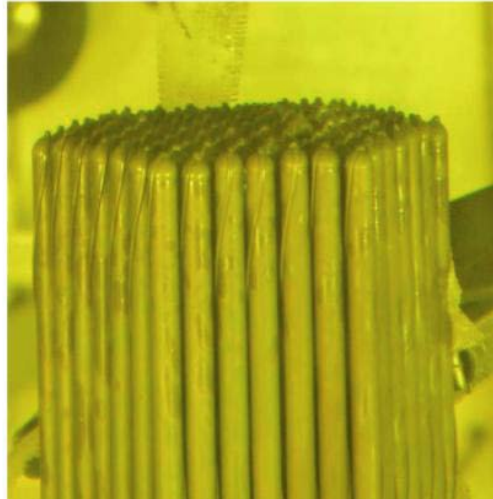


FIG 3. External view of the end of a bundle of fuel rods of a reference fuel assembly with claddings from steel ChS68, irradiated up to 83 dpa

Investigations of strength and plastic properties of the specimens of the reference fuel assembly irradiated up to damage dose 83 dpa showed that material retains deformation ability and relatively high strength characteristics.

Calculated estimations of stress-strain state of the fuel pin claddings from steel ChS68 of the reference fuel assemblies allow to make a forecast that the fuel rod serviceability will be ensured up to the dose of ~ 92 dpa.

For achievement of the damage doses not less than 110 dpa steel EK164 was designed. This steel possesses increased structural-phase stability and stability under irradiation, that is important for phased increase of fuel burn-up up to ~ 15% h.a. in BN reactors.

Steel EK164 has higher nickel concentration than its precursors and complex alloying by titanium, niobium, vanadium, boron, phosphorus and cerium (Table 2).

Table 2. Chemical composition of steel EK164

Content of elements, wt. %											
C	Si	Mn	Cr	Ni	Mo	Nb	Ti	V	B	P	Ce
0.05-0.09	0.3-0.6	1.5-2.0	15.0-16.5	18.0-19.5	2.0-2.5	0.1-0.4	0.25-0.45	0.15	0.001-0.005	0.010-0.025	0.15

For the purpose of experimental justification of the workability of steel EK164 eight experimental fuel assemblies with claddings from steel EK164 were manufactured and irradiated in reactor BN-600.

- five fuel assemblies – up to damage dose 74-84 dpa and maximum fuel burn-up 9,1-10,7 % h.a.;
- three fuel assemblies – on increased parameters, up to damage dose 85-96 dpa and maximum fuel burn-up 13,2 % h.a.

The results of investigations after irradiation have shown that swelling of steels EK164 and ChS68 after irradiation in one experimental fuel assembly by the damage dose 77 dpa was (3,9±0,6) % and (7,2±0,6) %, respectively. The creep deformation does not exceed 0,3%, value of residual ductility after irradiation, determined on ring and tube specimens of steel EK164, is larger than on specimens of steel ChS68.

For the purpose of further reduce of swelling of steel EK164, the works over improvement of metallurgical and tube production technologies were carried out. The results

of post-irradiation investigations of fuel pin claddings from a fuel assembly that was irradiated up to 84 dpa have shown that improvement in technology leads to further reduce of swelling of steel EK164. At comparable damage doses ~ 84 dpa swelling of cladding tubes from steel EK164, manufactured by advanced technology, is about 3 times less than swelling of cladding tubes from steel ChS68 of a similar technological performance.

With increasing of damage dose up to 96 dpa swelling of cladding tubes from steel EK164 was $(5,8 \pm 1,7) \%$.

The works over improvement of functional properties of steel EK164 for reaching the damage doses not less than 110 dpa are going on.

1.2 Ferritic-martensitic steels EK181 and ChS139

As a cladding material that provides workability of a fuel rod up to damage doses ~140 dpa are considered heat-resistant precipitation-hardening 12%Cr steels EK181 and ChS139 [3, 4].

These steels differ from steel EP450 (table 1), first of all, by additional alloying by carbon, tungsten and some reduction in chromium content (Table 3). Such alloying, coupled with certain heat treatment, provides the formation of structure that is characterized by high stability of nanosized carbide phases (Figure 4 [5]), resistance to recrystallization processes and improves characteristics of high-temperature strength in comparison with steel EP450 (Figure 5).

Table 3. Chemical composition of steels EK181 and ChS139

Steel	Content of elements, wt. %														
	C	Si	Mn	Cr	Ni	Mo	Nb	Ti	W	V	B	Ta	Ce	N	Zr
EK181	0,10-0,21	0,1-0,8	0,5-2,0	10,0-13,5	<0,1	<0,1	<0,01	0,03-0,3	0,8-2,5	0,05-0,4	0,001-0,008	0,05-0,2	0,001-0,10	0,02-0,15	0,05-0,2
ChS139	0,19-0,25	0,1-1,0	0,5-0,8	10,0-12,5	0,5-0,8	0,4-1,1	Nb + Ta = 0,2-0,4	0,03-0,3	0,5-2,0	0,2-0,4	0,002-0,006	Nb + Ta = 0,2-0,4	0,001-0,10	0,02-0,15	0,05-0,2

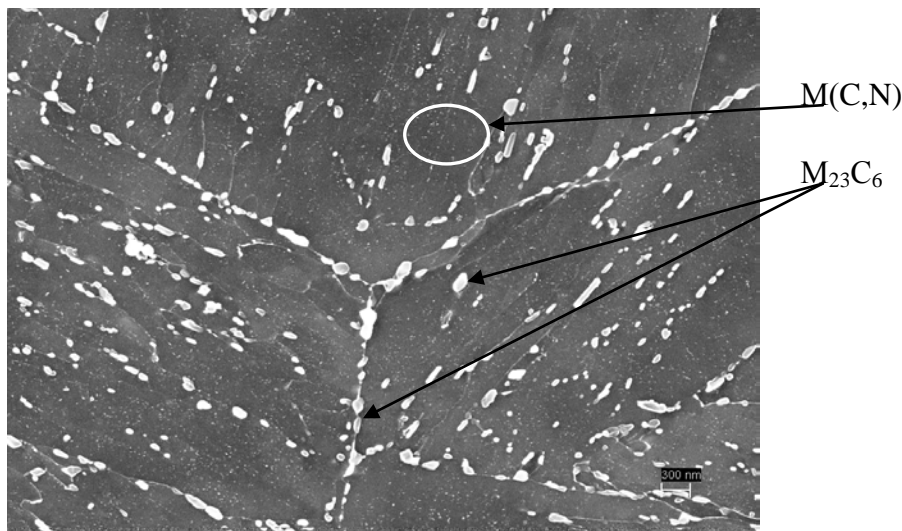


FIG 4. Carbide phases in structure of steel EK181 after quenching and tempering

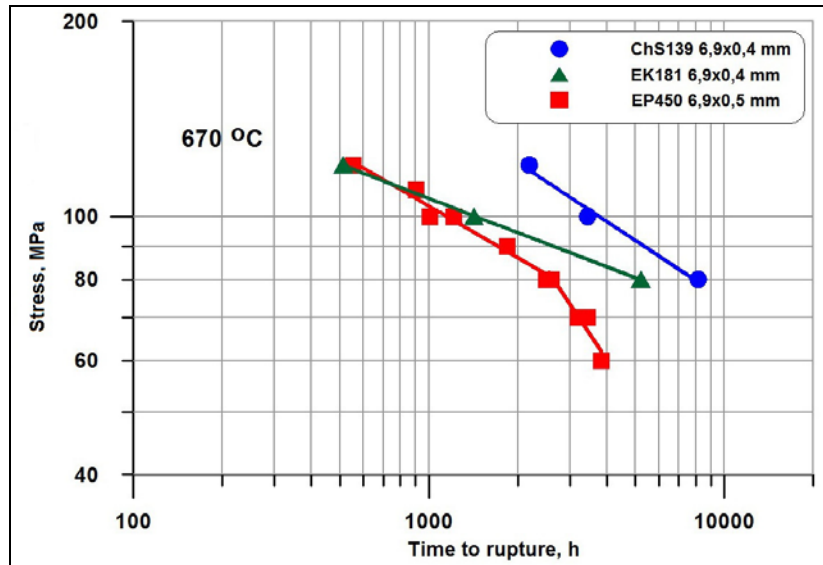


FIG 5. Long-term strength at uniaxial tension at temperature 670 °C of cladding tubes from steels EP450, EK181, ChS139

The results of investigations of initial properties of heat-resistant steels EK181 and ChS139 show prospects of its application as cladding material for BN reactors.

Pilot batches of cladding tubes Ø6,9×0,4 mm and Ø9,3×0,6 mm from steels EK181 and ChS139 were produced.

For the purpose of forming the optimal structural-phase state in cladding tubes, at present time the improvement of technological processes of production of cladding tubes from steels EK181 and ChS139 is ongoing. In particular, in tube production the new methods of heat treatment are being tested and the regimes of the heat treatment are being optimized.

Processes of the argon-arc welding and heat treatment after welding of joints of cladding tubes and plugs from steels EK181 and ChS139 were tested. Received results show acceptable quality of welded joints in technological cycle of fuel rods production.

In 2012 the first stage of irradiation of material test assemblies with specimens from steels EK181 and ChS139 up to 80 dpa was finished.

Investigations of irradiated up to 80 dpa specimens are planned in 2013-2014.

Irradiation of material test assemblies up to damage dose 134 dpa is ongoing.

1.3 Oxide dispersion strengthened (ODS) steels

For achievement of damage dose more than 140 dpa in JSC VNIIMN ODS ferritic-martensitic steels are developing. Necessary improvement of creep and long-term strength characteristics is achieved by dispersion strengthening of matrix steels by nanoparticles of yttrium and titanium oxides.

For producing ODS steels the following technological process is used [6-8]:

- producing of the matrix steel powder with spherical or whisker shape of particles by the centrifugal atomization of melt from revolving crucible in inert gas atmosphere;
- mechanical alloying of received powder by blending nanoparticles (20-80 nm) of Y₂O₃ in vibration high-energy mill;
- filling of steel cans by the produced powder blend, decontamination and sealing of cans;

- hot extrusion at 1150 °C of cans with powder blend in hot-extruded bar with drawing no more than 10–12 and subsequent mechanical treatment.

For manufacturing of ODS steels the different matrix steels are used. The wide range of research on the R&D of ODS steel based on the ferritic–martensitic steel EP450 with the addition of nano-scale oxide particles has been carried out. At present time, steel EP450 (Table 1) is a leading material used for wrapper tubes of reactors BN-600 and BOR-60.

The experimental batches of cladding tubes Ø 6,9×0,4 mm from steel EP450 ODS were produced.

Steel EP450 ODS shows considerable superiority in creep and long-term strength characteristics in comparison with matrix steel EP450 [6-8].

Figure 6 shows the microstructure of a cladding tube from steel EP450 ODS, and Table 4 - data of thermal creep of tube specimens from steels EP450 and EP450 ODS [8].

The technology of sealing of cladding tubes from steel EP450 ODS by pressurized resistance welding was worked out [8].

At present time investigations of influence of long-term thermal aging at different temperatures on structure and mechanical properties of ODS steels are being carried out. Besides, the first positive results regarding corrosion resistance of ODS steels in coolants (Na, Pb) and in products of fuel fission were received.

Investigations of radiation resistance of ODS steels are planned (irradiation of specimens from ODS steels in material test assemblies in reactor BN-600).

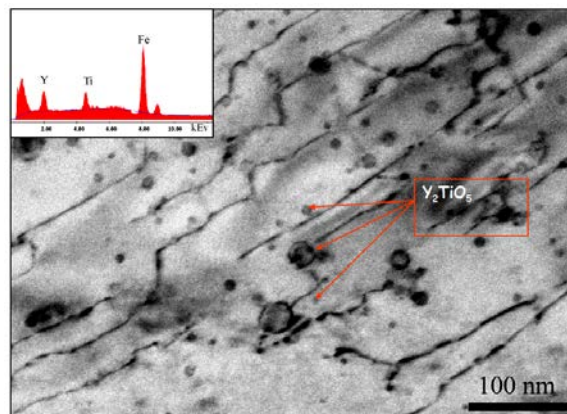


FIG 6. Microstructure of a cladding tube from steel EP450 ODS

Table 4. Data of thermal creep of tube specimens from steels EP450 and EP450 ODS

Material	Test temperature, °C	Stress, MPa	Time to rupture, hours	Creep rate, %/h	Comment
EP450	700	120	23	$8 \cdot 10^{-2}$	$\delta=2,83 \%$
EP450 ODS	650	140	9086	$3,23 \cdot 10^{-5}$	$\delta=7,92 \%$
	700	120	1080	$2,20 \cdot 10^{-4}$	$\delta=7,08 \%$

2. Structural core materials of fast reactors with lead and lead-bismuth eutectic coolants

Fuel pin claddings of reactor BREST-OD-300 are the most stressful elements of fuel assemblies (time being in core is 5-6 years), which are exposed to lead coolant, products of fuel transmutation (at temperatures up to 650 °C), neutron field with damage dose up to 125 dpa and tensile stresses, especially in the end of campaign, and other factors.

One of the basic requirements for the cladding material of reactor with lead coolant is corrosion and erosion resistance in lead. For protection against liquid metal corrosion it is necessary to maintain the oxygen regime of coolant in a certain range. Requirements for corrosion resistance and the requirements for high irradiation resistance restrict the range of possible materials for core elements of the lead-cooled reactors.

Development of steels for cladding tubes of reactors with lead coolant and the operating experience of this type of reactors has shown that for the levels of temperature 400-650 °C (the parameters of reactor BREST-OD-300) can be used heat resistant 12% Cr steels alloyed by silicon. This element increases the tendency of steel to form a protective film on the surface of samples (products) and promotes healing of defects in the film and thus increases the corrosion and erosion resistance of steels in heavy liquid metal coolant.

The most explored and tested in reactors of this type is steel EP823 (Fe-12Cr-1,2Si-0,8Mo-0,3V-0,3W-0,3Nb-0,16C). At present time steel EP823 is considered as the basic material for cladding tubes and elements of fuel assemblies of reactor BREST-OD-300.

A prospective direction in creation of cladding materials for reactor BREST-OD-300 is the use of bi-metallic cladding tube with layer from corrosion resistant silicon-containing steel, which contacts with coolant, and the basis from heat resistant steel such as EP823.

In addition, as a promising cladding materials for fast reactors with lead and lead-bismuth eutectic coolants are considered ODS steels of different compositions. In particular, in 2012 samples of steels EP823 ODS and (Fe-16Cr-4Al-2W-0,3Ti)ODS were put to corrosion testing in dynamic test bench with lead coolant.

Conclusion

It is shown that for sodium cooled reactors the key challenge is creation of radiation resistant and heat resistant cladding materials, which must ensure the achievement of damage doses at least 140 dpa.

The solution of this problem is provided by phased use as cladding materials of austenitic steels ChS68 and EK164 (maximum damage doses ~ 92 and ~110-115 dpa, respectively), precipitation-hardening heat resistant ferritic-martensitic steels EK181 and ChS139 (maximum damage dose ~140 dpa) and oxide dispersion strengthened (ODS) steels (maximum damage dose more than 140 dpa).

For development of core materials for reactors with lead and lead-bismuth eutectic coolants the most serious challenge is corrosion resistance of materials in coolant. Therefore at present time a very wide range of works on study of corrosion resistance of candidate materials is carrying out. As the basic material for the cladding tubes is considered a ferritic-martensitic steel EP823 with high silicon content.

REFERENCES

- [1] RESHETNIKOV F.G., MITENKOV F.M., TROYANOV M.F. Status and prospects of development of radiation-resistant structural core materials of fast reactors in USSR. International Conference on Radiation Materials, Alushta, 1990, Vol. 1, p.p. 15-23
- [2] BAKANOV M.V., KRYUKOV O.V., BUDANOV U.P. et al. Optimization of structural state of cladding tubes from steel ChS68 in cold-worked condition. Nuclear Energy, 2005, Vol. 1, p.p. 139-145
- [3] LEONTEVA-SMIRNOVA M.V., IOLTUKHOVSKY A.G., ARUTUNOVA G.A. et al. "Investigation of heat treatment conditions on the structure of 12% chromium reduced activation steels". Journal of Nuclear Materials, 2002, V. 307-311, p. 466-

- [4] CHERNOV V.M., LEONTEVA-SMIRNOVA M.V. , M.M. POTAPENKO et. al. Structural Materials for Fusion Power Reactors – the RF R&D Activities. Nuclear Fusion 2007, 47, p. 839-848
- [5] A.N. TYUMENTSEV, V.M. CHERNOV, M.V. LEONTYEVA-SMIRNOVA et al. Microstructural features of ferritic-martensitic (12% Cr) steel EK181 after different heat treatments. Journal of Technical Physics, 2012, Vol. 82, Issue 1
- [6] A.A. NIKITINA, V.S. AGEEV, M.V. LEONTYEVA-SMIRNOVA, B.V. SAFRONOV, A.P.CHUKANOV, V.V. TSVELEV, M.M. POTAPENKO, V.V. SAGARADZE «Development of ODS ferritic-martensitic steels for Inoovative Nuclear Fast Breeder Reactors» Structural Materials for Innovative Nuclear Systems. Workshop Proceedings Karlsruhe, Germany, 4-6 June 2007 (Nuclear Energy Agency) pp. 127-135
- [7] V.S. AGEEV, A.A. NIKITINA, A.P. CHUKANOV, M.V. LEONTYEVA-SMIRNOVA, M.M. POTAPENKO, B.V. SAFRONOV, V.V. TSVELEV R&D of ODS steels for fuel pin claddings of fast neutron reactors. International Conference on Fast Reactors and Related Fuel Cycles (FR09) December 7 – 11, 2009, Kyoto, Japan
- [8] A.A. NIKITINA, V.S. AGEEV, A.P. CHUKANOV, V.V. TSVELEV, N.P. POREZANOV, O.A. KRUGLOV «R&D of ferritic–martensitic steel EP450 ODS for fuel pin claddings of prospective fast reactors». Journal of Nuclear Materials. Vol. 428 (2012) pp. 117–124